

ARRHYTHMOGENIC SARCOPLASMIC RETICULUM CALCIUM LEAK IN ISOLATED VENTRICULAR CARDIOMYOCYTES

CHANGES IN HEART FAILURE AND MECHANISMS OF PHARMACOLOGICAL MODULATION

PhD Thesis

*Myocardial Function Section, National Heart and
Lung Institute, Imperial College London*

Dr Markus B Sikké BSc MBBS MRCS MRCP

*Wellcome Trust Clinical Research Fellow in Cardiology, National Heart and Lung Institute,
Imperial College, London*

SUPERVISORS

Dr Kenneth T MacLeod

*Reader in Cardiovascular Physiology, National Heart and Lung Institute, Imperial College,
London*

Dr Alexander R Lyon

BHF Senior Lecturer, National Heart and Lung Institute, Imperial College, London

Prof Sian E Harding

*Professor of Cardiac Pharmacology, National Heart and Lung Institute, Imperial College,
London*

ABSTRACT

Cardiomyocyte contraction involves sarcolemmal depolarization causing a small influx of Ca^{2+} which is then amplified via a larger release from the sarcoplasmic reticulum (SR). Under certain conditions SR Ca^{2+} is released in the absence of depolarization - so called SR Ca^{2+} leak. This is thought to be a key cause of arrhythmogenesis in heart failure (HF).

The aims of this thesis were to assess how SR leak changes in a rat model of HF induced by chronic myocardial infarction (MI) and the mechanism of modulation using I_{Na} blockers. Several novel methodologies were developed to do this including the use of hierarchical statistical analysis which reduced the chance of type I errors in comparison to standard techniques.

Detailed assessment of the HF model showed that there was fluid retention and eccentric hypertrophic remodelling of an impaired left ventricle by 16 weeks post MI which were more marked compared with earlier timepoints. Although under basal conditions Ca^{2+} leak was similar in HF and control cells, leak enhancement in response to isoprenaline was more marked in HF cells and there were significant heterogeneities in leak when comparing the borderzone to remote regions. At an earlier stage (8 weeks post MI) we found more frequent Ca^{2+} waves even under basal conditions. Analysis of Ca^{2+} leak in 3-D for the first time using a novel microscopy technique showed that arrhythmogenic waves originate from regions of preserved t-tubules. Finally we explored the use of flecainide to inhibit SR leak and showed that it acts via reduction of I_{Na} , which enhances Ca^{2+} efflux via the $\text{Na}^+/\text{Ca}^{2+}$ exchanger.

In conclusion this thesis has drawn on several novel methodologies to gain a deeper understanding of SR leak, both in terms of how it changes in HF and by exploring a novel mechanism by which it can be reduced.

TABLE OF CONTENTS

FRONT MATTER

Abstract	2
Statement of Originality	8
Copyright Declaration	9
Acknowledgements	10
List of Figures	12
List of Tables	15
List Of Equations	17
Abbreviations	18
Symbols	21
1 INTRODUCTION	22
1.1 EXCITATION-CONTRACTION COUPLING IN THE NORMAL CARDIOMYOCYTE	22
1.2 THE SARCOPLASMIC RETICULUM	23
1.2.1 <i>Control of contractility by increasing Ca^{2+} sequestration into the SR</i>	25
1.2.2 <i>Control of other key proteins involved in CICR</i>	25
1.2.3 <i>Contribution of CaMKII</i>	26
1.3 SR LEAK	27
1.3.1 <i>Ca^{2+} sparks</i>	27
1.3.2 <i>Sparks vs Quarks</i>	28
1.3.3 <i>Ca^{2+} Waves</i>	28
1.3.4 <i>SR Ca^{2+} Leak and Triggered Arrhythmia</i>	29
1.4 HEART FAILURE	30
1.4.1 <i>Epidemiology and Burden of Disease</i>	30
1.4.2 <i>Arrhythmogenic Changes in Ca^{2+} Handling in Heart Failure</i>	30
1.5 INTERPLAY BETWEEN CELLULAR TRIGGERED ACTIVITY AND RE-ENTRY	31
1.5.1 <i>Re-entrant Arrhythmias</i>	31
1.5.2 <i>The role of SR leak in arrhythmias in the intact heart</i>	32
1.5.3 <i>How does SR leak cause ventricular arrhythmia</i>	33
1.6 TARGETING SR LEAK TO REDUCE THE RISK OF VENTRICULAR ARRHYTHMIA	34
1.6.1 <i>The cardiac ryanodine receptor</i>	34
1.6.2 <i>Targeting RyR2 by reducing phosphorylation</i>	36
1.6.3 <i>Targeting RyR2 directly</i>	37
1.6.3.1 <i>Rycals</i>	37
1.6.3.2 <i>Flecainide</i>	38
1.7 CONCLUSION	39
1.8 HYPOTHESES	39
2 METHODS	41
2.1 ANIMAL MODELS	41
2.2 RAT MYOCARDIAL INFARCTION	41
2.2.1 <i>Complications</i>	42
2.2.2 <i>Planimetry to Ensure Large Myocardial Infarctions</i>	43
2.3 BIOMETRIC AND FUNCTIONAL MEASURES OF CONTRACTILITY	44
2.3.1 <i>Biometry</i>	45
2.3.2 <i>Echocardiography</i>	45
2.3.3 <i>Pressure-Volume Loops</i>	47

2.3.4	<i>Validity of the use of Age-Matched Control versus Sham Animals</i>	49
2.4	ISOLATION OF RAT CARDIAC MYOCYTES	49
2.5	EXPERIMENTS ON INTACT ISOLATED RAT CARDIOMYOCYTES	50
2.5.1	<i>Cell preparation and dye loading</i>	50
2.5.2	<i>Cell selection</i>	50
2.5.3	<i>Experimental setup</i>	50
2.5.4	<i>Imaging Ca²⁺ Sparks, Waves and Transients using Confocal Line Scanning</i>	51
2.5.5	<i>Imaging Using Epifluorescence Microscopy</i>	53
2.5.5.1	Epifluorescence imaging of fluo-4	53
2.5.5.2	Epifluorescence imaging of fura-2	53
2.5.6	<i>Data analysis</i>	54
2.5.6.1	Ca ²⁺ Transients	54
2.5.6.2	Transient dyssynchrony	54
2.5.6.3	Ca ²⁺ Waves	57
2.5.6.4	Ca ²⁺ Sparks	58
2.5.6.5	Epifluorescence Data Analysis	60
2.6	STATISTICAL ANALYSIS	60
3	HIERARCHICAL STATISTICAL TECHNIQUES TO REDUCE RISK OF TYPE I ERROR IN CARDIOMYOCYTE STUDIES	62
3.1	AIMS	62
3.2	INTRODUCTION	62
3.3	METHODS	65
3.3.1	<i>Rat HF Model and Myocyte Imaging</i>	65
3.3.2	<i>Statistical Analysis</i>	66
3.3.2.1	Hierarchical Statistical Techniques	66
3.3.2.2	Running the models	68
3.4	RESULTS	68
3.4.1	<i>Ca²⁺ Transient Morphology in HF versus AMC</i>	68
3.4.2	<i>Ca²⁺ Spark Data</i>	71
3.5	DISCUSSION	74
3.5.1	<i>Studies of Ca²⁺ Fluxes in Isolated Cardiomyocytes are Inconsistent</i>	74
3.5.2	<i>Hierarchical Statistical Analysis Improves the Analysis of Ca²⁺ Flux Data Compared with Basic Statistical Tests</i>	75
3.5.3	<i>Alternatives to Hierarchical Statistics – Aggregation and Disaggregation</i>	75
3.5.4	<i>Improving Statistical Testing in Cardiomyocyte Studies</i>	76
3.5.5	<i>Limitations</i>	77
3.6	CONCLUSIONS AND IMPLICATIONS	77
4	IN VIVO CARDIAC FUNCTION IN RATS FOLLOWING MYOCARDIAL INFARCTION	79
4.1	AIMS	79
4.2	INTRODUCTION	79
4.3	METHODS	80
4.4	RESULTS	80
4.4.1	<i>Biometry Suggests Fluid Retention, Pulmonary Oedema and Cardiac Hypertrophy in HF Model</i> ..	80
4.4.2	<i>Echocardiography reveals impaired systolic function and progressive LV dilatation following MI</i>	84
4.4.3	<i>PV Loops show reduced systolic and diastolic function post MI with progressive reduction in ESPVR slope</i>	88
4.5	DISCUSSION	93
4.5.1	<i>Biometric data shows early exaggerated cardiac hypertrophy and later fluid retention and pulmonary oedema in HF model</i>	93

4.5.2	<i>Echocardiography reveals increasing LV dilatation over time post MI but Preserved Cardiac Index</i>	94
4.5.3	<i>PV Loops confirm progressive LV dilatation and show progressive reduction in ESPVR post MI</i>	94
4.5.4	<i>Conclusions and Implications</i>	95
5	CHANGES IN Ca^{2+} TRANSIENTS AND SPONTANEOUS SR Ca^{2+} LEAK IN CARDIOMYOCYTES FROM RATS WITH ESTABLISHED HEART FAILURE	97
5.1	AIMS	97
5.2	INTRODUCTION	97
5.3	METHODS	98
5.4	RESULTS	98
5.4.1	<i>Cell size.....</i>	98
5.4.2	<i>Ca^{2+} transient morphology and synchronicity under basal conditions.....</i>	99
5.4.3	<i>Ca^{2+} Transient morphology and synchronicity under β-adrenergic stimulation</i>	101
5.4.4	<i>Ca^{2+} transient morphology and synchronicity in the borderzone.....</i>	103
5.4.5	<i>Ca^{2+} spark frequency and morphology under basal conditions, β-adrenergic stimulation and in the borderzone</i>	105
5.4.6	<i>Wave Characteristics and Frequency.....</i>	109
5.4.7	<i>SR Ca^{2+} Content</i>	111
5.5	DISCUSSION	112
5.5.1	<i>Cardiomyocyte hypertrophy</i>	112
5.5.2	<i>Ca^{2+} transient morphology and dyssynchrony</i>	113
5.5.3	<i>Ca^{2+} Spark Frequency and Morphology</i>	114
5.5.4	<i>Effects of β-adrenergic stimulation on transients and sparks</i>	114
5.5.5	<i>Spontaneous SR Ca^{2+} release is reduced at the borderzone.....</i>	115
5.6	CONCLUSIONS AND IMPLICATIONS	116
6	OBLIQUE PLANE MICROSCOPY REVEALS THAT ARRHYTHMOGENIC CALCIUM WAVES ORIGINATE IN REGIONS OF WELL ORGANIZED T-TUBULES IN HEART FAILURE	118
6.1	AIMS	118
6.2	INTRODUCTION	118
6.3	METHODS	119
6.3.1	<i>The OPM experimental setup.....</i>	119
6.3.2	<i>Sample Preparation and Imaging Protocols</i>	121
6.3.3	<i>Time-lapse 3-D data analysis</i>	121
6.3.4	<i>Time-lapse 2-D data analysis</i>	122
6.3.5	<i>Identification of T-tubules.....</i>	123
6.3.6	<i>Definitions of Subcellular Locations Used for Analysis.....</i>	124
6.3.7	<i>Linescan Data.....</i>	125
6.3.8	<i>Statistical Modelling and Significance Testing.....</i>	125
6.4	RESULTS	126
6.4.1	<i>In Vivo Cardiac Function and Cellular Phenotype in HF Model Animals Used for OPM Studies....</i>	126
6.4.2	<i>Study of spontaneous Ca^{2+} wave origins from time-lapse 3-D OPM imaging.....</i>	126
6.4.3	<i>Spark data from time-lapse 2-D OPM imaging.....</i>	129
6.4.3.1	<i>Spark Frequency.....</i>	129
6.4.3.2	<i>Spark Morphology is Dependent on Subcellular Spark Region</i>	130
6.5	DISCUSSION	132
6.5.1	<i>Novel methodologies used in this study.....</i>	132
6.5.2	<i>Novel biological insights into the origins of Ca^{2+} waves in HF</i>	132
6.5.3	<i>Comparisons with previous data.....</i>	133

6.5.4	<i>Explaining the propensity for tubulated regions to initiate waves</i>	133
6.5.5	<i>Limitations</i>	134
6.6	CONCLUSION	135
7	FLECAINIDE REDUCES Ca^{2+} SPARK AND WAVE FREQUENCY VIA INHIBITION OF THE SARCOLEMMA SODIUM CURRENT	136
7.1	AIMS	136
7.2	INTRODUCTION	136
7.3	METHODS	136
7.3.1	<i>Ventricular myocyte isolation and Ca^{2+} imaging of intact myocytes</i>	136
7.3.2	<i>Voltage-Clamp Technique</i>	137
7.3.3	<i>CamKII Inhibition</i>	137
7.3.4	<i>Assessment and Modulation of NCX function</i>	137
7.3.5	<i>Permeabilized Cardiomyocyte Experiments</i>	138
7.3.6	<i>Data-Pairing and Statistical Analysis</i>	138
7.4	RESULTS	139
7.4.1	<i>Flecainide has no effect on the Ca^{2+} Transient or SR Ca^{2+} Load</i>	139
7.4.2	<i>Flecainide reduces Ca^{2+} Spark and Wave Frequency & Ca^{2+} Wave Velocity</i>	140
7.4.3	<i>Specific I_{Na} Blockade Decreases Spark and Wave Frequency</i>	141
7.4.4	<i>How does I_{Na} reduction decrease Ca^{2+} Waves?</i>	143
7.4.5	<i>Mechanism of Wave Reduction with flecainide</i>	147
7.4.6	<i>Experiments on permeabilized myocytes confirm absence of direct effect of Na^+ and Flecainide on RyR</i>	149
7.5	DISCUSSION	152
7.5.1	<i>Main Findings</i>	152
7.5.2	<i>Mechanism of Wave Reduction Does Not Depend on CaMKII</i>	152
7.5.3	<i>Wave Reduction Does Not Result from Reduced SR Ca^{2+} Load</i>	153
7.5.4	<i>I_{Na} Reduction Increases Ca^{2+} Efflux via NCX which Reduces Ca^{2+} Waves</i>	153
7.5.5	<i>I_{Na} Blockers and SR Ca^{2+} Release</i>	154
7.6	CONCLUSIONS AND IMPLICATIONS	154
8	SUMMARY AND FINAL CONCLUSIONS	155
8.1	KEY METHODOLOGICAL TECHNIQUES	155
8.2	<i>IN VIVO DATA CONFIRMS PROGRESSION OF HF</i>	156
8.3	CARDIOMYOCYTE STRUCTURE AND FUNCTION IN HF	156
8.3.1	<i>Cell morphology and Ca^{2+} transients</i>	156
8.3.2	<i>SCR in HF</i>	157
8.3.3	<i>Correlation of cell ultrastructure and SCR</i>	157
8.4	MODULATING SCR BY REDUCING I_{Na}	157
8.5	FINAL CONCLUSIONS	158
9	APPENDICES	159
9.1	APPENDIX FOR METHODS CHAPTER (2)	159
9.1.1	<i>Biometric Correction to the Cube of Tibia Length is more appropriate than raw Tibia Length</i>	159
9.1.2	<i>Transient Analysis Macro (ImageJ)</i>	161
9.1.3	<i>Macro for Transient Dyssynchrony Analysis (ImageJ)</i>	171
9.1.4	<i>Macro for Wave Detection and Characterization (ImageJ)</i>	176
9.1.5	<i>Macro for Spark Image Pre-Processing (ImageJ)</i>	181
9.1.6	<i>Caffeine Transient Macro (ImageJ)</i>	183
9.1.7	<i>Assessing Most Appropriate Criterion Value Using the F-Score</i>	189

9.1.7.1	Selection of Criterion Value for Spark Detection	189
9.2	APPENDIX FOR HIERARCHICAL STATISTICS CHAPTER (3)	191
9.2.1	<i>Search Strategy For Murine Post-MI Studies of Ca^{2+} Handling</i>	191
9.2.2	<i>Table of Ca^{2+} Handling Changes in Post MI mouse HF models</i>	192
9.2.3	<i>Table of Spark Parameters in Post MI mouse HF models</i>	192
9.2.4	<i>Table of Spark Parameters in Pressure Overload Models</i>	192
9.2.5	<i>Syntax for 3-Level Random Intercept Hierarchical Model in SPSS</i>	193
9.3	APPENDIX FOR Ca^{2+} TRANSIENT AND SPARK DATA IN ESTABLISHED HF CHAPTER (5).....	194
9.3.1	<i>Statistics in multi-level models for Ca^{2+} transient and spark data in 16WMI model</i>	194
9.4	APPENDIX FOR OPM CHAPTER (6)	202
9.4.1	<i>Code For Spark Detection in 2D (Matlab)</i>	202
9.4.1.1	Description of algorithm	202
9.4.1.2	Matlab Code.....	202
9.4.1.3	LOCATE Sparks SUBPROC.....	208
9.4.1.4	Masked_Mean Subproc	208
9.4.1.5	Masked_mean_and_std Subproc	209
9.4.2	<i>Defining Sparks Versus Noise in 2D OPM Data</i>	210
9.4.3	<i>Appendix 4 – ROC Co-ordinate Table for Prediction of True Positive Sparks in OPM dataset</i>	215
9.4.4	<i>Correlation of linescan data versus 2D data</i>	223
9.4.5	<i>Example Syntax in SPSS to Give Significance Tests of Pairwise Comparisons of Interaction between HF and Spark_Location</i>	225
9.4.6	<i>Tables of hierarchical statistics for assessment of spark parameters vs location</i>	225
9.5	APPENDIX FOR I_{Na} AND WAVES CHAPTER (7).....	234
9.6	APPENDIX OF PRIZES, PUBLICATIONS AND ABSTRACTS RELATED TO THIS THESIS.....	241
9.6.1	<i>Prizes</i>	241
9.6.2	<i>Publications</i>	241
9.6.3	<i>Abstracts</i>	242
10	REFERENCE LIST	245

STATEMENT OF ORIGINALITY

The material presented in this report is the original work of the author. Any contributions from others are clearly stated below (page 10).

COPYRIGHT DECLARATION

The copyright of this thesis rests with the author and is made available under a Creative Commons Attribution Non-Commercial No Derivatives licence. Researchers are free to copy, distribute or transmit the thesis on the condition that they attribute it, that they do not use it for commercial purposes and that they do not alter, transform or build upon it. For any reuse or redistribution, researchers must make clear to others the licence terms of this work.

ACKNOWLEDGEMENTS

Thanks to Tom Collins for always being ready and able to explaining many aspects of myocyte biology in the first year of this project and helping with patch clamp experiments (approx half of the flecainide patch clamp experiments were performed by him and the other half by me under his supervision). Thanks to Peter O’Gara for his unparalleled abilities in myocyte isolation, the vast majority of isolations were performed by him. Thanks to Christina Rowlands who performed the majority of fura-2 experiments included in this thesis.

I supervised two BSc students during this project who both worked very hard - thanks to Mit Shah for his input into initial flecainide experiments (although no data included from these unpaired experiments in this final draft). Thanks to Becker Al-Khayatt also for performing ranolazine wave experiments which are not included in this thesis but solidified some hypotheses.

Thanks to Sunil Kumar and Chris Dunsby for building and running the OPM as well as programming spark analysis code in Matlab. Thanks to Vincent Maioli for writing the code for t-tubule identification in 2D. Thanks also to Fabiana Gordon in the Statistical Advisory Service at Imperial who helped me decide on the most appropriate statistical techniques for data analysis and checked through the statistical models I used in this thesis.

Finally thanks to my supervisors who have been a source of guidance and mentoring throughout this project and when planning the next steps. Ken is literally an award winning supervisor having won the NHLI award for supervision in 2013 based on my nomination. The highlights of being supervised by him include his open door policy, his opportunistic teaching (including at the pub – I still have the napkin on which he drew the quantification of rate of inactivation of the Ca^{2+} channel) and his pastoral care which helped me through difficult times. Furthermore his technical ability to disassemble and re-assemble a microscope was something I started off by admiring and gave me the confidence to do the same myself so that I could collect the best data I could. Probably most importantly for a supervisor and a scientist he never pressurizes that the results of an experiment should go one way or another. Ken is interested only in the scientific truth rather than following dogmatically what has been found previously.

Sian was an ever-present guiding star in my research and laid down the ground rules for good research practice and good writing techniques very early on in this project. She has allowed me the freedom to take my research in my own direction but gently nurtured some of the more fruitful paths that I ended up going down. Her regular research meetings were a real highlight and allowed me initially to hone my presentation skills and then later to contribute to discussions regarding a wide range of research. Sian made me feel like a valued member of the team despite my relative inexperience and her reputation around the world made it much easier to present my work to my peers nationally and internationally.

Alex guided me to become part of the group and planned the first stages of my research. His energy, commitment and unparalleled abilities to network and multi-task continue to be hugely inspirational to me. He is a real rising star of cardiovascular research and I feel privileged to have been supervised by him. He has been an amazing example of how a successful scientific and clinical career can be combined and can even complement each other. I value his advice and mentorship and with his

continued help I hope to be able to follow in his footsteps towards becoming a clinician-scientist. I sincerely hope to continue working with Ken, Sian and Alex in the future.

This work is dedicated to my parents Christa and Bernard for working so hard and sacrificing so much so that I could reach this point. And to my wife Kelly and children Evan, Alex and Luka who are the light of my life...

LIST OF FIGURES

Figure 1-1. Schematic diagram of excitation contraction coupling in the ventricular cardiomyocyte.	23
Figure 1-2. E1-E2 Ca transport scheme via which SERCA2a transports Ca into the SR lumen.	24
Figure 1-3. Re-entry of Excitation.	32
Figure 1-4. Examples of spiral waves	32
Figure 1-5. The leaky ryanodine receptor and therapies which stabilize the channel	36
Figure 2-1 ECG Changes observed during rat MI	42
Figure 2-2. Planimetry to Assess MI Size and Ensure High Quality Surgery	44
Figure 2-3. Echocardiographic Imaging and Measurements Obtained	47
Figure 2-4. Diagram showing the calculation of energy efficiency from PV loops.	48
Figure 2-5. Cardiac function of sham rats is not markedly different to cardiac function of AMC rats at same age.	49
Figure 2-6. Imaging of $[Ca^{2+}]_i$ Using Confocal Microscopy in Line scan Mode	52
Figure 2-7. Dyssynchrony analysis of Ca^{2+} Transients	56
Figure 2-8. Differences in Wave Morphology.	58
Figure 2-9. Pseudosparks	59
Figure 3-1. Hierarchical structure of data attained from studies of isolated cardiomyocytes.	65
Figure 3-2. Graphical representation of difference between standard linear regression and random intercept model.	67
Figure 3-3. Transient amplitude characteristics in AMC and HF cells.....	70
Figure 3-4. Examples of hierarchical data structure of Ca^{2+} Transient Parameters.....	71
Figure 3-5. Spark characteristics in AMC and HF cells.	73
Figure 3-6. Hierarchical clustering of spark data.	74
Figure 4-1. There is progressive increase in BW/TL ³ over time in the HF model.	81
Figure 4-2. LW is increased at 16WMI stage suggestive of pulmonary oedema.	82
Figure 4-3. Cardiac hypertrophy is present in HF at all timepoints but is most marked at 4WMI stage.	83
Figure 4-4. LV wall and cavity dimension in HF versus control animals.	85
Figure 4-5. Representative M-mode echocardiography images showing increase in LVIDd 16W following MI	86
Figure 4-6. Pump function is reduced following MI.....	87
Figure 4-7. Representative PA Doppler waveforms in AMC and MI.....	88
Figure 4-8. Steady state PV loop measurements in 4 and 16W MI hearts.	89
Figure 4-9. End diastolic pressure and dP/dt max and min post MI.....	90
Figure 4-10. Dynamic measures of cardiac function measured with PV loops.	91
Figure 4-11. Representative PV loops during IVC occlusion in 16WAMC and 16WMI rats.....	92
Figure 5-1. Cells are longer and wider in HF. The subset of HF cells from the borderzone are shorter than cells from remote regions.....	99
Figure 5-2. Transient morphology is not altered in HF.	100
Figure 5-3. Transient dyssynchrony does not change significantly in HF.	101
Figure 5-4. Effects of 30nM isoprenaline on Ca^{2+} transient characteristics in AMC and HF cells.....	102
Figure 5-5. Dyssynchrony of Ca^{2+} transients +/- isoprenaline in HF vs AMC myocytes.	103
Figure 5-6. Analysis of transients of cells from the borderzone versus remote areas.	104

Figure 5-7. Analysis of transient dyssynchrony in cells isolated from borderzone versus remote regions.....	105
Figure 5-8. Spark frequency and morphology are not altered in HF	106
Figure 5-9. Spark FWHM and mass are enhanced by isoprenaline in HF but not AMC cells.....	108
Figure 5-10. Spark Morphology is unchanged in borderzone regions.....	109
Figure 5-11. Waves exhibit similar characteristics and frequency in AMC vs HF.	110
Figure 5-12. Wave free survival is prolonged in borderzone cells.....	111
Figure 5-13. SR load and caffeine transient decay rate does not change in HF. There is no significant difference between these parameters in the borderzone versus remote regions within HF cells. ...	112
Figure 6-1. The OPM experimental setup.	120
Figure 6-2. Time-lapse 2-D spark imaging with OPM.....	122
Figure 6-3 Identification of T-Tubule locations within cardiomyocytes.	124
Figure 6-4. <i>In vivo</i> cardiac function and cellular phenotype of HF rats.	127
Figure 6-5. Montages showing time-lapse 3-D OPM of spontaneous calcium wave origin.	128
Figure 6-6. T-tubule modulation in relation to wave origin.	129
Figure 6-7. Spark frequency varies according to cell region.	130
Figure 6-8. Changes in spark morphology by cell region	131
Figure 7-1. Experimental Protocol and Effects of Flecainide on Ca^{2+} transients and Ca^{2+} sparks.....	139
Figure 7-2. Effects of 5 μM flecainide on Ca^{2+} waves.	141
Figure 7-3. Effects of specific I_{Na} inhibition by tetrodotoxin (TTX) on SR Ca^{2+} release events.....	143
Figure 7-4. Possible hypotheses to explain how I_{Na} can contribute to wave initiation and propagation.	145
Figure 7-5. Elucidation of “Mechanism A” as most likely cause for reduction in Ca^{2+} waves due to I_{Na} blockade.....	146
Figure 7-6. Role of CaMKII and NCX in wave reduction by flecainide.	148
Figure 7-7. Neither changing $[\text{Na}^+]$ nor [flecainide] has any effect on waves in permeabilized cardiomyocytes.....	150
Figure 7-8. Raw data from permeabilized cells.....	151
Figure 7-9. Fluorescence trace of permeabilised myocyte immediately after application of flecainide.	152
Figure 9-1. Simple model and real data from control rats showing HW/TL^3 is constant with changes of overall body size whilst HW/TL is unstable.....	159
Figure 9-2. F-Score and Criterion.	190
Figure 9-3. Transformations of raw data to give approximately Gaussian distributions.	211
Figure 9-4 Histogram of spark area distribution.....	212
Figure 9-5. ROC curves for automated selection of noise-related sparks.	213
Figure 9-6. Table showing area under the curve for each predictor.	214
Figure 9-7. Noise-exclusion criteria results in a reduction of the prominence of small “noise” sparks.	214
Figure 9-8. Positive skew in 1D spark amplitude data reduced by 2D analysis of same data.	223
Figure 9-9. Correlation of 2D data with 1D data extracted from the same dataset analysed with criterion 6.....	224
Figure 9-10. Effect of stimulation frequency on Ca^{2+} waves and effect of flecainide on Ca^{2+} transient morphology.....	234
Figure 9-11. Supplementary effects of I_{Na} blockers on Ca^{2+} waves.....	235

Figure 9-12. Hierarchical model analyzing wave frequency with flecainide	236
Figure 9-13. Ca^{2+} spark morphology is not significantly altered by flecainide.....	237
Figure 9-14. F/F0 traces of a single cell in a control experiment and with rapid wash on of 50 μM TTX.	238
Figure 9-15. Mechanism of wave reduction with flecainide supplementary data	239
Figure 9-16. Effect of altering concentration of free Ca^{2+} on waves	240

LIST OF TABLES

Table 2-1. Fatal complications of rat MI surgery.	43
Table 2-2. Categorization of MI Size	44
Table 2-3. Dyssynchrony of transients in Figure 2-7.....	57
Table 3-1. Summary of changes in electrically evoked Ca^{2+} transients and SR load assessment in rat models of post MI HF.....	63
Table 3-2. Summary of studies which have assessed spark parameters in murine species following MI.....	64
Table 3-3. Analysis of Ca^{2+} transient parameters using standard and hierarchical statistical tests.	69
Table 3-4. Spark data analysed by hierarchical versus standard statistical tests.	72
Table 6-1. Summary of the number of cells and waves assessed during time-lapse 3-D imaging of spontaneous calcium waves.	126
Table 9-1. Example syntax for assessment of the effects of isoprenaline on transient amplitude in HF and control cells.....	194
Table 9-2. Estimates of fixed effects for Ca^{2+} transient amplitude +/- isoprenaline in HF vs control cells.	194
Table 9-3. Estimates of fixed effects for Ca^{2+} transient time to peak +/- isoprenaline in HF vs control cells.	195
Table 9-4. Estimates of fixed effects for Ca^{2+} transient time to peak +/- isoprenaline in HF vs control cells.	195
Table 9-5. Estimates of fixed effects for Ca^{2+} transient time to 90% decay (TD90) +/- isoprenaline in HF vs control cells.	196
Table 9-6. Estimates of fixed effects for Ca^{2+} transient dyssynchrony of time to 50% peak (dysTt50P) +/- isoprenaline in HF vs control cells.	196
Table 9-7. Estimates of fixed effects for Ca^{2+} transient dyssynchrony of time to peak (dysTtP) +/- isoprenaline in HF vs control cells.....	197
Table 9-8. Estimates of fixed effects for Ca^{2+} transient dyssynchrony of amplitude (dysAmp) +/- isoprenaline in HF vs control cells.....	198
Table 9-9. Estimates of fixed effects for Ca^{2+} transient dyssynchrony of Tau (dysTau) +/- isoprenaline in HF vs control cells.	198
Table 9-10. Estimates of fixed effects for Spark Frequency +/- isoprenaline in HF vs control cells. ...	198
Table 9-11. Estimates of fixed effects for Spark Amplitude +/- isoprenaline in HF vs control cells. ...	199
Table 9-12. Estimates of fixed effects for Spark FWHM +/- isoprenaline in HF vs control cells.....	199
Table 9-13. Estimates of fixed effects for Spark FDHM +/- isoprenaline in HF vs control cells.....	200
Table 9-14. Estimates of fixed effects for Spark Mass +/- isoprenaline in HF vs control cells.....	200
Table 9-15. Estimates of fixed effects for Spark mediated SRMass +/- isoprenaline in HF vs control cells.	201
Table 9-16. R^2 values and p values of correlations between 1D and 2D data.	224
Table 9-17. Estimates of fixed effects for analysis of spark frequency in detubulated vs tubulated regions.....	225
Table 9-18. Estimates of fixed effects for analysis of spark frequency in epitubular vs paratubular regions.....	227
Table 9-19 Estimates of fixed effects for analysis of spark amplitude in detubulated vs tubulated regions.....	228

Table 9-20. Estimates of fixed effects for analysis of spark amplitude in epitubular vs paratubular regions..... 229

Table 9-21. Estimates of fixed effects for analysis of spark area in detubulated vs tubulated regions. 230

Table 9-22. Estimates of fixed effects for analysis of LogArea in epitubular vs paratubular regions. 231

Table 9-23. Estimates of fixed effects for analysis of LogFDHM in detubulated vs tubulated regions. 232

Table 9-24 Estimates of fixed effects for analysis of LogFDHM in epitubular vs paratubular regions. 233

LIST OF EQUATIONS

Equation 2-1. Equation to calculate energetic efficiency from PV loops.....	48
Equation 2-2. Calculation of $[Ca^{2+}]_i$ using fura-2 fluorescence.	53
Equation 2-3. First order decay equation.	54
Equation 3-1. Conventional linear regression.....	66
Equation 3-2. Linear regression including HF as a parameter	66
Equation 3-3. The basic random intercept model	67
Equation 3-4. Three level random intercept model	68
Equation 9-1. Accuracy	189
Equation 9-2. Recall (or sensitivity)	189
Equation 9-3. Precision (or positive predictive value)	189
Equation 9-4. F-Score	189

ABBREVIATIONS

1D	One Dimensional
2D	Two Dimensional
3D	Three Dimensional
AC	Adenylyl Cyclase
ACE	Angiotensin Converting Enzyme
AHA	American Heart Association
AHF	Acute Heart Failure
AMC	Age Matched Control
Ao	Aorta
AOTF	Acousto-Optic Tunable Filter
AP	Action Potential
APD	Action potential duration
AT	Acceleration time (derived from pulmonary artery blood velocity trace)
AT/ET	Ratio of pulmonary artery acceleration time to ejection time
ATP	Adenosine Triphosphate
BW	Body weight
BZ	Borderzone
C1	Cylindrical lens 1
CABG	Coronary Artery Bypass Grafting
CaMKII	Calcium/calmodulin–dependent serine/threonine kinase II
cAMP	cyclic Adenosine Monophosphate
CCF	Congestive Cardiac Failure
CHF	Chronic Heart Failure
CI	Cardiac Index (cardiac output corrected to body weight)
CICR	Calcium Induced Calcium Release
CMO	Cell Mask Orange
Cri1	First Criterion (used in spark detection algorithms)
Cri2	Second Criterion (used in spark detection algorithms)
CRU	Calcium Release Unit
DAD	Delayed After Depolarization
DHPR	Dihydropyridine receptor
DMEM	Dulbecco's Modified Eagle Medium
DysTt50P	Dyssynchrony of time to 50% peak amplitude of transient
DysTt90P	Dyssynchrony of time to 90% peak amplitude of transient
DysTtP	Dyssynchrony of time to peak amplitude of transient
DysAmp	Syssynchrony of the peak amplitude of the transient
DysTau	Dyssynchrony of decay constant (tau) of transient
EAD	Early After Depolarization
EC	Excitation-Contraction
ECG	Electrocardiogram
ESC	European Society of Cardiology
ET	Ejection time (derived from pulmonary artery blood velocity trace)
F(t)	Fluorescence at time t

F_{membrane}	Fluorescence intensity of the membrane
F/F_0	Peak fluorescence in relation to baseline fluorescence
FKBP12.6	FK binding protein 12.6
FP1	Focal Plane 1
GRK	G-Protein coupled Receptor Kinase
HCM	Hypertrophic Cardiomyopathy
HF	Heart Failure
I-1	Inhibitor-1
I_{Ca}	L-Type Calcium Current
ICC	Intraclass correlation
I_{Ti}	Transient Inward Current
IVC	Inferior vena cava
K	Potassium (refers to ionic form K^+ unless otherwise stated)
KH	Krebs-Henseleit
L1	Spherical lens 1
LVAD	Left Ventricular Assist Device
LA	Left atrium
LAD	Left Anterior Descending [coronary artery]
LogAmp	Logarithm of spark amplitude
LogArea	Logarithm of spark Area
LogFDHM	Logarithm of spark full duration at half maximum
lps	lines per second
LTCC	L-Type Calcium Channel
LV	Left Ventricle
LVAWd	Left ventricular anterior wall thickness in diastole
LVAWs	Left ventricular anterior wall thickness in systole
LVEDP	Left ventricular end systolic pressure
LVEDV	Left ventricular end systolic volume
LVESV	Left ventricular end systolic volume
LVH	Left Ventricular Hypertrophy
LVIDd	Left ventricular internal diameter in diastole
LVIDs	Left ventricular internal diameter in systole
LVPWd	Left ventricular posterior wall thickness in diastole
LVPWs	Left ventricular posterior wall thickness in systole
MI	Myocardial Infarction
M_N	Normalized Modulation
Na	Sodium (refers to ionic form Na^+ unless otherwise stated)
NCX	Sodium-Calcium Exchanger
NICE	National Institute of Clinical Excellence
NYHA	New York Heart Association
OPM	Oblique Plane Microscope
PA	Pulmonary artery
$PA V_{\text{max}}$	Maximum velocity of blood movement in the pulmonary artery
PCI	Percutaneous Coronary Intervention
PDE	Phosphodiesterase

PKC	Protein Kinase C
PLB	Phospholamban
P _o	Open probability (of a channel)
PP1	Type 1 Protein Phosphatase
PROMISE	Prospective Randomized Milrinone Survival Evaluation Trial
PV	Pressure-volume (as in PV loops)
RAAS	Renin Angiotensin Aldosterone System
REVIVE II	Randomized Multicenter Evaluation of Intravenous Levosimendan Efficacy Trial
ROC	Receiver Operated Characteristic
RyR	Ryanodine Receptor (refers to RyR2 unless otherwise stated)
RyR2	Ryanodine Receptor 2 (cardiac isoform)
sc	subcutaneous
sCMOS	scientific Complementary Metal–Oxide–Semiconductor
SCD	Sudden Cardiac Death
SCR	Spontaneous Ca ²⁺ Release (from the sarcoplasmic reticulum)
SD	Standard Deviation
SERCA2a	Sarcoplasmic/Endoplasmic Reticulum Ca ATPase
SHIFT	Systolic Heart failure treatment with the I _f inhibitor ivabradine Trial
SHR	Spontaneously hypertensive rat
siRNA	small inhibitory RNA
SLIF	scattered light intensity fluctuation
SLN	Sarcolipin
SOICR	Store-overload-induced Ca ²⁺ release
SR	Sarcoplasmic reticulum
SURVIVE	Survival of Patients with Acute Heart Failure In Need Of Intravenous Inotropic Support
TAC	Transverse Aortic Constriction
TD50	Time to 50% decay (of Ca ²⁺ transient) from peak fluorescence
TD90	Time to 90% decay (of Ca ²⁺ transient) from peak fluorescence.
TL	Tibia length
TL1	Tube Lens 1
TnC	Troponin C
TOI	T-tubule Organization Index
TNF- α	Tumour Necrosis Factor- α
TnI	Troponin I
T-Tubule	Transverse Tubule
UK	United Kingdom
VAD	Ventricular Assist Device
VT	Ventricular Tachycardia
VTI	Velocity-Time Integral
VF	Ventricular Fibrillation

SYMBOLS

λ	Rate constant (reciprocal of decay constant)
τ	Decay constant
χ^2-2LL	Chi-squared test pertaining to goodness of fit of one statistical model over another

1 INTRODUCTION

Excitation-contraction (EC) coupling has been reviewed previously (Bers, 2001, 2002). Hence while the process in the normal cell will be covered briefly here, the emphasis will be placed on how the process can become deranged and result in arrhythmia through Ca^{2+} release from the sarcoplasmic reticulum (SR) which is not controlled by sarcolemmal excitation – so-called spontaneous SR Ca^{2+} release (SCR). This pathological process is thought to occur preferentially in heart failure (HF) and so this condition will be introduced together with a description of some of the changes in EC coupling which may make SCR more likely in HF.

1.1 Excitation-contraction coupling in the normal cardiomyocyte

EC coupling is the process by which depolarization of the sarcolemmal membrane as part of the action potential (AP) brings about activation of the contractile apparatus of the cell to produce cellular contraction in the systolic phase of the cardiac cycle. EC coupling results in a time-dependent increase and decrease in intracellular Ca^{2+} ($[\text{Ca}^{2+}]_i$) with every heartbeat which provides the signal to contract. Depolarization as part of the AP activates sarcolemmal Ca^{2+} channels (predominantly L-Type) and results in an influx of Ca^{2+} from extracellular fluid into the cell. There is amplification of this relatively small influx into a much larger Ca^{2+} release from the sarcoplasmic reticulum (SR) – so-called calcium induced calcium release (CICR) (Figure 1-1). In order for this to occur the L-Type Ca^{2+} Channels (LTCCs) are closely associated with clusters of cardiac ryanodine receptors (RyR2s) in the SR membrane. Ca^{2+} entry via the LTCCs induces opening of the RyRs which cooperatively gate and open in unison to produce the large cytoplasmic Ca^{2+} transient. The elevated cytoplasmic Ca^{2+} concentration ($[\text{Ca}^{2+}]_i$), interacts with Troponin C and alters its interaction with Troponins I and T. Troponin T binds tropomyosin and the changes to the troponin-tropomyosin complex which are brought about by increased $[\text{Ca}^{2+}]_i$ result in a shift of this complex into the axial groove of the actin filament (Bers, 2001). The resulting reduction in steric hindrance allows the binding of myosin's S1 head to actin and hence sarcomere shortening and the production of cardiac contractile force. Relaxation occurs as a result of the reduction of $[\text{Ca}^{2+}]_i$ by the sequestration of Ca^{2+} back into the SR and its extrusion to extracellular solution via the sarcolemma. This is brought about predominantly via the ATP-dependent uptake of Ca^{2+} into the SR by SERCA2a but also via the extrusion of Ca to the extracellular space by the sodium calcium exchanger (NCX) as well as other more minor contributions (e.g. mitochondria, sarcolemmal Ca^{2+} ATPase). The extrusion by NCX almost precisely matches influx via LTCCs during steady-state contraction. The relative contributions of SERCA2a and NCX to $[\text{Ca}^{2+}]_i$ efflux varies dependent on species with a 9:1 ratio in rodents and 7:3 in larger mammals. The fluxes across the sarcolemma of cardiomyocytes (influx via LTCC and efflux via NCX) are 10-100 times greater than in skeletal muscle, which affords cardiac myocytes the ability to rapidly alter their SR load in response to adrenergic stimulation (Eisner & Trafford, 2009) and also endows the cell with a longer AP which makes tetany almost impossible.

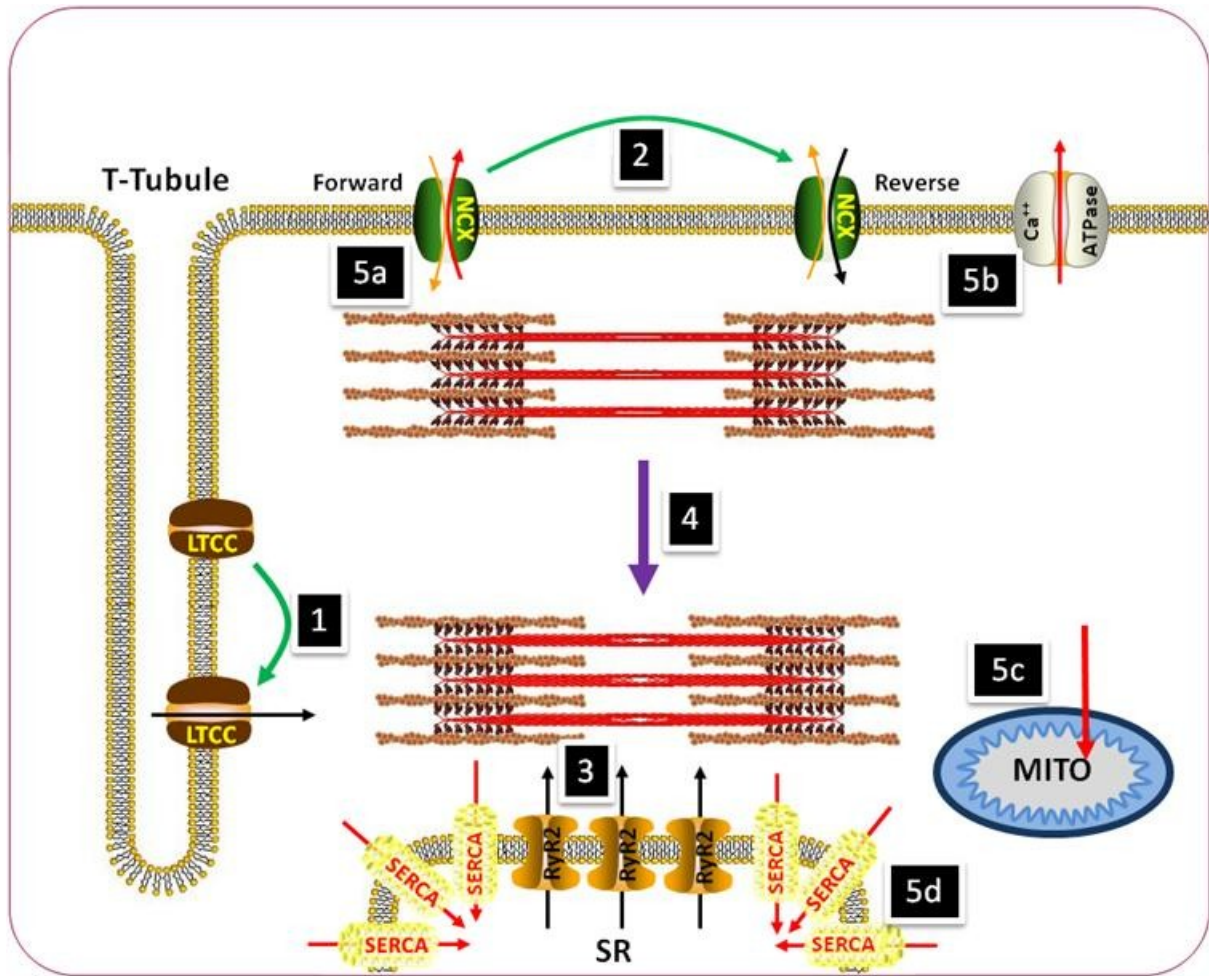


Figure 1-1. Schematic diagram of excitation contraction coupling in the ventricular cardiomyocyte. 1. Sarcolemmal depolarization causes L-Type Ca^{2+} channels (LTCC) to open resulting in influx of Ca^{2+} during systole. Ca^{2+} enters initially through the LTCC. 2. During the early stages of the action potential, the Na^+ - Ca^{2+} exchanger (NCX) also transitions from functioning in forward mode (Na^+ in Ca^{2+} out) to reverse mode (Ca^{2+} in Na^+ out) to further enhance the rise in $[\text{Ca}^{2+}]_i$. 3. The initial rise in $[\text{Ca}^{2+}]_i$ induces a larger release of Ca^{2+} from the sarcoplasmic reticulum (SR) via ryanodine receptors (RyR2) resulting in a large rise in $[\text{Ca}^{2+}]_i$. 4. This causes contraction of the myofilaments. 5. $[\text{Ca}^{2+}]_i$ is subsequently reduced to bring about diastole through movement out of the cytosol (a) via NCX in forward mode and (b) the sarcolemmal Ca^{2+} ATPase. (c) Ca^{2+} is also buffered by mitochondria. (d) The majority of Ca^{2+} movement in diastole is into the SR via SERCA2a. Green arrows – transitions brought about by sarcolemmal depolarization. Black arrows – routes of influx of Ca^{2+} to the cytosol during systole. Purple arrow – contraction of myofilaments. Red arrows – routes of efflux of Ca^{2+} during diastole.

1.2 The sarcoplasmic reticulum

The SR provides the large store of Ca^{2+} ready to be released in systole as a result of CICR. Other than relatively small areas of the terminal cisternae which are closely apposed to the sarcolemma, known as the junctional SR, most of the SR is specialized for Ca^{2+} uptake (the longitudinal SR) such that the vast majority of protein particles in the SR membrane are SERCA2a (Stewart & MacLennan, 1974; Franzini-Armstrong, 1975). SERCA2a transports the Ca^{2+} released during ECC back into the SR lumen against the electrochemical $[\text{Ca}^{2+}]$ gradient using chemical energy from ATP. The mechanism of Ca^{2+}

pumping follows the E1-E2 model (Figure 1-2). An initial state in which 2 Ca^{2+} ions can be accepted from the cytosol (E1) transitions, via an intermediate occluded state, to a final state (E2) in which the lumen is accessible by the Ca^{2+} ions concurrent with a sudden reduction in affinity of the protein for Ca^{2+} thus facilitating its rapid release into the SR (MacLennan & Green, 2000; Wuytack *et al.*, 2002). There are different SERCA isoforms which are functionally adapted to their location: SERCA1a is predominantly expressed in fast-twitch skeletal muscle; SERCA1b is expressed mainly in developing foetal fast-twitch skeletal muscle; SERCA2a is the dominant isoform in cardiomyocytes, but is also expressed in slow-twitch skeletal and smooth muscle; SERCA2b expression occurs in most cell types (the so-called “house-keeping” isoform), and predominates in vascular smooth muscle; finally SERCA3a and 3b are expressed in the reticuloendothelial system (Leberer *et al.*, 1989; Schulte *et al.*, 1993).

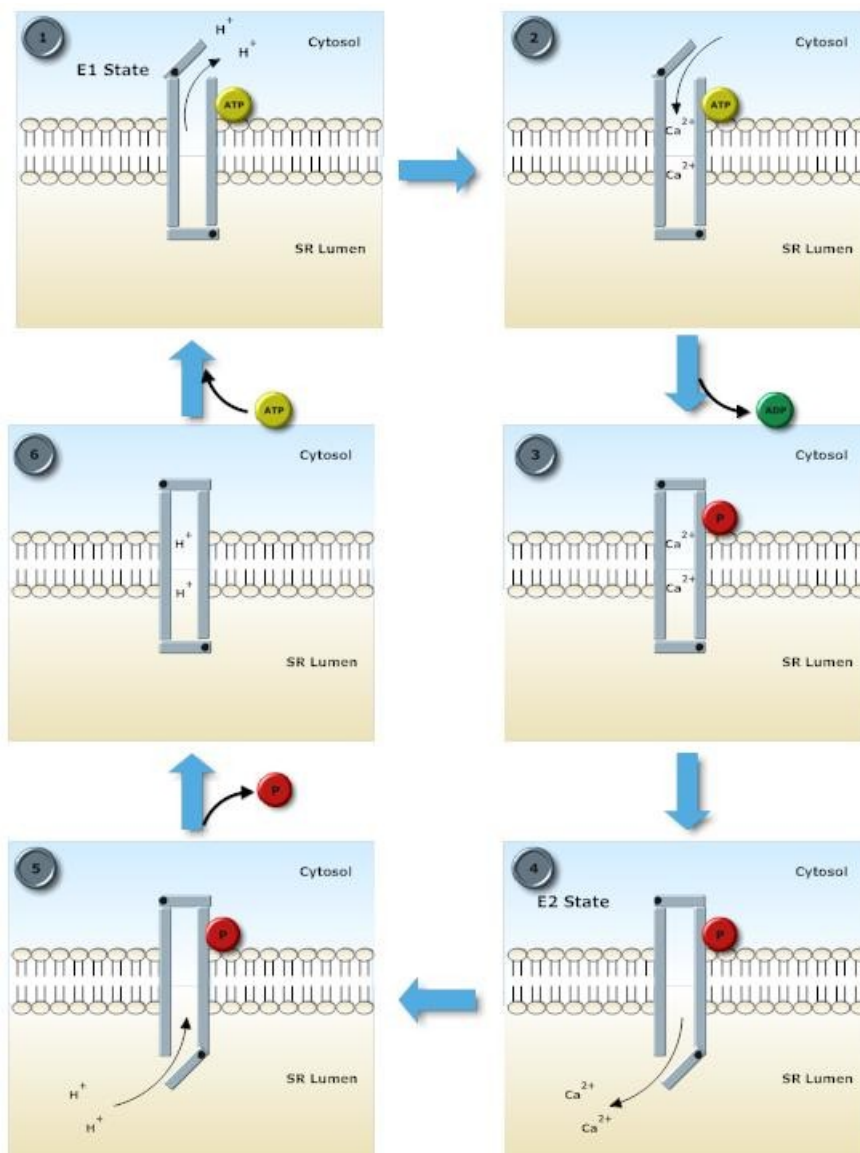


Figure 1-2. E1-E2 Ca transport scheme via which SERCA2a transports Ca into the SR lumen.

Stage 1 – In the E1 conformation, the high affinity Ca^{2+} binding sites are accessible by the cytosol. Protons leave the pump as ATP binds to allow access to the cytosol; stage 2 – 2 Ca^{2+} ions bind with high affinity; stage 3 – bound ATP is used to phosphorylate aspartate-351 causing a conformational

change which occludes Ca^{2+} . At this point the pump is in the high-energy unstable phosphointermediate condition; stage 4 – a further conformational change brings about the E2 form of SERCA2a where the SR lumen is accessible to Ca^{2+} . Ca^{2+} ions are released because of a lower affinity in the E2 state; stage 5 – protons replace Ca^{2+} ; stage 6 – aspartate-351 is dephosphorylated, bringing the pump into a low energy intermediate form which is unstable and returns to the E1 state.

1.2.1 Control of contractility by increasing Ca^{2+} sequestration into the SR

SERCA2a is a key regulator of cardiac contractile force. An increase in SERCA2a function augments SR Ca^{2+} content which increases Ca^{2+} transient amplitude (and thus force generated). This is because SR Ca^{2+} release is steeply dependent on SR Ca^{2+} content (Gyorke & Gyorke, 1998; Shannon *et al.*, 2000; Bode *et al.*, 2011). The function of SERCA2a is dynamic, matching cardiac function to physiological demands by increasing during exercise or other forms of stress. Binding of phospholamban (PLB) to SERCA2a inhibits the pump and reduces Ca^{2+} influx into the SR lumen by decreasing its Ca^{2+} affinity 2 to 3 times (Tada *et al.*, 1975) and also by reducing energetic efficiency (Frank *et al.*, 2000). At physiologically-relevant values of diastolic $[\text{Ca}^{2+}]$ the presence of PLB reduces the Ca^{2+} transport rate from about 90 to 30 $\mu\text{M}\cdot\text{s}^{-1}$ (Bers, 2001). β -adrenergic stimulation causes a conformational change of PLB secondary to phosphorylation of the Ser16 site by Protein Kinase A (PKA) (Talosi *et al.*, 1993). This change reduces the affinity of active monomeric PLB for SERCA2a but enhances affinity for other PLB molecules such that detached PLB forms homopentamers, an inactive reservoir of the protein (Cornea *et al.*, 1997; Kimura *et al.*, 1997; Hou *et al.*, 2008). In this way the affinity of SERCA2a for Ca^{2+} is increased and uptake rate enhanced.

PLB can also be phosphorylated at Thr17 by Ca^{2+} /calmodulin-dependent protein kinase II (CaMKII). This site appears to be more important in frequency-dependent responses (Hagemann *et al.*, 2000; Zhao *et al.*, 2004) such as the force-frequency relationship and frequency-dependent acceleration of relaxation which are often impaired in diseased myocardium (Pieske *et al.*, 1992). Apart from PLB binding, pump function is modulated significantly by the intracellular cytosolic milieu including adenosine triphosphate (ATP), pH, $[\text{Mg}^{2+}]$ and $[\text{Ca}^{2+}]$ (Dupont, 1977; Bers, 2001), and by post-translational modification including sumoylation (see below). Sarcolipin (SLN) is a 31 amino acid structure originally identified in skeletal muscle (MacLennan *et al.*, 2003) but more recent analyses indicate that SLN is also expressed in cardiac tissue, and it controls contractile function predominantly in the atria (Babu *et al.*, 2007). Compared with PLB, much less is known about SLN but they have similar transmembrane sequences suggesting they share a similar genetic heritage and they may bind to the same regulatory site on SERCA2a.

1.2.2 Control of other key proteins involved in CICR

Activation of cAMP-dependent protein kinase A (PKA) has a multitude of effects on CICR via phosphorylation of other down-stream proteins. The activity of PKA is targeted towards certain key effector proteins by A-kinase-activating proteins (AKAPs) which bind the regulatory unit of PKA in the vicinity of proteins which are to be phosphorylated. Phosphorylation occurs when PKA is activated by cAMP, initiating dissociation of the catalytic and regulatory subunits and hence active phosphorylation (Manni *et al.*, 2008). For example, muscle-specific AKAP (mAKAP) targets PKA RyR2 (Marx *et al.*, 2000; Kapiloff *et al.*, 2001), AKAP15/18 α localizes PKA to L-type Ca^{2+} channels and AKAP18 δ targets PKA to phospholamban (Lygren *et al.*, 2007).

The relative contributions of the targeting of these other proteins in increasing cardiac contractile force is debated. Phosphorylation of the LTCC certainly leads to prolonged and exaggerated L-Type calcium current (I_{Ca}) resulting in a longer plateau phase of the cardiac action potential (AP) at a higher sarcolemmal membrane potential which both increases the stimulus to RyR2 opening and increases SR Ca^{2+} content over the longer term (Reuter, 1974; Osterrieder *et al.*, 1982; Catterall, 2000). The SR Ca^{2+} release channel RyR2 (see also section 1.6.1) may also have an important role in the control of CICR. There is biochemical and lipid bilayer experimental evidence that PKA phosphorylates RyR2 at Ser2808 (humans and murine species) or 2809 (rabbits) and that this enhances its sensitivity to $[Ca^{2+}]_i$ (Takasago *et al.*, 1991; Valdivia *et al.*, 1995; Marx *et al.*, 2000). Marks and colleagues argue that this is a key component of the normal physiological response to PKA-induced phosphorylation (Shan *et al.*, 2010b). Mice with RyR2s which cannot be phosphorylated at this site exhibit blunted heart rate and contractile responses to catecholamines. These results appear to contradict those of Macdonnell *et al.* who found normal chronotropic and inotropic responses to isoprenaline in these mice (MacDonnell *et al.*, 2008).

The crux of the disagreement is largely based on the work of Eisner and colleagues. They argue that an increase in RyR2 open probability (P_o), as induced by their experiments using low dose caffeine (Trafford *et al.*, 2000), cannot be responsible for any maintained elevation of systolic Ca^{2+} because of compensatory changes in other elements of the CICR system to return transient amplitude back to pre-intervention levels (autoregulation). They found similar autoregulation when blocking RyR2 with tetracaine. This type of effect was first observed in 1972 when Fabiato observed only a transient rise in Ca^{2+} wave frequency in the presence of caffeine in skinned myocytes (Fabiato & Fabiato, 1972). In experiments on permeabilised myocytes, where there is no contribution of I_{Ca} , cAMP-dependent changes in Ca^{2+} spark frequency were found to be attributable to changes in phosphorylation of phospholamban rather than RyR2 (Li *et al.*, 2002), seemingly supporting the view that altering RyR2 function does not have a major role in PKA-mediated amplification of CICR. On the other hand recent work by Eisner's group has shown that in cells which are already Ca^{2+} overloaded in the presence of isoprenaline, tetracaine can have a sustained effect on Ca^{2+} transient amplitude (Venetucci *et al.*, 2006). Hence the polarised viewpoints seem to be coming closer together.

1.2.3 Contribution of CaMKII

It is important to note that PKA is not the only kinase with the ability to phosphorylate key elements of the CICR cascade. Another important kinase is CaMKII, a multimeric holoenzyme found in cardiac muscle. It is activated by the Ca^{2+} -calmodulin complex when Ca^{2+} levels are high and autophosphorylates at Thr287 thus allowing persistence of activity beyond the initial elevation of $[Ca^{2+}]_i$ which activates it (Miller & Kennedy, 1986; Kushnir & Marks, 2010). In the heart, it is hypothesized that CaMKII usually cycles between a phosphorylated active state during the systolic Ca^{2+} transient and a dephosphorylated resting state during diastole. At faster heart rates, however, there is insufficient time for CaMKII to dephosphorylate which could lead to a progressive increase in the level of autophosphorylated and activated CaMKII. This has been termed molecular "memory" (Putney, 1998; De Koninck, 1998) and contributes to the positive force-frequency relationship in the cardiomyocyte (Maier & Bers, 2007; Kushnir & Marks, 2010). CaMKII activity is often increased in response to positive inotropes since they may change both the frequency (via their positive chronotropic effects) and size of the regular oscillations in Ca^{2+} that provide the signal for activation of CaMKII. Similar to PKA, CaMKII can phosphorylate and alter the activity of numerous Ca^{2+} cycling

proteins (Maier & Bers, 2007). An important debate is how much contribution of the effects of CaMKII relates to phosphorylation of RyR2 (as opposed to other mechanisms such as PLB phosphorylation). Undoubtedly RyR2 is phosphorylated by CaMKII at a different site than PKA and this leads to elevated P_o of the channel in bilayer experiments (Wehrens *et al.*, 2004) but, similar to the debate relating to PKA-mediated RyR2 phosphorylation above, Eisner *et al.* (Eisner *et al.*, 2010) believe this cannot account for frequency dependent positive inotropy.

1.3 SR leak

The SR is not only an important store of Ca^{2+} which can be released during contraction, but also the potential origin of spontaneous arrhythmogenic SR Ca^{2+} release. Diastolic SR Ca^{2+} leak results from activation of RyR2 and release of Ca^{2+} from the SR in the period between normal Ca^{2+} transients. Such SR Ca^{2+} leak manifests either as leak which is visible by high-speed confocal fluorescence imaging as Ca^{2+} sparks (Cheng *et al.*, 1993) or waves (Cheng *et al.*, 1996) or as more subtle leak which has been called Ca^{2+} quarks (Lipp & Niggli, 1996, 1998) or spark-independent Ca^{2+} release (Zima *et al.*, 2010). In the case of quarks and sparks this means activation of single/few or a cluster of RyRs respectively and, in the case of waves, this means propagation of an internal CICR signal across the cell. SR leak has an important physiological role in prevention of SR Ca^{2+} overload and maintaining flux balance across the SR membrane. However, as described below, SR leak can also be pathological, particularly in terms of arrhythmia initiation.

1.3.1 Ca^{2+} sparks

Calcium sparks were first observed by Cheng *et al.* via confocal microscopy in line-scanning mode (see section 2.5.4) in the presence of a Ca^{2+} -sensitive fluorophore (Cheng *et al.*, 1993). A spark is a local increase in $[Ca^{2+}]_i$ of approximately 200nM which occupies a small volume of the cytosol (Guatimosim *et al.*, 2002). Initially sparks were thought to be related to the opening of a single RyR2 channel, however this opinion has since been revised given that the current carried by a single RyR2 is probably around 0.07-0.4pA (Mejia-Alvarez *et al.*, 1999; Guatimosim *et al.*, 2002), as compared to spark flux of 2-4pA suggesting dozens of RyR2s opening per spark. This functional unit of Ca^{2+} release is termed the RyR cluster or calcium release unit (CRU).

Sparks arise from clusters of RyR2s being activated by a variety of factors, the most important being luminal and cytosolic $[Ca^{2+}]$ (Gyorke & Gyorke, 1998). There must be control mechanisms in place to terminate sparks in order to prevent a perpetual Ca^{2+} release but these are debated. Theories include stochastic inactivation, local SR Ca^{2+} depletion and RyR inactivation by associated proteins such as calsequestrin and sorcin (Stern & Cheng, 2004). These mechanisms together with the coupled gating of closely associated RyRs (Marx *et al.*, 1998) as well as adaptation (reduction in open probability with rapid elevation of $[Ca^{2+}]_i$ (Gyorke & Fill, 1993)) results in a CRU in which channels open and close in unison to produce a spark.

Relatively soon after the discovery of sparks by Cheng, Cannell and Lederer, the same authors described their occurrence in more detail showing that they were the building-blocks of the Ca^{2+} transient (Cannell *et al.*, 1995). These building-blocks could be evoked by very short step depolarizations of the cells using voltage clamp such that a full transient was not evoked. What remained were smaller rises in Ca^{2+} that had a similar morphology to sparks. This and other work since has suggested that the Ca^{2+} transient is the sum of spark-mediated rises in Ca^{2+} at each dyad (where 5-15 LTCCs and 50-200 RyRs are situated in close proximity) such that Ca^{2+} transiently rises to

150 μ M in the microdomain of the dyadic space (Gaur & Rudy, 2011). The Ca^{2+} transient is a result of I_{Ca} inducing a 10^3 - 10^6 fold increase in spark frequency that produces the Ca transient (Guatimosim *et al.*, 2002). There is stability inbuilt into this system since the closure of the CRU (as an individual spark) is predictable and dictated by intrinsic properties of the RyR2 (Stern & Lakatta, 1992; Cannell *et al.*, 1995). This gives a high degree of control despite the high gain of the system. Such stability means that under normal conditions diastolic Ca^{2+} leak rarely results in internal CICR and a resulting Ca^{2+} wave (section 1.3.3).

1.3.2 Sparks vs Quarks

For some time sparks were thought to be the elementary unit of EC coupling – they were thought to be the smallest, indivisible components of the system. An alternative theory was proposed by Lipp and Niggli in 1996 who used flash photolysis to induce CICR in guinea-pig myocytes (Lipp & Niggli, 1996). They found that not all CICR took place in the form of Ca^{2+} sparks and they termed the alternative mechanism of release a Ca^{2+} quark which they proposed may be the release of Ca^{2+} from a single RyR2. It has been proposed that such non-spark Ca^{2+} release may originate from rogue RyR2s - i.e. RyR2 channels that are not in the usual terminal cisternae of the SR apposed to t-tubules but elsewhere in the SR membrane (Brochet *et al.*, 2011). Measurement of quarks is technically very difficult although attempts have been made via simultaneous visualization of small spark-like events simultaneously with the depletion in local Ca^{2+} within the SR (Brochet *et al.*, 2005). Using such techniques it has been shown that, at least in rabbit ventricular myocytes, diastolic Ca^{2+} leak via quarks is quantitatively similar to that released in the form of sparks (Zima *et al.*, 2010).

1.3.3 Ca^{2+} Waves

The consequences of Ca^{2+} waves – periodic, slowly propagating contractions of cardiomyocytes – were observed before Ca^{2+} sensitive fluorophores were in widespread use. Fabiato and Fabiato observed cyclic contractions in myocytes that had been mechanically skinned which varied in frequency and amplitude depending on $[\text{Ca}^{2+}]$ of the bathing solution (Fabiato & Fabiato, 1972). Such activity has also been observed in more intact muscle preparations such as papillary muscle and has been termed scattered light intensity fluctuation (SLIF) because of the characteristic change seen in light scatter from a laser source when these events occur (Lappe & Lakatta, 1980; Stern *et al.*, 1983). The mechanism of these events was characterised more fully when Cheng *et al.* observed that in most Ca^{2+} waves enhanced Ca^{2+} spark activity is found just prior to initiation and also that waves can be shown to be made up of sequential sparks at 1.9 μ m intervals (Cheng *et al.*, 1996). Therefore waves are initiated and sustained by sequentially activated sparks occurring at similar intervals to the average sarcomere length.

Ca^{2+} wave propagation can be considered to be the result of saltatory conduction via sparks enhancing $[\text{Ca}^{2+}]_i$ at an adjacent dyad, or alternatively as the result of increased SR Ca^{2+} uptake in adjacent regions raising local SR $[\text{Ca}^{2+}]$ (Bers, 2001). The latter mechanism was first proposed by Takamatsu and Weir (Takamatsu & Wier, 1990). It was later shown that Ca^{2+} wave propagation was not impeded by application of thapsigargin after the SR was already loaded with Ca^{2+} suggesting this mechanism was of little importance (Lukyanenko *et al.*, 1999). However more recent experiments with rapid release via photolysis of a caged SERCA2a inhibitor have shown that wave propagation slows immediately after photolysis (Keller *et al.*, 2007). The authors suggested that the results of Lukyanenko could be explained by off-target effects such as elevation in $[\text{Ca}^{2+}]_i$ seen with longer-term application of SERCA2a inhibitors.

1.3.4 SR Ca²⁺ Leak and Triggered Arrhythmia

Ca²⁺ waves are thought to be important in the etiology of a number of different forms of ventricular tachyarrhythmia, particularly in Heart Failure (HF) and Catecholaminergic Polymorphic Ventricular Tachycardia (CPVT) (Zhou *et al.*, 2011a). One of the most convincing arguments for the important role of SR Ca²⁺ leak in the aetiology of malignant ventricular arrhythmias is the direct link between genetic abnormality and arrhythmia in CPVT. The condition was first described by Reid and colleagues in 1975 in a case of bidirectional ventricular tachycardia in a 6 year old girl induced by exertion and emotional stress (Reid *et al.*, 1975). Later genetic studies have shown that cases such as this relate to genetic abnormalities of the gene coding for RyR2 or genes coding for other closely associated proteins such as calsequestrin (Priori & Chen, 2011). Dozens of different mutations have been identified in CPVT probands, predominantly involving point mutations affecting a single nucleotide. The consequences of most of these mutations on the channels in bilayer experiments is that they exhibit increased sensitivity to luminal [Ca²⁺] (Jones *et al.*, 2008). As such, the mechanisms for these arrhythmias are thought to be associated with elevated levels of spontaneous sarcoplasmic reticulum (SR) Ca²⁺ release for a given SR load (Shannon *et al.*, 2003; Zhou *et al.*, 2011a). This has been termed store-overload-induced Ca²⁺ release (SOICR) (Jiang *et al.*, 2004).

In cardiomyocytes isolated from mice exhibiting these mutations there is enhanced SR Ca²⁺ leak, both at baseline and in the presence of isoprenaline (Knollmann & Chopra, 2006; Kashimura *et al.*, 2010). This can result in triggered cellular activity and subsequent arrhythmia via extrusion of excess cytoplasmic Ca²⁺ via NCX which exchanges 3 Na⁺ ions for 1 Ca²⁺, resulting in depolarization of myocytes towards threshold potential for voltage-gated sodium channels. This NCX-mediated current (or I_{TI}) is termed a delayed after depolarization (DAD). The resulting depolarization can lead to “triggered arrhythmia” at the level of the cell, with a large fraction of the total SR Ca²⁺ content (approx 60%) needing to be released in order to produce a large enough DAD to reach a threshold for action potential initiation (Schlotthauer & Bers, 2000). As such, whilst a high Ca²⁺ spark frequency may cause a change in the resting membrane potential of the myocyte, a wave is probably required to cause an “ectopic” action potential (Priori & Chen, 2011). The potential mechanisms by which DADs may lead to arrhythmia at the level of the whole heart are explored in section 1.5.

Cellular triggered activity also comes in the form of early after depolarizations (EADs). These are a different entity resulting in a second depolarization prior to the end of the action potential, perhaps as a result of reactivation of LTCCs (Bers, 2001), although more recent evidence also points to an important role for SR Ca²⁺ leak in EAD genesis (Volders *et al.*, 2000; Zhao *et al.*, 2012).

The major control methods acting on CICR (section 1.2) also have the potential to increase such triggered arrhythmias, as exemplified by CPVT in which catecholaminergic activation of these mechanisms causes potentially fatal arrhythmias. Higher SR Ca²⁺ load and increased I_{Ca}, both induced by enhancing PKA and CaMKII activity, have the potential to increase spontaneous diastolic Ca²⁺ leak from the SR. This is due to a combination of an increased SR load providing a luminal trigger for RyR2 opening, and also due to enhanced cytosolic Ca²⁺ which also activates RyR2 (Gyorke & Gyorke, 1998). EADs are also exacerbated by PKA-mediated activation due to enhancement of I_{Ca} and a reduction of Ca²⁺ dependent inactivation of LTCCs (Zeng & Rudy, 1995).

1.4 Heart Failure

1.4.1 Epidemiology and Burden of Disease

Heart failure (HF) has reached epidemic proportions in Western countries. The prevalence of symptomatic systolic cardiac failure is approximately 1% of the Western European population with a further 2% having asymptomatic systolic dysfunction or symptomatic heart failure without systolic dysfunction (Cleland *et al.*, 2001). The Framingham heart study measured the lifetime risk for congestive cardiac failure at 20% in both men and women (Lloyd-Jones *et al.*, 2002). The financial toll is substantial. In the UK there are approximately 120,000 acute heart failure admissions to hospital per annum, with an estimated cost of £900M – that is 2% of the NHS budget (NHS England, 2009). The increased prevalence in developed countries reflects improved survival during acute myocardial infarction resulting from early access to reperfusion therapy, and the aging population with current mean life expectancy in the UK now almost 80 years. Other factors including increasing survival in cancer patients receiving cardiotoxic chemotherapies, the obesity epidemic and the high prevalence of hazardous levels of alcohol consumption (National Clinical Guideline Centre, 2010) will further fuel the rise in prevalence of heart failure.

Equally concerning is the poor prognosis in the heart failure population, despite effective implementation of current evidence based therapies. The median survival following diagnosis with heart failure is less than three years, and five year survival is only 32% in patients with systolic dysfunction and little better (35%) in patients with heart failure and preserved ejection fraction (Owan *et al.*, 2006; Jhund *et al.*, 2009). The mode of heart failure related death can be broadly split into deaths from “pump-failure” and sudden cardiac death (SCD) with small numbers ascribable to other causes (e.g. myocardial infarction, pulmonary embolism and stroke). Recent compilation of data from 10,538 ambulatory patients with New York Heart Association (NYHA) class II to IV heart failure confirms the importance of both these major modes of death with 1014 sudden deaths and 684 pump-failure deaths over 16 735 person-years of follow-up (Mozaffarian *et al.*, 2007).

1.4.2 Arrhythmogenic Changes in Ca^{2+} Handling in Heart Failure

SERCA2a function and SR Ca^{2+} load have been found to be reduced in several models of HF and in human HF cardiomyocytes (Gwathmey & Morgan, 1985; Gwathmey *et al.*, 1987; Beuckelmann *et al.*, 1992; Del Monte *et al.*, 1995; Hasenfuss, 1998). All else being equal, therefore, it would follow that spontaneous SR Ca^{2+} leak, would also be reduced. On the contrary, many researchers, including our own group (Lyon *et al.*, 2009, 2011), find that leak is enhanced in HF. This forms the basis of a Ca^{2+} paradox in HF (Kass *et al.*, 2008). The reasons for the paradox remain unclear and may involve increased intracellular $[\text{Na}^+]$ in HF which could hinder Ca^{2+} efflux via NCX and thus enhance RyR2 opening via interaction with Ca^{2+} -sensitive sites at the cytosolic domain (Sossalla *et al.*, 2010). Another important mechanism might be a reduced threshold for SR Ca^{2+} leak in HF similar to that characterized in catecholaminergic polymorphic ventricular tachycardia (Jiang *et al.*, 2004). This could enhance leak despite lower SR Ca^{2+} content. The leak threshold may differ in different models and aetiologies of HF (Respress *et al.*, 2012).

There are several modifications to the RyR2 which occur in HF and may reduce the threshold for spontaneous SR Ca^{2+} release. There is evidence that phosphorylation of RyR2, and reduced binding of the channel's stabilizer FK506 binding protein 12.6 (FKBP 12.6) as a result, causes an increase in SR Ca^{2+} leak in HF (Marx *et al.*, 2000; Kushnir & Marks, 2010). Other post-translational modifications

to RyR2 such as nitrosylation and oxidation may also be important and have been reviewed elsewhere (Aracena *et al.*, 2005; Vassort & Lacampagne, 2005; Zissimopoulos *et al.*, 2007). The leaky SR in HF both predisposes to arrhythmias via the depolarizing influence of the NCX current and reduces contractility due to further depletion of SR Ca^{2+} content. Each occurrence of SR Ca^{2+} leak could also be more arrhythmogenic in HF than in the healthy heart due to an increase in NCX activity which has been seen in some settings, although this is not always associated with reduced SERCA2a activity (Hasenfuss *et al.*, 1999; Pogwizd *et al.*, 2001). Kho *et al.* identified a common regulator for SERCA2a and NCX in the small ubiquitin-like modifier type 1 (SUMO1) protein. This protein both up-regulates SERCA2a function and down-regulates NCX function, and is reduced in a mouse model of HF. These mice showed reduced SERCA2a Ca^{2+} uptake and enhanced NCX function (Kho *et al.*, 2011). In addition there is downregulation of inward rectifying potassium channel (I_{K1}) expression (Pogwizd *et al.*, 2001) which normally stabilizes resting membrane potential. The result is that for any given spontaneous Ca^{2+} leak in HF cells, a greater membrane potential (V_m) depolarization occurs via NCX. The transient outward current (I_{to}) density has also been shown to decrease in heart failure patients (Beuckelmann *et al.*, 1993). I_{to} plays a major role in controlling the duration of the action potential and it is thought that such a decline in current is one of the reasons for action potential duration (APD) prolongation in HF. APD prolongation will provide a setting for EADs because the opportunity for Ca^{2+} current reactivation is increased.

1.5 Interplay between cellular triggered activity and re-entry

1.5.1 Re-entrant Arrhythmias

Re-entrant mechanisms on the macroscopic, whole-heart scale are observed in a number of tachyarrhythmias. This is most obvious in the presence of an anatomical re-entrant pathway such as in atrioventricular nodal re-entrant tachycardia (AVNRT) or Wolff-Parkinson-White (WPW) syndrome. Here, in otherwise conductive tissue, there is a core of electrically inert tissue – an anatomical obstruction which is normally present in all hearts (e.g. blood vessels). In the presence of uniform conduction there is no arrhythmogenic potential (Figure 1-3A). However in the presence of asymmetrical decremental conduction and unidirectional conduction block a circus-loop leads to re-entry and subsequent arrhythmia (Figure 1-3B) (Bers, 2001).

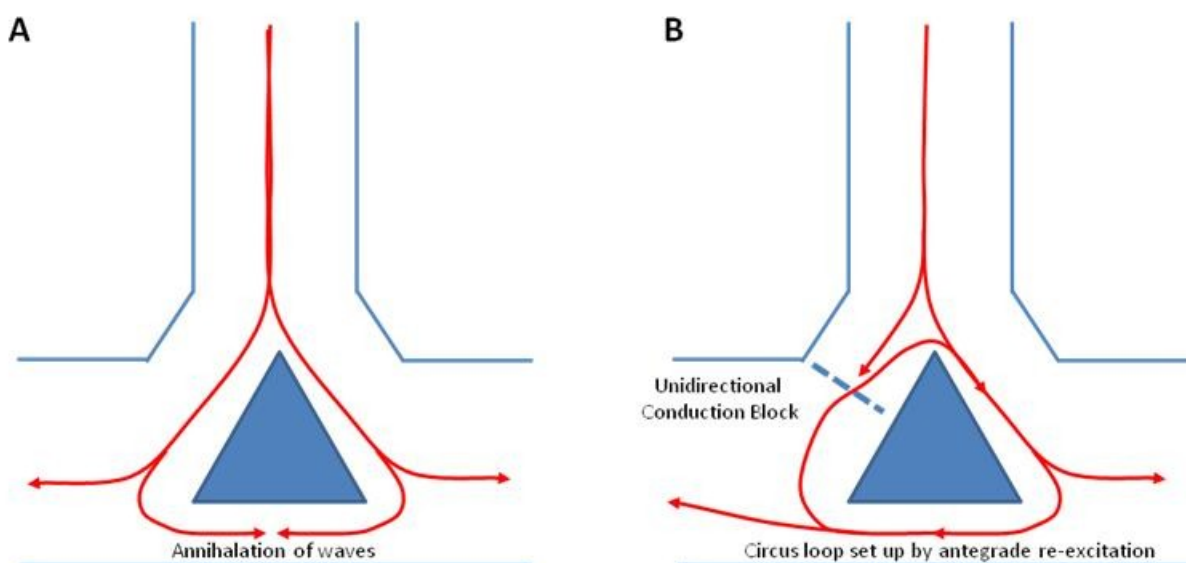
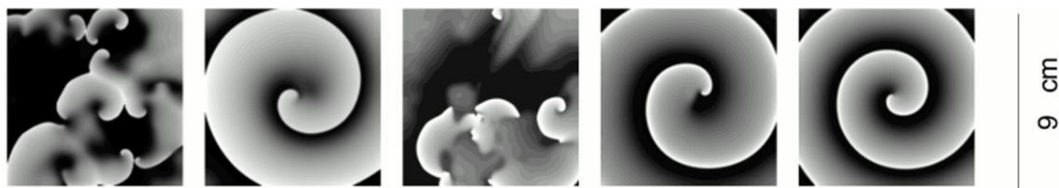


Figure 1-3. Re-entry of Excitation.

Model of re-entry around an anatomical obstruction. (A) In normally conducting tissue a wave of depolarization may bifurcate around an anatomical obstruction and subsequently annihilate when the waves meet head-on. (B) In the case of a unidirectional conduction block in one of the arms of the bifurcation, a re-entrant circuit is set up. This type of abnormality is commonly the cause of WPW or AVNRT-related tachyarrhythmias.

Anatomical obstructions and non-uniform conduction are not a pre-requisite for re-entrant tachyarrhythmias. Instead, within relatively uniform tissue the shape of the wave of depolarization can result in a core of slower moving conduction which can functionally act in the same manner as the anatomical inert tissue outlined above. Spiral waves are an important example of this functional (rather than structural) mechanism of re-entry (Figure 1-4). The stability of such spiral waves depends on the source-sink mismatch which is set-up by having a high-degree of convex curvature at the centre of such a spiral wave. Conduction from cell to cell in multi-cellular tissue depends on depolarization travelling from an excited cell (electrical source), to an unexcited cell (electrical sink). In the centre of a spiral wave where the excitation front is highly convex, the source is relatively less than the sink since the convex wave diverges into a larger area downstream and hence conduction slows (Kléber & Rudy, 2004).

**Figure 1-4. Examples of spiral waves**

Examples of spiral waves simulated in 2-dimensional models. The high degree of convex curvature at the centre of the spiral causes conduction slowing relative to the periphery of the spiral. Reproduced from Qu et al (Qu et al., 1999).

1.5.2 The role of SR leak in arrhythmias in the intact heart

There is good reason to believe that spontaneous SR Ca^{2+} release can not only cause triggered arrhythmias due to membrane depolarization of a particular myocyte or group of myocytes but that it might also contribute to sustained forms of arrhythmia. Clinically, ventricular fibrillation (VF) is often preceded by ventricular tachycardia (VT) of variable duration. VT (sometimes itself related to SR Ca^{2+} overload) leads to a reduction in diastolic time required for efficient intracellular Ca^{2+} removal and thus a vicious cycle of increasing Ca^{2+} overload (Omichi et al., 2004). In modelling guided by single-cell voltage clamp experiments, Chudin et al showed that in the absence of spontaneous SR Ca^{2+} release, wavebreak did not occur such that rapid pacing could not induce VF (Chudin et al., 1999). In the same study it was noted that when VF was induced with spontaneous release active and this was then inactivated, multiple VF wavelets re-coalesced to form a single stable rotor consistent with VT. In these modelling experiments this was related to SR Ca^{2+} leak causing amplification NCX-mediated inward currents which produced APD prolongation inhomogeneously throughout the tissue. Areas of prolonged repolarization interact with the next passing wavefront to cause wavebreak.

Such data is backed up by the majority of experimental data in the literature. Firstly, experimental manoeuvres used to induce VF are often associated with increases in SR Ca^{2+} content and spontaneous Ca^{2+} release. Examples include glycoside intoxication, removal of extracellular K^+ , elevation of $[\text{Ca}^{2+}]_o$ and treatment with veratrine and aconitine (Clusin *et al.*, 1982). Furthermore efforts to inhibit SR Ca^{2+} release have usually resulted in reduced VF in experimental models. Perhaps the earliest examples are the experiments of Hadju *et al* who showed that ryanodine was an antiarrhythmic agent when administered to cats and dogs with digitalis-induced VT (Hajdu & Leonard, 1961). Since that work a number of other studies have revealed the benefits of modulating SR Ca^{2+} release in ventricular tachyarrhythmias. Thandroyden *et al* showed that either blocking SR Ca^{2+} release with ryanodine, or entirely emptying the SR of Ca^{2+} prevented VF in a rat ischaemia-reperfusion model (Thandroyen *et al.*, 1988). Although the data are convincing regarding a role for SCR in VF initiation, under some circumstances VF is inducible even in its absence suggesting other factors are at work. One study showed that even in the presence of $10\mu\text{M}$ ryanodine, which blocked aftercontractions on a whole-heart level, VF could be induced by introduction of K^+ -free media (Merillat *et al.*, 1990). This study highlighted the importance of I_{Ca} in VF since LTCC blockade and reduction of $[\text{Ca}^{2+}]_i$ was able to prevent VF and cardiovert VF which had already been initiated, supporting previous evidence of LTCC as a critical component of persistent VF (Akiyama, 1981).

1.5.3 How does SR leak cause ventricular arrhythmia

Early investigators observing cellular oscillations in isolated cardiomyocytes, particularly when they are rapid, were struck by the similarity of these oscillation on the microscopic level with VF on the macroscopic level (Mercer & Dower, 1966). While we have observed similar ventricular myocyte “fibrillation”, this is often associated with impending cellular death rather than being a transient phenomenon that can be rescued. It is therefore unlikely to play a major role in the majority of VF which, with the advent of microarray and optical mapping techniques, has been shown to be related to abnormal circus movement of depolarization within the myocardium. As such the link between spontaneous SR Ca^{2+} release must be more complex than widespread fibrillation of individual myocytes caused by $[\text{Ca}^{2+}]_i$ oscillations. Subsequent theories have therefore focused on the role of Ca^{2+} leak in causing DADs and triggered arrhythmia at the cellular level (section 1.3.4).

This theory of triggered activity may be plausible when observing isolated cardiomyocytes, which exhibit triggered action potentials following Ca^{2+} waves, especially in the presence of beta-adrenergic agonists. However, there is reason to believe that this may not be the most relevant mechanism by which SR Ca^{2+} release results in arrhythmias in the intact heart. In ventricular muscle each cardiomyocyte is coupled to as many as 11 others by gap junctions (Hoyt *et al.*, 1989). Since such myocytes are electrically connected, the depolarization of a myocyte caused by NCX-mediated I_{T1} (section 1.3.4) would be shared between its neighbours, and through them to the whole 3D syncytium of cardiomyocytes. Hence a large number of myocytes would need a simultaneous wave and simultaneous inward NCX current in order to cause a DAD in intact tissue. This concept has been demonstrated in intact tissue (Fujiwara *et al.*, 2008), and was quantified in modelling by Weiss and co-workers who demonstrated that in 3D tissue, over 800,000 contiguous cells would need to simultaneously exhibit Ca^{2+} waves in order to cause a single ventricular ectopic beat (Weiss *et al.*, 2011). The probability of this occurring is extremely low if there is a stochastic element to SR Ca^{2+} release as is widely suspected, unless there is a mechanism of synchronization of Ca^{2+} waves in intact tissue which so far only been observed in non-physiological conditions (Fujiwara *et al.*, 2008).

Furthermore the potential for Ca^{2+} wave propagation between cells is unreliable, particularly through end-plates, and is too slow to result in synchronous I_{Ti} activation in a large number of cells simultaneously (Li *et al.*, 2012). It should be noted that a different group has argued that simultaneous waves in fewer (e.g. 12) contiguous cells would be required to produce ectopy although this has only been published in abstract form (Ullah *et al.*, 2014).

Other theories are required to explain how spontaneous SR Ca^{2+} release leads to arrhythmias in intact tissue. Much recent progress has been made in better defining this link. One example of a mechanism that circumvents the source-sink mismatch concept is that of DADs occurring in conducting tissue such as Purkinje fibres. Here there is insulation from multiple connections such that Purkinje cells may be connected to just 2 others, thus vastly reducing the sink and reducing the number of myocytes that would be required to undergo simultaneous Ca^{2+} waves to produce an extrasystole (Weiss *et al.*, 2011). There is experimental evidence for such a mechanism in a mouse model of CPVT (R4496C+/-) (Cerrone *et al.*, 2007). Optical mapping in this model revealed focal endocardial sites of ectopy consistent with the location of Purkinje fibres. Furthermore bidirectional VT was converted to monomorphic VT by ablation of RV Purkinje fibres. Isolated Purkinje fibres also exhibited spontaneous SR Ca^{2+} release leading to triggered action potentials. It is therefore conceivable that much of the work on ventricular cardiomyocytes performed in this condition is merely a surrogate (albeit one that is representative) for what is occurring in the Purkinje fibres.

On the other hand it is conceivable that SR Ca^{2+} release can result in fatal arrhythmias without bringing a single myocyte to threshold for AP production. Such a mechanism is elegantly demonstrated in the recent study of Johnson *et al.*, which demonstrated that spontaneous SR Ca^{2+} release results in a smaller subsequent systolic Ca^{2+} transient within a myocyte (Johnson *et al.*, 2013). This results in reduced Ca^{2+} dependent inactivation (CDI) of the LTCC which causes prolongation of the plateau phase of the AP and enhances Ca^{2+} influx. In a drug-induced (I_{Ks} -inhibition) model of long QT syndrome, this resulted in increased beat-to-beat inhomogeneity of repolarization and torsades de pointes (TdP). Furthermore, pharmacological interventions that stabilize SR Ca^{2+} release (ryanodine, tetracaine, CamKII inhibition, Mg^{2+} and flecainide) reduced TdP in this setting. This type of effect of SCR on sarcolemmal ion currents could also result in spatially discordant beat by beat variations in APD, even in homogeneous tissue (Weiss *et al.*, 2011). This can result in wavebreak as a wave of depolarisation from a short APD region arrives at a long APD region such that re-entry can commence.

1.6 Targeting SR Leak to reduce the risk of ventricular arrhythmia

1.6.1 The cardiac ryanodine receptor

The RyR is a Ca^{2+} release channel which exists as a large homotetramer made up of 4 monomers. Each monomer contains has a molecular mass of 565 kDa and contains about 5000 amino acids (Takeshima *et al.*, 1989). Three RyR isoforms are present in mammals with RyR1 being predominantly expressed in skeletal muscle, RyR2 being found in the heart and brain and RyR3 being widely distributed (Giannini *et al.*, 1995). The N-terminal of the protein is extremely large and makes up the cytosolic domain, most of which serves as a scaffold for the binding of signaling proteins which can then have an effect on gating of the channel pore which is located at the carboxyl terminal (Marks *et al.*, 2002). One aspect of this regulation includes the modification of binding of a stabilizing protein FK506 binding protein 12.6 (FKBP12.6) via phosphorylation (section 1.2.2).

FKBP12.6 binding to isolated channels reduces the occurrence of subconductance states, thus stabilizing the channel towards the closed condition with longer, but more sharply demarcated openings (Brillantes *et al.*, 1994). In addition FKBP12.6 appears to be important in the coupled gating of adjacent RyR2 channels which could also contribute to stability of the CRU *in vivo* (Marx *et al.*, 1998). Other groups who have studied the effect of FKBP12.6 on SR leak have sometimes shown a stabilizing influence of the protein (Yano *et al.*, 2000), although this finding is not ubiquitous (Timerman *et al.*, 1996; Galfré *et al.*, 2012).

In addition to FKBP12.6, the RyR2 macromolecular complex also includes PKA and its targeting protein muscle A-kinase anchoring protein (mAKAP), protein phosphatase 1 (PP1) and its targeting protein spinophilin and protein phosphatase 2 (PP2) and its targeting protein PR130 (Marks *et al.*, 2002). FKBP12.6 was shown to be dissociated from RyR2 as a result of phosphorylation of the channel by PKA (Marx *et al.*, 2000), although experimental evidence from another group are discrepant and suggest that it is possible for FKBP12.6 to bind to RyR2 which has been phosphorylated at the PKA site (Xiao *et al.*, 2004). Channels isolated from humans with idiopathic dilated cardiomyopathy exhibited 3-4 phosphorylated PKA sites per RyR2 channel were compared with approximately 1 site on average in non-failing samples (Marx *et al.*, 2000). Hence the RyR2 channels in heart failure are “hyperphosphorylated”, although there remains a debate about what effect this, or the effect of CaMKII phosphorylation of the channel, might have *in vivo* (section 1.2.2-1.2.3). If we accept that these changes contribute to the leaky SR phenotype shown in many models of HF then it is clear that stabilization of the RyR2 might reduce the risk of fatal arrhythmias in the condition. Such agents would also clearly have a role in the treatment of CPVT (Figure 1-5).

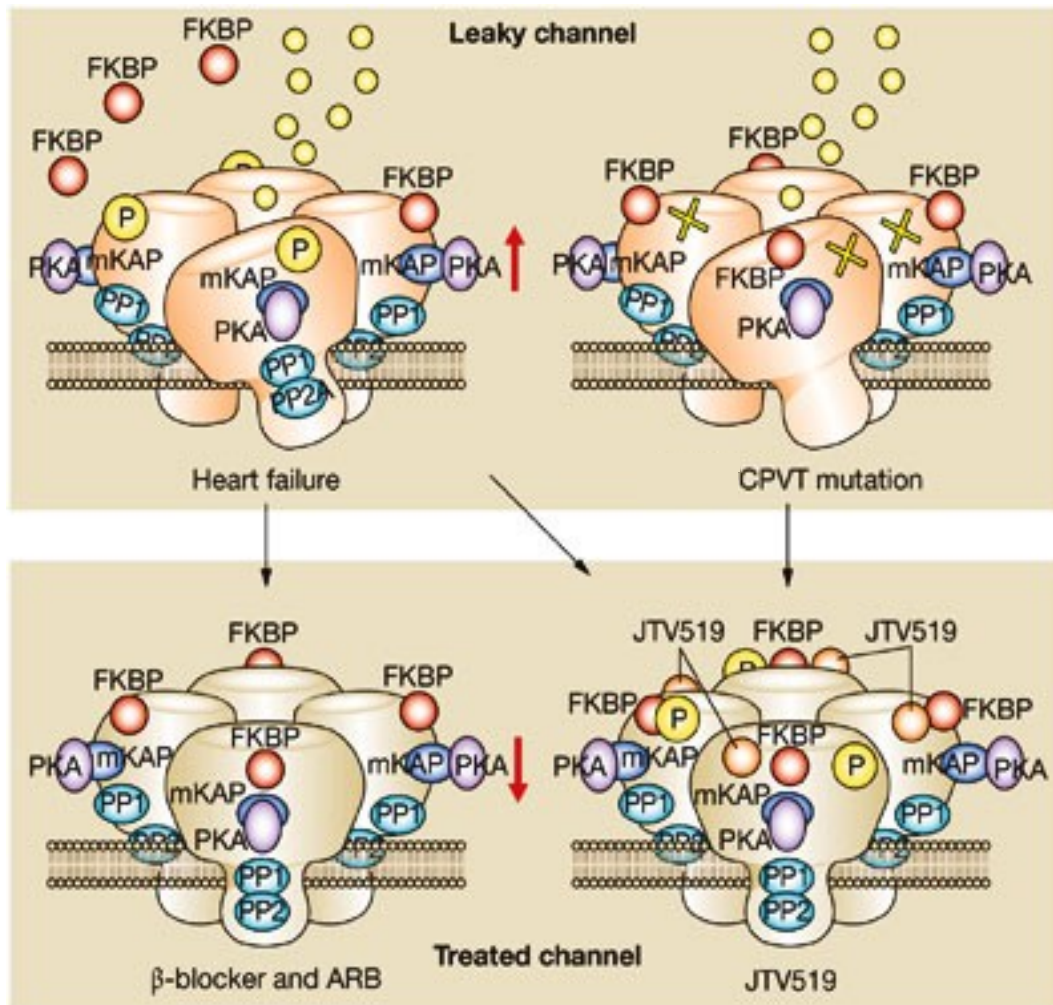


Figure 1-5. The leaky ryanodine receptor and therapies which stabilize the channel

In HF (upper left panel), the channel is thought to be leaky in part due to PKA-mediated phosphorylation of the cytosolic domain (upper aspect in figure) at serine 2808/9 depending on species. Both β -blockers and angiotensin II receptor blockers (ARB) stabilize the channel by reducing such phosphorylation and allowing FKBP binding which stabilizes the channel (lower left panel). In CPVT (upper-right panel), The RyR2 is more leaky due to the genetically induced abnormalities (yellow crosses) in RyR2 or associated proteins. The PKA-mediated phosphorylation sites are not necessarily occupied although when they are there is even greater leak (e.g. during exercise or emotional stress). The new RyR2 antagonists such as JTV519 aim to stabilise leaky channels (either HF associated or in CPVT – lower right panel) by acting directly on it. ARB – angiotensin II receptor blocker; CPVT – Catecholaminergic polymorphic ventricular tachycardia, FKBP – FK506 binding protein 12.6; PKA – protein kinase A; PP – protein phosphatase; P phosphate group; small yellow circles – Ca^{2+} leak. Adapted from Yano *et al* (Yano *et al.*, 2006).

1.6.2 Targeting RyR2 by reducing phosphorylation

Given the findings above some authorities have proposed a central role for RyR2 hyperphosphorylation in the pathogenesis of cardiac failure with the suggestion that reducing the excess SR Ca^{2+} leak that results would go some way towards slowing the decline in HF patients (Yano *et al.*, 2006; Marks *et al.*, 2014). It is interesting to note, therefore, that both angiotensin II receptor blockers (ARBs) and β -blockers have been shown to reduce PKA-mediated phosphorylation of RyR2

(Reiken *et al.*, 2001, 2003; Doi M *et al.*, 2002; Okuda *et al.*, 2004). These agents are two of the most widely used pharmacological classes of drug which have prognostic benefits in HF (Hunt *et al.*, 2005; Dickstein *et al.*, 2008).

Reiken *et al.* showed that chronic oral administration of 25mg metoprolol twice a day protected RyR2 from hyperphosphorylation in a pacing induced canine model of heart failure (Reiken *et al.*, 2001). This restored the level of FKBP12.6 binding and also reduced the open probability back to normal levels in bilayer experiments. These results were recapitulated by the same group in samples from humans with heart failure who had been treated with β -blockers, and also by a different group in the same canine HF model using propranolol instead of metoprolol (Doi M *et al.*, 2002; Reiken *et al.*, 2003). In the same model it was shown that chronic therapy with valsartan (an ARB) could prevent RyR2 hyperphosphorylation and restore SR leak (as assessed using SR membrane vesicles) to normal levels (Okuda *et al.*, 2004). A caveat to these results is that it would be over-simplistic to state that the beneficial effects of these agents are based on their activity on RyR2 since β -blockers down-regulate the increase in adrenergic signaling and ARBs mitigate the consequences of upregulation of the renin-angiotensin-aldosterone system which occur in HF. The phosphorylation of RyR2 is a small part of these signaling cascades and the beneficial effects of these agents are likely to be the result of their activity on multiple targets.

Recent work has also shown that some β -blockers have direct activity on RyR2, in particular carvedilol (Zhou *et al.*, 2011b). This agent was found to reduce both mean open time and open probability of RyR2s in bilayer preparations and also to reduce SCR events in intact myocytes in contrast to other beta-blockers. More targeted analogues with reduced β -blocker activity were also presented in the same study and have similar effects.

1.6.3 Targeting RyR2 directly

Ryanodine receptors are so-called because of their avid binding to the plant alkaloid ryanodine (Meissner, 1994). In bilayer studies, low concentrations (1nM to 10 μ M) result in the RyR2 permanently adopting a sub-conductance conformation (Rousseau *et al.*, 1987). At much higher concentrations (0.3-2mM) ryanodine binds to different, lower-affinity sites and completely blocks RyR2 (Meissner, 1986; Bers, 2001). The effect of low dose ryanodine in intact tissue is to produce a slow leak of SR Ca^{2+} during rest but allows transient re-accumulation of Ca^{2+} during stimulation trains (Bers *et al.*, 1987). With higher concentrations or longer applications of ryanodine, SR function is completely inhibited (Marban & Wier, 1985). Because of ryanodine's almost irreversible binding to RyR2 and the gradual decline in SR function seen following application it is difficult to use as an agent in intact cells, let alone as a potential therapeutic agent. In intact animals it causes a decline in LV systolic and diastolic function (Kalthof *et al.*, 1995; Prabhu & Rozek, 1997). Non-ryanoid compounds which block RyR2 have also been identified including peptide toxins and local anaesthetic agents (Sutko *et al.*, 1997). Such compounds have not found utility in specific therapy of SR leak because of their narrow therapeutic window and off-target effects, although local anaesthetic agents in particular have been indispensable as agents to interrogate RyR2 function in isolated cardiomyocytes (Trafford *et al.*, 2000).

1.6.3.1 Rycals

Agents such as JTV519 (K201) and S107 are relatively new compounds, under investigation which aim to reduce Ca^{2+} leak by more specific activity at RyR2. These agents have been named Rycals by

some investigators because of their proposed mechanism of action of enhancing the binding of RyR2 and FKBP12.6 (calstabin) (Andersson & Marks, 2010). JTV519 is a 1,4-benzothiazepine derivative which has off-target effects on multiple sarcolemmal ion currents including I_{Na} , I_{K1} , I_{Ca} and I_{Kr} . The net effect of this is APD shortening to a variable degree depending on species (Currie *et al.*, 2011). The primary mechanism of action of this agent at the level of the RyR2 is thought to be related to its effects on domain zipping. Conceptually in the resting state the N-terminal domain and central domain make close contact (domain zipping) at several subdomains which imparts stability to the closed state of the channel. When these interactions are weakened, for example by pharmacological agents or mutations, the resulting domain unzipping can result in an increase in open probability, in part due to FKBP12.6 dissociation (Oda *et al.*, 2005). JTV519 prevents this domain unzipping to restore stability of the channel.

In the intact isolated rat cardiomyocyte JTV519 has been shown to reduce diastolic SR Ca^{2+} release event frequency, amplitude and number of simultaneous release points per wave (Elliott *et al.*, 2011). This appears to occur independent of FKBP12.6 since even in the presence of high concentrations of FK506 the drug is able to reduce SR Ca^{2+} leak (Hunt *et al.*, 2007). In experiments on permeabilized rabbit cardiomyocytes it has been shown that, in contrast to tetracaine, SR load is reduced following application of JTV519 (Loughrey *et al.*, 2007). This was due to dual inhibition of RyR2 opening and SERCA2a activity, the latter of which would not be expected to be desirable in the treatment of heart failure. Nevertheless there seems to be a beneficial effect of the agent when administered to animals with heart failure. Yano *et al.* showed the prevention of adverse ventricular remodelling in a canine tachy-pacing model (Yano *et al.*, 2003). Wehrens *et al.* also showed a beneficial effect of the agent in an ischaemic mouse model of HF in terms of preservation of ejection fraction, although this effect was not present in an FKBP12.6 knockout transgenic mouse strain (Wehrens *et al.*, 2005a) suggesting that, in their hands and in contrast to the study of Hunt *et al.* (Hunt *et al.*, 2007), FKBP12.6 is critical to the mechanism of action of the agent. The benefits of the agent have also been extended to a norepinephrine-induced rat model of diastolic dysfunction (Kaneko *et al.*, 2006).

S107 is a derivative of JTV519 which is more specific for the RyR2 and is orally available (Currie *et al.*, 2011). This has been used to treat seizures in a transgenic mouse heterozygous for the RyR2-R2474S mutation which exhibit cardiac arrhythmias and seizures (Lehnart *et al.*, 2008). The agent also successfully reduced isoprenaline-induced ventricular arrhythmia in a model of muscular dystrophy which exhibits a leaky SR (Fauconnier *et al.*, 2010). In a different transgenic HF model which mimics the effects of PKA hyperphosphorylation, S107 successfully reduced SR Ca^{2+} leak in myocytes isolated from chronically treated animals and also reduced deterioration in LV contractility over time (Shan *et al.*, 2010a). In the same study the agent reduced the rate of decline of LV function following myocardial infarction in wild-type animals suggesting a possible important role in the therapy of acquired HF. At present, information on effects of this agent on other aspects of CICR are not yet available, so it is unclear whether off-target effects may also be contributing to the benefits seen in these models (Currie *et al.*, 2011).

1.6.3.2 Flecainide

Flecainide, a drug that has been used for many years clinically for its sodium current (I_{Na}) reducing properties, has recently been shown to have efficacy in the treatment of CPVT patients (Watanabe *et al.*, 2009; van der Werf *et al.*, 2011). Knollmann and colleagues have shown that flecainide

reduces Ca^{2+} wave frequency in both intact and permeabilized myocytes and have suggested that this is related to a direct action on the cardiac ryanodine receptor (RyR2) via an open-state block of the channel (Watanabe *et al.*, 2009; Hilliard *et al.*, 2010; Galimberti & Knollmann, 2011). In these studies they find no change in SR Ca^{2+} content, an increase in Ca^{2+} spark frequency and a reduction in spark mass. They relate this to the action of flecainide at RyR2 where they observe that the drug induces brief closures to a subconductance state (Hilliard *et al.*, 2010). In contrast, experiments in both intact and permeabilized myocytes were repeated by Liu *et al* (albeit in a different mouse model of CPVT), and no effect on Ca^{2+} wave frequency was found despite similar experimental conditions (Liu *et al.*, 2011a). The conclusion of Liu *et al* was that the reduction in I_{Na} caused by flecainide decreased the propensity for DADs to trigger action potentials. This debate is taken up further in chapter 7.

1.7 Conclusion

Through this introduction we have highlighted the importance of CICR and control mechanisms which amplify CICR in the process of EC-coupling. We have highlighted different forms of SR Ca^{2+} leak and ways in which this leak can be pathological, particularly in terms of ventricular arrhythmia initiation. We have also highlighted some of the changes in CICR which are thought to occur in HF and described why SR leak may be particularly arrhythmogenic in this condition. Finally we have appraised some of the known pharmacological strategies for reducing SR leak which target the cardiac ryanodine receptor.

1.8 Hypotheses

The overarching hypothesis at the beginning of this work was borne from previous work which suggested that SERCA2a gene transfer can reduce ventricular arrhythmia frequency in rats despite an absence of reduction of Ca^{2+} spark frequency (Lyon *et al.*, 2011). This led us to the hypothesis that it was not an increase in spark frequency but a change in spark morphology that resulted in arrhythmogenic SR Ca^{2+} release in HF. The resulting aim was to assess the differences in spark morphology that made HF cells arrhythmogenic in terms of Ca^{2+} wave and DAD genesis (i.e. a pro-arrhythmic spark “fingerprint”). This hypothesis could not be explored in detail since we found no major difference in either frequency or morphology of sparks in HF compared with control cells under basal conditions (Chapter 5). Hypotheses 1-6 listed below are sub-hypotheses resulting from the above overarching hypothesis and aimed firstly to show robustly whether there were true differences in SR Ca^{2+} leak in HF cells versus control cells under basal conditions and secondly whether exploration of leak under different conditions or in specific subcellular compartments might hold the key to enhanced arrhythmogenesis in HF. Finally hypothesis 7 explores a novel mechanism by which arrhythmogenic Ca^{2+} leak can be reduced. The background to each of these sub-hypotheses and specific aims to help test them are explained further in the chapters referenced below:

1. Hierarchical statistical methodologies can be used to reduce the risk of Type I errors in the analysis of data derived from isolated cardiomyocytes (Chapter 3).
2. There is progression of biometric, echocardiographic and pressure-volume loop derived measures of HF over time following myocardial infarction in the rat (Chapter 4).
3. Ca^{2+} transient morphology, amplitude and synchronicity across the myocyte are adversely affected by HF (Chapter 5).

4. Spontaneous Ca^{2+} sparks are also altered in HF with measures of frequency, amplitude and morphology changed in a way that contributes to the proarrhythmic phenotype of the condition (Chapter 5).
5. Use of oblique plane microscopy (OPM) can help assess whether features of sparks depend on their proximity to t-tubules within a cardiomyocyte (Chapter 6).
6. The likelihood of Ca^{2+} waves originating from a particular point in the cell depends on local t-tubule structure and organization (Chapter 6).
7. Flecainide can reduce the frequency of spontaneous Ca^{2+} leak events and does so via alteration in sarcolemmal ion fluxes rather than activity at RyR2 (Chapter 7).

2 METHODS

Methods used in the remainder of this thesis conform to the following. Any variation in techniques for a specific experiment, will be stated in the relevant chapter.

2.1 Animal Models

Male Sprague-Dawley (SD) rats were used for animal studies. They were housed in groups of 2-5 per cage at $21\pm1^{\circ}\text{C}$ on a 12h light:dark cycle and provided with standard rat chow and water *ad libitum*. All studies were carried out with the approval of Home Office, United Kingdom, under project license 70/6568 up until June 2012 and 70/7399 (a revision of the previous license) thereafter. Animal surgical procedures and perioperative management were carried out in accordance with the United Kingdom Home Office Guide on the Operation of the Animals (Scientific Procedures) Act 1986, which conforms to the Guide for the Care and Use of Laboratory Animals published by the U.S. National Institutes of Health under assurance number A5634-01.

2.2 Rat Myocardial Infarction

All studies were performed on adult male SD rats weighing 200-250g. In order to ensure no litter effect (whereby animals from individual litters have different characteristics than those of other litters), animals from individual cages were separated and randomly assigned to HF or control groups. The technique is similar to the technique of Johns et al (Johns & Olson, 1954), originally published in 1954. The modifications to this technique are as used by Lyon et al. (Lyon *et al.*, 2009). Animals were anaesthetised using isoflurane 5%, reducing to 1.5% once intubated and ventilated. Pre-operative medication was administered as follows: 0.015-0.03mg buprenorphine (0.05-0.1mg/kg), 1.25-1.5mg enrofloxacin (5mg/kg), and 2.5 ml 0.9% saline subcutaneously (sc). The rat was connected via the endotracheal tube (16G intravenous cannula) to the Harvard Ventilator (Harvard Apparatus, Massachusetts), and ventilated using volume-controlled ventilation at a rate of 90/min, with a tidal volume of 2-2.5ml, giving a minute volume of 180-225ml/min. These settings were optimized using a pulse oximeter on a sample of 5 rats to find the rate and volume which provided optimal oxygenation.

Surgery was performed with the rat secured in the left lateral position using micropore tape (3M, UK) on an electrical heat-pad. A shaved area over the left side of the precordium was sterilised with 1% chlorhexidine (Hibiscrub™, Astra Zeneca, UK) and a sterile field was established. A left parasternal incision was made with subsequent separation of two heads of pectoralis major to reveal underlying ribs. These were separated in the 4th interspace by blunt dissection. The thymus gland was retracted and held to expose and stabilize the heart. The pericardium was removed from the anterior surface of the heart using blunt dissection. The left anterior descending coronary artery (LAD) was ligated by passing a 6-0 Prolene suture (Johnson and Johnson Medical Ltd, UK) through the LV wall 2mm inferior to the infero-medial corner of the left atrial appendage and tying it firmly. Puncture and exit sites were separated by approximately 2mm. The LAD is not visible in the intact rat heart (even using an operating microscope), hence a decision regarding adequacy of infarction must be made via other means. In the first 30 animals electrocardiographic (ECG – Cardiostore, Vetronic, UK) monitoring via placement of standard limb leads was used to confirm myocardial infarction (Figure 2-1). Subsequently ECG monitoring was not required due to improved visual recognition of MI (pallor and hypokinesis of the anterior wall extending to the apex). Multiple sutures were sometimes required to produce adequate infarction.

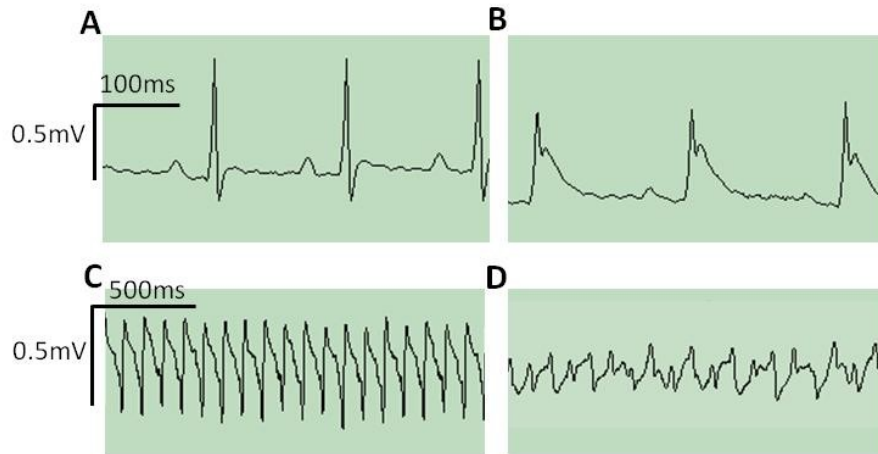


Figure 2-1 ECG Changes observed during rat MI

(A) Normal ECG prior to MI. (B) ST-elevation 5 minutes after LAD ligation. Examples of arrhythmia observed following MI include (C) ventricular tachycardia (VT) and (D) ventricular fibrillation (VF).

Closure involved initial placement of a 22G Abbocath®-T catheter (Hospira Venisystems™, Ireland) with a sidehole cut into it to act as a chest drain. Following closure of the ribs using 4-0 Ethibond continuous suture (Johnson and Johnson Medical Ltd, UK), apposition of chest wall and pleura was re-established via aspiration of the chest drain. Continuous positive airways pressure (CPAP) was delivered by switching the exhaust tube to one submerged beneath 5 cm water. The thoracotomy and skin were closed using a 4-0 Ethibond continuous suture.

Anaesthesia was stopped and 100% oxygen was continued. Animals were ventilated until they showed signs of spontaneous movement at which time they were extubated and placed in an oxygen-enriched, temperature-controlled recovery chamber for at least 2 hours. Post operative pain management involved repetition of buprenorphine administration if rats showed signs of distress such as piloerection or limited mobility.

A small group of animals were sham operated via the same process but without ligating the LAD. *In vivo* cardiac function then measured by echocardiography to ensure there was no deterioration in function caused by the process of anaesthesia and thoracotomy.

2.2.1 Complications

Over the course of these studies a total of 209 MIs were performed, although some of these were studied only by other groups and so not all contributed to data within this thesis. Of these 163 survived until sacrifice. Therefore mortality rate was 22%. Complications causing death are detailed in Table 2-1.

Complication	Number of Animals	% of Cases
Sudden death within 24h of procedure but after recovery	19	7.9%
Intra-operative tachyarrhythmia (refractory VT/VF)	14	6.5%
Sudden death after 24h (deaths at 8, 10, 14, 22, 24 weeks)	5	2.3%
Ventilation issues (2 subcutaneous emphysema due to tracheal rupture, 1 lung hyperinflation)	3	1.4%

Intra-operative bleeding	3	1.4%
Culled due to humane end point being reached	2	0.9%

Table 2-1. Fatal complications of rat MI surgery.

Non-fatal complications included tachyarrhythmias which reverted to sinus rhythm spontaneously or after internal cardiac massage using DeBakey forceps (5.1% of cases) and non-fatal bleeding from the ventricular needle puncture site which usually resolved with gentle swab pressure. Wound dehiscence due to removal of one or more sutures by the animal gnawing occurred in 16 cases (7.4%) and on one occasion led to the animal being culled due to a humane end-point being reached. In the other 15 cases wound dehiscence was successfully managed conservatively with topical antiseptic and INTRASITE gel (Smith & Nephew, London). In all such cases the wound closed fully by secondary intention within a week.

2.2.2 Planimetry to Ensure Large Myocardial Infarctions

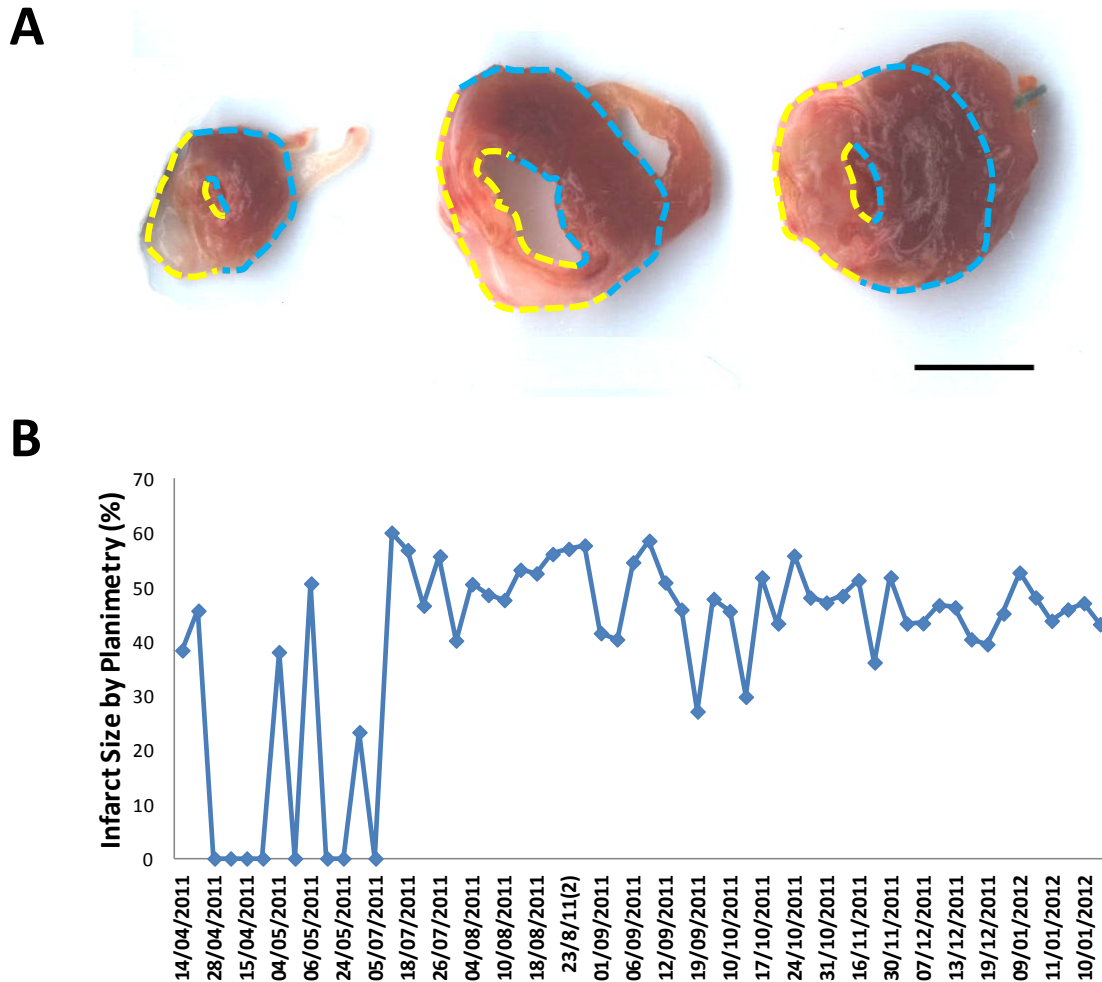
During the initial learning curve, 4 week models were performed since it was deemed to be important to become consistent in the technique of surgical ligation of the LAD prior to keeping animals for the full 16 weeks required to produce the heart failure model. At 4 weeks animals were killed following cervical dislocation following brief exposure to 5% isoflurane until righting reflex was lost. Hearts were explanted and the basal half was used for cell isolation (section 2.4) whilst the apical half was used for planimetric assessment of MI size which was based on the technique of Pfeffer et al. (Pfeffer *et al.*, 1985a, 1985b)

The apical portions of heart were flash frozen in liquid nitrogen for twenty seconds. Hearts were partially thawed and sliced into 4-6 2mm biventricular sections using a coronal cardiac matrix (Zivic Laboratories). The slices were placed between clear microscope slides and scanned using a Hewlett-Packard 6200C scanner. After adjusting the contrast image to help delineate the margins of the scar, planimetry of the images was performed using Image J software (NIH).

The endocardial and epicardium circumference of the scar were measured for each section, followed by the total endocardial and epicardial circumference of the left ventricle (Figure 2-2A). The sum of the endocardial scar lengths for all sections was divided by the sum of the endocardial circumferences for all sections to give the percentage of endocardial scar). Similarly the sum of the epicardial scar lengths for all sections was divided by the sum of the epicardial circumferences for all sections to give the percentage of epicardial scarring. A summary measure of infarct size was calculated as the the sum of the epicardial and endocardial scar length divided by the sum of total circumferences for each section expressed as a percentage. If scar did not extend to the epicardium then epicardial infarct circumference was deemed to be zero. Pfeffer et al have previously classified rat MI into small, medium and large categories using planimetry (Table 2-2). (Pfeffer *et al.*, 1985b) We aimed for MIs to reach the large category (>40%). Cells studied from hearts with smaller infarcts are excluded from our results. The MI surgery has a significant learning curve and to assess progress in terms of MI consistency, MI size was assessed over time (Figure 2-2B). After 14 cases infarct size became much more consistent. Once this confirmed over several months, planimetry was no longer performed. Instead biometric and functional measures of impaired cardiac function (section 2.3) and a visual assessment at the time of sacrifice (scar extending over most of the anterior wall and including the apex of the heart) were used to ensure infarct size was sufficient.

Percentage Scarring	Infarct Size
<20%	Small
20-30%	Moderate
>40%	Large

Table 2-2. Categorization of MI Size

**Figure 2-2. Planimetry to Assess MI Size and Ensure High Quality Surgery**

(A) Slices of rat heart 4 weeks post myocardial infarction is shown with both epicardial and endocardial outlines of scar (yellow dotted lines) and non-scarred (blue dotted lines) ventricular wall. In this case the LV wall of the non-scarred ventricle is hypertrophic. The summary scar size is 47% in this case. Scale bar 5mm. (B) Learning curve of MI surgery is shown with inconsistency of infarct size in several cases near the beginning of the project with consistency improving over time.

2.3 Biometric and Functional Measures of Contractility

A major aim of these studies was to assess how HF affects SCR in isolated cardiomyocytes. It was therefore important to confirm HF in terms of reduced cardiac contractile function and biometric measurements.

2.3.1 Biometry

Previous studies have shown, in similar models, that heart weight (HW) increases in HF animals. (Semb *et al.*, 1998; Lutgens *et al.*, 1999; Lyon *et al.*, 2009) This has typically been expressed as a fraction of body weight (BW) in order to correct for changes in the size of the rat. However, a study by Yin *et al* on senescent rats showed that correction of HW to tibia length (TL) was more closely correlated with cellular hypertrophy than the correction to BW in senescent rats. A ratio of HW to a measure other than BW may be particularly important in HF states because of the potential of peripheral oedema to produce an elevated BW. We therefore measured HW, BW and TL to allow both corrections to be performed. BW was measured on the live anaesthetized animal prior to cervical dislocation. HW was measured by taking the heart following explantation and washing with Krebs solution (section 2.4), then squeezing out excess solution and drying the heart by laying on a paper towel and turning. The heart was then weighed on a scale accurate to the nearest mg. TL was measured by dissecting into the posterior aspect of the animals hind-limb following death, dislocating the tibia posteriorly and measuring from the base of the heel to the tibial plateau with electronic calipers (RS components). Lung weight (LW) was also measured in a set of animals to assess whether it was increased consistent with pulmonary oedema.

In our experiments, where rats are still growing following surgery (200-250g at time of operation up to 700-800g for the largest 16WMI animals) we felt that TL alone as a correction for HW may be inappropriate. This is because a volume measurement (for which mass is a surrogate) when corrected to a linear measurement will always increase with size of an animal even in the absence of a change in relative mass of the two objects. This is shown by way of a simple model in Appendix 9.1 where we show that the ratio of HW to the cube of TL (HW/TL^3) is more stable with changes in size when growth of the heart is proportional to growth of the body. Real data from control animals shows a similar pattern to the model and is also shown in Appendix 9.1. Although TL^3 has not been published previously as an appropriate correction for HW, this also makes sense in terms of published data in the field of allometry. BW is proportional to LV mass to the first power but TL to approximately the third power (Alexander *et al.*, 1979; de Simone *et al.*, 1992).

2.3.2 Echocardiography

Echocardiography was originally shown to be a reproducible technique for the monitoring of cardiac remodeling following MI in the rat by Litwin *et al.* (Litwin *et al.*, 1995) Our technique is a modification of theirs. Echocardiography was performed under anaesthesia (2 % isoflurane) immediately prior to sacrifice. A Visualsonics Vevo 770 was used and initially B-mode imaging using the RMV10B probe was attempted. However tissue penetration was difficult to achieve with rats weighing more than 300g. The RMV716B probe achieved good tissue penetration (Figure 2-3A) but B-mode imaging was too slow to acquire LV dimensions accurately. M-mode imaging with this probe provided a good solution with good tissue penetration and excellent temporal resolution (Figure 2-3B). The parasternal long axis view was used to position the scan-line just below the papillary muscles. Measurements obtained via M-mode imaging as standard are listed and shown in Figure 2-3B:

- Heart rate (HR)
- Left ventricular anterior wall thickness in diastole (LVAWd)
- Left ventricular internal diameter in diastole (LVIDd)
- Left ventricular posterior wall thickness in diastole (LVPWd)
- Left ventricular anterior wall thickness in systole (LVAWs)

- Left ventricular internal diameter in systole (LVIDs)
- Left ventricular posterior wall thickness in systole (LVPWs)

Calculations attained from these measures are as follows. Formulae are provided within the cardiac package of measurements in the Vevo 770 machine:

- Diastolic volume (in μl) = $7/((2.4+\text{LVIDd})^3)$
- Systolic volume (in μl) = $7/((2.4+\text{LVIDs})^3)$
- Ejection Fraction (%) = $(1-(\text{Systolic volume}/\text{Diastolic volume})) \times 100$

Subsequently the probe was angled superiorly to focus on the pulmonary artery (PA) (Figure 2-3C). The PA was used to measure flow since it was easier to attain a clear image of this artery at an angle which allowed velocity measurement (compared with the aorta), and PA flow equals aortic flow. Dimensions of the PA were measured with B-mode imaging. Blood velocity in the PA was then measured over time by placing the pulsed wave Doppler cursor in line with the artery and in the centre. The maximum velocity (PA V_{max}) and the velocity time integral (VTI - i.e. the area under the curve of the velocity trace) were measured (Figure 2-3D). Acceleration time (AT) and ejection time (ET) were also measured. The following values were calculated using this data:

- Stroke Volume (Pulsed Wave) = $7.85 \times \text{PA diameter}^2 \times \text{PA VTI}$
- Cardiac output (CO – ml/min) = $\text{HR} \times \text{Stroke volume}/1000$
- Cardiac Index (CI - ml/kg/min) = CO/BW

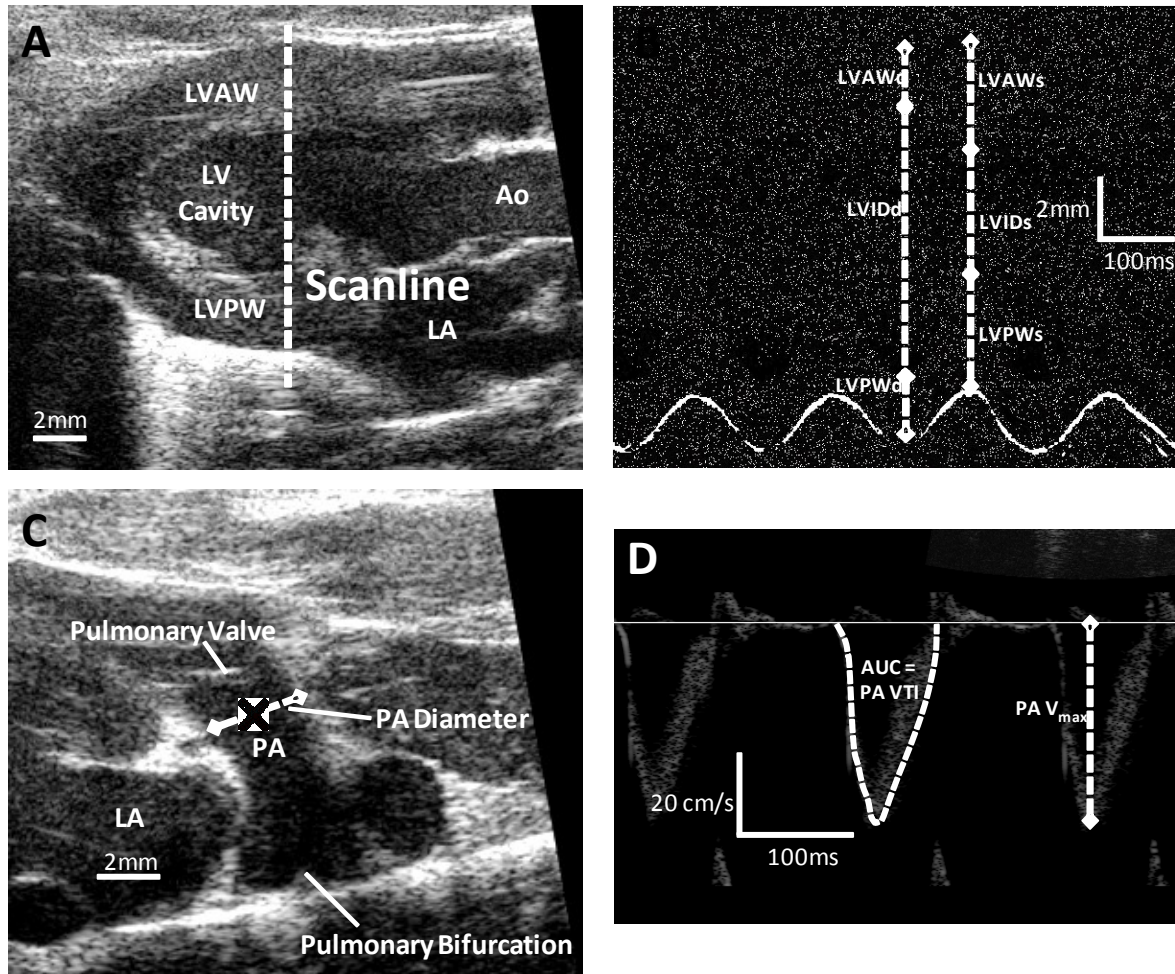


Figure 2-3. Echocardiographic Imaging and Measurements Obtained

(A) The left ventricle was imaged in the parasternal long axis view with care being taken that LV was horizontal within the field of view and that left atrium (LA) and aorta (Ao) could be seen. The brighter pericardial layers can clearly be distinguished from the left ventricular anterior wall (LVAW) and posterior wall (LVPW). The scanline is placed just inferior to the papillary muscles. (B) M-mode imaging shows good temporal resolution and allows measurement of thickness of ventricular walls and cavity in systole (LVAWs/LVPWs/LVIDs) and diastole (LVAWd/LVPWd/LVIDd). The gradient of the systolic movement of the posterior wall gives the maximal velocity of its contraction (LVPW V_{max}). (C) Superior tilting of the probe from the parasternal long axis position allows imaging of the pulmonary artery (PA) with an excellent angle for measuring blood velocity. In this view LA and descending Ao can also be seen, together with bifurcation of the first part of the PA (pulmonary trunk) into right and left pulmonary arteries. The pulsed wave Doppler cursor is placed at the centre of the line used to measure PA diameter and the angle of detection matched to the angle of the PA. (D) Measurements of PA blood velocity allow quantification of the maximal velocity (PA V_{max}) and the velocity time integral (PA VTI) through assessment of the area under curve (AUC) of the velocity trace.

2.3.3 Pressure-Volume Loops

In order to assess other aspects of myocardial function, pressure-volume (PV) loop studies were performed in a similar manner to Lyon et al. (Lyon et al., 2009) PV loop studies were performed under general anaesthesia (1.5% isoflurane) while the animal was intubated. A 1.9F Scisense PV

catheter attached to the ADVantage acquisition system (Scisense Inc., Ontario, Canada) was introduced into the LV apex via a subcostal incision. Steady state and dynamic (inferior vena cava [IVC] occlusion) studies were performed. Data were recorded using Labchart 6 software (AD Instruments, Oxford, UK) and analyzed offline using PVAN 3.6 software (Millar Instruments, Texas, USA). Steady-state measurements were attained under conditions of spontaneous cardiac contraction with no intervention applied to the animal and include measures of volume and pressure in systole and diastole. The maximal rates of change in pressure in systole and diastole were also assessed to give dP/dt max and dP/dt min respectively. Dynamic measures apply to the situation where preload is adjusted to gain preload-independent measures of cardiac function. In this study the slopes of the end systolic pressure volume relationship (ESPVR) and end diastolic pressure volume relationship (EDPVR) were assessed. These are preload independent measures of systolic and diastolic function (Pacher *et al.*, 2008). Finally myocardial energetic efficiency is also calculated as per Equation 2-1 via the method of Suga *et al.* (Suga *et al.*, 1985; Suga, 2003). This parameter is calculated as the proportion of cardiac energy production used in the generation of cardiac contractile force compared with the total energy used by the heart which is closely correlated with the pressure volume area (PVA).

$$\text{Energetic Efficiency} = \frac{\text{Stroke Work}}{\text{Pressure Volume Area}}$$

Equation 2-1. Equation to calculate energetic efficiency from PV loops.

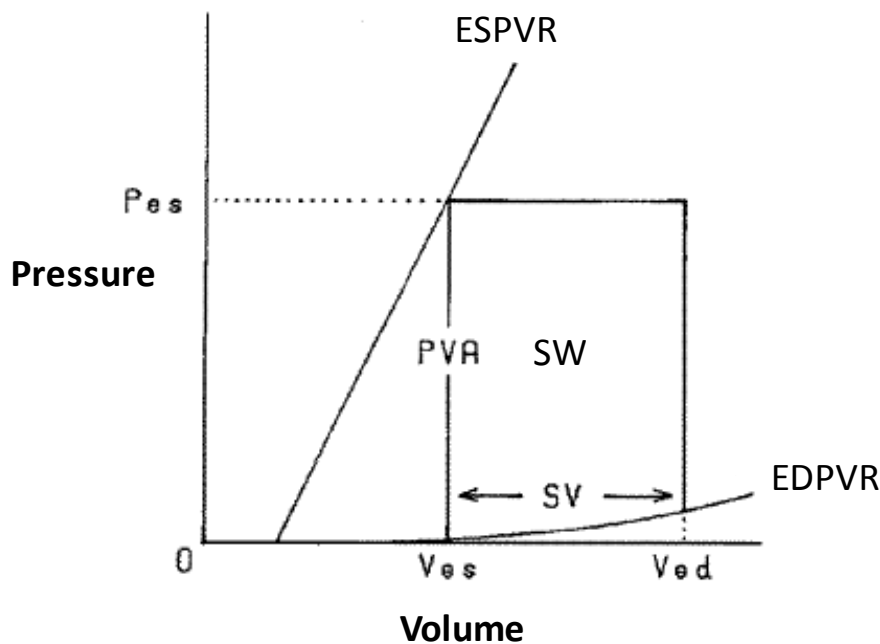


Figure 2-4. Diagram showing the calculation of energy efficiency from PV loops.

Schematic showing the PV loop can be used to calculate energetic efficiency of cardiac function. A simplified PV loop is shown starting at end diastolic volume (V_{ed}) with isovolumic contraction causing an upward deflection which eventually leads to ejection of blood as pressure increases to that approaching end systolic pressure (P_{es}) and causing a leftward deflection until end-systolic volume (V_{es}) is reached. ESPVR and EDPVR (defined above) are also shown. The total area bounded

by ESPVR, EDPVR and the loop is the pressure volume area (PVA) and is representative of the total energy use of the heart. Stroke work (SW) is the area bounded by the loop itself and is representative of energy used to produce mechanical movement. Energy efficiency is SW/PVA. Adapted from Suga *et al* (Suga *et al.*, 1985).

2.3.4 Validity of the use of Age-Matched Control versus Sham Animals

Age-matched controls (AMCs) have been used in several studies as a comparator for animals with MI (Takahashi *et al.*, 1990; Pfeffer *et al.*, 1991; Creemers *et al.*, 2003; Lyon *et al.*, 2011). The other option is to compare HF animals to sham-operated controls. The comparison with AMC animals has advantages in terms of being less time-consuming and expensive, however there is a possibility that the anaesthetic and thoracotomy alone may cause some impairment of cardiac function. An early comparison was therefore performed between AMC animals and sham-operated animals. Four animals had sham operations and four had no operation (AMC). The animals underwent echocardiography after 4 weeks. There was no change in LV dimension of function, suggesting that no major change in cardiac function was produced by the anaesthetic and thoracotomy. Thus AMC animals were used in the remainder of the study.

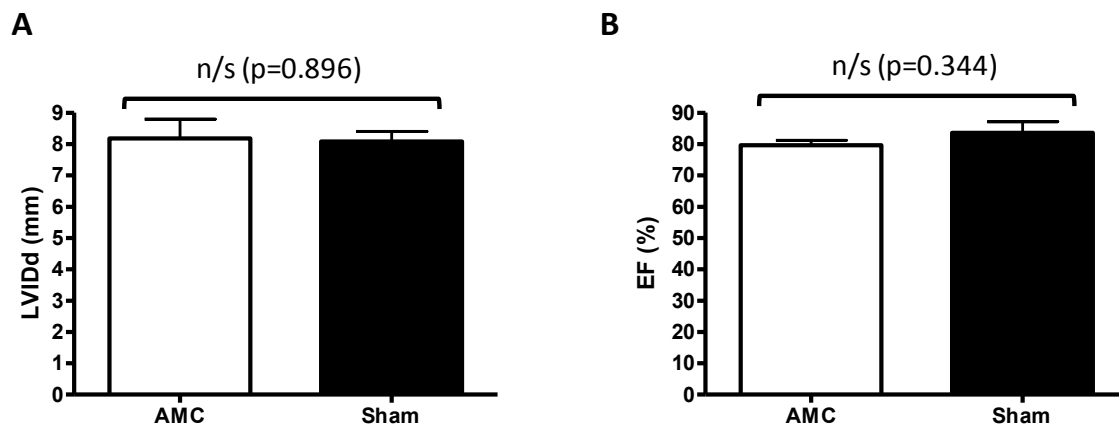


Figure 2-5. Cardiac function of sham rats is not markedly different to cardiac function of AMC rats at same age.

(A) LVIDd is unchanged in sham animals, suggesting there is no cardiac dilatation as a result of the procedure. (B) There is no significant change in EF either. n=7 rats in each group.

2.4 Isolation of rat cardiac myocytes

This was performed by Peter O’Gara (See Acknowledgements) using techniques previously described (Sato *et al.*, 2005). Animals were killed by cervical dislocation. Heart and aorta were explanted quickly and placed in ice-cold oxygenated Krebs-Henseleit (KH) solution (119mM NaCl, 4.7mM KCl, 0.94mM MgSO₄, 1mM CaCl₂ 1.2mM KH₂PO₄, 25mM NaHCO₃, 11.5mM glucose; 95% oxygen, 5% carbon dioxide), containing heparin (4 Units/ml) to prevent clotting. The heart was trimmed free from adherent tissue and then the aorta tied to the cannula of a Langendorff set-up. The heart was surrounded by a heated jacket, to maintain temperature at 37°C, and retrogradely perfused with KH solution for 5 minutes at a steady flow of 6-8mL/min/g, followed by perfusion with a pre-oxygenated

'low calcium solution' (LC) containing 12-15 μ M calcium (120mM NaCl, 5.4mM KCl, 5mM MgSO₄, 5mM pyruvate, 20mM glucose, 20mM taurine, 10mM HEPES, 5mM nitrilotriacetic acid; 100% oxygen), for a further 5 minutes. The heart was subsequently perfused for 10 minutes with re-circulating enzyme solution (ES), containing 1g/L of type-2 collagenase (Cooper Biomedical), 0.8g/L of hyaluronidase (Sigma-Aldrich, Poole, UK) and 0.1% bovine serum albumin. The heart was cut down from the Langendorff cannula into a small volume of the collagenase/hyaluronidase ES, and the atria and right ventricle removed. In some isolations in rats with myocardial infarctions the left ventricle (LV) was split into an approximate 3mm region around the perimeter of the infarct (borderzone-BZ) and remote LV prior to further isolation. The LV was chopped onto 2-4mm³ sections and transferred to a tube containing 10mL of the same enzyme solution and gently shaken for 5 minutes at 37⁰C (100% O₂). The tissue was filtered through a 300 μ m nylon gauze and the supernatant discarded. Filtered tissue was re-suspended in 10ml of the pre-oxygenated (100% O₂) collagenase/hyaluronidase ES and gently shaken at 37⁰C (100% O₂) for a further 30 minutes. The cell suspension was then filtered through a 300 μ m nylon gauze, centrifuged at low speed for 1 minute, and the supernatant discarded. The resulting cell pellet was re-suspended in pre-oxygenated (100% O₂) 200 μ M calcium ES. Rat myocyte suspensions, stored at room temperature (RT), typically consisted of 60-70% rod shaped, viable, Ca²⁺-tolerant myocytes.

2.5 Experiments on Intact Isolated Rat Cardiomyocytes

2.5.1 Cell preparation and dye loading

The Ca²⁺-sensitive fluorescent dye fluo-4 was used to monitor localized changes in [Ca²⁺]_i. 1ml aliquots of cells were incubated with 10 μ M fluo-4 AM (Invitrogen) and 0.16% pluronic acid (Invitrogen) for 30 minutes. Cells were then centrifuged at 10G for 1 minute to form a pellet. The supernatant was discarded and the cells were resuspended in 2 ml Dulbecco's Modified Eagle Medium (DMEM) (Gibco BRL, Life Technologies). The wash step was repeated and cells left at room temperature for 30 minutes to allow de-esterification of the indicator prior to commencing microscopy. If Ca²⁺ sparks were not being assessed (i.e. wave or transient experiments), no pluronic acid was used for loading. Alternatively fura-2 AM was used for ratiometric measurement of [Ca²⁺]_i. In this case, loading protocol was similar but 5 μ M fura-2 AM was added to 1 ml cells for 30 minutes in the absence of pluronic acid.

2.5.2 Cell selection

Cardiomyocytes were used within 6 hours and selected at random in each bath. Candidates were screened for acceptability against specific exclusion criteria. Cells with rounded edges, obvious cytoplasmic vesicles, automatic activity prior to stimulation, major ultrastructural defects, absence of clear striations or cells that were not incompletely isolated (e.g. cell pairs) were not used. To ensure selection was un-biased the first cell in each bath that met inclusion criteria was studied. After each line-scan the cells were re-assessed to ensure they remained healthy and if they met any of the exclusion criteria above, data collected was excluded since large fluxes in cytoplasmic [Ca²⁺] are common during cell deterioration.

2.5.3 Experimental setup

A cell superfusion system was used to ensure rapid switching between solutions and minimal change in experimental temperature. A fast exchange open diamond RC24N superfusion chamber (Warner Instruments) was mounted on the stage of an inverted Nikon Eclipse TE-300 microscope with a "Bio-

Rad Radiance 2000" confocal attachment. A Nikon 40x oil immersion lens was used. The floor of this chamber was a glass coverslip. Cells were loaded into chamber using a pipette following application of 3µl of natural mouse laminin to the base, allowing cells to adhere to the coverslip. All experiments were conducted at 37°C with the cells protected from light to avoid bleaching of the fluorescent indicator.

External field stimulation via a 5ms bipolar pulse through platinum electrodes was performed at 1.5× threshold voltage. Generally 0.5 Hz stimulation was used as a baseline with rates increased as required for a particular protocol up to 5Hz. Standard superfusate is normal Tyrode (NT) solution (140 mM NaCl, 6mM KCl, 1 mM MgCl₂, 2mM CaCl₂, 10 mM glucose, and 10 mM HEPES, adjusted to pH 7.4 using 1M NaOH. NT was either used with or without addition of pharmacological agents which are outlined in specific chapters. Where agents were added this was performed in a cross-over manner whereby 50% of cells had the agent applied after control solution whereas in 50% of cells the agent was present initially and then washed off. This methodology was designed to limit the effects of photobleaching, phototoxicity and cell damage on experimental results (Sikkel *et al.*, 2013a).

2.5.4 Imaging Ca²⁺ Sparks, Waves and Transients using Confocal Line Scanning

Fluo-4 was excited using the 488-nm line of an argon laser and the emitted fluorescence collected through a 520-nm filter. The microscope was used in line-scanning mode whereby a single line across the cell (but avoiding the nucleus) is repeatedly scanned to build-up a 1-D image over time (Figure 2-6 A-B). Different cells were used for assessment of different Ca²⁺ release phenomena (transients, waves and sparks) in order to avoid photobleaching and laser damage.

Contraction under steady-state conditions for at least 2 minutes was observed prior to making any recordings. In the case of Ca²⁺ transient recordings five thousand lines were collected at 600 lines per second (lps). Laser power was set to 10.0%, with an iris setting of 8mm, giving a z-axis depth of 4.2 µm. A smaller iris (3mm, z-depth 1.5µm) was used for assessment of dyssynchrony. Electrically evoked contraction continued at 0.5Hz during the recording.

Ca²⁺ waves (Figure 2-6B) were assessed following a period of steady state contraction at 0.5 Hz for at least 2 minutes and then an increase in pacing rate to 5Hz for 30s. A subsequent 30s quiescent period was imaged for assessment of waves. Confocal settings were the same as for transients other than a reduction in scan speed to 166lps. Figure 2-6C shows how the line scan image relates to changes in average fluorescence across the line over time.

Ca²⁺ sparks (Figure 2-6B) were recorded following cessation of steady-state stimulation at 0.5Hz for at least 2 mins. The 15s time-period following the final Ca²⁺ transient was imaged. Settings for recording included laser power of 20% and iris of 3mm (z-axis depth of 1.5µm). Scan speed was 600lps.

SR Ca²⁺ content was assessed via rapid superfusion of 20mM caffeine immediately following the decay of the last stimulated Ca²⁺ transient following at least 2 mins steady-state contraction at 0.5Hz. Settings were the same as those used to record Ca²⁺ transients.

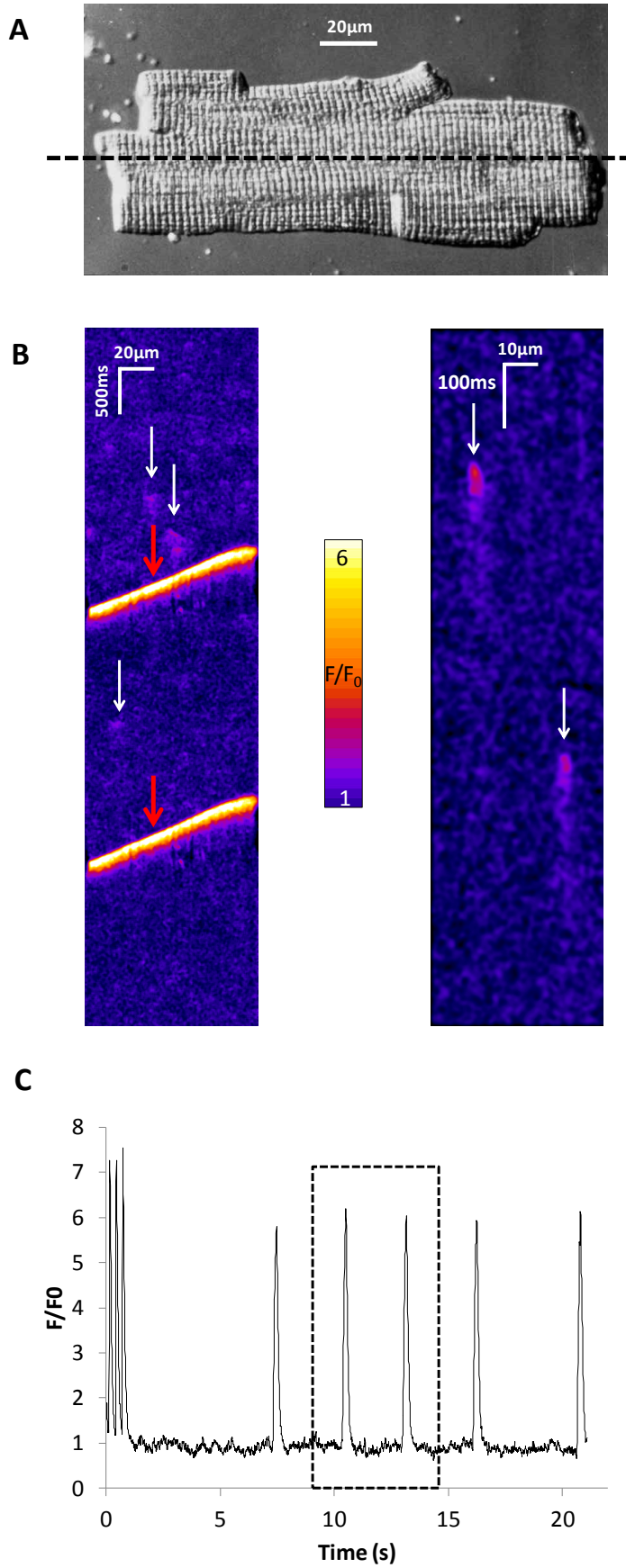


Figure 2-6. Imaging of $[Ca^{2+}]_i$ Using Confocal Microscopy in Line scan Mode

(A) Image of isolated ventricular cardiomyocyte. To form the line scan a line is selected across the length of the cell which will be repeatedly scanned. The z-depth is adjusted to approximately the centre of the cell. (B) Line scans optimized for wave detection (left) at a scan rate of 166 lines per second (lps) and z-depth 4.2µm, and for spark detection (right) at a faster scan rate of 600lps and a smaller z-depth of 1.5µm. Waves are indicated by red arrows and sparks by white arrows. Sparks are visible at the slower scan rate but better demarcated at faster rates. (C) Fluorescence signal change over time in a cardiomyocyte derived by averaging fluorescence signal across the entire line at each timepoint. This shows rapid evoked Ca^{2+} transients at 5Hz followed by a quiescent period during which 5 Ca^{2+} waves are seen. The boxed region indicates the time interval imaged in (B), left panel.

2.5.5 Imaging Using Epifluorescence Microscopy

For some experiments epifluorescence microscopy was used to give an indication of $[Ca^{2+}]_i$ using either fluo-4 or fura-2 loaded cells.

2.5.5.1 Epifluorescence imaging of fluo-4

This was performed with light via an epifluorescence illuminator from a 100-W xenon lamp equipped with an interference filter. Cells were selected and extracellular regions were excluded with the aid of a video system which could also be used for edge detection as described. (Terracciano & Macleod, 1996) The excitation wavelength was 485nm and emitted light passed through a 520nm long-pass filter. Fluorescence output was assessed using a PMT via a Digidata 1440A data acquisition system. PClamp software (Molecular Devices, Sunnyvale, Ca) was used to collect data at a sampling rate of 2kHz. The superfusion system was as described above (section 2.5.3) attached to a Nikon TE300 inverted microscope. Background subtraction was performed on each cell by measuring the fluorescence of the same field of view but not including any cellular material.

2.5.5.2 Epifluorescence imaging of fura-2

In experiments in which diastolic $[Ca^{2+}]_i$ was measured, fura-2 was used as the Ca^{2+} -sensitive fluorophore and fluorescence determined using a photomultiplier system (Ionoptix Inc.). Data were acquired using Ionwizard software. Background subtracted epifluorescence was measured and the fluorescence ratio (R) was determined using the fluorescence recorded at 510 nm when illuminating the specimen at the isosbestic point for Fura-2 (360nm) (giving the numerator) and at (380nm) (giving the denominator). $[Ca^{2+}]_i$ was determined according to Equation 2-2.

$$[Ca^{2+}]_i = K_d \beta (R - R_{min}) / (R_{max} - R)$$

Equation 2-2. Calculation of $[Ca^{2+}]_i$ using fura-2 fluorescence.

R is the ratio of fluorescence of the cell at 360 and 380nm. K_d is the dissociation constant of Ca^{2+} from fura-2 and was taken to be 386nM as per the intracellular determination performed by Kajita and Yamaguchi (Kajita & Yamaguchi, 1993). β is the ratio of fluorescence of fura-2 at 380nm in zero Ca^{2+} and saturating amounts of Ca^{2+} , R_{max} and R_{min} represent the ratios of fura-2 fluorescence in saturating and effectively “zero” Ca^{2+} respectively. β , R_{max} and R_{min} were experimentally determined by imaging capillary tubes containing, for zero Ca^{2+} (in mM): KCl (150), NaCl (10), $MgCl_2$ (3), HEPES (10), EGTA (10) with 1µM fura-2 pentapotassium and pH to 7.4 with KOH and for saturating Ca^{2+} (in

mM): KCl (150), NaCl (10), MgCl₂ (3), HEPES (10), CaCl₂ (1) with 1μM fura-2 pentapotassium and pH to 7.4 with KOH, which was performed for each filter-set.

2.5.6 Data analysis

Lasersharp 2000 (Bio-Rad, UK) software was used to collect images from the confocal microscope. Subsequently a combination of custom macros and an open source plugin were used within ImageJ (National Institute of Health) to assess characteristics of Ca²⁺ transients, waves and sparks.

2.5.6.1 Ca²⁺ Transients

I coded a macro to assess transient characteristics. The full macro is shown in Appendix 9.1. The functions of the macro are as follows:-

- Assess background fluorescence from a region outside the cell and subtract from intracellular fluorescence
- Select a region of the cell to be assessed for transients
- Calculate mean fluorescence along the linescan at each sampled time-point
- Apply a Gaussian filter to smooth transients (default filter set to a cutoff frequency of 10% of sampling frequency)
- Assess number of transients returning to within 10 standard deviations of baseline fluorescence.
- Peak and baseline fluorescence assessed for each transient.
- Thresholds based on these values, as well as curve fitting commands used to assess:-
 - Peak Fluorescence (F/F_0)
 - 10%-90% rise time (ms)
 - Time to Peak (ms)
 - Time to 50% decay (TD50 - ms)
 - Time to 90% decay (TD90 - ms)
 - Decay constant calculated by best fit to first order decay (Equation 2-3) beginning from 50% decay (τ – ms)
 - Rate constant calculated by reciprocal of τ (λ – ms⁻¹)

$$F(t) = F(0) e^{-t/\tau}$$

Equation 2-3. First order decay equation.

F (fluorescence) at time (t) is related to initial fluorescence (F(0)), in this case defined as fluorescence at 50% decay.

A modification of this macro (Appendix 9.1.6) was used to assess the amplitude of caffeine-induced Ca²⁺ transients.

2.5.6.2 Transient dyssynchrony

Transient dyssynchrony was also assessed via a custom-made macro which I coded (Appendix 9.1.3). This macro is designed to compare synchronicity of rise and fall of the Ca²⁺ transient across the cell. It performs the following steps:-

- User sets number of transients to analyse for dyssynchrony

- Automatically detects beginning of transients through rise in fluorescence
- Splits each transient into multiple sub-transients. The width of these sub-transients is based on mean resting sarcomere length in the rat cardiomyocyte under our experimental conditions. This was calculated from confocal transmission images (Figure 2-7A) with subsequent Fourier transform (Figure 2-7B) revealing the dominant cycle length (1.8 μ m in this case, mean of 10 cardiomyocytes 1.77 μ m \pm 0.03).
- Smooths sub-transients using a 50ms boxcar.
- Assesses rise characteristics of each sub-transient in terms of time to 50%, 90% and 100% of peak (Tt50P, Tt90P, TtP).
- Assesses peak amplitude of each sub-transient (relative to an average F_0 across the cell prior to the transient – F/F_0)
- Assessed decay of each sub-transient in terms of tau.
- Calculates dyssynchrony of above measures by calculating their standard deviation for each transient, and then a mean dyssynchrony by assessing the mean of these measures in all transients in the cell
- As a result the macro output includes the following:
 - DysTt50P – Mean of the dyssynchrony of time to 50% peak in the cell.
 - DysTt90P – Mean of the dyssynchrony of time to 90% peak in the cell.
 - DysTtP – Mean of the dyssynchrony of time to peak in the cell.
 - DysAmp – Mean of the dyssynchrony of peak amplitude in the cell.
 - DysTau – Mean of the dyssynchrony of tau in the cell.

An example of the use of the macro is given in Figure 2-7C-F and Table 2-3. Figure 2-7C shows a normal synchronous transient whilst Figure 2-7D shows a dyssynchronous transient. A small number of sub-transients are analysed for illustration purposes. Each “lane” (arrows in Figure 2-7C & D) represents the limitations of a sub-transient although would be continued all the way through the transient (not shown to prevent obscuring transient in the figure). Figure 2-7E&F represent the rise-phase of the sub-transients of Figure 2-7C&D respectively. The extent of spread of sub-transient rise corresponds with the visual appearances of the transients. It is also important to note that peak amplitude is not as uniform across the cell in Figure 2-7D as in Figure 2-7C – hence the additional analysis of DysAmp and not simply the time to peak amplitude. The rise phase of the part of the transient in Figure 2-7D to the right of the red line is also less synchronous than the part to the left. A full analysis of these transients, and the right and left halves of Figure 2-7D separately is shown in Table 2-3. The data is obtained by using the macro to assess the transients and corresponds well with the visual impression of dyssynchrony.

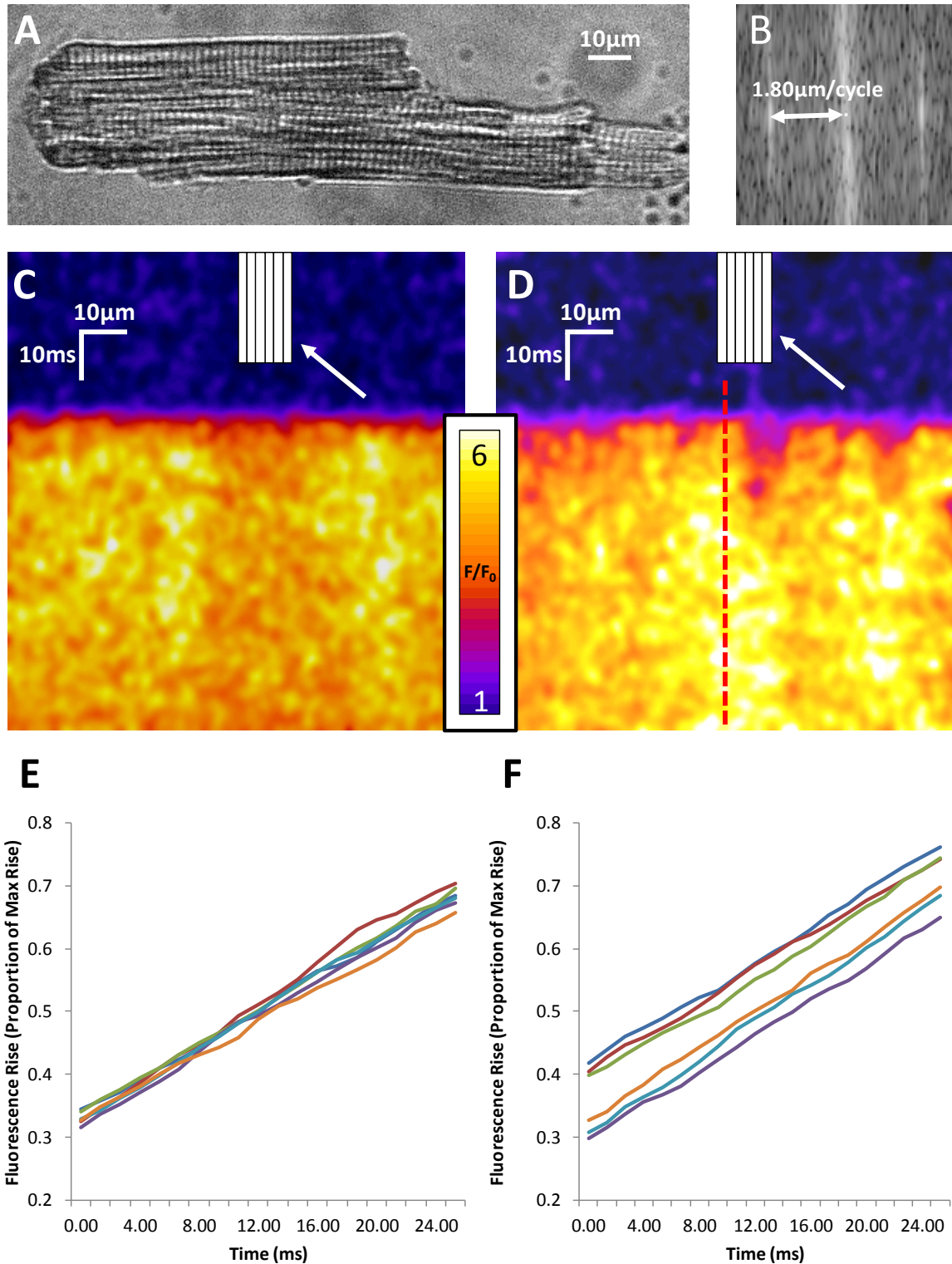


Figure 2-7. Dyssynchrony analysis of Ca^{2+} Transients

(A) A representative transmission image of a rat cardiomyocyte. (B) The fast Fourier transform of this transmission image shows that sarcomere length is $1.8\mu\text{m}$ which was used to define the width of a subtransient for the assessment of dyssynchrony. (C) A synchronous Ca^{2+} transient recorded by confocal line scan, the beginning of the outlines of 6 example subtransients is shown (arrow). (D) A dyssynchronous Ca^{2+} transient with subtransients (arrow) in the equivalent position. (E) Analysis of

the rise-phase of these sub-transients in C. (F) Rise phase of sub-transients in D shows increased spread.

	DysTt50P (ms)	DysTt90P (ms)	DysTtP (ms)	DysAmp (F/F ₀)	DysTau (ms)
Figure 2-7C	1.564	1.347	3.821	0.317	14.612
Figure 2-7D	2.592	2.976	8.103	0.552	19.668
Figure 2-7D (left half)	1.72	1.911	7.968	0.443	6.140
Figure 2-7D (right half)	3.252	3.933	9.136	0.441	24.253

Table 2-3. Dyssynchrony of transients in Figure 2-7.

All measures of dyssynchrony are increased in the transient from Figure 2-7D versus Figure 2-7C. The part of the transient in Figure 2-7D to the right of the red line is more dyssynchronous than the part on the left.

2.5.6.3 Ca^{2+} Waves

I coded a macro to assess wave characteristics (Appendix 9.1.4). This macro functions as follows in order to assess wave characteristics in a semi-automated manner:-

- Assess background fluorescence from a region outside the cell and subtract from intracellular fluorescence
- Applies a 3x3 boxcar filter to smooth the image
- Selects a region of the cell to be assessed for waves
- Asks user number of waves
- Asks user to draw a line along the waves in order to calculate the velocity (in $\mu\text{m/s}$) by dividing distance traversed (i.e. x distance) by time taken (i.e. y-distance)
- Assesses baseline fluorescence prior to wave onset.
- Assesses the peak fluorescence intensity at each value of x along the cell and then takes an average of this peak fluorescence – this solves the problem of the slurring of the Ca^{2+} transient which would occur if peak fluorescence was assessed as an average across the line and approximates to what would be obtained using MacQuaide et al's alternative method of straightening the line scan prior to assessment. (MacQuaide *et al.*, 2007)
- Asks user about the morphology of each wave. In particular whether they are aborted, interrupted or simultaneous (Figure 2-8).
- The output from this macro is:-
 - Wave velocity ($\mu\text{m/s}$)
 - Wave amplitude (F/F_0)
 - Wave frequency (waves/s)
 - Wave-free survival (time to first wave – s)
 - Wave morphology – whether wave is aborted, interrupted or simultaneous, or a combination

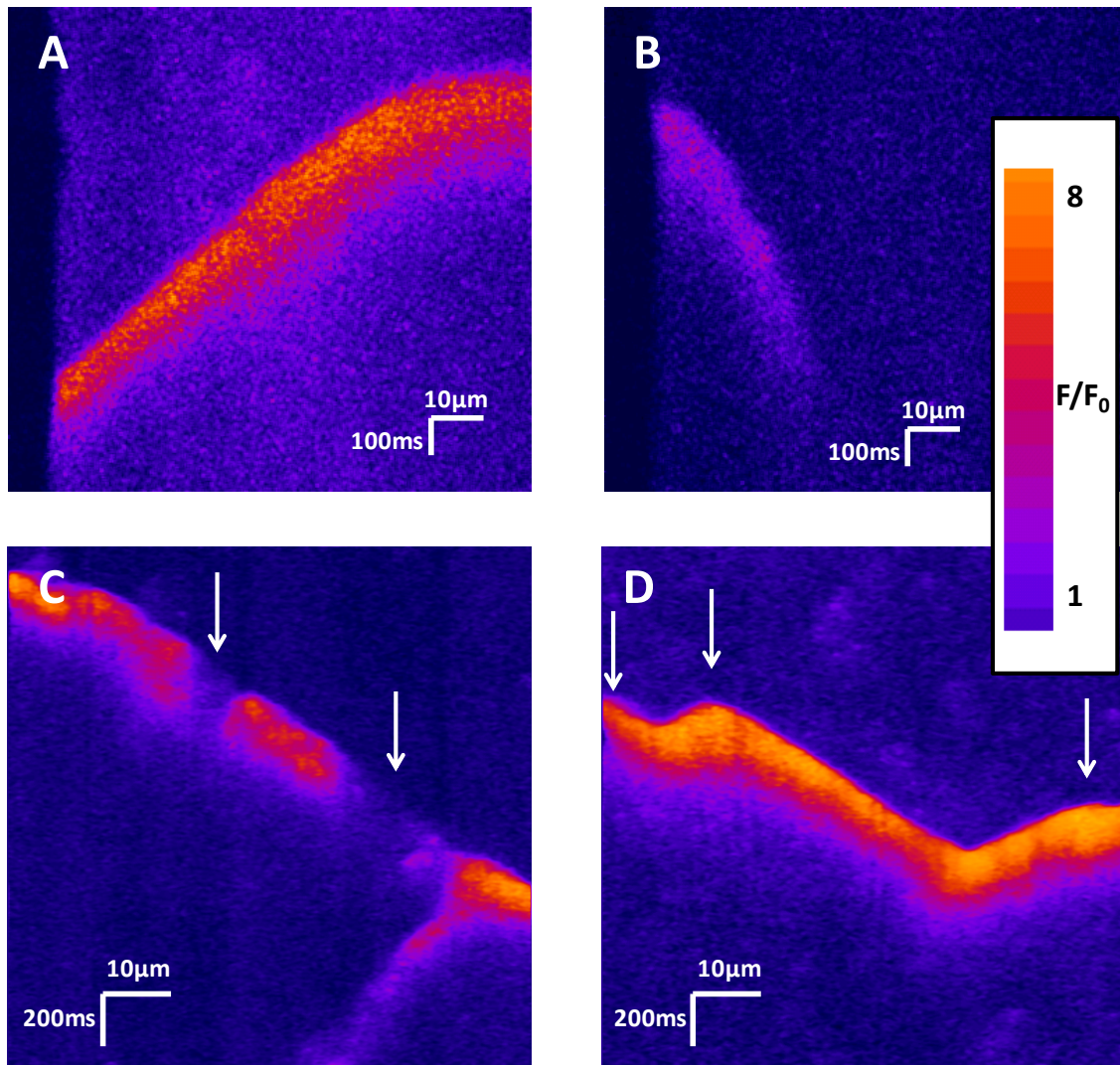


Figure 2-8. Differences in Wave Morphology.

(A) A normal wave which starts at a single point (in this case at the right edge of the cell) and then traverses the whole cell before extinguishing. (B) An aborted wave which travels across part of the cell and then stops. (C) An interrupted wave which traverses the entire cell but with regions in which Ca^{2+} release is interrupted (arrows) before continuing. (D) A simultaneous wave which begins at multiple points along the length of the cell (arrows).

2.5.6.4 Ca^{2+} Sparks

Sparkmaster is an ImageJ plugin (Picht *et al.*, 2007) which has been used by our laboratory and others (Yamamoto *et al.*, 2008; Zima *et al.*, 2008; Pickering *et al.*, 2009; Lyon *et al.*, 2009) to assess both frequency and morphology of Ca^{2+} sparks. Hence this was used as the basis for spark analysis in this thesis. A macro was written to convert images into an appropriate format for use in sparkmaster (8-bit Tagged Image File Format [TIFF]) since it was found that use of the original biorad file format caused problems (due to the encoding of time and distance data within pixel size). This macro also removes the part of the image outside the cell automatically and is shown in Appendix 9.1.5.

Sparkmaster is highly dependent on the original image quality. When there is a poor signal to noise ratio, numerous “pseudosparks” are falsely identified as sparks. These are small blips in fluorescence

due to amplified noise which is probably the result of Sparkmaster correcting to a very low baseline fluorescence to give an output in terms of F/F_0 . They are usually identifiable as being narrow ($\sim 1\mu\text{m}$) with extremely short duration ($<20\text{ms}$). This is shown in Figure 2-9.

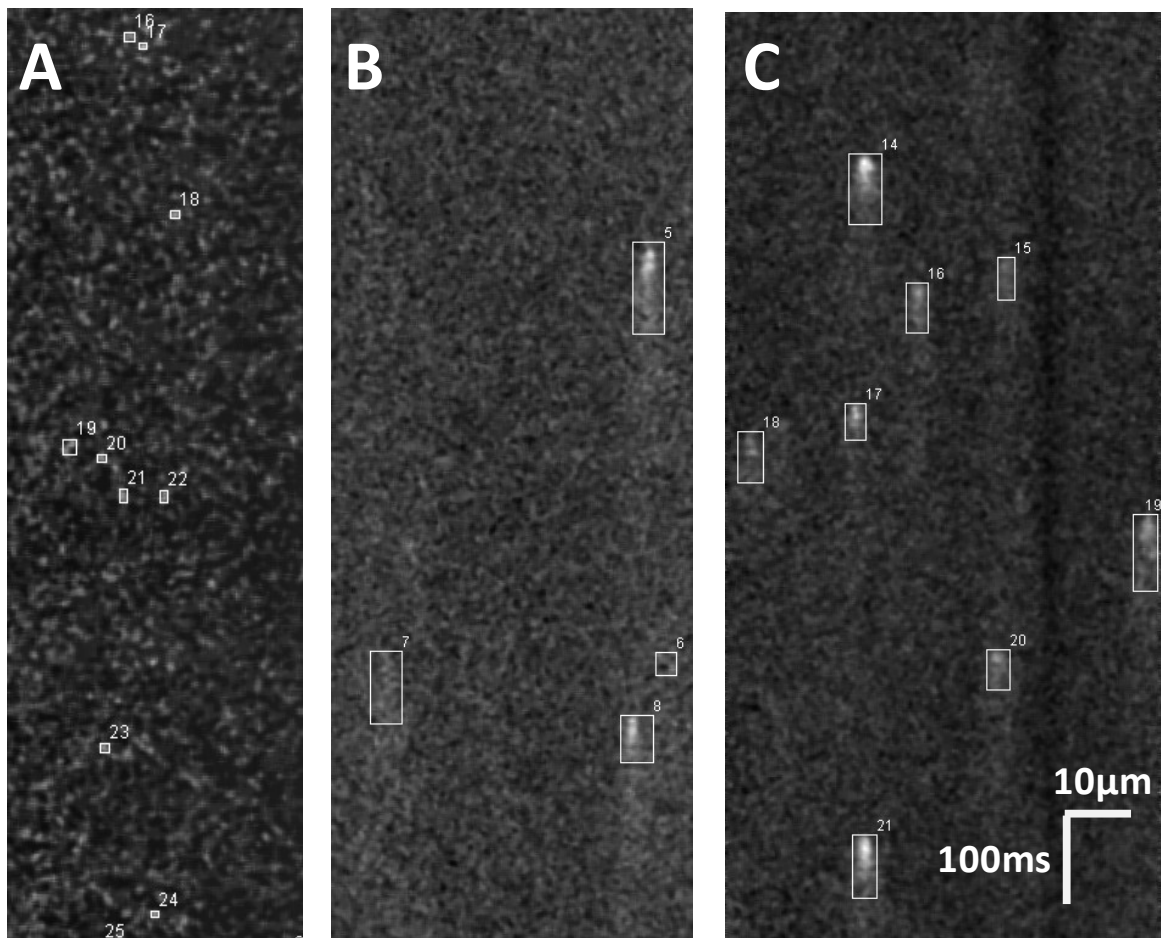


Figure 2-9. Pseudosparks

Scale-matched F/F_0 plots of 3 line scans exemplifying how initial image quality effects spark detection. Linescan (A) contained a large number of “pseudosparks” (sparks detected by Sparkmaster shown in numbered boxes). (B) A linescan with better image quality and at least 2 true positive sparks. (C) A linescan with very good image quality and robust detection of Ca^{2+} sparks.

Given the findings in Figure 2-9, the quality of data obtained can have a great impact of the results of a study of spark frequency and morphology. In order to ensure that this has a minimal effect in this study, sparks were only assessed in linescans containing at least one visually identified spark which was correctly detected by Sparkmaster. In addition linescans in which pseudosparks were identified were discarded. Sparks were also assessed visually to ensure that all sparks identified by sparkmaster corresponded to a visible spark on the linescan. Once image acquisition had been improved by cleaning microscope optics, optimizing dye loading (section 2.5.1), and optimizing confocal settings for acquisition (section 2.5.4), the problem of false positive pseudospark detection was rare.

Analysis options in sparkmaster were set as follows:

- Scan speed: usually 750 lines per second, depending on scan speed.
- Pixel size: extracted from Biorad format file and placed into computer “clipboard” by macro (Appendix 9.1.5) so that the number could be inserted into Sparkmaster
- Number of Intervals – can use up to 5 such that on a varying background fluorescence over time spark detection is corrected. I have found minimal incremental benefit, and sometimes detrimental effects at greater than 3 intervals so all analysis done at 3.
- Output – no difference to sparks detected, merely image output
- Extended kinetics – always used for more detailed spark morphology – does not change spark detection but merely gives more information on morphology of each spark.
- Ember mode – slows processing, but no inherent difference in normal spark analysis – turned on when prolonged sparks present in a particular linescan.
- Criterion – a threshold of standard deviations away from F_0 where spark detection occurs. Set to 4.2 or 3.8 depending on image quality (and probability of false positive sparks). However for any comparisons it was ensured that sparks were always assessed at the same criterion setting.

A method of defining which criterion value to use for a particular dataset using the harmonic mean of precision and recall based on a comparison of the results of Sparkmaster and those of an expert observer is shown in Appendix 9.1.7.

2.5.6.5 Epifluorescence Data Analysis

For fluo-4 epifluorescence data pClamp software (Molecular Devices, Sunnyvale, Ca) was used for analysis. Background fluorescence was subtracted. The inbuilt “threshold search” function was used for automated analysis of transients and waves. Threshold was set at 10% above baseline fluorescence for transients and 20% above baseline fluorescence for waves. For transients, output included time to peak, max rise rate, max decay rate, TD50, tau and peak amplitude (F/F_0). For waves, output included wave time, time to peak, max rise rate, max decay rate, area under curve, peak amplitude (F/F_0) and overall frequency for the cell. For Fura-2 measurement calibration and background subtraction were performed at the time of acquisition within the IonWizard software (Ionoptix, Dublin, Ireland). The same software was used for analysis using the inbuilt “monotonic transient analysis” function which gave similar output measures as the equivalent command in pClamp.

2.6 Statistical analysis

A portion of this thesis is dedicated to the description of the use of hierarchical statistics as a more appropriate methodology than standard techniques for the analysis of data obtained from isolated cardiomyocytes (Chapter 3). Where this was not an appropriate technique e.g. physiological data, differences between more than two groups were assessed using one-way analysis of variance test (ANOVA) with a post-hoc Tukey’s Multiple Comparison Test and differences between two groups were assessed using Student’s *t*-test if the data was parametric or a Mann-Whitney test if not. Paired *t*-tests were used if the same cell was being assessed under different conditions. *p* values of less than 0.05 were deemed to be statistically significant. Unless stated otherwise, results are displayed as arithmetic mean \pm standard error of the mean. Statistical significance testing was performed using IBM SPSS Statistics or GraphPad Prism (Graphpad Software, USA, Version 5). Figures were

constructed with Sigmaplot (Systat Software, USA, Version 12), GraphPad Prism (Graphpad Software, USA, Version 5) or IBM SPSS Statistics.

3 HIERARCHICAL STATISTICAL TECHNIQUES TO REDUCE RISK OF TYPE I ERROR IN CARDIOMYOCYTE STUDIES

3.1 Aims

- To review the consistency of findings pertaining to SR Ca^{2+} fluxes in murine HF models
- To assess whether conclusions regarding Ca^{2+} transient and spark assessment differ depending on use of hierarchical or standard statistics in our model
- To explore the intra-class correlation of these parameters in order to assess the need for use of hierarchical statistics in this setting

3.2 Introduction

Changes in Ca^{2+} handling at the single cell level which occur in HF are thought to play a key role in the pathophysiology of the disease (Epstein & Morgan, 1991). Surprisingly, however, studies using isolated ventricular cardiomyocytes show a great deal of variability in results. In the example of left ventricular hypertrophy these inconsistencies have previously been explored (Song *et al.*, 2005). Several studies show that Ca^{2+} handling is depressed in hypertrophy. In particular some studies show a reduced peak F/F_0 and prolonged decay of Ca^{2+} transients even in the compensated phase where cardiac systolic function is preserved (Gwathmey & Morgan, 1985; Gomez *et al.*, 1997; Siri *et al.*, 2013), while others find enhancement of these parameters (i.e. larger peak F/F_0 and/or more rapid decay) (Bing *et al.*, 1991; Brooksby *et al.*, 1993; Shorofsky *et al.*, 1999). Both of these circumstances have been explained entirely plausibly in these studies. Reduced amplitude of transients despite compensated whole-organ function can be explained by inferring that cellular hypertrophy and increased cross-sectional area of the ventricular wall compensates for the cellular defect, particularly in the presence of enhanced β -adrenergic tone *in vivo* (Gomez *et al.*, 1997). In the opposing studies, enhancement of Ca^{2+} handling is seen as an inherent part of the compensation of whole organ function (Bing *et al.*, 1991).

The model used in the current study is a chronic myocardial infarction rat model of HF. This is a well described model which has been in use for over 50 years (Johns & Olson, 1954). In our hands (Lyon *et al.*, 2009) and others (Cheung *et al.*, 1994; Zhang *et al.*, 1995; Huang *et al.*, 1999; Anand, 2002; Soppa *et al.*, 2008), haemodynamic and echocardiographic parameters consistently show impaired contractile function at the level of the organ. Changes in Ca^{2+} transient amplitude and kinetics may play an important role in the dysfunction of the organ (Epstein & Morgan, 1991; Holt *et al.*, 1998). In order to review the consistency, or otherwise, of findings pertaining to Ca^{2+} handling in isolated cardiomyocytes in this model we searched several online databases to find studies using isolated myocytes in murine species following myocardial infarction (for search strategy see Appendix 9.2). Table 3-1 summarizes the findings of 18 studies which have assessed SR Ca^{2+} release induced by electrically evoked +/- caffeine transients in rat post MI HF models as compared to an appropriate (sham or age-matched) control. The models in the table are placed in order of time post MI the animals were studied (i.e. chronicity of HF model). An equivalent table for mouse models is shown in Appendix 9.2.2.

Publication	Wks Post MI	Ca ²⁺ Transient Amplitude			Transient Decay Time			SR Ca ²⁺ content			Diastolic [Ca ²⁺] _i		
		↓	↔	↑	↓	↔	↑	↓	↔	↑	↓	↔	↑
Cheung <i>et al.</i> , 1994	3					✓ *							
Huang <i>et al.</i> , 1999	3						✓						
Zhang <i>et al.</i> , 1995	3		✓			✓						✓	
Anand, 2002	6		✓			✓							
Sande <i>et al.</i> , 2002	6					✓							
Holt <i>et al.</i> , 1998	6	✓					✓						✓
Soppa <i>et al.</i> , 2008	6			✓			✓			✓			✓
Lee <i>et al.</i> , 2009	7		✓				✓		✓			✓	
Maczewski & Mackiewicz, 2008	8		✓				✓		✓				
Kaprielian <i>et al.</i> , 1999	8			✓					✓			✓	
Loennechen, 2002	8			✓			✓						✓
Yoshida <i>et al.</i> , 2001	8		✓			✓						✓	
Cheng <i>et al.</i> , 2011	8			✓			✓						
Saraiva <i>et al.</i> , 2003	9	✓				✓							
Loennechen <i>et al.</i> , 2002	13			✓			✓						✓
Lyon <i>et al.</i> , 2009	16						✓						
Lyon <i>et al.</i> , 2011	16						✓	✓					
Ait Mou <i>et al.</i> , 2011	18	✓					✓						
TOTAL		3	5	5	0	6	11	1	3	1	0	4	4
TOTAL (%)		23	38	38	0	35	65	20	60	20	0	50	50

* At physiological Ca²⁺ (increased decay time at supraphysiological Ca²⁺ of 5mM)

Table 3-1. Summary of changes in electrically evoked Ca²⁺ transients and SR load assessment in rat models of post MI HF.

Ticks refer to whether parameters (evoked Ca²⁺ transient amplitude and decay time, SR Ca²⁺ content and diastolic [Ca²⁺]_i) are significantly reduced (↓), the same (↔) or increased (↑) in myocytes isolated from post MI animals compared with control animals in the post MI HF model in (A) mice and (B) rats.

The results presented in Table 3-1 are surprising. First, many studies do not fit into the accepted paradigm for Ca²⁺ mediated alterations in contractility in HF (Wehrens *et al.*, 2005b), with more studies showing enhanced amplitudes of Ca²⁺ transients than a reduction in amplitude. Secondly the results are inconsistent with each other in some parameters, although there is somewhat greater consistency in the assessment of transient decay (which is prolonged in 65% of rat studies and reduced in none) and diastolic [Ca²⁺]_i (elevated in 50% and reduced in none) than in the other parameters assessed. Thirdly, there is no apparent time-dependent shift in parameters following MI as would be expected for parameters that change from a “compensated” to “de-compensated” cellular phenotype.

A similar review was performed for spark parameters within the same model (Table 3-2) and within models of pressure overload induced hypertrophy – the spontaneously hypertensive rat (SHR) and transverse aortic constriction (TAC) models (Appendix 9.2.4). Similar to the Ca^{2+} transient results above the consistency of parameters between studies is variable.

Publication	Rat/ Mouse	Wks Post MI	Spontaneous Ca^{2+} Spark Frequency			Ca^{2+} Spark Amplitude			Ca^{2+} Spark Width			Ca^{2+} Spark Duration		
			↓	↔	↑	↓	↔	↑	↓	↔	↑	↓	↔	↑
Huang <i>et al.</i> , 2008	Rat	6				✓								
Lee <i>et al.</i> , 2009	Rat	7			✓		✓				✓		✓	
Ibrahim <i>et al.</i> , 2012	Rat	12			✓			✓			✓			✓
Lyon <i>et al.</i> , 2009	Rat	16			✓			✓						
Lyon <i>et al.</i> , 2011	Rat	16			✓									
Gomez <i>et al.</i> , 2001	Rat	24					✓						✓	
TOTAL			0	0	4	1	2	2	0	0	2	0	2	1
TOTAL (%)			0	0	100	20	40	40	0	0	100	0	67	33

Table 3-2. Summary of studies which have assessed spark parameters in murine species following MI.

Reasons given in these publications for such discrepancies in their findings include a possible compensated phase following MI (Soppa *et al.*, 2008), or differences in other elements of the myocyte (e.g. myofilaments). For example Cheng *et al.* found enhanced Ca^{2+} amplitudes and reduced myocyte contractility leading them to conclude there was a reduction in myofilament sensitivity to Ca^{2+} (Cheng *et al.*, 2011). Another factor that may be important is the statistical testing used. The above studies generally use standard statistical tests in a setting in which data points may not be truly independent from each other. Studies of isolated cardiomyocytes all have a hierarchical data structure with large numbers of isolated cardiomyocytes having their origins in a smaller number of hearts (Sikkel *et al.*, 2013b).

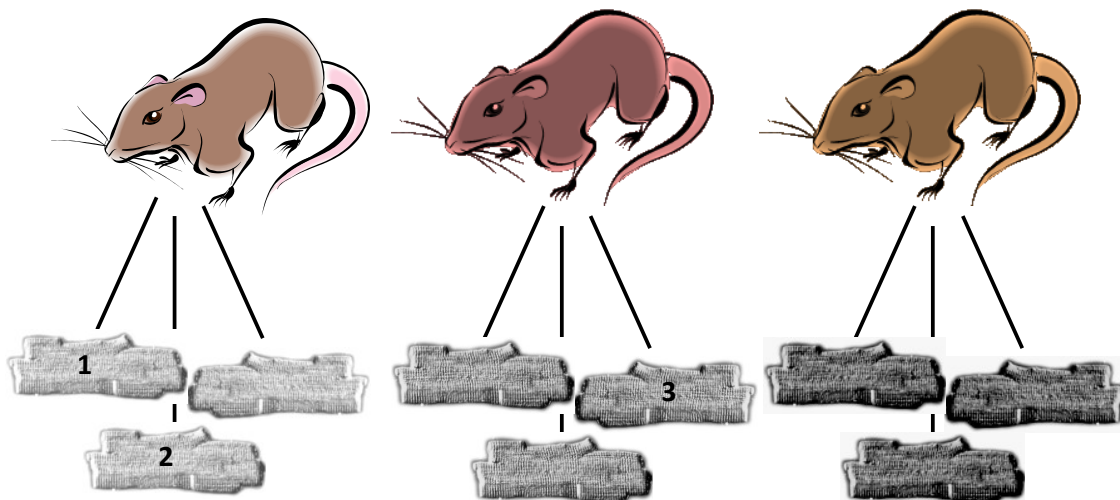


Figure 3-1. Hierarchical structure of data attained from studies of isolated cardiomyocytes.

Multiple cardiomyocytes originate from each isolation. Differences in the animals from which the myocytes originate (indicated by differences in colour tone), as well as slight variations in quality of isolation or experimental conditions on any one day, may result in measurements taken from the myocyte from one rat being more closely related to each other than to measurements from a different isolation. i.e. measurements in cell 1 are more likely to be similar to those in cell 2 versus those in cell 3 in the diagram. A fundamental condition of standard statistical tests (e.g. t-tests), that of independence of data points, is therefore contravened.

In analysing whether parameters from myocytes are significantly different between myocytes from animals with HF versus controls most investigators believe they have two options. The first is to average data from each isolation, which many investigators would prefer not to do since richness of data and statistical power is lost. The second is to ignore the issue of hierarchy and perform a standard statistical test. In a hierarchical data-set, this reduces standard error estimates and frequently leads to spuriously “significant” results (type I errors) (Hox, 2010). This is all too common, even in studies published in the most prestigious scientific journals, and has been termed “pseudoreplication” (Lazic, 2010). Unfortunately in many cases it is unclear which option has been used because of a lack of detail given in statistical methodologies in studies. However in many cardiomyocyte studies “n-numbers” are quoted as the number of cells suggesting that standard statistical tests on the whole dataset have been used.

A third option, which has recently been used in the study of human cardiomyocytes from patients with hypertrophic cardiomyopathy (Coppini *et al.*, 2013), is the use of hierarchical statistical methodologies. These techniques can be used to assess whether there is a significant intra-subject correlation in the parameter assessed, and if so account for this correlation in significance testing between groups. The aim of this part of the work is to assess the use of hierarchical statistical techniques on data obtained using myocytes from the post MI rat HF model.

3.3 Methods

3.3.1 Rat HF Model and Myocyte Imaging

The chronic rat HF model was produced surgically via LAD ligation as described in section 2.2. Cells were isolated 8 weeks following ligation (section 2.4), loaded with Fura2-AM (section 2.5.1) and imaged using ratiometric techniques (section 2.5.5.2) to assess electrically evoked Ca^{2+} transients at 1 Hz (experiments performed by Christina Rowlands – see Acknowledgements). In a separate set of experiments isolated cardiomyocytes were loaded with fluo4-AM (section 2.5.1) and spontaneous Ca^{2+} sparks were assessed using confocal microscopy (section 2.5.4). All experiments were performed at 37°C in NT solution containing 2mM Ca^{2+} (section 2.5.1). The control group consisted of myocytes isolated from age-matched controls. Data were viewed using Ionwizard and ImageJ (NIH) and analysed with a combination of custom-built macros and Sparkmaster (2.5.6). Amplitude and morphology of 5 Ca^{2+} transients per cell were averaged to give final parameters for that cell. Sparks were treated as separate data points.

3.3.2 Statistical Analysis

Data were analysed using IBM SPSS statistics in two ways. Firstly using standard statistical tests: for each parameter of interest, an independent samples t-test was performed in which the two groups were defined by whether myocytes came from an AMC or HF heart. Secondly, hierarchical statistical techniques were used. These techniques are more appropriate for the data since it has a nested structure (Hox, 2010).

3.3.2.1 Hierarchical Statistical Techniques

It is important to describe hierarchical statistical methodologies. These have been reviewed extensively previously (Hox, 2010) and this is a developing area in the field of statistics such that the description here will only be a brief introduction of the simple forms of hierarchical modeling used in the present study.

As described above the data structure in studies of isolated cardiomyocytes is inherently hierarchical. The lower level of measurements from cells is nested within the upper level of individual rat hearts (or isolations). The statistical model most appropriate for the data analysed in this study is the random intercept model. This is the simplest form of hierarchical model, but because the data structure is also very simple with only a single predictor (i.e. absence or presence of HF) and data within a single isolation having HF state in common (i.e. we do not have data from the same rat before and after HF), it is also the most appropriate in this setting. The random intercept model is a modification of the conventional equation for linear regression:

$$Y_i = b_0 + b_1X_i + \varepsilon_i$$

Equation 3-1. Conventional linear regression

Where Y is the outcome measure, b_0 is the intercept, b_1 is a coefficient, X is the predictor variable and ε is the error term. Y, X and ε all vary as a function of i which represents an individual case of data. In our data Y is an outcome measure in terms of SR Ca^{2+} release quantification (e.g. transient amplitude). For the current study X represents the absence or presence of HF and is thus classified as a “dummy-coded” variable (Field, 2009), in other words, despite this being a linear regression, HF is a predictor variable which can only hold the values of 0 or 1. Since HF is always the predictor in this study we will place it within the linear regression equation:

$$Y_i = b_0 + b_1HF_i + \varepsilon_i$$

Equation 3-2. Linear regression including HF as a parameter

A random intercept model means that for each subject at the highest level of the hierarchy, there can be a different intercept. In the current data set that means that we do not necessarily expect cells from each heart to have the same mean transient amplitude. Graphically this is shown in Figure 3-2.

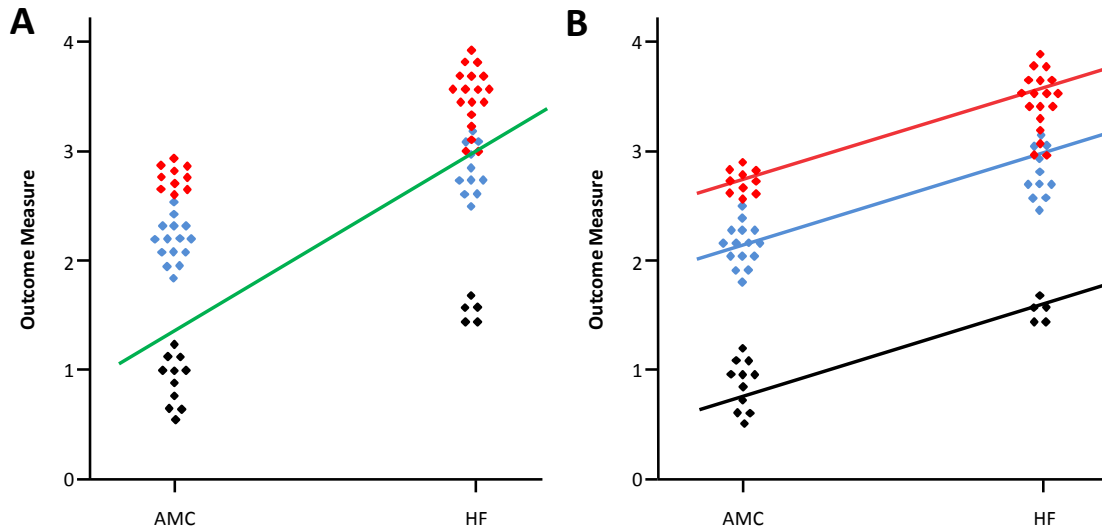


Figure 3-2. Graphical representation of difference between standard linear regression and random intercept model.

(A) Data represents a generic outcome measure in cells from rat 1 (black), 2 (blue) and 3 (red) in the absence and presence of HF. This illustrates some potential issues with standard linear regression (and with a dummy variable this approximates to a t-test). Firstly there is clustering of data depending on which animal cells have come from. This violation of the assumption of independence of data points will produce an increased rate of Type I error. Secondly, a large number of cells from a single animal can be unduly weighted in the analysis leading to a steep (green) regression line. (B) With the random intercept model, the intercept b_0 is allowed to vary depending on which rat the cells have come from. This is an oversimplification since cells will not be obtained pre- and post-HF such that each isolation from AMC rats and each isolation from HF hearts will have its own intercept.

Including a random intercept requires a modification to the equation for standard linear regression as follows:

$$Y_{ij} = b_0 + u_{0j} + b_1 HF_{ij} + \varepsilon_{ij}$$

Equation 3-3. The basic random intercept model

Each outcome measure now varies with both specific case (i) and which isolation that case originates from (j). The additional term u_{0j} is the term which models the variation of the intercept for each isolation from the average intercept (b_0).

The levels of hierarchy differed for transient and spark analysis. For transient analysis there was a single piece of data per cell (averaged transient amplitude or morphological parameters). As such this is a two-level hierarchy, with the upper level being the isolation and the lower level the cells (represented in Equation 3-3). For spark morphological parameters there was a three-level hierarchy with isolations at the highest level, cells at the intermediate level and spark parameters at the lowest level of the hierarchy. This required a modification to the equation modeled:

$$Y_{ijk} = b_0 + u_{0j} + v_{0jk} + b_1 HF_{ijk} + \varepsilon_{ijk}$$

Equation 3-4. Three level random intercept model

In Equation 3-4 u_{0j} represents the random intercept for spark parameters for that isolation and v_{0jk} represents the additional adjustment in intercept made for the specific cell. The other measures have subscript “ijk” because they represent the value of the parameter for the individual spark which is within its individual isolation (j) and cell (k).

The necessity for a hierarchical model was assessed using the change in -2 Log Likelihood (a measure of “goodness of fit” of the hierarchical model. This can be used to calculate whether there is a significant improvement in model fit over a standard test based on a chi-squared test comparing the -2 Log Likelihood for the respective models (χ^2 -2LL). This can be used to assess whether the use of a hierarchical model is necessary in a particular data set and is the preferred method for comparisons of this kind in the statistical literature (Thum, 1997; Goldstein *et al.*, 2002; Field, 2009). The intraclass correlation coefficient (ICC) is also used to measure the degree of correlation within subjects. This measure represents the proportion of total variability in an outcome measure that is attributable to the isolation of origin. The ICC can be expressed as a percentage between 0 and 100. If observations are entirely independent then ICC is 0%. On the other hand an ICC of 100% implies that observations from each isolation are all exactly the same.

3.3.2.2 Running the models

Initial exploration of data showed that whilst parameters pertaining to Ca^{2+} transients were normally distributed, spark morphological parameters were skewed as has been shown previously (Cheng *et al.*, 1999). The logarithmic transformations of morphological characteristics were therefore used and are referred to as LogAmp, LogFWHM, LogFDHM for the logarithm of spark amplitude, full width at half maximum (FWHM), full duration at half maximum (FDHM). Ca^{2+} transient and spark measures were the dependent variables in the statistical models. The only independent variable was the presence or absence of HF. Each model used was assessed for validity by ensuring predicted values closely corresponded to those observed. Residuals were assessed for normality and symmetry. χ^2 -2LL was used as described to assess whether the hierarchical model was necessary for each outcome measure. ICC was also assessed and reported. Estimated marginal means were used to assess significance between AMC and HF groups.

3.4 Results

3.4.1 Ca^{2+} Transient Morphology in HF versus AMC

Ca^{2+} transients were assessed at 1Hz in AMC (76 cells from 10 isolations) and HF cells (79 cells from 10 isolations) using the ratiometric dye Fura2-AM. The ratio of the isosbestic point for Fura-2 (360nm) to the unbound form (380nm) was used as a measure of $[\text{Ca}^{2+}]_i$. Several parameters were assessed using automated transient analysis in IonWizard (Ionoptix Inc) including diastolic ratio, peak systolic ratio, transient amplitude (peak ratio/diastolic ratio), time to 50% peak, time to 50% decay (TD50) and tau of decay.

Table 3-3 shows how the method of analysis changes the outcome in terms of significance of results. The first method of analysis was a t-test comparing the parameters within HF cells and AMC without accounting for the hierarchical nature of the data. The second method is a linear regression which simply shows equivalence with the t-test since HF is coded as a dummy variable. The final method of

analysis is the random intercept model. The data from the random intercept model includes χ^2 -2LL. This is an assessment of whether random intercepts significantly improve the analysis. The ICC (discussed above) is also included.

Parameter	Independent samples t-test		Standard Regression		Multilevel Random Intercept Model			
	Standard error of difference	p-value	Standard error of difference	p-value	Standard error of difference	p-value	χ^2 -2LL p-value	ICC (%)
Diastolic ratio	0.0120	n/s 0.248	0.0119	n/s 0.245	0.0203	<u>n/s</u> <u>0.623</u>	*** <0.001	27
Peak systolic ratio	0.0396	** 0.004	0.0394	** 0.004	0.0653	* <u>0.046</u>	** 0.002	23
Transient amplitude	0.0306	*** <0.001	0.0303	*** <0.001	0.0493	* <u>0.010</u>	** 0.006	21
Time to 50% Peak (ms)	5.20×10^{-4}	* 0.018	5.16×10^{-4}	* 0.017	7.16×10^{-4}	<u>n/s</u> <u>0.109</u>	* 0.021	12
Time to 50% Decay	4.86×10^{-3}	n/s 0.444	4.83×10^{-3}	n/s 0.440	9.82×10^{-2}	<u>0.400</u>	*** <0.001	44
Tau	8.55×10^{-3}	n/s 0.535	8.50×10^{-3}	n/s 0.532	0.0177	<u>0.424</u>	*** <0.001	47

Table 3-3. Analysis of Ca^{2+} transient parameters using standard and hierarchical statistical tests. Elements of the analysis of each parameter are shown. The independent-samples t-test is shown as the commonest standard technique used to compare cellular data. The standard regression uses a linear regression with a dummy variable coded 0 or 1 for absence or presence of HF. It is shown to highlight the close approximation to a standard t-test in terms of standard error and p-value. When the random intercept is introduced the results change substantially (see text for details). The 2 level model was most appropriate for all Ca^{2+} transient parameters and the p-values for these models are shown in bold and underlined.

The results of the hierarchical (multilevel) model shows the difference when the intra-subject correlation in Ca^{2+} transient parameters is taken into account. The differences in peak ratio and transient amplitude remain significant although the increase in the p-value in time to 50% peak means that this is no longer significant. The standard error of the difference is larger in the hierarchical model which shows that the standard error is underestimated when standard techniques are used. In each case χ^2 -2LL shows that the hierarchical model fits the data significantly better than the standard regression model. Furthermore assessment of the ICC shows that a substantial portion of the variation in each parameter is accounted for by which isolation the cell comes from. This is most marked with the decay parameters (Time to 50% decay and Tau) where the ICC is >40%.

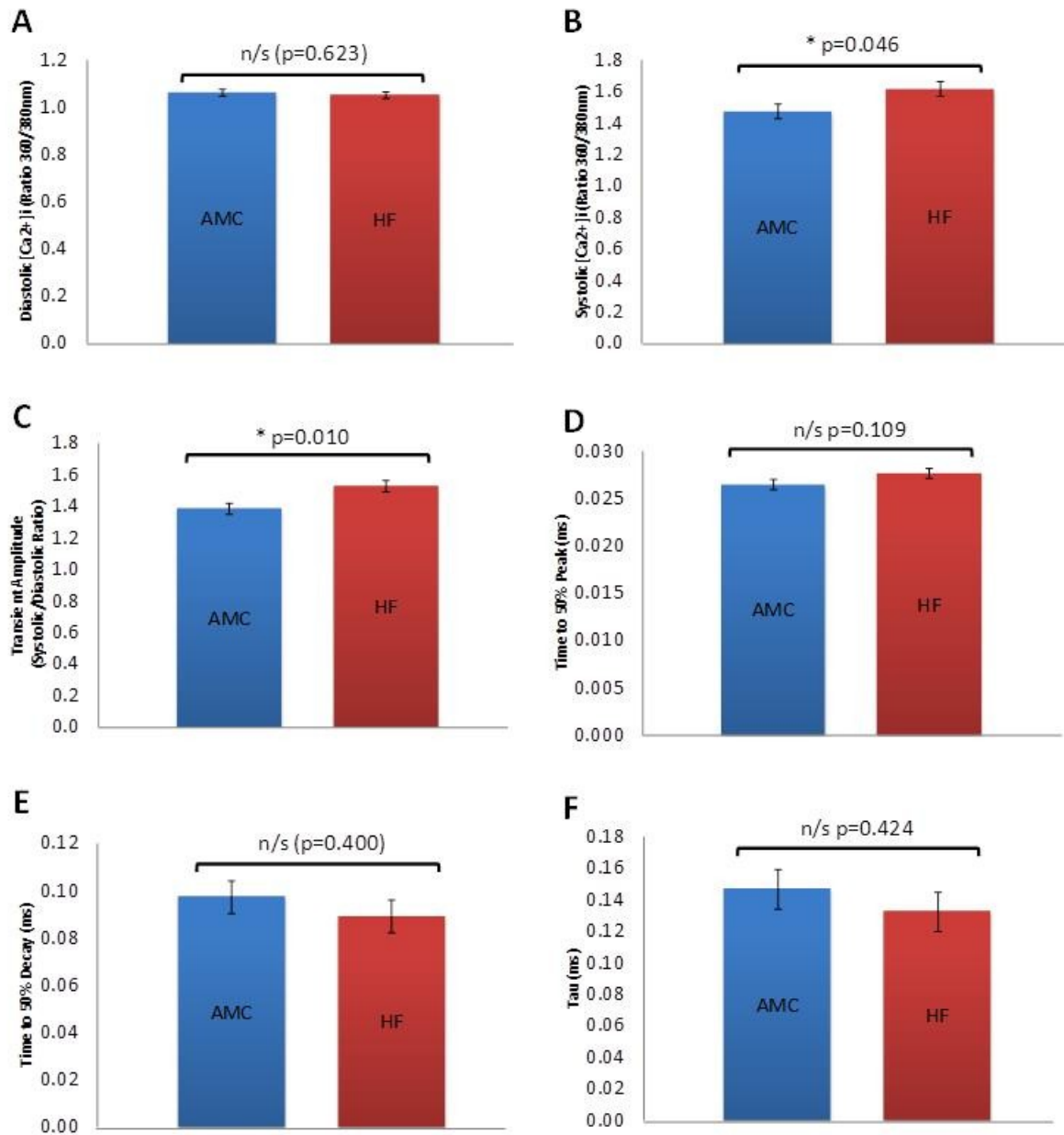


Figure 3-3. Transient amplitude characteristics in AMC and HF cells.

Significance values represent results of hierarchical models. (A) Diastolic Ca^{2+} is not significantly different between the two groups, (B) however systolic Ca^{2+} is significantly increased, leading to (C) a significant increase in transient amplitude (systolic Ca^{2+} /diastolic Ca^{2+}). Neither duration of (D) the rise phase of the Ca^{2+} transient or (E-F) the decay phase are significantly different between AMC and HF cells.

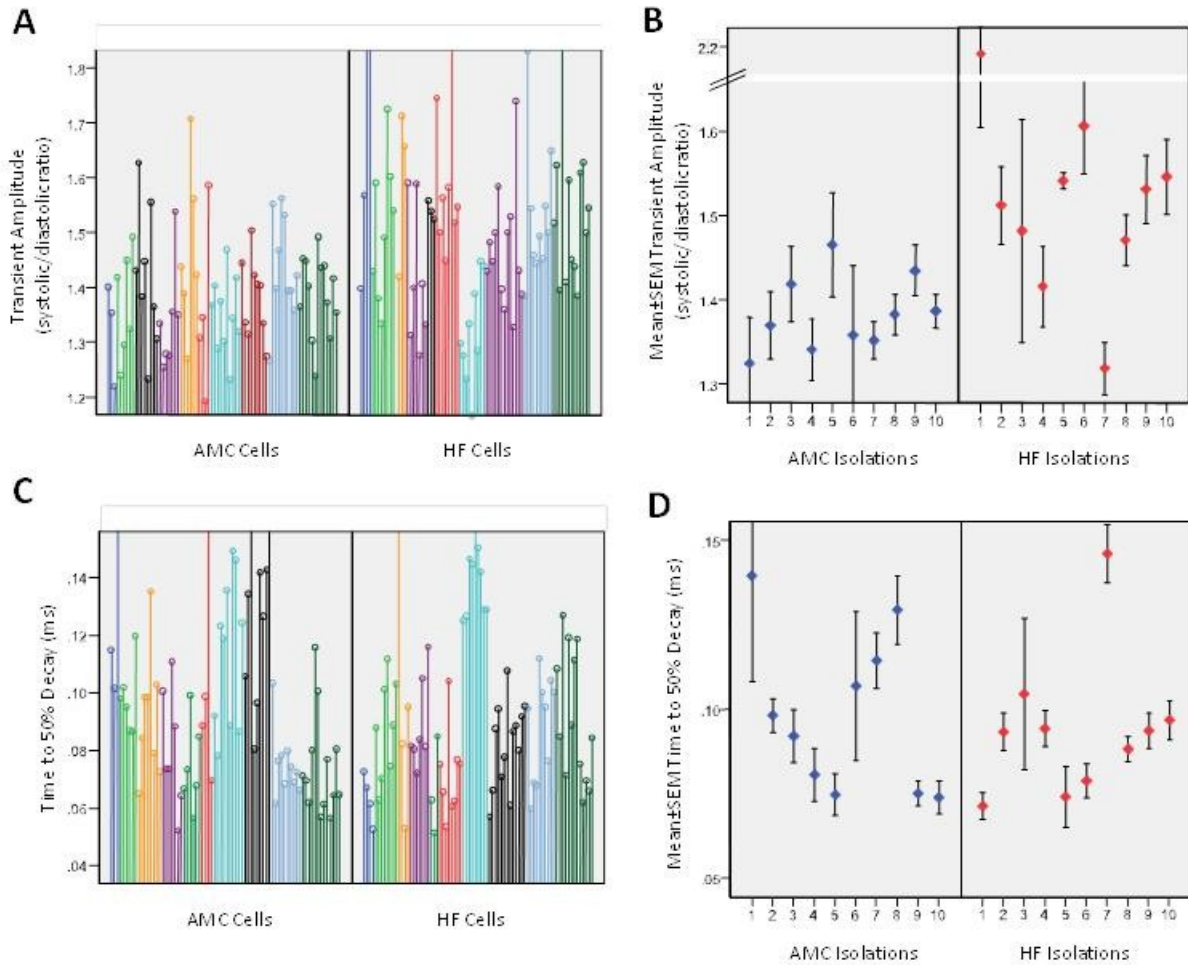


Figure 3-4. Examples of hierarchical data structure of Ca^{2+} Transient Parameters

(A) Ca^{2+} transient amplitude in individual cardiomyocytes (each line is the result from a single myocyte). Hierarchical data structure is evident since there is clustering of results within each isolation (represented by different colours). However, overall it is notable that amplitude tends to be greater in HF isolations. (B) Summary of data in A shows that each isolation forms a cluster of results with a distinct mean and standard error of mean (SEM). (C) Distinct populations within isolations are also noted in time to 50% decay data, although there is no clear pattern in HF cells in comparison to AMC. (D) Summary of data in C. The visual impressions of the overall trend between HF and AMC for both amplitude and time to 50% decay are accurately reflected by the p values pertaining to the relevant hierarchical model (0.01 and 0.40 respectively).

3.4.2 Ca^{2+} Spark Data

Ca^{2+} sparks were assessed in 344 sparks from 17 cells from 7 isolations for AMC and 352 sparks from 22 cells from 5 isolations for HF. The data was assessed using a 2 level random intercept model for data relevant to the cell (i.e. spark frequency). For data relevant to each spark (i.e. morphological parameters logAmplitude, logFWHM and logFDHM), a 2- or 3-level random intercept model was used depending on whether the model was improved by addition of a 3rd level as assessed by χ^2 -2LL (Table 3-4). Since SPSS does not contain menu functions to perform a 3 level model, syntax was

written and used (Appendix 9.2.5). Table 3-4 also highlights the difference in the p-value and standard error of the different models used. The ICC for the 3-level model describes the correlation of two randomly chosen sparks within the same cell when it is taken into account that two sparks within the same cell must have originated from the same isolation (Hox, 2010).

	Independent samples t-test		2-Level Hierarchical Model				3-Level Hierarchical Model			
	Standard error of difference	p-value	Standard error of difference	p-value	χ^2 -2LL p-value ^a	ICC (%) ^b	Standard error of difference	p-value	χ^2 -2LL p-value ^c	ICC (%) ^d
Spark Freq	0.537	0.886	n/s 0.664	<u>n/s</u> <u>0.540</u>	* 0.048	24	e	e	e	e
LogAmp	9.00×10^{-3}	*** <0.001	0.0320	** 0.001	*** <0.001	47	0.0641	<u>n/s</u> <u>0.239</u>	*** <0.001	58
LogFWHM	0.0113	n/s 0.381	0.0185	<u>n/s</u> <u>0.782</u>	*** <0.001	7	f	f	f	f
LogFDHM	0.0168	* 0.023	0.0289	<u>n/s</u> <u>0.778</u>	*** <0.001	8	0.0357	n/s 0.869	n/s 0.343	8

a – Over standard regression (which approximates closely to t-test)

b – At cell level

c – Over 2-level model

d – At cell level and isolation level

e – 3-level model not appropriate since frequency data are at the cell level

f – Error running 3-level model since minimal difference between isolations for this parameter

Table 3-4. Spark data analysed by hierarchical versus standard statistical tests.

The p-value pertaining to the most appropriate hierarchical statistical test for each parameter is shown in bold and underlined. This is a 2-level model for spark frequency, LogFWHM and LogFDHM and a 3-level model for LogAmp. Once the most appropriate test has been selected there are no longer statistically significant differences in any spark parameter between AMC and HF.

Results of the most appropriate statistical test including the corrected SEM estimate are shown in Figure 3-5. None of the spark parameters are significantly different between AMC and HF. The 3-level clustering of data is illustrated with respect to logAmp in Figure 3-6.

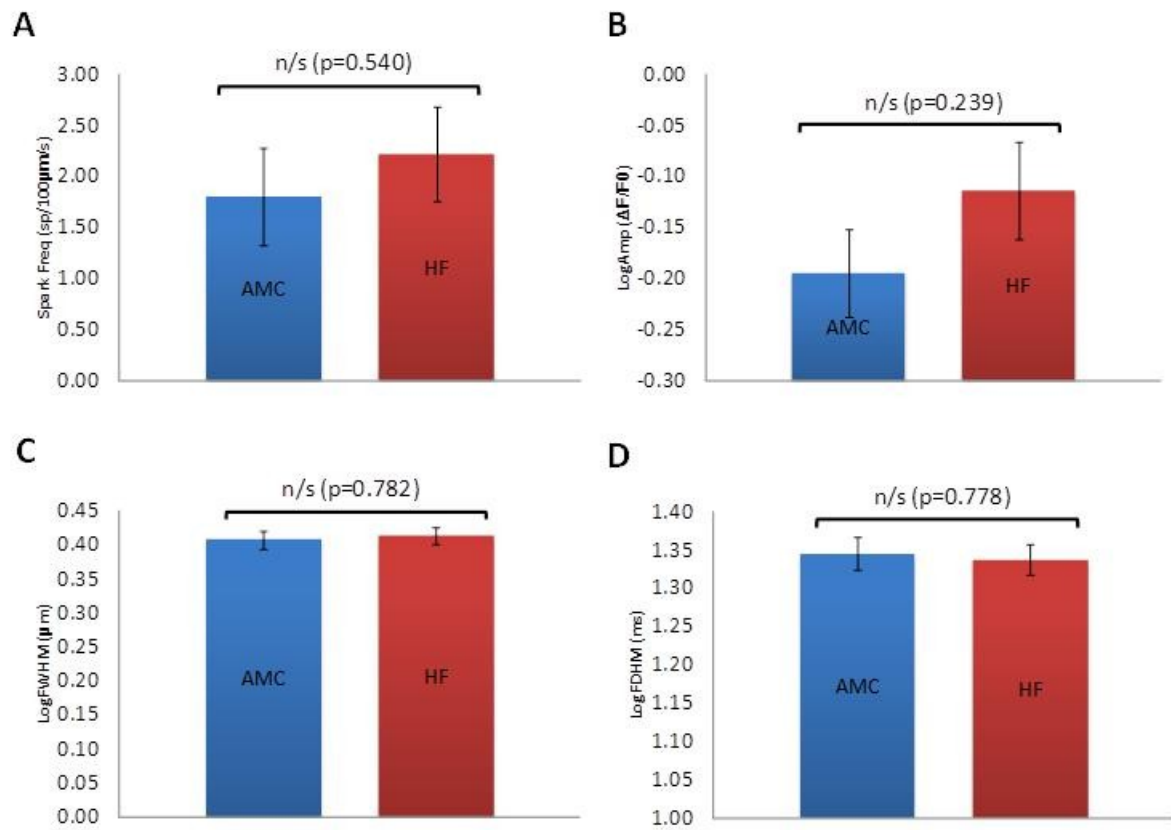


Figure 3-5. Spark characteristics in AMC and HF cells.

Results of hierarchical models are shown. After correction for intra-subject variability none of the parameters tested changed significantly between AMC and HF including (A) spark frequency (B) logAmp (C) logFWHM and (D) logFDHM.

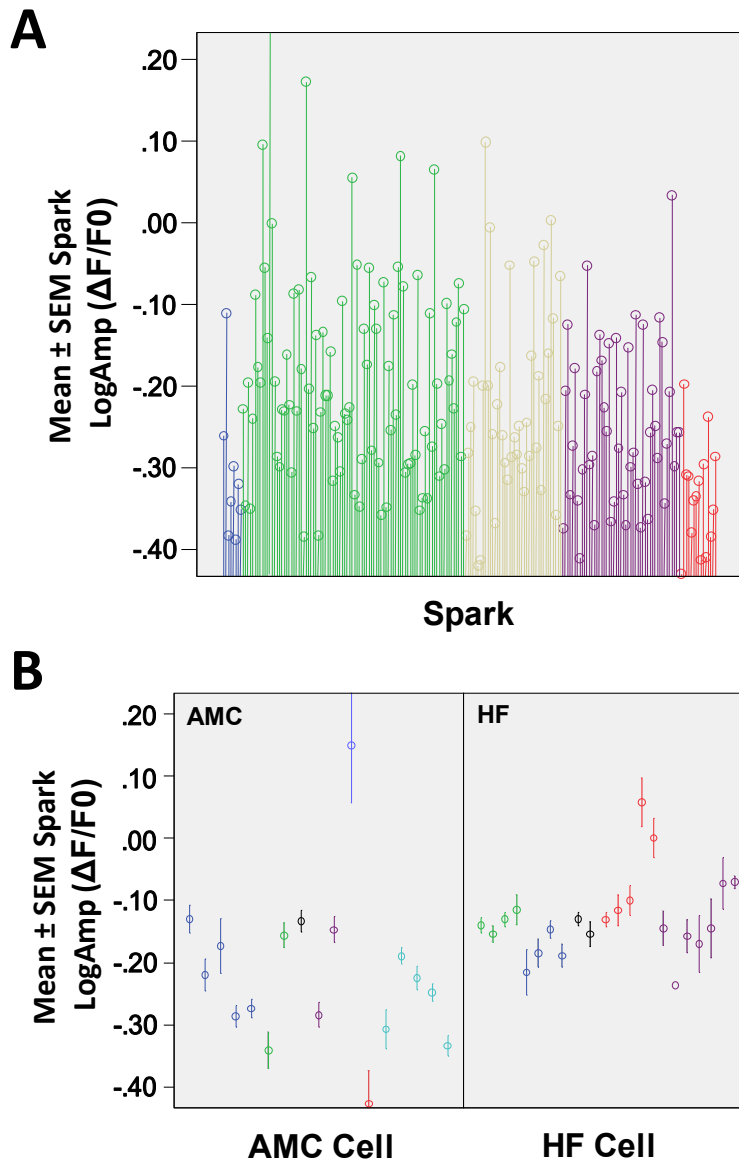


Figure 3-6. Hierarchical clustering of spark data.

(A) Individual spark amplitude data is represented by each line. Data is from 5 cells (colour coded) from a single isolation. It can be seen that data is clustered within individual cells. (B) Mean and SEM of data from each cell. Different isolations are colour coded. Note there is clustering of data with cells from the same isolation exhibiting sparks with more similar amplitude than comparing two cells from different isolations. This nesting of data (sparks within cells and cells within isolations) is the reason a 3-level hierarchical model is most appropriate for data analysis in the case of spark amplitude.

3.5 Discussion

3.5.1 Studies of Ca^{2+} Fluxes in Isolated Cardiomyocytes are Inconsistent

Studies assessing the differences between Ca^{2+} fluxes in HF and control cells following myocardial infarction give widely differing results. This is usually put down to differences in the specific models or species used. However Table 3-1 and Table 3-2 show that even in the rat in the same HF model (LAD ligation), results vary between studies. Precise experimental conditions could be different

between these studies, thus explaining these differences. However the problem of pseudoreplication has been identified as a cause of type I error in other research fields (Lazic, 2010; Sikkel *et al.*, 2013b) and so we questioned whether this might contribute to errors here.

3.5.2 Hierarchical Statistical Analysis Improves the Analysis of Ca^{2+} Flux Data Compared with Basic Statistical Tests

We tested this theory by starting with a basic model which treats each data point as independent i.e. comparisons using an independent-samples t-test. We then added a random intercept at 2-levels (transient data) and 3-levels (spark data), calculated the ICC and compared the fit of the models. The ICC varied dependent on which parameter was being tested and was not negligible in any of the parameters. Even where the ICC was low, for example 8% of the variability of spark logFDHM was explained by the hierarchical context of the spark, there was still a substantial difference in the analysis. When analysed with standard methodologies there was a significant difference in logFDHM between HF and control ($p=0.023$) whereas when analysed with a more appropriate 2 or 3-level model this difference was not significant ($p=0.778$ and 0.869 respectively). There was a much larger ICC calculated for some parameters – for example spark logAmp had an ICC of 58% and Ca^{2+} transient tau had an ICC of 47%. In the absence of hierarchical methods one would falsely assume that these large correlations were negligible.

In the majority of parameters the hierarchical model provided a significant improvement assessed by χ^2 -2LL compared with the basic model. Furthermore, analysis via a hierarchical model changed the conclusions drawn from this data. In the analysis of Ca^{2+} transient data, time-to-50%peak was found to be increased in HF using a t-test but this change was not significant in the hierarchical model. In the spark data both logAmp and logFDHM were significantly different in HF using the basic model but these changes were non-significant using the more appropriate 3-level model. This would greatly change any conclusions drawn from the study. According to the hierarchical analysis the only major difference between HF and control according to our data is the finding that Ca^{2+} transient amplitude is increased. This is due to a significant increase in systolic Ca^{2+} whilst diastolic Ca^{2+} remains constant.

3.5.3 Alternatives to Hierarchical Statistics – Aggregation and Disaggregation

There has been very limited exploration of the concept of hierarchical data structure in the field of cardiomyocyte biology (Coppini *et al.*, 2013; Sikkel *et al.*, 2013b), although it has been explored more fully in the social sciences (Raudenbush & Bryk, 2002; Park & Lake, 2005; Hox, 2010). Early approaches in these fields mirror the experience with cardiomyocytes and so are relevant to the current discussion. In the absence of hierarchical statistics such data was analysed using two possible techniques: aggregation, meaning reducing several observations at the lowest level of the hierarchy to a single averaged observation at a higher level, and disaggregation, meaning ignoring the hierarchy and treating each observation as a separate individual.

Comparisons of aggregated data are statistically more robust because they are less likely to contravene the assumption of independence of data points. However much data is discarded which reduces statistical power available to detect a difference. In addition there can be some problems in the interpretation of aggregated data. A classic example of this was given by Robinson (Robinson, 1950) who assessed the 1930 US census and found that differing results could be obtained when the same data set is analysed at individual and aggregate levels. Analysed at the State level, Robinson

found that there was a correlation of 0.77 between the proportion of black individuals in the state and the proportion illiterate. However when analysed at the individual level, the correlation was almost absent (0.20). The conclusion drawn with the state level data would be that there were higher rates of illiteracy amongst blacks but this did not hold true with individual level data. This was later termed ecological fallacy, a term coined to refer to “the invalid transfer of aggregate results to the individual” (Selvin, 1958; Subramanian *et al.*, 2009). Such an error might apply to cardiomyocyte research. For example one could envisage a disease state which reduces Ca^{2+} transient amplitude in all but a few cardiomyocytes in which amplitude is greatly enhanced. The aggregate isolation-level data might suggest no change in amplitude whereas individual cell data with appropriate exploratory analysis would allow the correct inferences to be made.

Statistical analysis of disaggregated data can also be misleading (atomistic fallacy). For example, in epidemiological studies individual-level data has shown that coronary heart disease predominates in people of low income (O’Flaherty & Bishop, 2009). One might be tempted to conclude that countries with lower per capita incomes will have the highest mortality rates from coronary artery disease. However, this is not the case since in the poorest nations infectious diseases predominate (Diez-Roux, 1998; Fuster & Kelly, 2010). Within biological research, another important manifestation of atomistic fallacy is the use of standard statistical tests on disaggregated data. Standard tests lean heavily on the assumption of independence of observations (Hox, 2010) and when this is violated the estimates of standard errors are much too small leading to spuriously significant results – i.e. type I errors. This type of error has been called pseudoreplication by Lazic who described the prevalence of such errors in the neuroscience literature (Lazic, 2010). The issues raised in this study are conceptually similar to the issues in cardiomyocyte research – for example spuriously significant differences resulting from the degrees of freedom for t-tests being derived from numbers of brain neurons, nerve axons and histological slices rather than the number of animals.

3.5.4 Improving Statistical Testing in Cardiomyocyte Studies

An important conclusion that can be drawn from this study is that in the case of analysis of Ca^{2+} flux it is important not to assume independence of individual data points. This is also likely to apply to other aspects of cardiomyocyte physiology and biology because of the inherent hierarchy in the data structure with multiple myocytes originating from individual animal hearts.

In the absence of hierarchical statistics, aggregation of data is the simplest method that can be used to avoid atomistic fallacy. This can introduce some problems as outlined above but is an improvement on the alternative of disaggregation since standard statistical tests are more likely to be valid (Lazic, 2010). As such, if standard statistical tests are used it should be made clear that the number of observations used in the analysis corresponds to the number of isolations rather than cells.

Hierarchical methodologies are likely to become more commonplace in cardiomyocyte research because of their inherent advantages and because they are now relatively easy to access via standard statistical packages such as IBM SPSS Statistics, SAS (SAS Institute) and STATA (StataCorp). A disadvantage is that use of these models requires training in formulating a statistical model that fits the data appropriately and checking the validity of models formed – this training, or the statistical packages required might not be available to all researchers. However there are also further advantages that will become clearer as more research is done with these techniques. For

example the models used in this study are amongst the most simple hierarchical techniques with just 1 factor included (i.e. presence and absence of HF) with a random intercept. Many more factors could potentially be added which might better explain the outcome measure being looked at, and these factors could be at any of the hierarchical levels. For example in explaining Ca^{2+} transient amplitude one might include rat weight, heart weight and echocardiographic ejection fraction at the upper hierarchical level and at the level of the cell one might include cell size, sarcomere length and fraction of the cell that contains t-tubules in the statistical model. Such a model would allow more unifying conclusions to be drawn regarding the most important factors that influence Ca^{2+} transient amplitude.

3.5.5 Limitations

Although tempting to conclude that our hierarchical analysis proves an absence of change in SR Ca^{2+} release in HF versus AMC cells this is not necessarily the case. The other major possibility is that the sample size was too small to show a difference. Although cell and isolation numbers were relatively large compared to other studies of this sort (76 cells from 10 isolations for AMC and 79 cells from 10 isolations for HF in the case of Ca^{2+} transient measurements) this may not be large enough to provide the statistical power to show a true difference (i.e. type 2 error). This is particularly obvious when one envisages the 8 or so cells from each isolation coming from a population of several billion ventricular cardiomyocytes – the chance of these 8 cells being representative of the entirety of that ventricle is slim. A way round this would be to assess several hundred cells from each isolation which would not be possible without the use of higher throughput technologies than used in this study. That is not to say that hierarchical techniques are problematic but merely that they appropriately show an absence of difference where numbers of observations are too few. In fact the reduction in statistical power to detect differences as compared to standard tests is appropriately scaled to the interclass correlation of various parameters within the nested structure of the study as demonstrated by the data above (see Table 3-3 and Table 3-4).

3.6 Conclusions and Implications

In this study we have shown, via an initial review of the literature, that even within similar HF models there are apparent differences in the effects of HF on Ca^{2+} fluxes in isolated cardiomyocytes in different studies. These differences cannot be explained by disease progression alone and hence they may be the result of large differences in experimental methodologies between centres. Alternatively the conclusions drawn from these studies may not reflect the data due to statistical tests used violating the assumption of independence of data points. To illustrate the fact that use of standard statistical tests in hierarchical data can lead to type I errors we used both standard and hierarchical tests to assess the differences between Ca^{2+} fluxes in HF and control cardiomyocytes. We found significant differences in the conclusions of the study when the same data were analysed by the different methodologies.

If we had used standard t-tests alone the conclusion of this study would have been that Ca^{2+} transients in HF exhibited both higher amplitude and a longer time to peak and that these changes might result from sparks (the elemental subunits of transients) which were more prolonged and of greater amplitude. We went on to use hierarchical methodologies, which were more appropriate in

this data since ICC values were high and the hierarchical models provided a better fit to the data. Using these techniques we can conclude that Ca^{2+} transients in HF exhibit larger amplitudes but there are no significant changes in Ca^{2+} sparks to explain this. This is a somewhat less attractive conclusion but statistically more robust and either suggests that our study was underpowered to detect differences in sparks or that something else that was not included in our study (e.g. SR Ca^{2+} content) has a greater bearing on Ca^{2+} transient amplitude than the amplitude of spontaneous diastolic sparks. Comparing the two conclusions it is perhaps understandable that standard methodologies have been used widely in cardiomyocyte studies given the emphasis on mechanistic data required to publish in high impact journals. However, given the well-travelled pathway of cardiac therapies from cardiomyocyte to *in vivo* animal studies to human trials, robust statistics at the early stage of preclinical work may have important implications. Their use may help prevent wasting resources targeting spuriously abnormal elements of myocyte biology and ultimately assist in the assessment of the efficacy of therapeutics at the level of the cardiomyocyte which could lead to effective therapies for diseases like heart failure.

4 *IN VIVO* CARDIAC FUNCTION IN RATS FOLLOWING MYOCARDIAL INFARCTION

4.1 Aims

- To assess the presence of cardiac dysfunction in the rats used for subsequent cell isolation such that HF and control groups are adequately phenotyped.
- To assess the progression of cardiac dysfunction following myocardial infarction in the rat at different timepoints via echocardiographic and PV loop methodologies.

4.2 Introduction

One of the overarching aims of this PhD project was to assess some of the key differences in Ca^{2+} handling in cardiomyocytes from HF and control rats. As such, the presence of cardiac dysfunction in these animals and its severity had to be carefully assessed. Several methods were important in this assessment. Firstly biometric measurements were used with ratios of heart weight to body weight and heart weight to the cube of tibia length (TL^3) to quantify cardiac hypertrophy (section 2.3.1). Similarly corrected lung weight was measured as a surrogate for pulmonary oedema. Secondly to ensure that surgical technique was technically adequate to produce a substantial infarct, planimetry was used initially as has been outlined in section 2.2.2. However, the presence of scarring does not necessarily infer a reduction in cardiac function at the level of the organ and so two further techniques were employed to assess this - echocardiography and PV loop analysis.

Echocardiography employs ultrasonic radiation which can be directed into a beam using an appropriate transducer. This imaging modality is widely used in clinical medicine, particularly in the assessment of cardiac structure and valvular function (Hoit, 2006). Here we used the technique to assess left ventricular function, cavity and wall dimensions and the velocity of blood flow using the pulsed wave Doppler technique.

Although echocardiographic assessment allows non-invasive assessment of cardiac function, PV loop analysis provides a different method of assessment whereby direct measurements of pressure and volume from within the LV cavity are obtained. These measurements are processed to provide distinct and complementary data regarding organ function in comparison to echocardiography. Suga *et al.* were the first to assess simultaneous pressure and volume in the left ventricle (Suga *et al.*, 1973). Development of conductance volumetry and miniaturization of the technology allowed the first simultaneous measurements of pressure and volume via catheters in rodent hearts (Ito & Takaki, 1996). Huntly Millar refined the technology into its current user-friendly form where a single catheter is inserted into the ventricle to provide instantaneous pressure and volume data in rodents (Georgakopoulos *et al.*, 1998). The advantage of the PV methodology over other available approaches including echocardiography is that it allows direct measurement of pressure and enables more specific measurement of LV performance independently from loading conditions and heart rate (Pacher *et al.*, 2008). This can be important in the assessment of cardiac contractility in HF since compensatory mechanisms exist which increase preload, for example via the renin-angiotensin-aldosterone axis (Braunwald, 2008). Hence in the presence of such compensatory mechanisms one may underestimate the degree of cardiac dysfunction. The ability to perform these measures relates to the ability to change pre-load and afterload in the course of dynamic PV loop measurements, for

example by restricting venous return to the heart by occluding the inferior vena cava (IVC) to reduce preload. As such the relationship between preload and the parameter of interest can be assessed rather than simply the parameter at a preload which is defined by the individual animal's hydration status, neurohormone levels and morbidity.

4.3 Methods

Methods are outlined fully in sections 2.2 and 2.3. Statistics were performed using standard techniques such as independent samples t-tests and ANOVA as described in section 2.6.

4.4 Results

4.4.1 Biometry Suggests Fluid Retention, Pulmonary Oedema and Cardiac Hypertrophy in HF Model

Biometric measurements included body weight (BW), heart weight (HW), lung weight (LW) and tibia length (TL). BW and TL were used as factors to correct to body size. The cube of TL (TL^3) was used to correct rather than raw TL for reasons outlined in section 2.3.1 and Appendix 9.1. HF data was gathered at 3 timepoints following MI – 4 weeks (4WMI), 8 weeks (8WMI) and 16 weeks (16WMI) with corresponding age-matched control (AMC) animals at each stage.

Initial comparisons were made for BW and showed that control animals were still growing throughout the experiments with no significant difference between the weights of AMC and HF animals at any stage (Figure 4-1A). TL was also increasing throughout the timepoints but there was no change in HF TL compared with control TL at any timepoint (Figure 4-1B). In order to assess whether there was a possibility of fluid retention at any timepoint BW was corrected to TL^3 (see section 2.3.1 and Appendix 9.1.1 for explanation). We found that at the 16W timepoint there was a significant increase in BW/TL^3 in MI versus AMC (Figure 4-1C). In order to assess whether there was progression of this relative increase in BW over the timepoints, BW/TL^3 for MI animals at each timepoint was normalized to the mean value of BW/TL^3 the corresponding AMC group. This showed that there was a significant increase in normalized BW/TL^3 between 4W and 16W after MI (Figure 4-1D) suggesting that there is progression of fluid retention over this time. Insufficient animals died at late stage to draw meaningful comparisons between mortality in the groups. As shown in section 2.2.1 most deaths occurred at an early stage within 24h of surgery. No late deaths (after 24h) occurred in MI rats planned for study at the 4W stage (40 rats survived), there was 1 death out of 22 rats planned for study at the 8W stage (5%) and there were 4 deaths out 49 rats planned for study at later stages (16W and beyond - 8%).

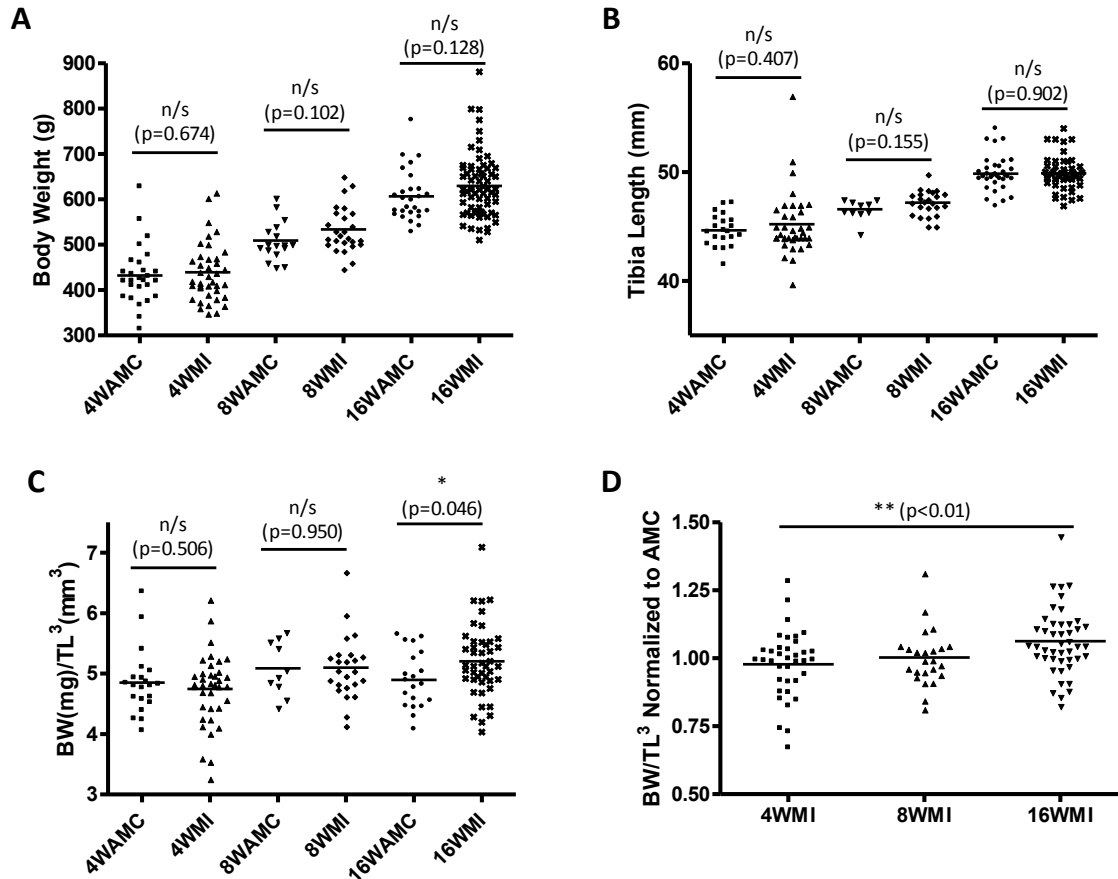


Figure 4-1. There is progressive increase in BW/TL³ over time in the HF model.

(A) BW increases over time but shows no significant difference in MI animals over AMC at each timepoint. (B) TL shows a similar pattern to BW. (C) Correcting BW to TL³ shows that BW increases out of proportion with rat size at 16W timepoint. (D) When BW/TL³ is normalized to the mean value for AMC, the progressive increase in this parameter, which may indicate fluid retention, is shown. n=10-68 rats in each group.

Fluid retention could include excess fluid in the form of, for example, abdominal ascites, organ congestion and peripheral oedema. However there was also a possibility of pulmonary oedema suggesting raised pulmonary venous pressure in these animals. We assessed this using LW as a surrogate. LW was increased over AMC at the 16W timepoint (Figure 4-2A) suggestive of pulmonary oedema. To ensure this increase was present relative to body size LW was corrected to BW (Figure 4-2B) and TL³ (Figure 4-2C). There was no significant increase in LW/BW, possibly because at this timepoint there is peripheral oedema as well as pulmonary oedema such that both numerator and denominator are increased thus cancelling each other out. When corrected to TL³ the significant increase in LW was again evident at 16W. To assess progression of pulmonary oedema over the different timepoints LW was normalized to the corresponding AMC group which showed a gradual increase in LW with time following MI, although this did not reach statistical significance (Figure 4-2D).

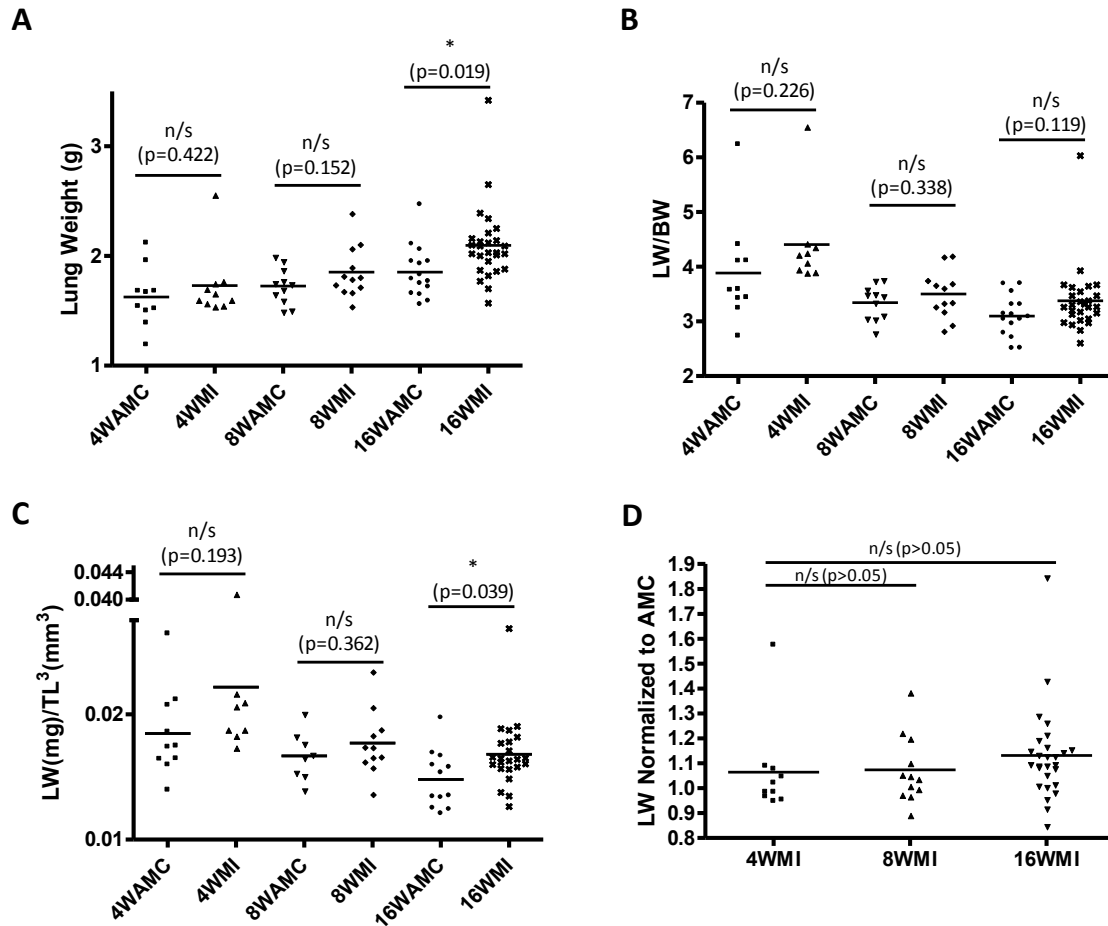


Figure 4-2. LW is increased at 16WMI stage suggestive of pulmonary oedema.

(A) LW is increased over control group and this reaches statistical significance by 16W stage. (B) LW/BW does not show any significant increase, possibly due to the presence of peripheral as well as pulmonary oedema. (C) When LW is corrected to TL³ there is a significant increase in MI compared with AMC at the 16W timepoint. (D) LW normalized to the mean LW of the corresponding AMC group shows an increase over the 3 MI timepoints but this is not statistically significant. n=8-27 rats in each group.

HW was measured and was significantly greater than the control group at all timepoints (Figure 4-3A). When corrected to BW these changes remained present and were similar when corrected to TL³ (Figure 4-3B-C). However it was evident that the degree of increase in HW relative to animal size in both these ratios was significantly greater at the 4WMI stage (Figure 4-3D-E). A similar pattern was seen in AMC animals however with the largest HW/BW and HW/TL³ values being seen at the 4WAMC stage as compared to 8WAMC and 16WAMC. In order to correct for this we normalized HW to the corresponding AMC mean HW at each timepoint (Figure 4-3F). Even when normalized the 4WMI HW was significantly greater than 8WMI but there was no significant difference between 4WMI and 16WMI.

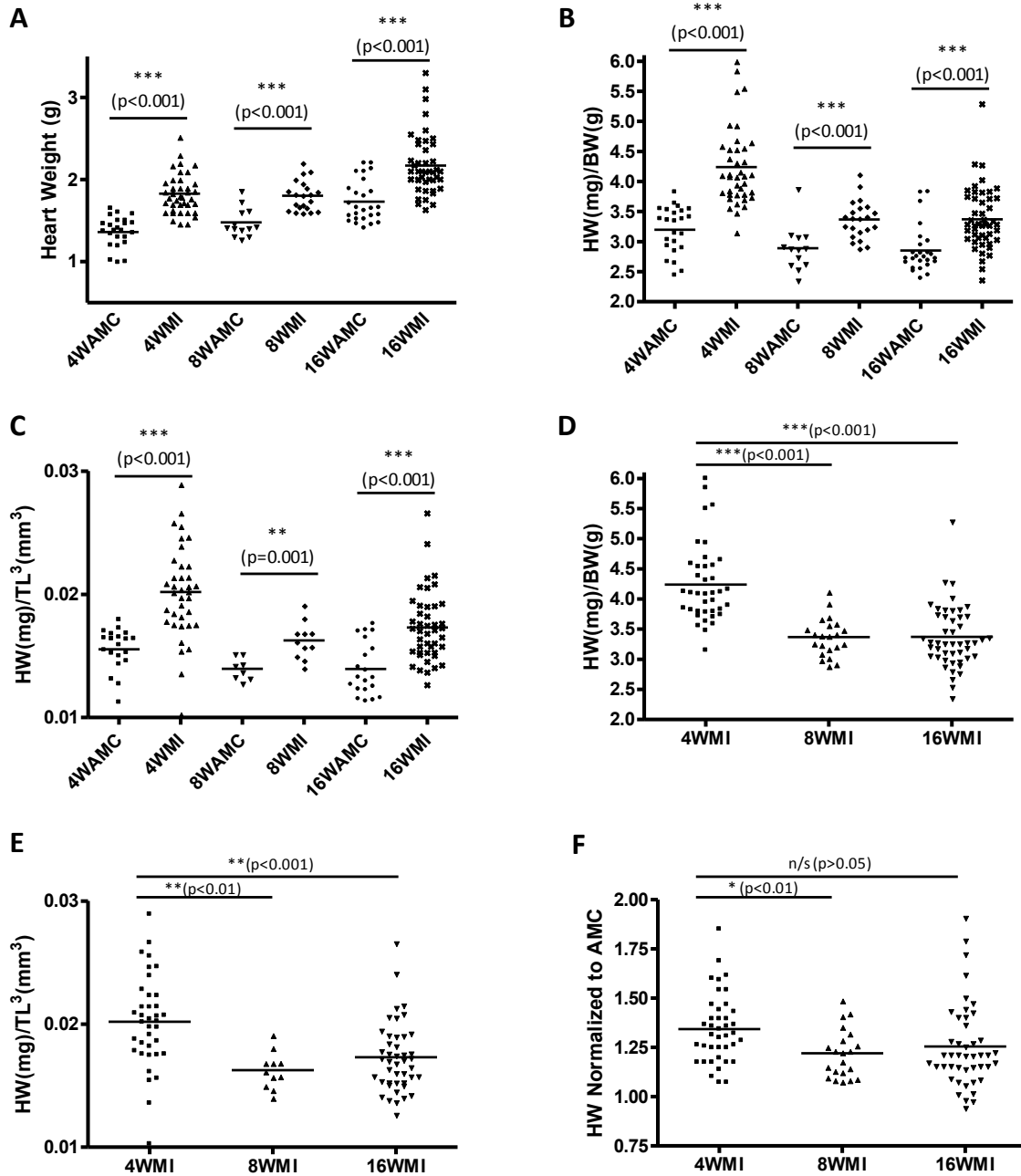


Figure 4-3. Cardiac hypertrophy is present in HF at all timepoints but is most marked at 4WMI stage.

(A) Raw HW data showing an increase over time and greater HW in MI rats compared with AMCs. (B) HW corrected to BW and (C) HW corrected to TL³ show a similar pattern, with a significant increase at each timepoint. (D-E) Both ratios show greatest hypertrophy at 4WMI stage. (F) When normalized to AMC HW, there remains greater hypertrophy at 4WMI stage compared with 8WMI but not 16WMI. n=8-48 rats in each group.

4.4.2 Echocardiography reveals impaired systolic function and progressive LV dilatation following MI

The above biometric data show that the 4WMI model can be classified as more hypertrophied and well compensated whilst the 16WMI can be classified as failing with probable peripheral and pulmonary oedema. The 8WMI model is intermediate between these two conditions. For collection of *in vivo* data via echocardiography and PV loops there was therefore a focus on the 4WMI and 16WMI timepoints.

M-mode echocardiography was performed in the parasternal long axis view. Measurements of LV walls and chambers were performed as described in section 2.3.2. We found a significant increase in LVIDd in the HF model over AMC at the 16W timepoint but not at the 4W timepoint (Figure 4-4A). To facilitate comparison of the timepoints we normalized LVIDd to the mean of the corresponding AMCs. This showed a significantly greater increase in the 16WMI versus the 4WMI ($19.6 \pm 1.5\%$ versus $8.6 \pm 2.7\%$) (Figure 4-4B). To assess hypertrophy echocardiographically we measured the LVPWd. Despite the biometric confirmation of hypertrophy, there was no significant increase in LVPWd in MI over control at either timepoint (Figure 4-4C), although this may simply relate to the inability of this technique provide the accuracy of wall thickness measurement required to resolve differences in thickness (at the sub millimeter scale). In terms of myocardial function, the anterior wall became static intra-operatively and this persisted throughout the different time-points as viewed by echocardiography. We suspected that the remote myocardium also had reduced function and we assessed this by measuring the increase in LVPW thickness in systole as compared to the baseline diastolic measurement. There was reduced function at both 4W and 16W in the MI compared with AMC groups but there was no difference in function between 4WMI and 16WMI groups (Figure 4-4D). Representative M-mode images are shown in Figure 4-5.

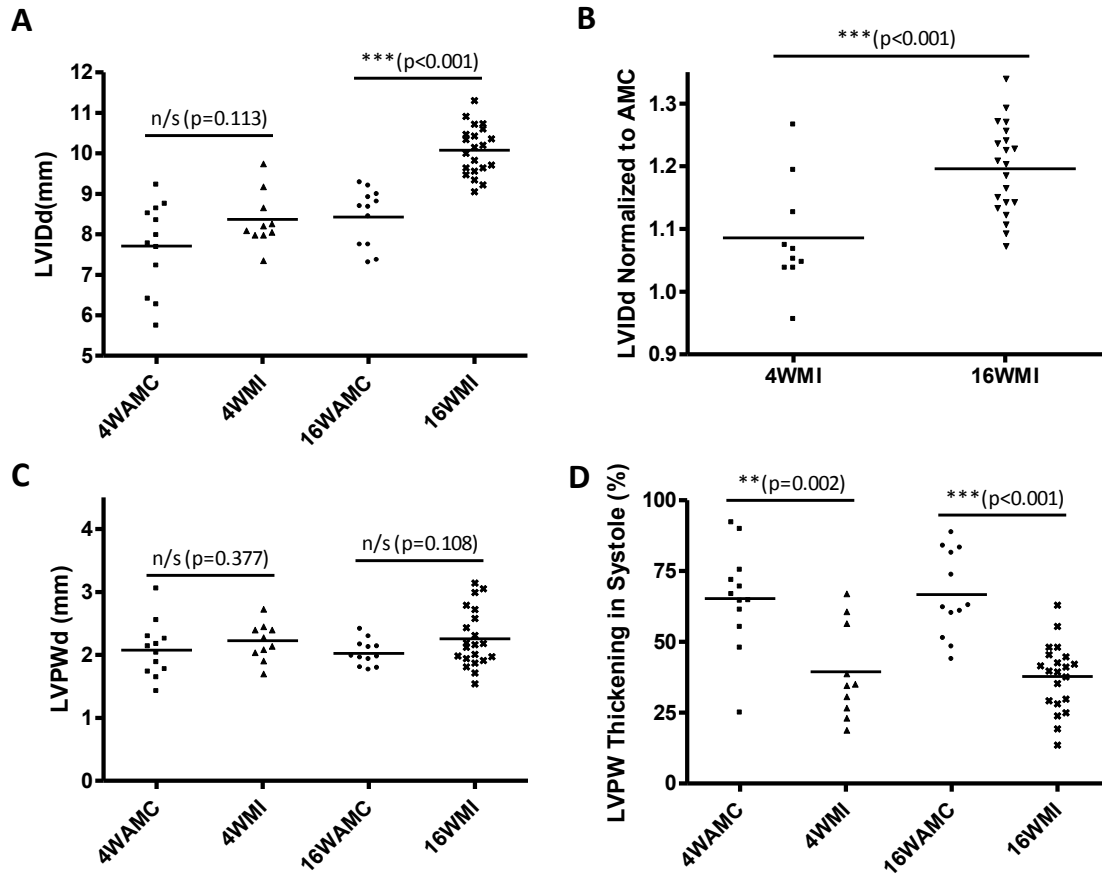


Figure 4-4. LV wall and cavity dimension in HF versus control animals.

(A) LVIDd is greater in MI versus control at 16W but not at 4W. (B) In order to assess if the dilatation is proportionally greater in the 16WMI model versus 4WMI we compared LVIDd normalized to the corresponding AMC. This showed a greater increase at 16W. (C) LVPWd was not greater in MI rats at either timepoint. (D) Impaired PW function was present at both 4W and 16W as indicated by reduced thickening of the wall in systole compared with diastole. $n=10-21$ rats in each group.

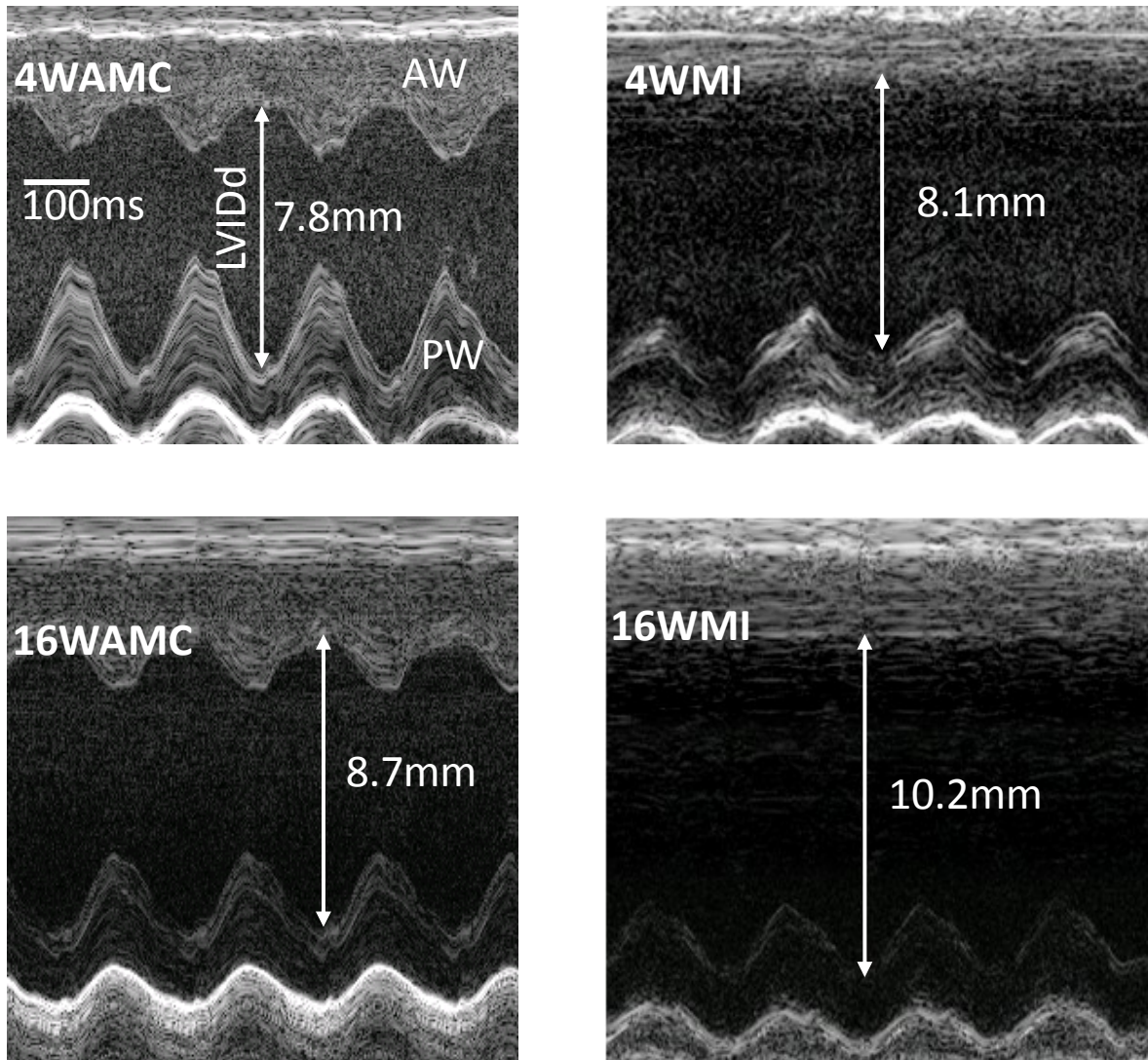


Figure 4-5. Representative M-mode echocardiography images showing increase in LVIDd 16W following MI

Top left panel shows 4WAMC M-mode echocardiography with contractile anterior (AW) and posterior wall (PW) and non dilated left ventricular internal diameter in diastole (LVIDd). At the same timepoint the MI rat (top right panel) exhibits absent AW contractility but minimally dilated LVIDd. In comparison at the 16W timepoint (bottom panels) there is greater LV dilatation. The reduction in PW function following MI is also evident at both timepoints.

In addition to chamber and wall dimensions, echocardiography can give a good indication of the cardiac pump function. We used two methods for this. Firstly we assessed the EF which revealed a reduction at both 4 and 16W timepoints in the MI group but no tangible progression between these timepoints (Figure 4-6A). Secondly we used the pulsed wave Doppler trace in the pulmonary artery to assess blood velocity and the integral of this velocity waveform to calculate cardiac index (i.e. cardiac output corrected to rat weight). PAV_{max} appeared reduced at both 4W and 16W following MI although this only reached significance at 16W (Figure 4-6B). However there was no quantitative difference between the reduction at the 4W and 16W timepoints as shown by the

normalized data in (Figure 4-6C). The mean cardiac index was not significantly reduced at either timepoint (Figure 4-6D). Representative PA Doppler traces are shown in Figure 4-7.

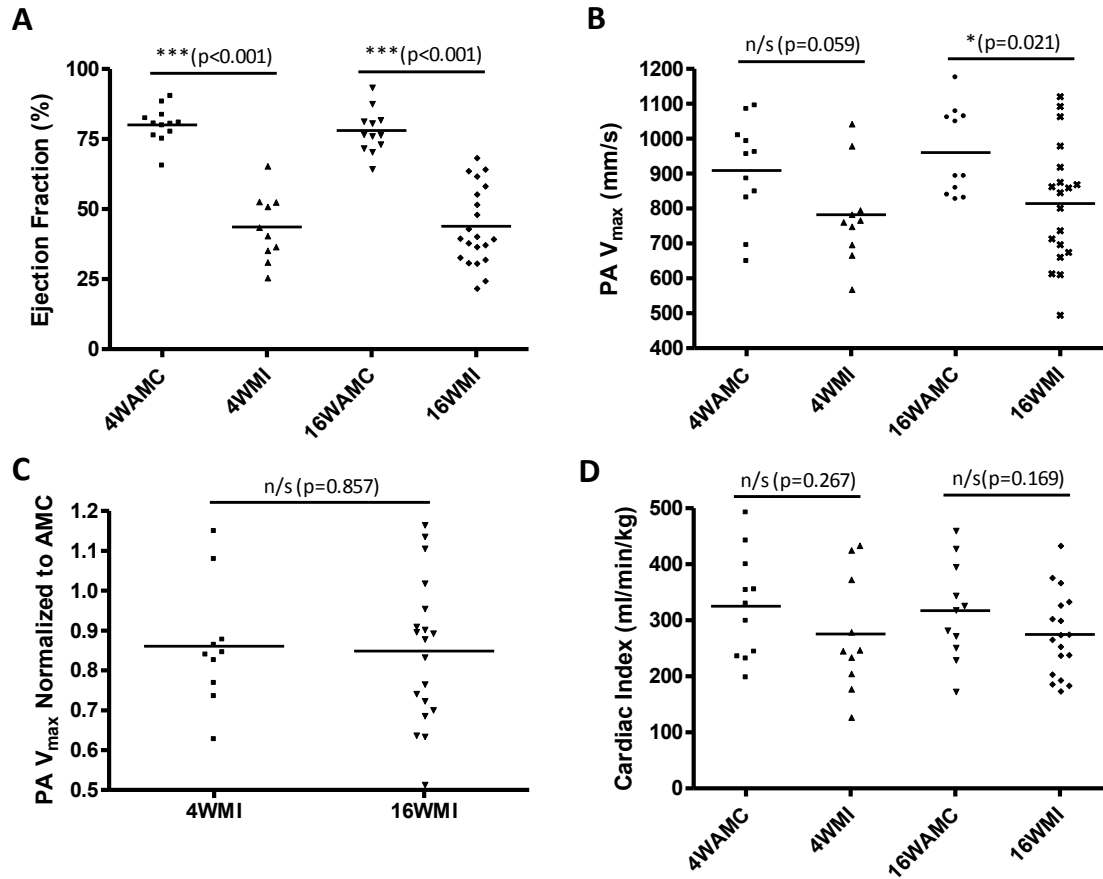


Figure 4-6. Pump function is reduced following MI.

(A) Ejection fraction is reduced in both 4 and 16W MI models to a similar extent. (B) PAV_{max} is reduced at both timepoints but only reaches significance at 16W. (C) When normalized to AMC values, PAV_{max} reduction is similar at 4 and 16W post MI. (D) Cardiac index shows is a not significantly reduced post MI at either timepoint. n=10-19 rats in each group.

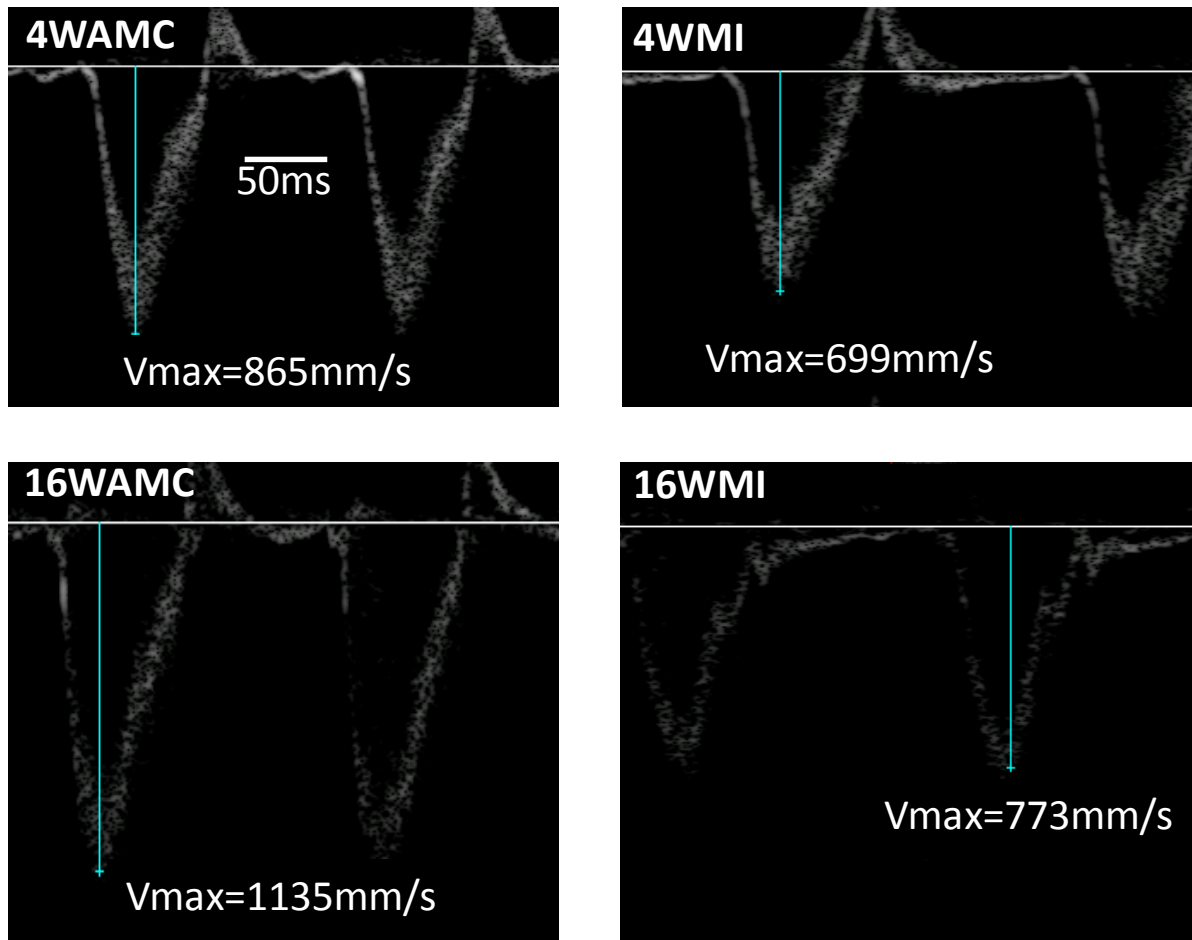


Figure 4-7. Representative PA Doppler waveforms in AMC and MI.

Representative measurements of PAV_{max} in MI animals compared with respective AMC animals at 4W (top panels) and 16W (bottom panels). The proportional reduction was similar at the two timepoints.

4.4.3 PV Loops show reduced systolic and diastolic function post MI with progressive reduction in ESPVR slope

Pressure volume loops were also used to assess systolic and diastolic function *in vivo* as described in section 2.3.3. This allowed direct measurement of pressure and volume at steady state and also during IVC occlusion to give preload-independent measures of cardiac function. Mirroring the echocardiographic data pertaining to LVIDd, there was no significant increase in LV end diastolic volume at the 4WMI stage but significant dilatation at the 16WMI stage compared to their respective controls (Figure 4-8A). Data normalized to AMC confirmed significant dilatation between 4WMI and 16WMI stages of HF (Figure 4-8B). End systolic volume was also greater at 16WMI stage compared with 16WAMC, although a comparison of normalized data did not reach significance between 4WMI and 16WMI (Figure 4-8C-D). There was a significant 22% drop in peak LV systolic pressure in 16WMI compared with 16WAMC and the drop in pressure between 4WAMC and 4WMI was similar in magnitude (19%) but did not reach statistical significance ($p=0.051$) (Figure 4-8E-F).

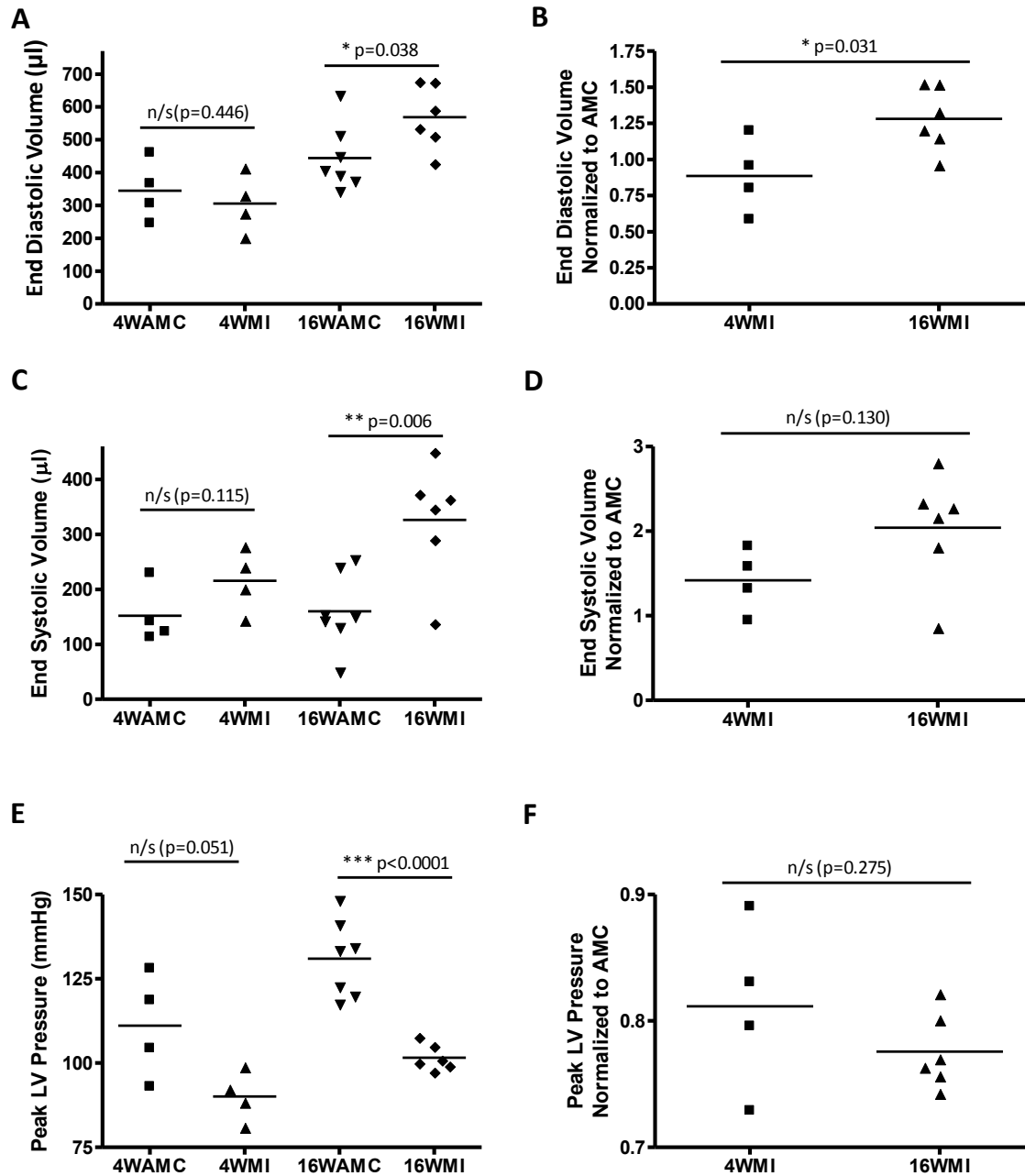


Figure 4-8. Steady state PV loop measurements in 4 and 16W MI hearts.

(A) End diastolic volume was significantly greater in 16WMI compared with 16WAMC. (B) When normalized to the respective AMC values it was found that the dilatation in 16WMI was significantly greater than 4WMI. (C) End systolic volume was also greater at 16WMI compared with 16WAMC, (D) although the difference between 4WMI and 16WMI did not reach significance. (E) Peak LV pressure was reduced in 16WMI vs 16WAMC but (F) the normalized data showed no change in 16WMI vs 4WMI. n=4-7 rats in each group.

Left ventricular end diastolic pressure (LVEDP) is a correlate of LV relaxation and this was significantly elevated at the 16WMI stage compared with 16WAMC (Figure 4-9A). The normalized data to compare 16WMI and 4WMI did not reach statistical significance (Figure 4-9B) although the

magnitude of increase was substantially greater in 16WMI (85%) compared with 4WMI (10%). Maximum rate of pressure change in systole (dP/dt max) was reduced in 16WMI versus 16WAMC but this difference did not reach significance at the 4W timepoint (Figure 4-9C). However the normalized data do not suggest any major difference between 4WMI and 16WMI for this parameter (Figure 4-9D). Similar results are shown for dP/dt min with a significant reduction in magnitude in 16WMI versus 16WAMC but no significant difference between 4WMI and 16WMI (Figure 4-9E-F).

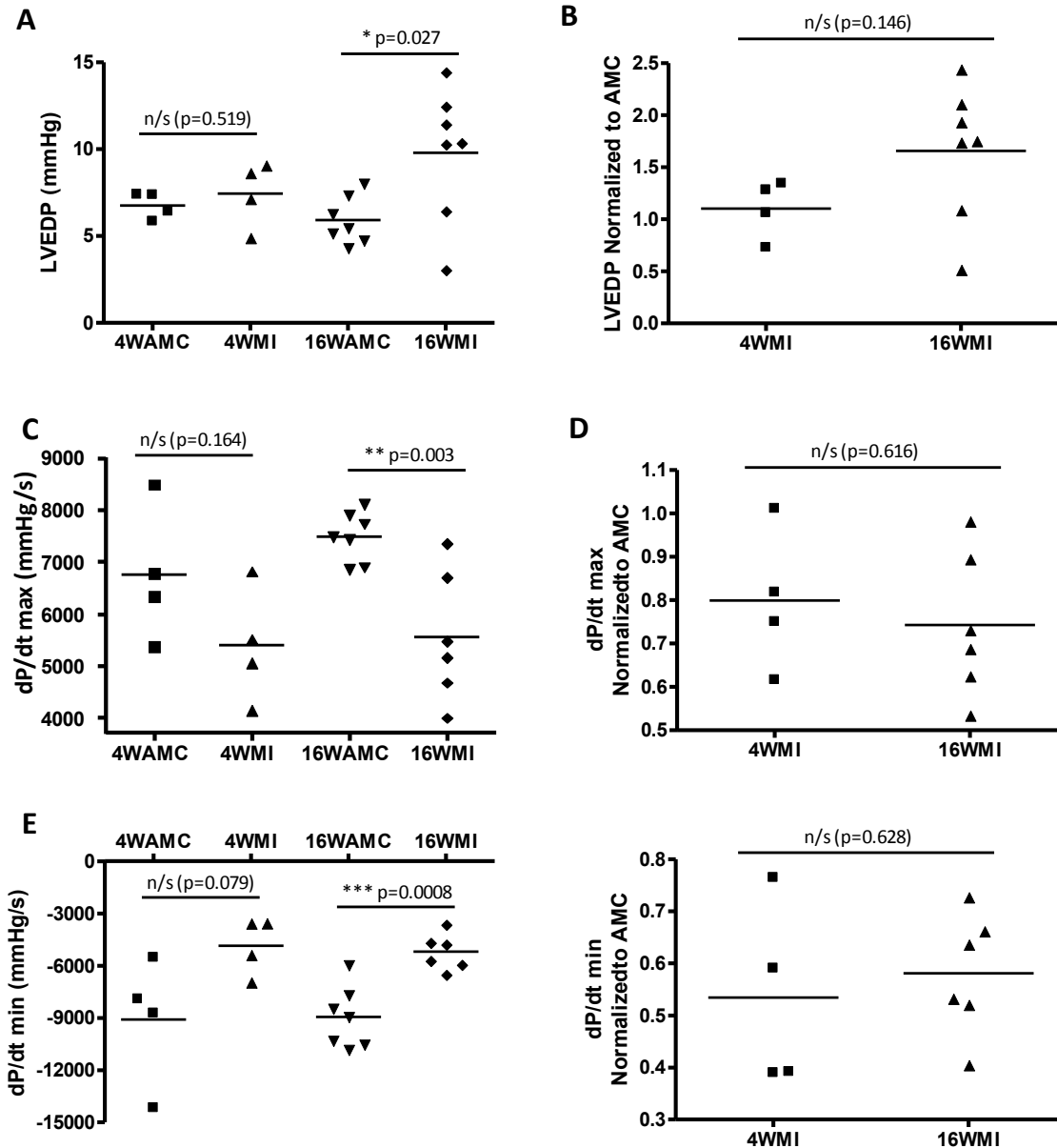


Figure 4-9. End diastolic pressure and dP/dt max and min post MI

(A) LVEDP is significantly increased by 16W post MI although normalized data (B) does not confirm a difference between 4WMI and 16WMI. (C) dP/dt max is significantly reduced at 16W post MI. (D) dP/dt max normalized to AMC is not significantly reduced at 16WMI stage compared with 4WMI. (E) Similarly magnitude of dP/dt min is significantly reduced at 16WMI versus 16WAMC although (F) normalized data suggest the change is similar at 4WMI and 16WMI stages. n=4-7 rats in each group.

IVC occlusion was used to give dynamic measures of systolic and diastolic function. This showed a significant reduction in ESPVR slope at 16WMI compared with 16WAMC (Figure 4-10A). This preload-independent measure of systolic function showed more significant impairment in 16WMI (64% lower than 16WAMC) compared with 4WMI (only 17% lower than 4WAMC) (Figure 4-10B). EDPVR was significantly greater in 16WMI compared with AMC although there was no difference in normalized data between 4WMI and 16WMI (Figure 4-10C-D). Energetic efficiency (see section 2.3.3 for definition) was reduced significantly at both 4WMI and 16WMI timepoints (Figure 4-10E) and the reduction in efficiency was similar at both 4WMI and 16WMI timepoints (Figure 4-10F).

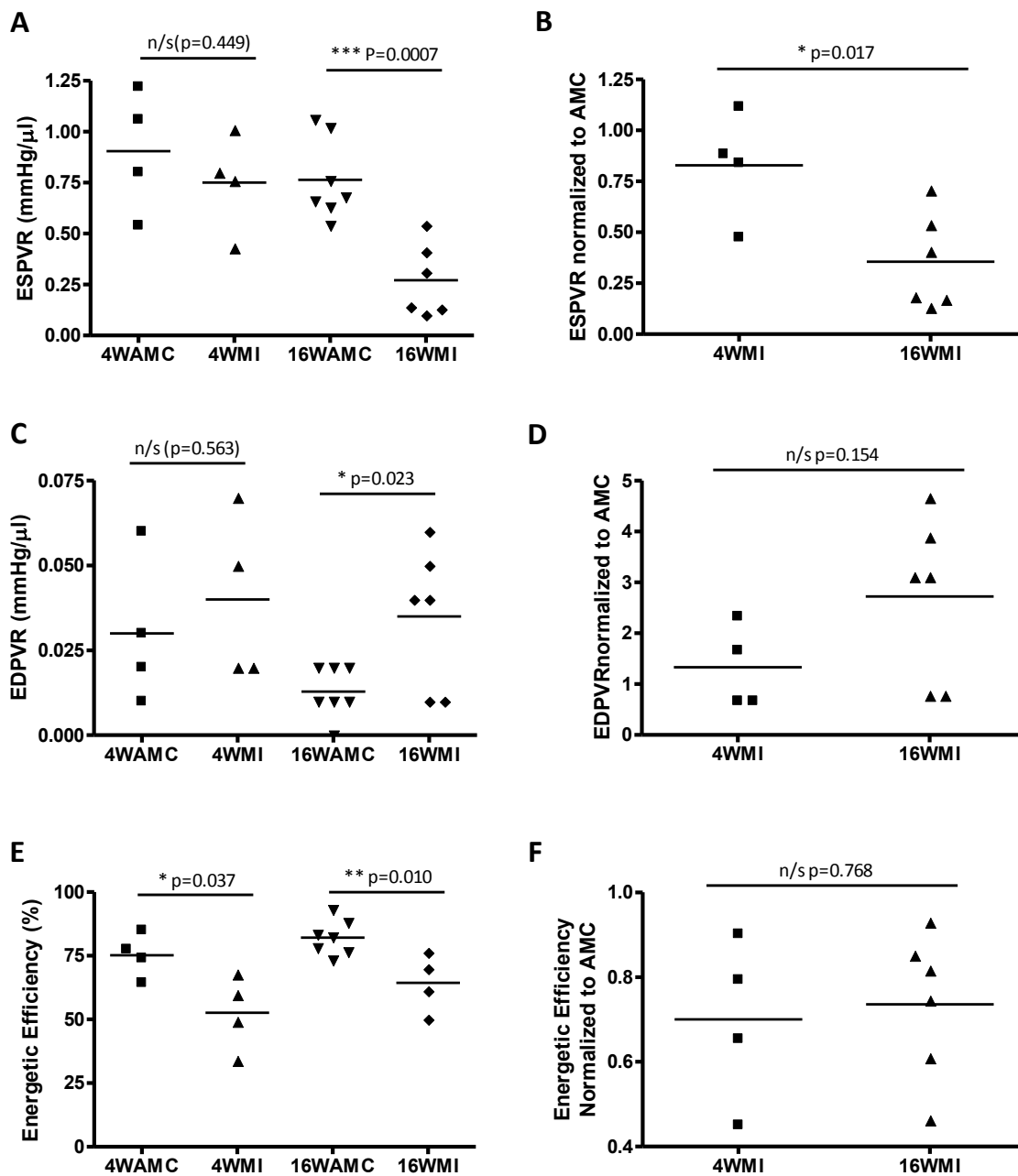


Figure 4-10. Dynamic measures of cardiac function measured with PV loops.

(A) The slope of ESPVR is significantly reduced only at 16WMI timepoint compared with AMC. (B) Normalized data confirm that ESPVR is significantly lower at 16WMI stage compared with 4WMI. (C) EDPVR is significantly elevated at 16WMI timepoint suggesting a stiffer ventricle although (D) the difference between 4WMI and 16WMI normalized to their respective AMCs does not reach statistical significance. (E) Energetic efficiency is reduced in MI rats compared with AMC at both timepoints. (F) There is no deterioration in energetic efficiency between 4WMI and 16WMI timepoints. $n=4-7$ rats in each group.

Representative examples of PV loops during IVC occlusion are shown in Figure 4-11. These loops illustrate several of the features outlined in the graphs above (see figure caption for further detail).

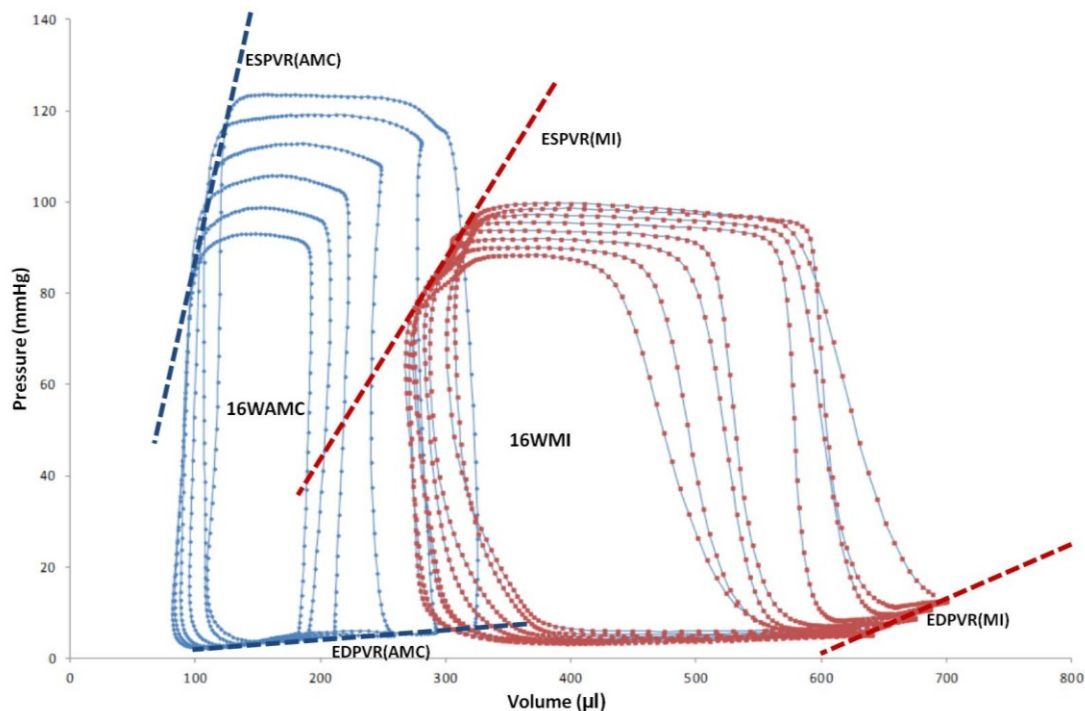


Figure 4-11. Representative PV loops during IVC occlusion in 16WAMC and 16WMI rats.

PV loops during IVC occlusion show several of the features outlined in data above. Loops from 16WAMC (blue) and 16WMI (red) are shown. The initial (largest) loop in both groups is representative of normal cardiac function (prior to IVC occlusion) and shows that peak pressure is lower in the MI heart compared with AMC and that volume of the LV in both systole and diastole is greater in the MI heart compared with AMC. When the IVC is occluded both volume and pressure drop and the loops become smaller. End systole is represented by the top-left corner of each loop and as the loops become smaller these points can be connected to form a line (ESPVR). When this line is steeper it suggests the heart's contractile function would respond better to a rise in pre-load. The relationship is shallower in the 16WMI heart compared with 16WAMC suggesting reduced contractile reserve post-MI. On the other hand the same relationship at end diastole (EDPVR) is steeper in the 16WMI heart revealing a stiffer ventricle.

4.5 Discussion

4.5.1 Biometric data shows early exaggerated cardiac hypertrophy and later fluid retention and pulmonary oedema in HF model

Biometric data confirmed significant differences between HF models at different stages post MI. Firstly body weight versus TL^3 was significantly greater over time following MI as shown in Figure 4-1. BW/TL has previously been used as an index of salt/water retention in HF models (Noma *et al.*, 1988). It is an imperfect measure since increases in BW/TL³ could also be caused by increased adiposity or muscle mass, the former of which is a possibility in HF considering these rats may be more sedentary. However our findings may be related to increased fluid retention which only becomes significant by 16W post MI. This is in keeping with the data collected on LW. LW is significantly increased over AMC by 16W post MI (Figure 4-2). This progression is similar to previous studies in the same model which showed an increase in wet lung weight and the ratio of wet:dry lung weight at 8 and 16 weeks post MI but not at 4 weeks (Dixon *et al.*, 1990; Hill & Singal, 1996). Therefore our data and previous data suggest progressive decompensation in this HF model with slow onset of fluid retention and pulmonary oedema which has not occurred by 4 weeks post MI but is significant by 16 weeks post MI. A potential proviso to this is that other changes which may increase lung weight such as airspace leukocytosis and collagen production have been found in this model previously and also be contributing to the change in lung weight in the current group of animals (Park *et al.*, 2009).

Changes in HW were more unexpected. Several studies have shown an increase in HW following rat MI (Semb *et al.*, 1998; Kaprielian *et al.*, 1999; Anand, 2002; Huang *et al.*, 2008), however there have been relatively few studies of the progression of HW over different time-points post MI. Peterson *et al.* assessed HW post MI at 7 timepoints in SD rats (Peterson *et al.*, 2000). They found relatively modest increases in HW which progressed over time following MI (9% at 5 weeks and 16% at 16 weeks). On the other hand we found greater increases in HW over AMC which did not become progressively greater with increased time following MI (34% at 4 weeks and 26% at 16 weeks). When HW was corrected to BW or TL^3 , it was significantly greater in 4WMI versus 8WMI and 16WMI (Figure 4-3D-E). There appeared to be a greater HW/BW in younger AMCs versus older AMCs (Figure 4-3B) and so to correct for this we normalized MI HW data to the mean AMC HW (Figure 4-3F). This showed significantly greater normalized HW in 4WMI versus 8WMI. It is important to note that we found significant hypertrophy in MI animals versus AMC at all timepoints but that the magnitude of this hypertrophy was reduced at later timepoints. A combination of factors may explain this. Isoyama *et al.* studied hypertrophic responses to aortic constriction in the rat and found that at 9 months of age the hypertrophic response was significantly greater than that in older rats when TAC was performed between 18 and 22 months of age (Isoyama *et al.*, 1987). This was found to be related to reduced ability to produce ribosomal RNA and protein in the older rats. Although in our study the stimulus to hypertrophy is produced at a single early timepoint it may be that this hypertrophy becomes more difficult to maintain for similar reasons. Loss of myocytes via necrosis or apoptosis may play a major role in transition from a hypertrophic compensated phenotype to a failing phenotype (Gill *et al.*, 2002) and this may be another factor involved in limiting the increase in LV mass at later MI timepoints.

4.5.2 Echocardiography reveals increasing LV dilatation over time post MI but Preserved Cardiac Index

In vivo functional data focused on 2 timepoints – the compensated hypertrophic 4WMI rats and failing 16WMI rats. Echocardiographic data was used to assess the dynamic function and dimensions of the heart at these timepoints. We found significant dilatation of the LV at 16W but not at 4W post MI (Figure 4-4A). A comparison of LVIDd normalized to AMC data confirmed a significantly greater dilatation over control values in 16WMI (20%) compared with 4WMI (9%). In terms of wall thickness the difference in PW thickness was not significant at either timepoint although the relative thickening of the posterior wall was significantly reduced at both 4 & 16WMI (Figure 4-4D). In terms of ventricular function (Figure 4-6), the ejection fraction (EF) was significantly reduced at both timepoints, corresponding with a reduced pulmonary artery V_{max} . However the overall effect was that cardiac index was unchanged. The overall picture suggests a dilating LV with reduced muscle function in which the dilatation means that despite a reduced EF, a similar volume of blood is ejected with each heart beat resulting in a similar cardiac output as the corresponding AMC overall. A similar picture is seen for both 4 and 16WMI models, however the dilatation is more severe at 16W suggesting that muscle function deteriorates progressively between 4 & 16 weeks post MI.

Litwin et al performed echocardiographic studies in the same model and made similar measurements, although they did not perform PA velocity measurement (Litwin *et al.*, 1994). They also found significant LV dilatation although this was of similar magnitude at both timepoints they used (17.5% at 1 week and 18.8% at 6 weeks). The absence of progressive dilatation in their study is probably related to the reduced latency post MI of their later timepoint. Like us, they also found no difference in PW thickness post MI at either timepoint but a significant reduction in PW thickening in systole at both timepoints (although as mentioned above it may be difficult to resolve small differences in wall thickness with echocardiography since this requires accuracy to the sub-millimetre scale). Assuming there is no increase in wall thickness our findings would also be in keeping with those found in humans. This type of LV remodeling has been described in humans following myocardial infarction or those with valvular dysfunction and is classified as eccentric hypertrophy (Grossman *et al.*, 1975). Here hypertrophy refers to an increase in LV volume without an increase in LV wall thickness (relative to diastolic diameter). This type of remodeling was observed by McKay et al following myocardial infarction in a study of 30 people (McKay *et al.*, 1986). They found that although LV end diastolic volume had increased by 20% by 2 weeks post ST-elevation MI, there was no significant change in the wall thickness of non-infarcted myocardial segments. Such changes allowed improvements in haemodynamic parameters such as LVEDP in between the initial cardiac catheterization and a repeat study 2 weeks later. Dilatation of the LV also allows cardiac index to remain constant despite the reduction in EF since diastolic volume is much greater. An MRI study in the post-MI rat model showed similar results to us in terms of cardiac index remaining well preserved post MI with no progressive reduction over the 4-16W time period (Nahrendorf *et al.*, 2001). This was associated with progressive LV dilatation between 4 and 16W post MI, in agreement with our results.

4.5.3 PV Loops confirm progressive LV dilatation and show progressive reduction in ESPVR post MI

Simultaneous measurement of pressure and volume allowed more detailed characterization of the HF model. Firstly it was confirmed that left ventricular end diastolic volume (LVEDV) progressively

increases over time post MI with a significant increase in normalized volumes between 4 and 16W post MI (Figure 4-8B). Left ventricular end systolic volume is also greater at 16WMI compared with 16WAMC. Peak LV pressure is significantly reduced at 16WMI compared with 16WAMC although there is no marked progression in the extent of this reduction compared with the 4WMI stage (Figure 4-8E-F). Impairment of ventricular function post MI was revealed by both steady state measurements and those during IVC occlusion. The steady state measurements showed a significant reduction in dP/dt max by 16W post MI although there was no obvious progression between 4WMI and 16WMI as shown by the data normalized to corresponding AMC values (Figure 4-9 B-C). ESPVR was significantly reduced by the 16WMI timepoint with significant deterioration between 4WMI and 16WMI suggesting reduced contractile reserve (Figure 4-10 A-B). In terms of diastolic function dP/dt min was significantly reduced in 16WMI versus 16WAMC and EDPVR was significantly increased over AMC by 16W post MI. LVEDP was also elevated in 16WMI versus AMC. Energetic efficiency was significantly reduced at both 4WMI and 16WMI timepoints

Our group has previously characterized this 16WMI rat model in terms of PV loops with similar results to the current study. Lyon et al found a significant increase in LV volume with a reduced ESPVR and reduced magnitude of both DP/dt max and dP/dt min in the 16WMI model (Lyon *et al.*, 2009). In terms of diastolic function, as with the current data, Lyon et al also showed an elevation in LVEDP at the 16WMI stage and an increase in EDPVR slope. In a different study Lyon et al showed reduction of efficiency at the 16WMI stage (Lyon *et al.*, 2011). Others have found similar results in the rat MI HF model. In a 10 week model following coronary artery ligation it was found that LVEDP was elevated and peak systolic pressure reduced in rats with large infarcts (approx 40-50% of LV circumference - a similar size to infarcts in this study) (Raya *et al.*, 1989). In a 4 week model Olivetti et al also found elevated LVEDP and reduced systolic pressure, and also found reduced dP/dt max (Olivetti *et al.*, 1991). Using a similar system to us with a catheter that measures pressure and volume simultaneously, Ahmet et al showed, like us, that dP/dt max and min were reduced in magnitude, and ESPVR slope was reduced in an 8WMI model (Ahmet *et al.*, 2004). What our study adds is how haemodynamic parameters assessed by PV loop analysis change depending on time following MI. We found that the increase in EDV was significantly greater at 16W post MI versus 4W. LVEDP also exhibited a markedly greater increase at 16 weeks versus 4 weeks (85% versus 10%) although this did not reach significance due to data scatter. Finally ESPVR was reduced to a greater extent in the 16WMI model versus the 4WMI model when compared to corresponding AMCs showing progressive reduction of inotropy in this model. One study which looked at progression of haemodynamic abnormalities post MI in the rat is that of Dixon et al (Dixon *et al.*, 1990). Although only a pressure catheter was used in this study it also showed more marked LV impairment at 16WMI stage versus earlier timepoints.

4.5.4 Conclusions and Implications

In summary, using three different measures of cardiac function *in vivo* we have shown significant and progressive impairment of LV function following myocardial infarction. Firstly biometric measures suggest progressive fluid retention and pulmonary oedema which is not present at the 4WMI stage but has developed by the 16WMI stage. This may be mediated by a reduced ability to compensate due to less marked increase in heart weight (i.e. reduced hypertrophy) at 16WMI versus 4WMI. Echocardiographic measures, including Doppler wave form of blood in the pulmonary artery, show reduced myocardial function post MI and significant progression of dysfunction with greater

dilatation at later timepoints. Finally PV loops confirm that the post MI HF model exhibits reduced peak LV pressure, increased LVEDP and reduced rate of pressure generation and relaxation. The progressive nature of the HF model is also confirmed with greater increases in volume and greater reduction in ESPVR slope in 16WMI rats versus 4WMI rats. Overall these changes correspond with the important paradigm of HF physiology outlined by Mann (Mann, 1999). An initial “index event” (in this case myocardial infarction) causes a decline in pump function. Compensatory mechanisms are activated which in the short term are able to restore cardiac function to a normal homeostatic range, but in the longer term can lead to secondary end organ damage within the ventricle. This downward spiral of decline in myocardial function eventually leads to symptomatic heart failure and death. The confirmation that the decline in cardiac function in the rat HF model follows this pattern over the 16 week period post MI studied confirms that the rat MI model is relevant as a model of human HF and that the study of myocytes at later timepoints may reveal changes in physiology that are relevant to progression of the disease.

5 CHANGES IN Ca²⁺ TRANSIENTS AND SPONTANEOUS SR Ca²⁺ LEAK IN CARDIOMYOCYTES FROM RATS WITH ESTABLISHED HEART FAILURE

5.1 Aims

- To assess the effects of HF on cell size.
- To compare Ca²⁺ transient morphology and synchronicity in rats with HF versus AMC, including effects of isoprenaline.
- To compare spontaneous Ca²⁺ spark frequency and morphology between HF and control groups, including effects of isoprenaline.
- To assess whether HF cells from the borderzone behave differently from HF cells from remote regions in terms of Ca²⁺ transients and sparks.

5.2 Introduction

The chronic HF model used by ourselves has been studied previously in terms of many of the elements detailed in the aims above. An increase in cell size has been noted in the rat myocardial infarction HF model previously (Olivetti *et al.*, 1991), as well as in larger animal models and humans with ischaemic cardiomyopathy (Gerdes *et al.*, 1992; Kramer *et al.*, 1998). We assessed length and width in myocytes isolated from our model in order to confirm the effects of infarction at the cellular level.

As detailed in Chapter 3 the findings in the rat HF model with respect to Ca²⁺ transient morphology are variable and may be effected by statistical methods used to analyse the data with a risk of Type I error being greater in the absence of recognition of the hierarchical nature of the data. Chapter 3 detailed some of the findings at the 8 week post-MI stage whereas this chapter details findings at the 16 week post-MI stage which, *in vivo*, we have shown to be decompensated in terms of both systolic and diastolic cardiac function (see Chapter 4).

We also assessed spontaneous Ca²⁺ spark morphology and frequency in the model compared with AMC. Again this has been studied previously and most studies have shown an increased frequency of spontaneous sparks in HF (Lee *et al.*, 2009; Lyon *et al.*, 2009, 2011; Ibrahim *et al.*, 2012), although these studies have been somewhat more variable in their findings regarding Ca²⁺ spark morphology (see Table 3-2). Initial analysis of both transients and sparks in the current study showed little difference in these parameters in HF cells. This was surprising given previous experimental data and also did not correlate well with the *in vivo* data. We therefore hypothesized that there may be differences in these parameters when cells are exposed to beta-adrenergic stimulation. HF is a syndrome in which there is chronic hyperadrenergic state (Cohn *et al.*, 1984) and therefore such conditions may provide closer correlation to *in vivo* function than assessment in simple electrolyte solution.

Another aspect we felt may be important to explore was the physical heterogeneity of the post-MI myocardium. This is particularly relevant to the question of arrhythmogenesis. Studies assessing human arrhythmogenesis post-MI by MRI have shown that an extensive heterogeneous peri-infarct region, or borderzone (BZ), is an independent predictor of propensity to arrhythmia and mortality

(Yan *et al.*, 2006; Schmidt *et al.*, 2007). We therefore hypothesized that myocytes isolated from the BZ may be particularly prone to cellular arrhythmic events such as Ca^{2+} sparks and waves

Our findings suggest that, in the current model, changes in systolic and diastolic function of the heart in HF cannot be attributed primarily to changes in the amplitude and morphology of the Ca^{2+} transient. However there is evidence of a differential effect of isoprenaline on sparks in HF and evidence of differences in the borderzone in terms of spontaneous SR Ca^{2+} release events. Such differences may help explain how HF results in an increased likelihood of ventricular arrhythmia.

5.3 Methods

Experiments were performed on myocytes isolated either from age matched control (AMC) rats or heart failure (HF) rats (i.e. 16 weeks post MI). Cells were loaded with fluo-4 AM as per section 2.5.1. Cells were imaged using confocal microscopy with selection criteria as per section 2.5.2. Pacing and imaging protocols using confocal line-scanning are shown in section 2.5.4. Automated analysis of line-scans was performed using custom-made macros (sections 2.5.6.1-2.5.6.4). Data analysis was performed using hierarchical methodologies which allowed inferences to be drawn in the presence of the hierarchical data structure as outlined in Chapter 3.

5.4 Results

5.4.1 Cell size

Cell size was measured using digitized microscope images of freshly isolated cardiomyocytes in low Ca^{2+} solution (200 μM) using an inverted microscope with a 16x objective lens. Analysis showed that HF cells were 10% longer than AMC cells (153.9 ± 1.16 vs $139.2 \pm 1.23 \mu\text{m}$, Figure 5-1A) and also wider by 17% (35.3 ± 0.43 vs $30.3 \pm 0.43 \mu\text{m}$, Figure 5-1B). This resulted in a 29% increase in cell area (Figure 5-1C). We also assessed differences in size between BZ cells and those remote from the infarct. Length was significantly shorter in the BZ by 6% compared with remote cells (148.1 ± 1.92 vs $157.4 \pm 1.66 \mu\text{m}$, Figure 5-1D), but there was no significant difference in width or area Figure 5-1E-F.

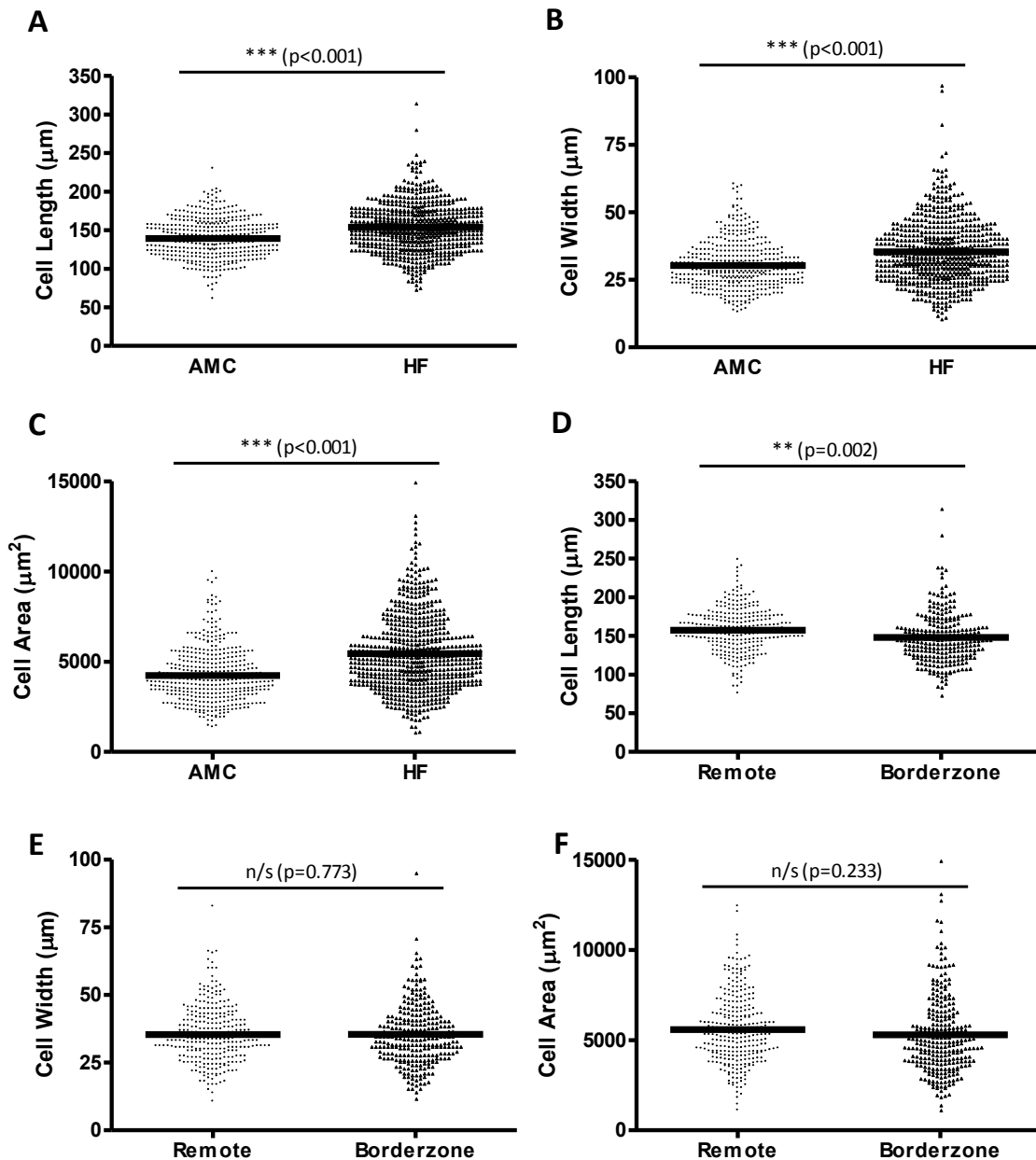


Figure 5-1. Cells are longer and wider in HF. The subset of HF cells from the borderzone are shorter than cells from remote regions.

(A) Cells are longer in HF compared with AMC. HF cells are also wider (B) and exhibit a greater area (C). (D) Within HF cells, those that are within the borderzone are shorter than cells remote from the infarct whereas (E) their width and (F) area are similar. $n=425$ cells from 10 isolations (AMC) and 680 cells from 10 isolations (HF). Of the HF cells 275 were isolated from borderzone and 405 from remote regions.

5.4.2 Ca²⁺ transient morphology and synchronicity under basal conditions

Ca²⁺ transients were recorded via confocal line scanning in cells contracting at 0.5Hz at 37°C in normal Tyrode (NT) containing 2mM Ca²⁺. We assessed the peak amplitude, time to peak (TtP), tau (time constant of transient decay) and time to 90% decay (TD90). No significant differences were

found between AMC and HF cells in these parameters (Figure 5-2). Further assessment showed that there was also no difference in baseline fluorescence in HF cells (HF 7.37 ± 0.59 fluorescence units vs AMC 7.00 ± 0.68 , $p=0.684$).

Since previous studies have shown enhanced dyssynchrony in HF we also assessed several types of dyssynchrony across the myocyte in HF cells and compared with AMC. We found no significant differences in any measure of dyssynchrony in HF (Figure 5-3).

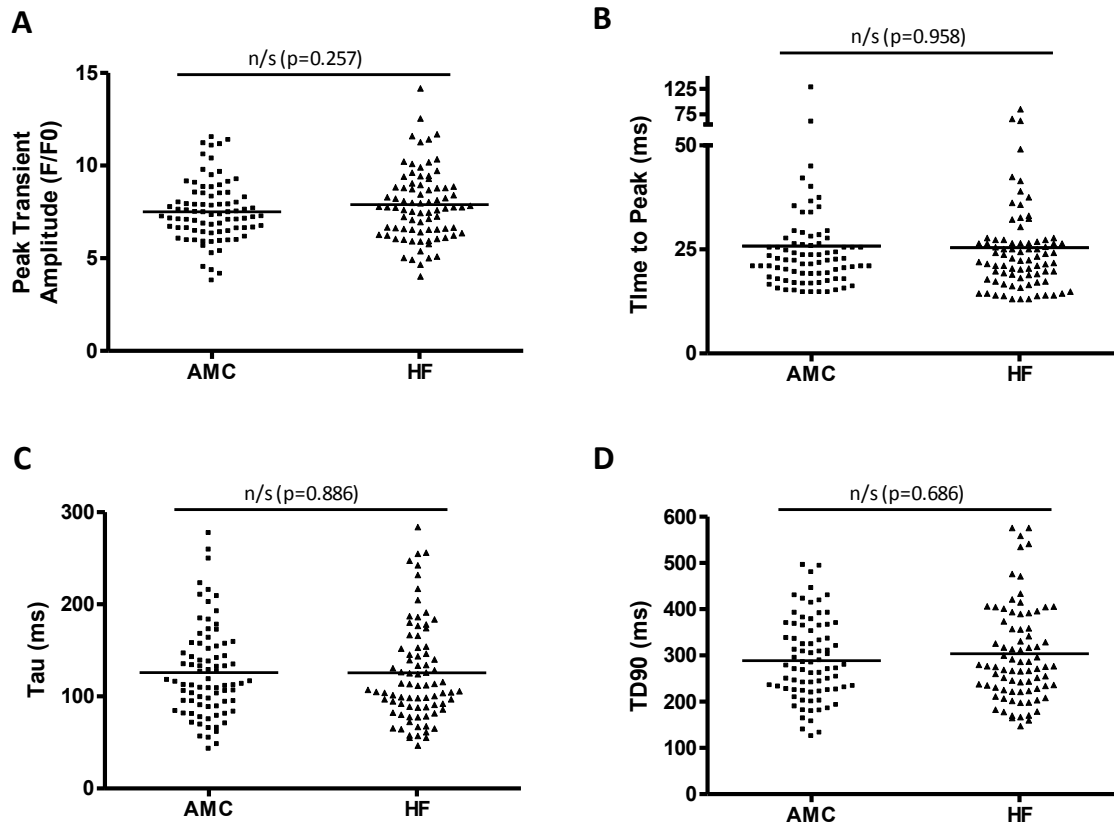


Figure 5-2. Transient morphology is not altered in HF.

(A) Peak amplitude, (B) Time to peak, (C) Tau, (D) and time to 90% decay (TD90) are all unchanged in HF when compared with AMC. $n=83$ cells from 12 isolations (AMC) and 80 cells from 16 isolations (HF).

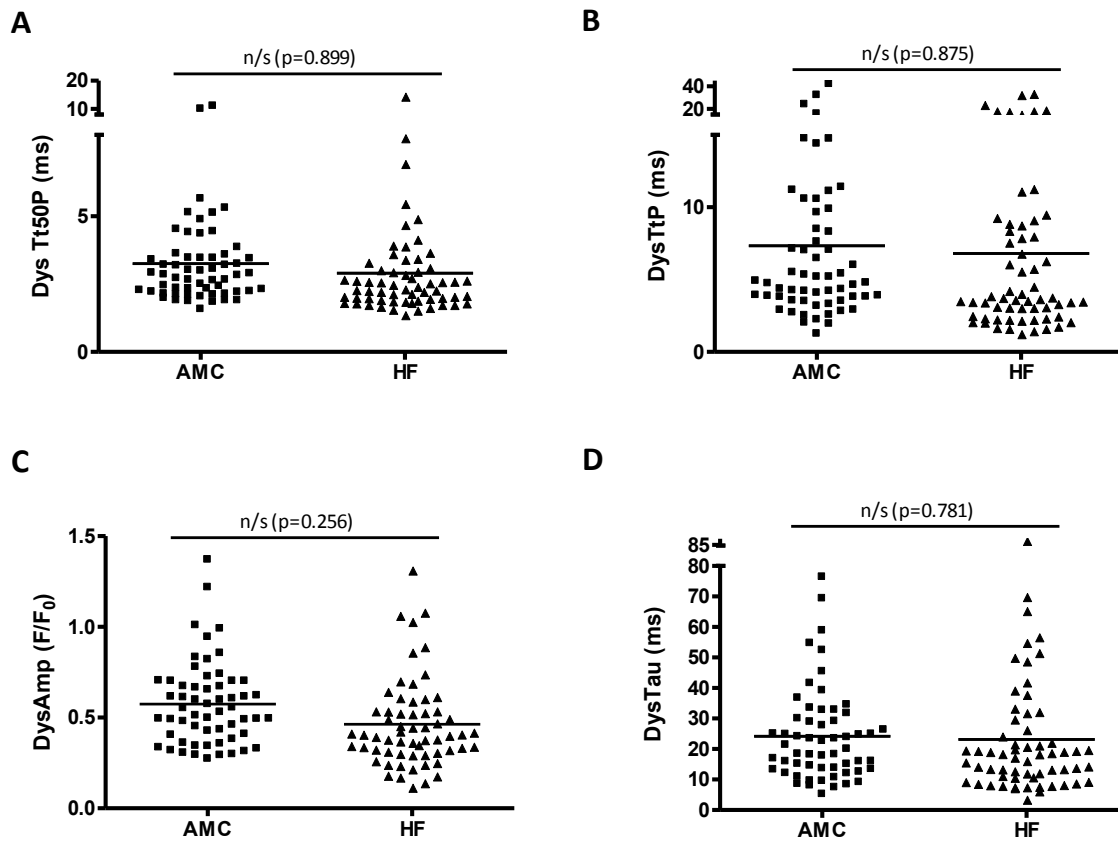


Figure 5-3. Transient dyssynchrony does not change significantly in HF.

Transient dyssynchrony was also assessed in AMC and HF cells. There was no significant change in (A) dyssynchrony of time to 50% peak (DysTt50P), (B) dyssynchrony of time to peak (DysTtP), (C) dyssynchrony of peak amplitude (DysAmp) or (D) dyssynchrony of transient decay (DysTau) between AMC and HF cells. n=58 cells from 7 isolations (AMC) and 59 cells from 12 isolations (HF).

5.4.3 Ca²⁺ Transient morphology and synchronicity under β -adrenergic stimulation

In order to assess the effect of a more physiological milieu on HF myocytes we assessed Ca²⁺ transients under conditions of β -adrenergic stimulation using NT with 30nM isoprenaline added. A hierarchical model was used for analysis on paired data in cells pre-and post-isoprenaline with the inclusion of an “interaction-term”. This is a term within the model that can identify whether the response to isoprenaline is significantly different between AMC and HF and provides a p-value to assess whether differences observed in the responses could be expected by chance. In terms of transient morphology we found that isoprenaline significantly enhances amplitude by 53.6% in AMC cells and 44.8% in HF cells (p<0.001 in both) with no significant difference in the response as assessed by the interaction term (p=0.760, Figure 5-4A). There was no difference in the time-to-peak in either group (Figure 5-4B). As expected there was a significant enhancement in rate of decay of Ca²⁺ transient, both in terms of shorter tau and TD90, in the presence of isoprenaline (Figure 5-4C-D). However, as with amplitude there was no significant difference in response when HF cells were compared with AMC.

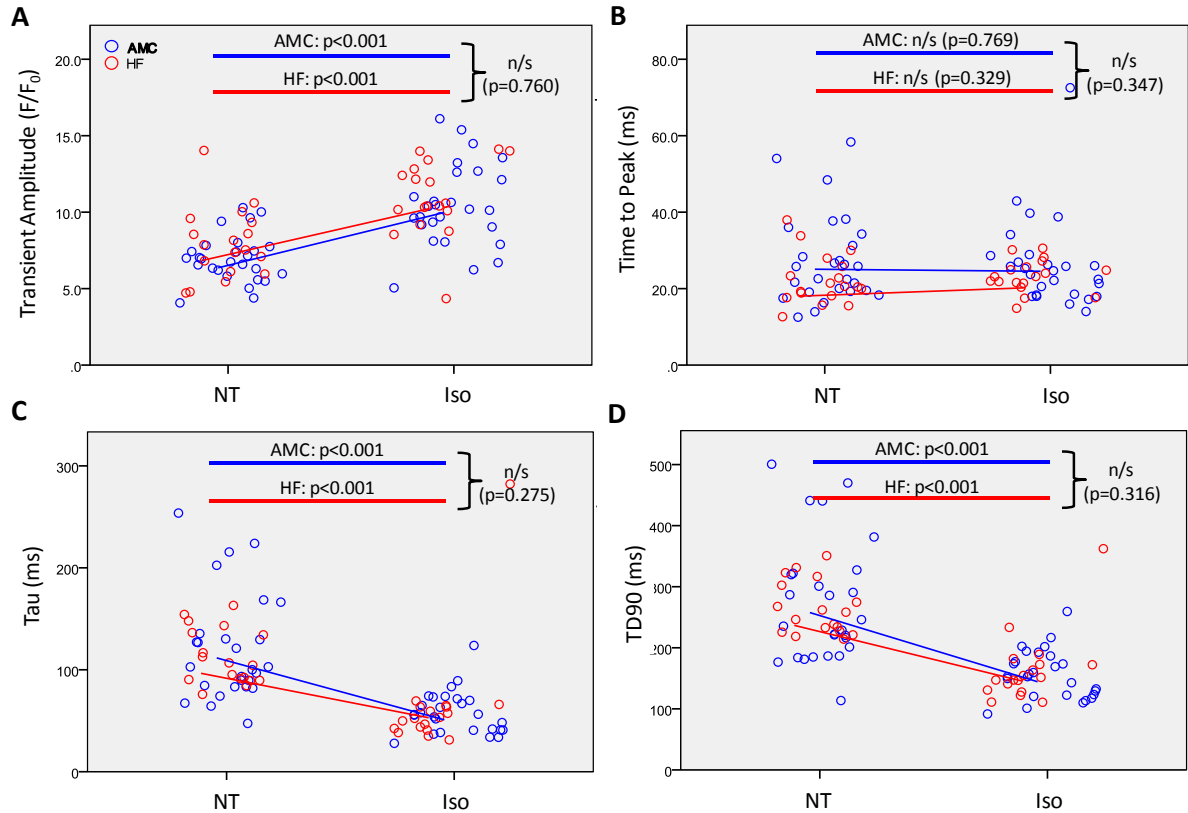


Figure 5-4. Effects of 30nM isoprenaline on Ca^{2+} transient characteristics in AMC and HF cells. (A) Isoprenaline causes a significant enhancement in Ca^{2+} transient amplitude in both AMC and HF cells, although the response is not statistically different in HF cells compared with AMC ($p = 0.760$). (B) There was no significant change in time to peak in the presence of isoprenaline in AMC or HF cells. (C) Decay times in terms of Tau and (D) Time to 90% decay (TD90) were both significantly reduced by isoprenaline but there was no difference in the response in HF cells compared with AMC. $n = 36$ cells from 5 isolations (AMC) and 54 cells from 5 isolations (HF), all cells had transients assessed both with and without isoprenaline.

We also assessed transient dyssynchrony under the same conditions and found isoprenaline alters dyssynchrony on a number of levels (see section 2.5.6.2, and Figure 5-5 legend for further detail and definitions). Firstly in terms of the rise phase of the Ca^{2+} transient, both DysTt50P and DysTtP were significantly reduced by isoprenaline but only in AMC cells (Figure 5-5A-B). However, in both cases the interaction term did not quite reach significance ($p = 0.06$ in the case of DysTtP). Secondly DysAmp was increased by isoprenaline in both AMC and HF to similar degrees (Figure 5-5C). Finally DysTau was reduced by isoprenaline, again to a similar extent in both AMC and HF (Figure 5-5D).

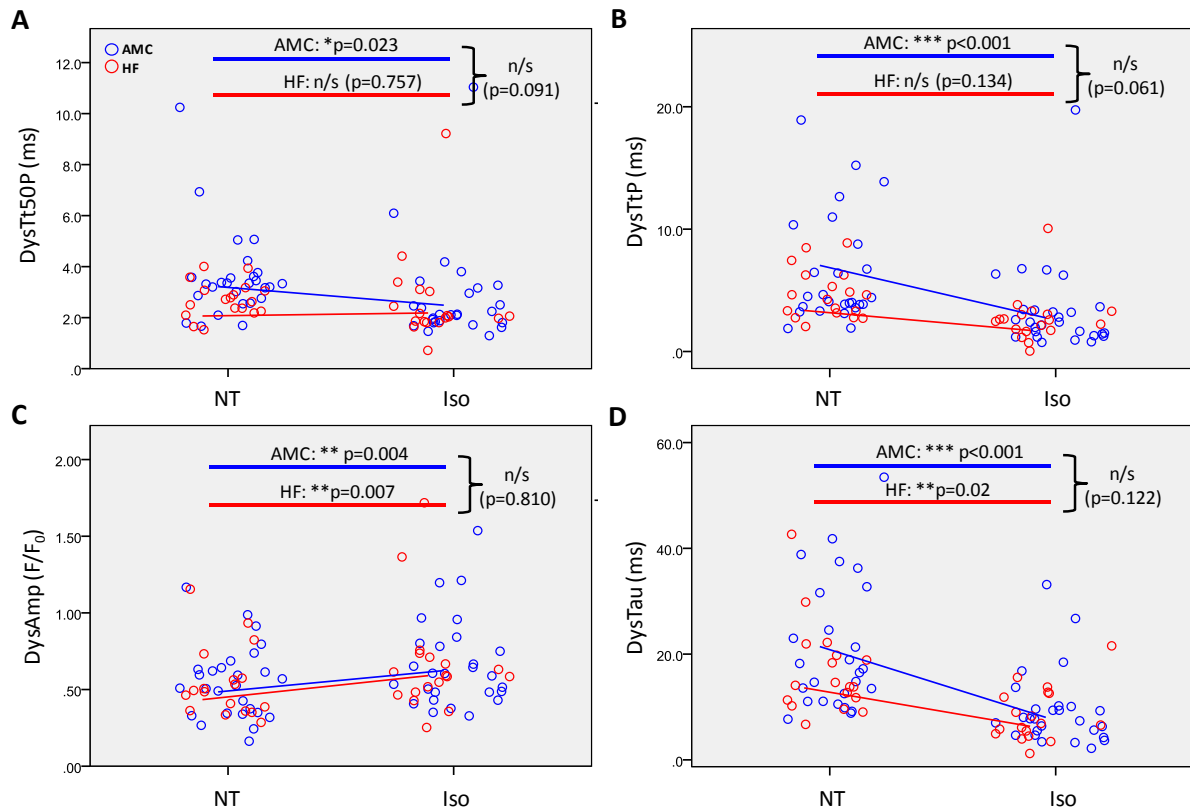


Figure 5-5. Dyssynchrony of Ca²⁺ transients +/- isoprenaline in HF vs AMC myocytes.

(A) Dyssynchrony of time to 50% peak (DysTt50P) is significantly reduced in AMC cells in the presence of isoprenaline but there is no significant difference in DysTt50P in HF cells pre and post Iso. However the statistical model suggests that the difference between these relationships is non-significant ($p=0.091$). (B) There is a similar pattern in the dyssynchrony of time to peak (DysTtP) with the difference between HF and AMC cells approaching significance ($p=0.061$). (C) Dyssynchrony of transient amplitude (DysAmp) is enhanced by isoprenaline in both AMC and HF cells. (D) Dyssynchrony of transient decay (DysTau) is reduced in both AMC and HF cells. $n=36$ cells from 5 isolations (AMC) and 54 cells from 5 isolations (HF), all cells had transients assessed both with and without isoprenaline.

5.4.4 Ca²⁺ transient morphology and synchronicity in the borderzone

The borderzone (BZ) in this study refers to a macroscopically identified peri-infarct region adjacent to scarred myocardium from which cells were isolated separately (see section 2.4). Since there was no significant difference between Ca²⁺ transient morphology in HF compared with AMC we wished to assess whether any changes were regional and hypothesized that any dysfunction might be evident if BZ cells were compared with remote cells. No significant differences were found in Ca²⁺ transient amplitude, time to peak or decay parameters between BZ and remote regions (Figure 5-6). With a similar rationale we studied BZ cells for dyssynchrony and again found no significant difference between these cells and cells remote from the infarct (Figure 5-7).

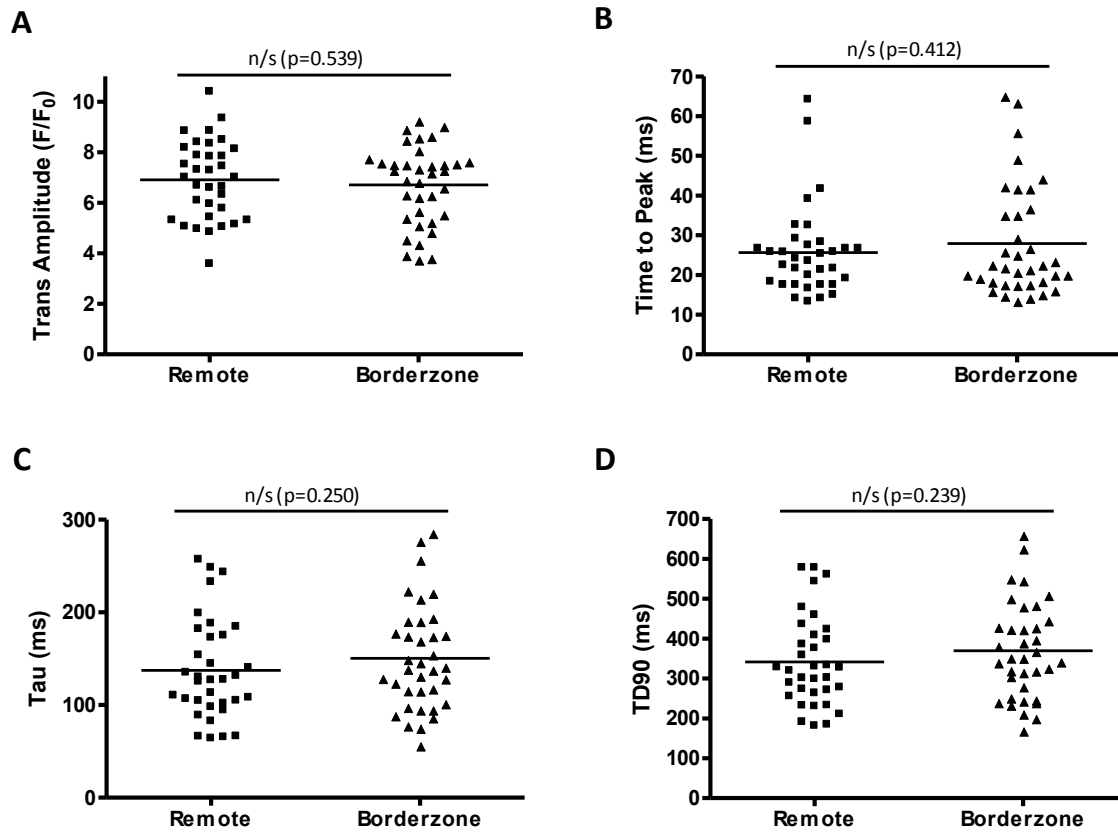


Figure 5-6. Analysis of transients of cells from the borderzone versus remote areas.

Ca^{2+} transient amplitude and morphology were assessed from borderzone regions and regions remote from the border. There was no difference in (A) amplitude, (B) time to peak, (C) decay rate in terms of tau and (D) time to 90% decay (TD90). $n=34$ cells from remote zone of 7 isolations and 36 cells from borderzone of same 7 isolations.

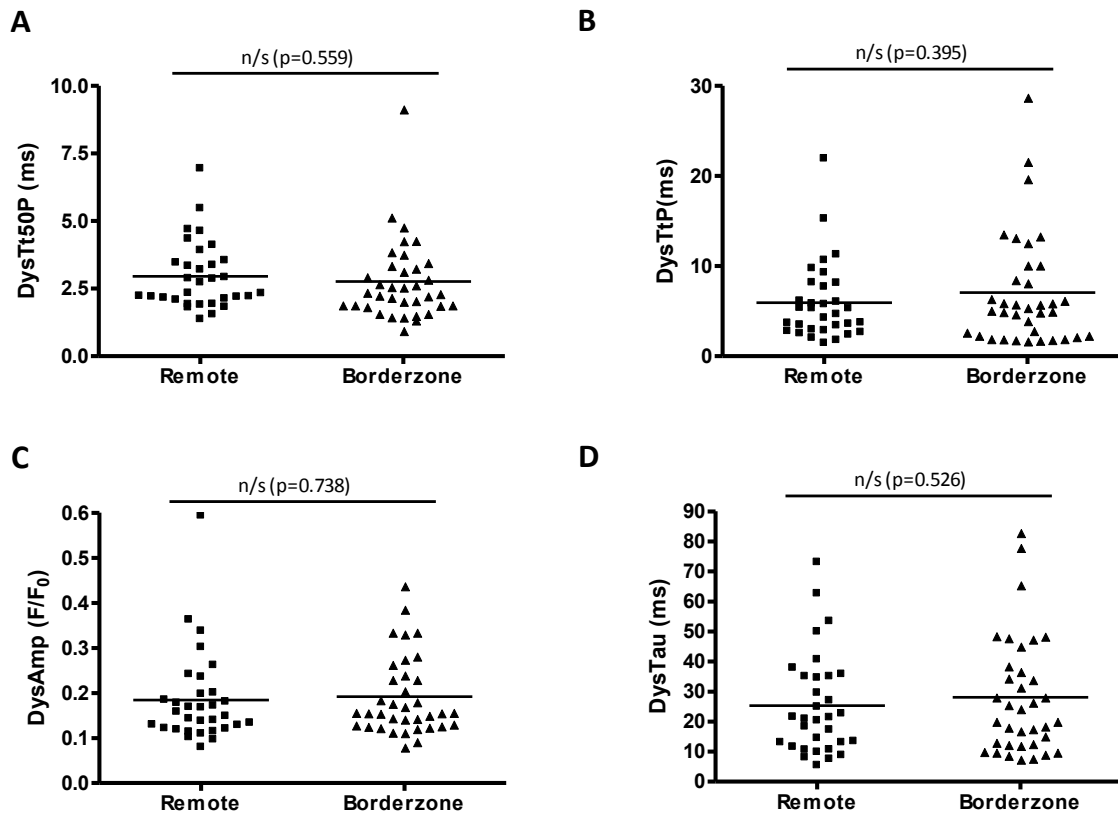


Figure 5-7. Analysis of transient dyssynchrony in cells isolated from borderzone versus remote regions.

There was no significant difference between transient dyssynchrony between remote regions and borderzone in terms of (A) dyssynchrony of time to 50% peak (DysTt50P), (B) dyssynchrony of time to peak (DysTtP), (C) dyssynchrony of amplitude (DysAmp) and (D) dyssynchrony of transient decay (DysTau). n=32 remote cells from 7 isolations and 36 borderzone cells from same 7 isolations.

5.4.5 Ca²⁺ spark frequency and morphology under basal conditions, β -adrenergic stimulation and in the borderzone

Spontaneous Ca²⁺ sparks are thought to be important in cardiac arrhythmogenesis and were assessed in order to ascertain the role they play in enhanced arrhythmogenesis in our HF model. Sparks were first assessed under basal conditions in NT containing 2mM Ca²⁺ at 37°C (see section 2.5.4 for further detail). Hierarchical statistical methods were used to analyse the data, with a 2-level model for cell-level data such as spark frequency and spark-mediated SR leak and 3 level models for data at the level of the individual spark (i.e. the morphological parameters: Amplitude, FWHM, FDHM and Mass). Because morphological data was skewed, log-transformations were used which resulted in approximately Gaussian distributions in a similar manner to before (see section 3.3.2.2). We found that none of the spark parameters assessed differed significantly between AMC and HF cells under basal conditions (Figure 5-8).

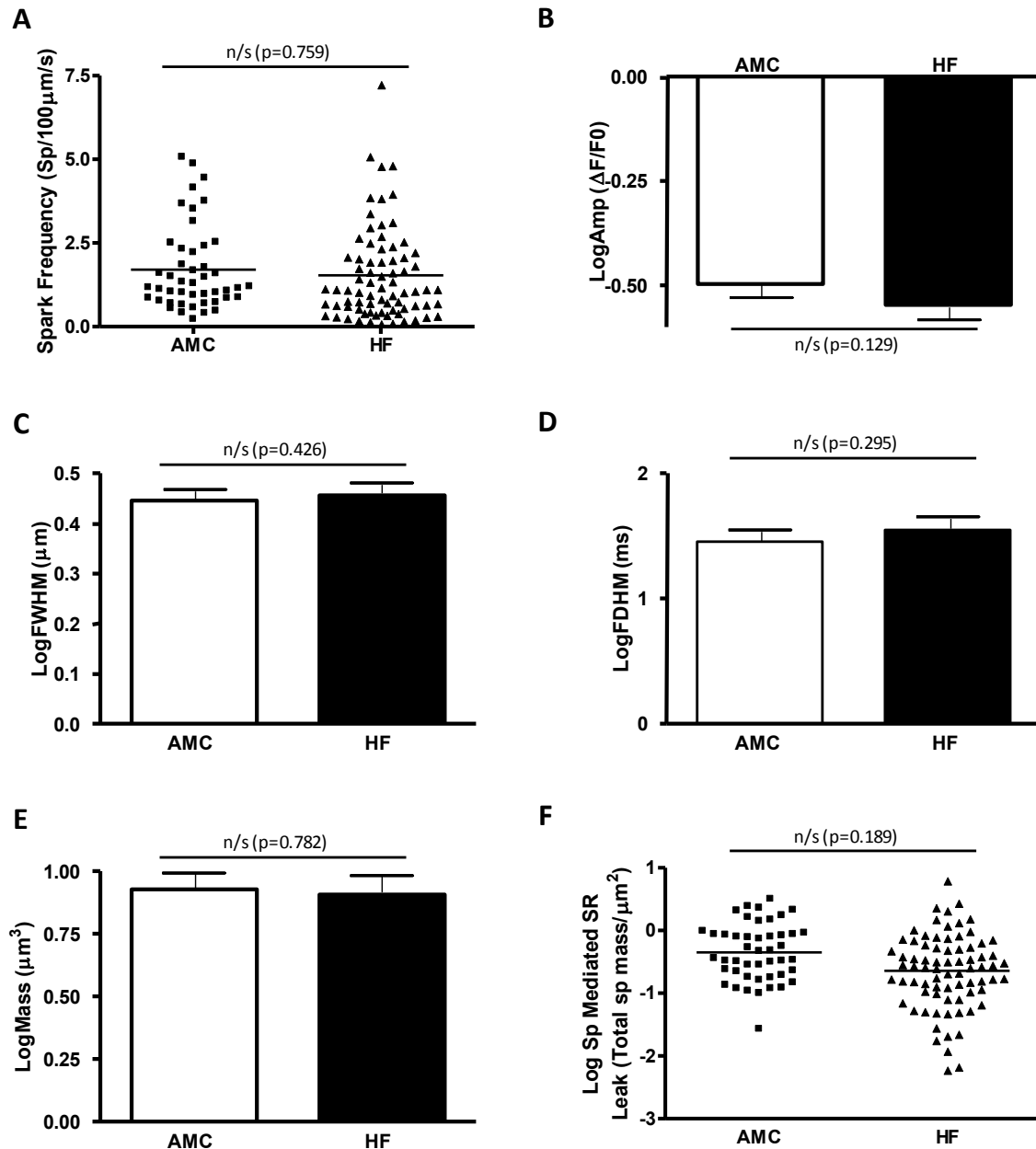


Figure 5-8. Spark frequency and morphology are not altered in HF

(A) Spark frequency in HF is not significantly different to AMC. Measures of morphology including (B) LogAmp, (C) LogFWHM, (D) LogFDHM and (E) LogMass are also unchanged. (F) The summary measure spark mediated SR leak is also unaltered. $n=550$ sparks from 46 cells from 6 isolations (AMC) and 1047 sparks from 76 cells from 20 isolations (HF).

We went on to assess the same spark parameters under conditions of β -adrenergic stimulation using 30nM isoprenaline. We aggregated morphological data to a cellular level by using mean values for amplitude, FWHM, FDHM and mass. This enabled us to look at paired spark data pre- and post-isoprenaline. Spark frequency was not enhanced by this concentration of isoprenaline (Figure 5-9A). Spark amplitude was significantly increased by isoprenaline in HF cells ($p=0.020$), although the difference was non-significant in AMC cells ($p=0.068$). However both the non-significant interaction

term ($p=0.831$) and inspection of the graph (Figure 5-9B) suggest that the difference between response in HF and AMC for this parameter is minimal. In the case of FWHM there is a significant difference between the response to β -adrenergic stimulation in AMC and HF. In AMC cells, isoprenaline does not change FWHM significantly ($2.83 \pm 0.081 \mu\text{m}$ with isoprenaline vs $2.94 \pm 0.124 \mu\text{m}$ without isoprenaline, $p=0.444$), whereas in HF there is a significant 13% increase in FWHM ($3.22 \pm 0.121 \mu\text{m}$ with isoprenaline vs $2.85 \pm 0.063 \mu\text{m}$ without isoprenaline, $p=0.006$). This difference in the response to isoprenaline is statistically significant ($p=0.017$, Figure 5-9C). FDHM was not significantly changed by isoprenaline (Figure 5-9D). Spark mass shows a similar relationship as FWHM (Figure 5-9E) and this is likely driven by the FWHM^3 term included in the equation used to calculate mass (Hollingworth *et al.*, 2001). Spark-mediated SR leak is increased significantly in HF ($p=0.011$), but not in AMC cells ($p=0.558$) although the p -value of the interaction term does not reach significance ($p=0.187$) suggesting this difference could be down to chance (Figure 5-9F).

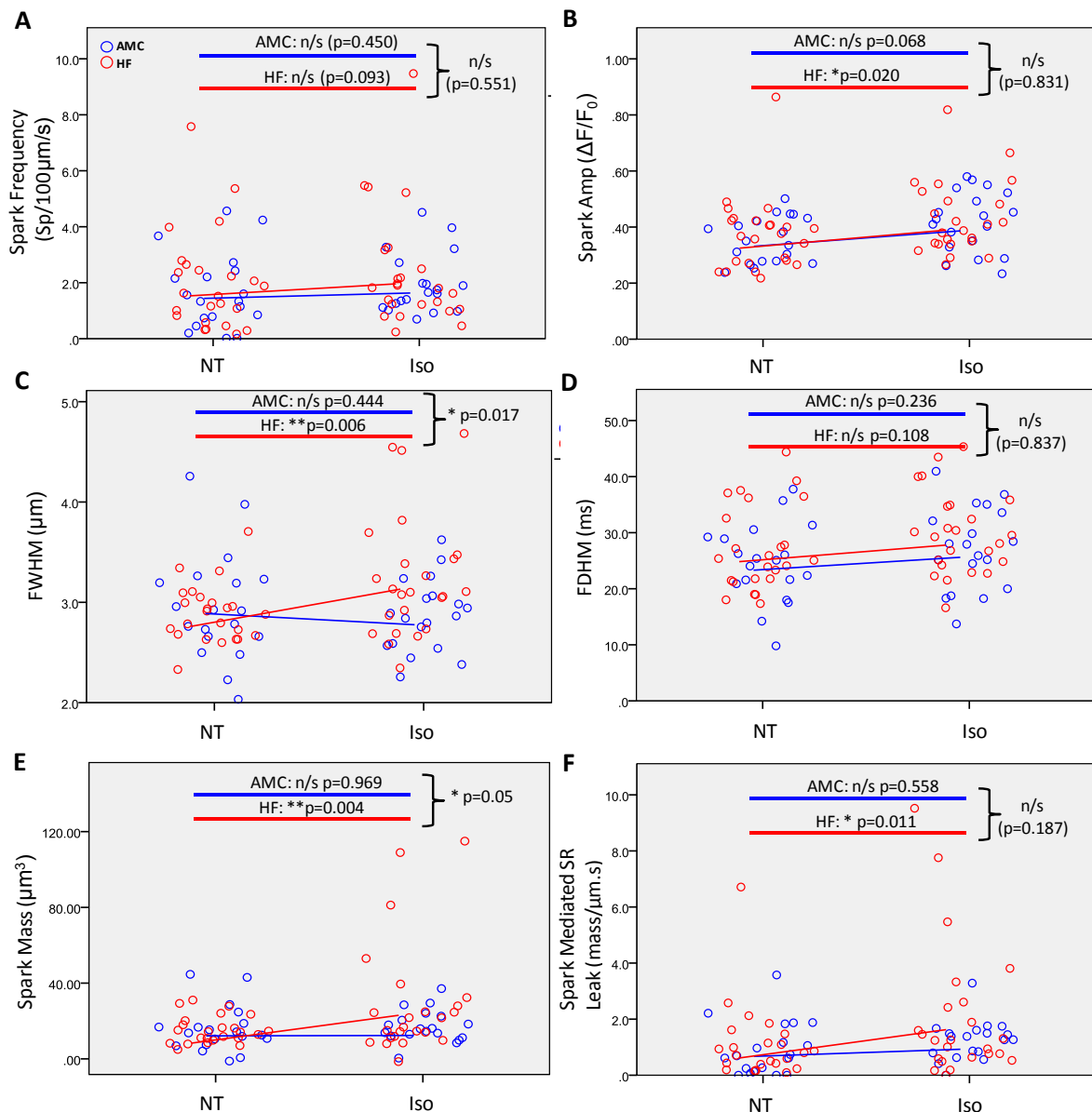


Figure 5-9. Spark FWHM and mass are enhanced by isoprenaline in HF but not AMC cells.

(A) 30nM isoprenaline does not cause a significant increase in spark frequency. (B) There is an increase in spark amplitude in HF cells caused by isoprenaline and a borderline significant increase in AMC cells with no significant difference between the relationships. (C) There is a more marked difference in the effects on FWHM with a significant increase in FWHM only in HF cells and a significant interaction between the effects of HF and isoprenaline proving a significant difference between the relationships. (D) Isoprenaline does not significantly alter FDHM. (E) Similar to FWHM, spark mass is also preferentially enhanced by isoprenaline in HF. (F) Overall spark mediated SR leak is only significantly increased by isoprenaline in HF although the difference between the relationship in HF and AMC does not reach significance. $n=510$ sparks from 19 cells (paired +/- isoprenaline) from 5 isolations (AMC) and 704 sparks from 24 cells (paired +/- isoprenaline) from 6 isolations (HF). Each point on the graph shows the mean of data in a single cell.

Sparks in cells isolated from the BZ were also assessed. No significant differences between BZ sparks and sparks from remote cells were found (Figure 5-10).

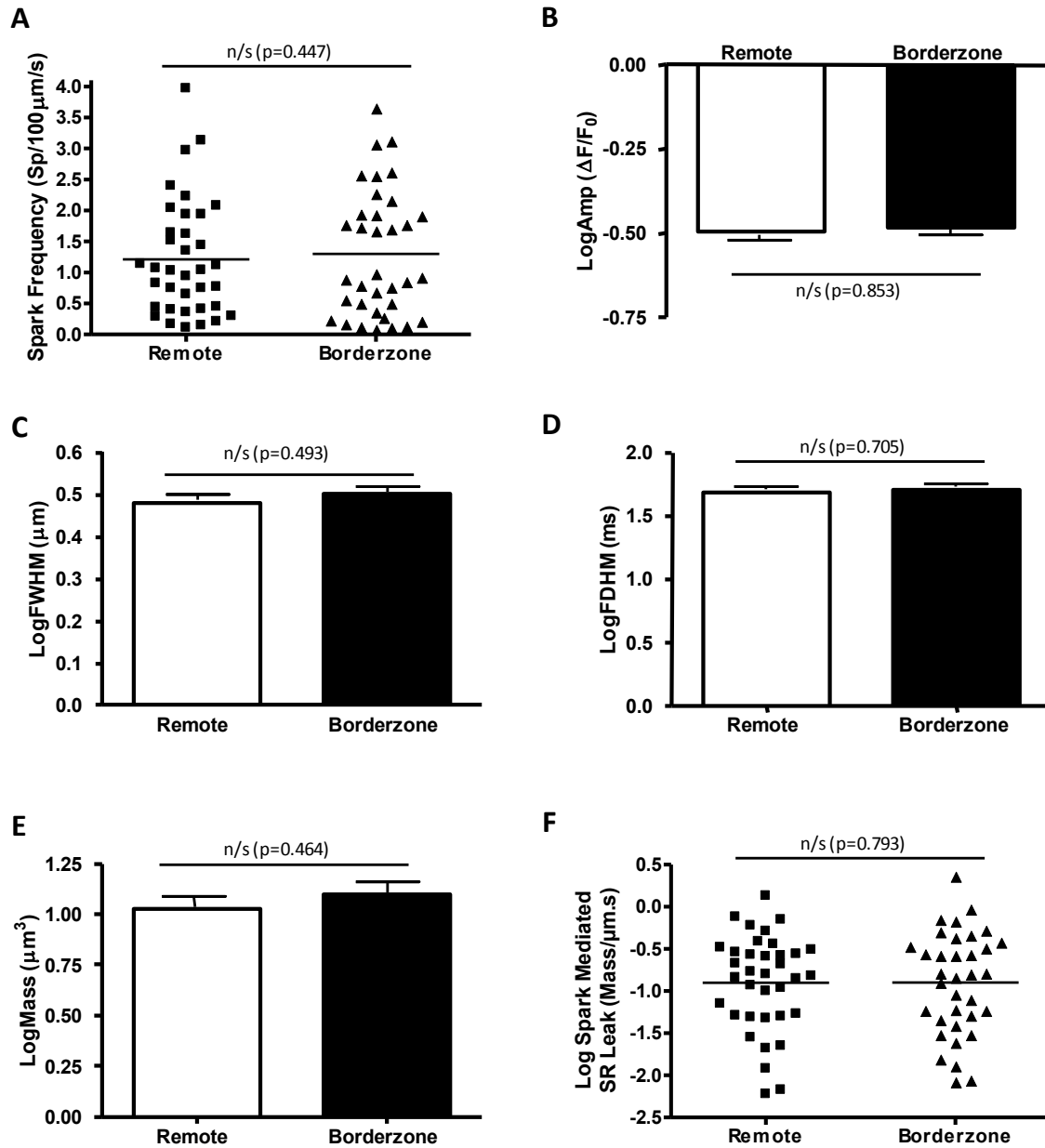


Figure 5-10. Spark Morphology is unchanged in borderzone regions

(A) Spark frequency is unchanged in borderzone vs remote regions. Morphological parameters including (B) LogAmp, (C) LogFWHM, (D) LogFDHM and (E) LogMass are also unchanged. The overall spark mediated SR leak is also no different in borderzone versus remote cells. $n=592$ sparks from 36 cells from 8 isolations (Remote) and 628 sparks from 35 cells from same 8 isolations (Borderzone).

5.4.6 Wave Characteristics and Frequency

Ca²⁺ waves were assessed as outlined in section 2.5.4 whereby an accelerated pacing rate of 5Hz preceded a 30s interval during which imaging was performed via confocal microscopy. We assessed wave velocity, wave free survival (i.e. time to first wave analysed via logrank test), wave amplitude

and wave frequency. For further information on how these parameters were calculated see section 2.5.6.3. None of the wave characteristics assessed differed between AMC and HF (Figure 5-11). We further assessed potential differences between BZ cells and remote cells in HF. We found that wave velocity was unchanged between the locations (Figure 5-12A). Wave-free survival was significantly longer in BZ cells than remote cells when analysed via survival analysis using the logrank test (Figure 5-12C). This analysis is non-hierarchical due to technical difficulty of survival analysis in hierarchical data-sets. However the analysis was re-done using hierarchical techniques by analyzing time-to first wave via a mixed model. This again showed a significant difference ($p=0.032$). Wave amplitude and overall wave frequency over the 30s period of detection were unchanged in BZ cells (Figure 5-12C-D).

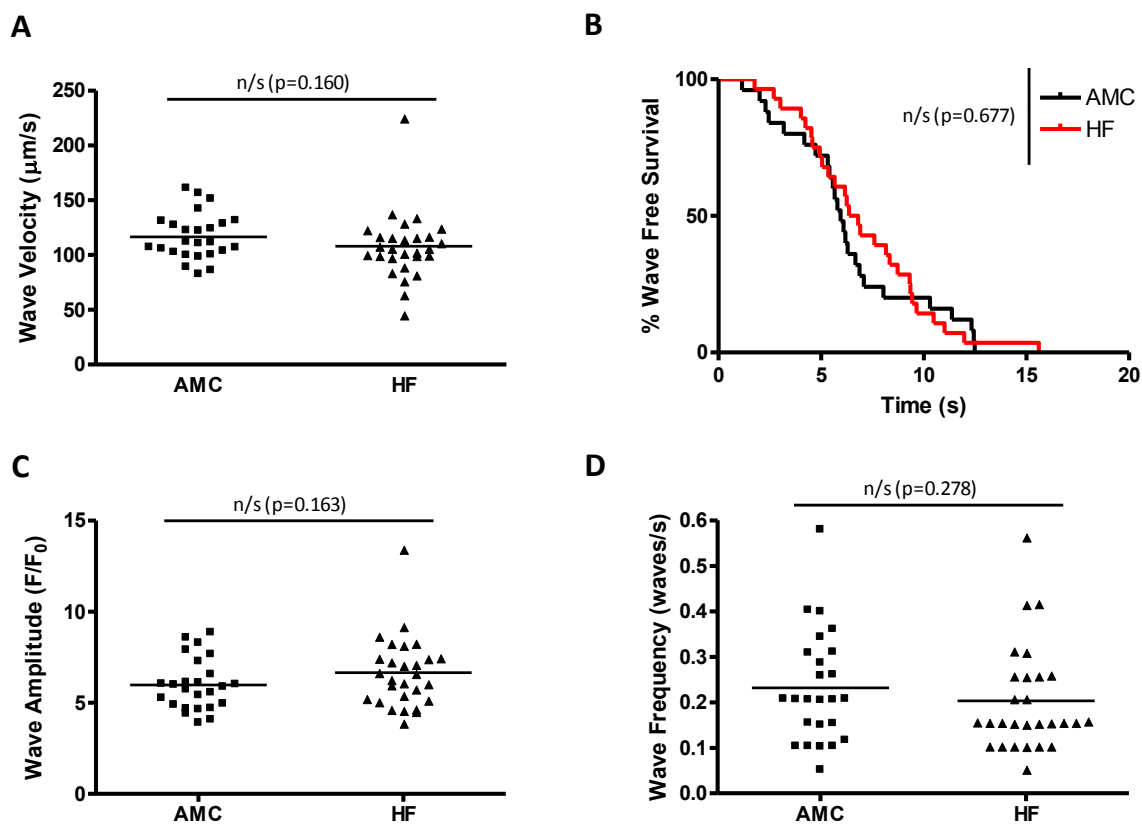


Figure 5-11. Waves exhibit similar characteristics and frequency in AMC vs HF.

(A) Wave velocity is unchanged in HF vs AMC. (B) The difference in wave-free survival is non-significant by Cox regression model. (C) Wave amplitude is unchanged in HF vs AMC. (D) Overall wave frequency is also unchanged. $n=25$ cells from 6 isolations (AMC) and 28 cells from 6 isolations (HF).

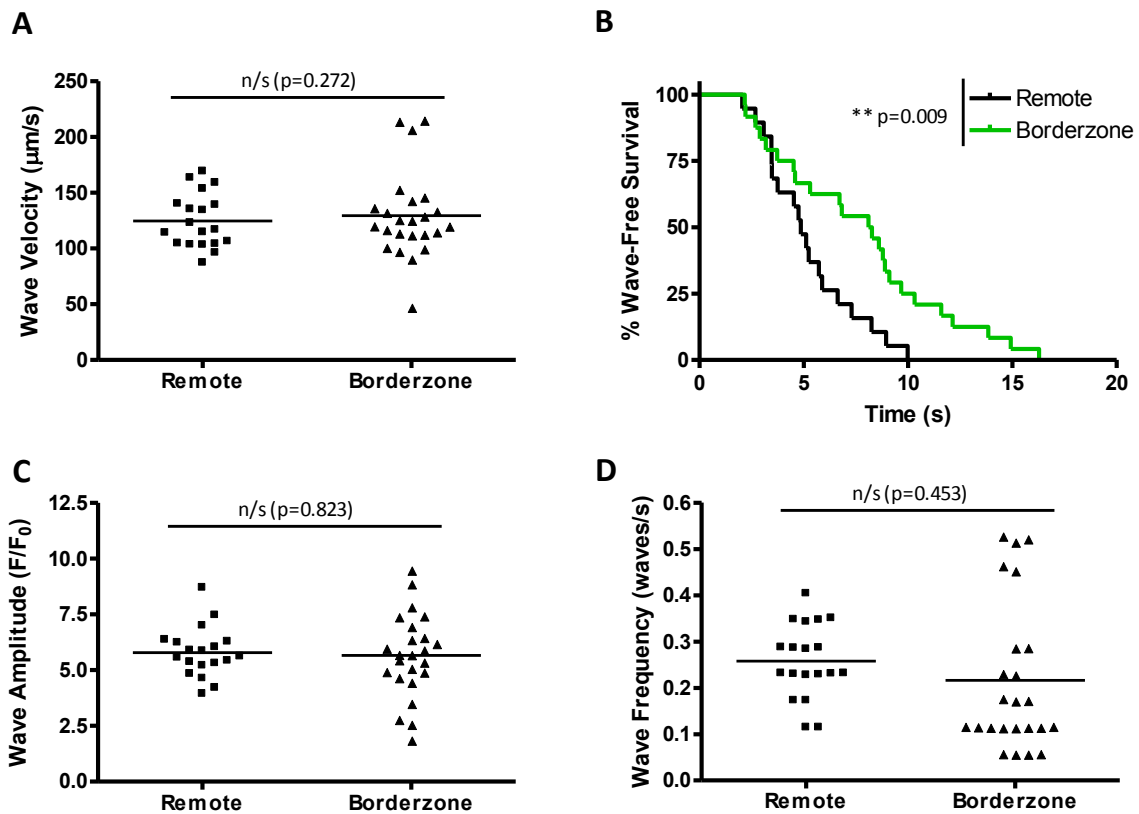


Figure 5-12. Wave free survival is prolonged in borderzone cells.

(A) Wave velocity is unchanged in borderzone versus remote cells. (B) Wave free survival analysis shows an increased time to 1st wave in borderzone cells. (C) Wave amplitude and (D) Overall wave frequency are unchanged in borderzone cells. n=19 cells from 6 isolations (remote) and 24 cells from same 6 isolations (borderzone).

5.4.7 SR Ca²⁺ Content

SR Ca²⁺ content was assessed by the amplitude of caffeine-induced Ca²⁺ transients as detailed in section 2.5.4 under basal conditions. In keeping with the absence of any difference in spark or transient amplitude under these conditions there was no difference in the SR Ca²⁺ content between AMC and HF (Figure 5-13A). Furthermore we assessed the decay rate of the caffeine-induced transient which is a measure of NCX function. Again there was no difference (Figure 5-13B). Similarly BZ SR Ca²⁺ content and NCX function were no different compared with that of remote regions (Figure 5-13C-D).

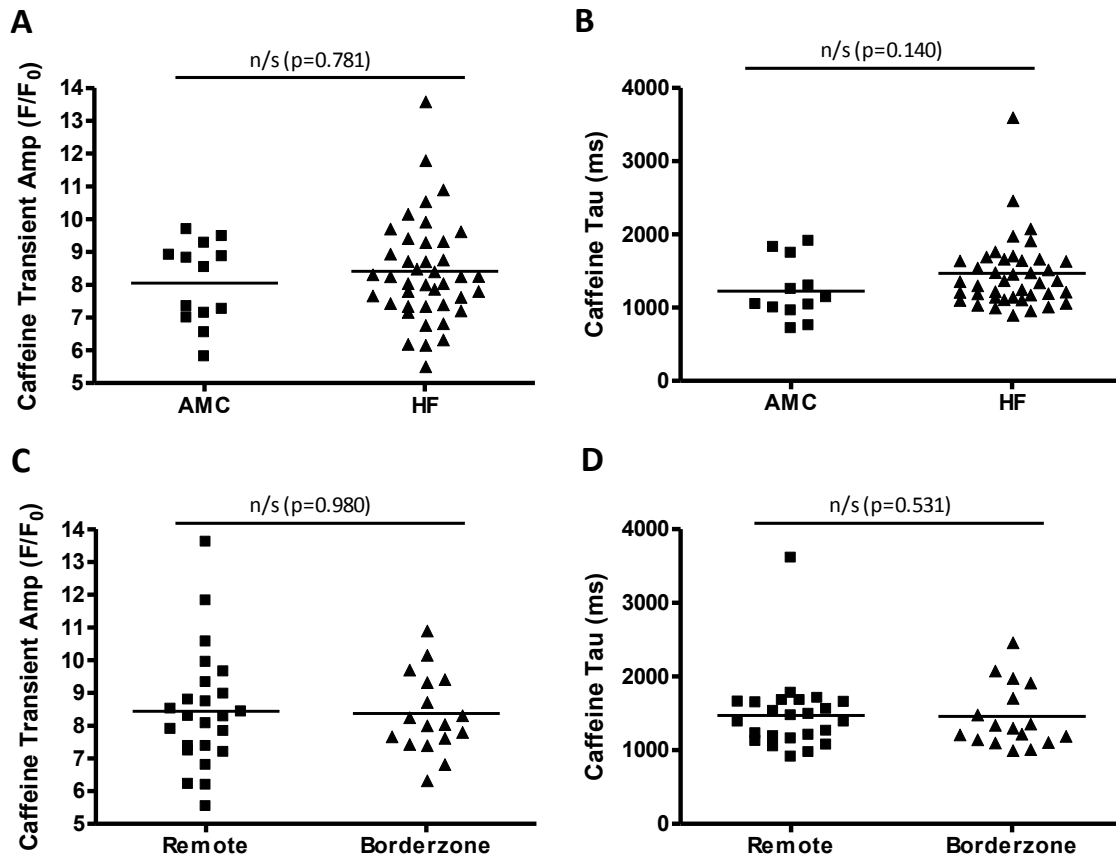


Figure 5-13. SR load and caffeine transient decay rate does not change in HF. There is no significant difference between these parameters in the borderzone versus remote regions within HF cells. (A) Caffeine transient amplitudes are not statistically different between AMC and HF. (B) Caffeine transient decay rate (tau), which is representative predominantly of NCX function, does not differ significantly between AMC and HF cells. Within HF cells these were subclassified as remote versus borderzone cells. There was no difference between these categories in terms of (C) caffeine transient amplitude and (D) caffeine transient decay rate (tau). n=13 cells from 8 isolations (AMC), 41 cells from 8 isolations (HF) of which 13 cells from 5 isolations are remote and 28 cells from 4 isolations are BZ.

5.5 Discussion

5.5.1 Cardiomyocyte hypertrophy

The aims of this chapter were to assess how SR Ca²⁺ release, particularly in terms of electrically evoked Ca²⁺ transients and spontaneous Ca²⁺ sparks differs between cells isolated from rats with HF versus AMC. Of vital importance was to ensure HF animals had typical features of HF and this was primarily performed via assessing data such as biometry, echocardiography and PV loops as detailed in chapter 4. As expected we showed an increased cardiac mass with evidence of pulmonary oedema. Furthermore we found an increase in body mass relative to TL³ which may represent peripheral fluid overload or alternatively an increase in adiposity. In addition there was systolic and diastolic dysfunction with a dilated left ventricle. Another typical feature of HF is an increase in cell

size of isolated cardiomyocytes as shown by Capasso and Anversa in the same model at an early stage post myocardial infarction (Capasso & Anversa, 1992). They showed a 36% increase in surface area, whereas we showed a comparable 29% increase in area. Studies in humans have been variable in terms of size changes in myocytes. One study of humans with ischaemic cardiomyopathy showed a significant increase in cell length, but cell width was not significantly different to control donor hearts (Gerdes *et al.*, 1992). Another study showed an increase in both length and width in a mixed sample of patients with both ischaemic and non-ischaemic heart failure resulting in a 77% increase in area (Zafeiridis *et al.*, 1998). Changes in cell length are primarily responsible for changes in chamber circumference and changes in width result in changes in wall thickness (Gerdes, 2002). Our findings suggest that both types of cellular remodeling occurred in this model.

5.5.2 Ca²⁺ transient morphology and dyssynchrony

As has been explored in chapter 3 and Table 3-1, previous findings with respect to Ca²⁺ transient amplitude and morphology in the post-MI rat model of HF are quite variable. Most studies have been at the 6-9 week stages with few studies as late as our 16W model which we have shown to exhibit decompensated HF. Of the studies performed at 16W that assessed Ca²⁺ transients, two were from our own group using Fluo-4 as the fluorophore (Lyon *et al.*, 2009, 2011) and showed an increased time-to-peak and slower decay rates (longer TD50 and TD90). Other studies at around this stage include that of Loennechen *et al.* who isolated cells from hearts at 1, 4 and 13W post-MI (Loennechen *et al.*, 2002). They used Fura-2 which enabled them to assess both systolic and diastolic Ca²⁺ as well as the difference between them (amplitude). They found a progressive increase in both systolic and diastolic [Ca²⁺] with the systolic [Ca²⁺] increasing to a greater extent than diastolic leading to an increase in amplitude which was most marked at 13W post-MI. Finally a study of 18W post MI rats using indo-1 as the fluorophore showed a reduction in transient amplitude and prolongation of transient decay (Ait Mou *et al.*, 2011). There are clearly experimental differences in these studies such as the use of fluorophore as well as possible differences in efficacy of ligation and infarct size (which were not reported in all studies). The use of standard, rather than hierarchical statistical techniques, may also have influenced the outcomes (see chapter 3). In the current study we found no significant differences between AMC and HF in terms of transient amplitude, time to peak, or decay rate (Figure 5-2). This is in contrast to the data in the current study at 8W post MI (Figure 3-3) where transient amplitude was noted to be higher in the post-MI group. Any comparison between experiments should be made with caution since Fura-2 was used in the 8WMI cell data whereas Fluo-4 was used in the data here. However the initial enhancement of Ca²⁺ transient amplitude may bear some relationship to the better compensated physiological data we observed at earlier stages post-MI (see chapter 4).

There have been several publications recently that have assessed not only the morphology of the Ca²⁺ transient as a whole but also the synchronicity of constituent elements of the transient. Many of these are summarised in a recent review (Heinzel *et al.*, 2008). Litwin *et al.* were the first to observe dyssynchrony of the Ca²⁺ transient, as observed by confocal line-scanning in a post-MI rabbit model of HF (Litwin *et al.*, 2000), and since then cardiomyocytes isolated from various models (including the rat post-MI model) and humans hearts with HF have been shown to exhibit dyssynchronous transients (Louch *et al.*, 2004, 2006; Heinzel *et al.*, 2008; Lyon *et al.*, 2009; Ibrahim *et al.*, 2012). These studies have predominantly assessed the dyssynchrony of the rise time of the Ca²⁺ transient across the cell. A recent study by Hohedanner *et al.* has extended the concept of

dyssynchrony and observed irregularities in the rate of Ca^{2+} transient decay in human cells with HF as well as in animal models (TAC model in mouse and ischaemic cardiomyopathy in pigs). We looked for changes in various forms of dyssynchrony in the current model including dyssynchrony of rise time, amplitude and decay rate (see section 2.5.6.2 for further detail). We found no change in any form of dyssynchrony in HF. Figure 5-3 shows that there were several dyssynchronous HF cells but similar numbers of dyssynchronous AMC cells. It is unclear why our data differ from previous assessments in HF. Certainly there are no reports of synchronous Ca^{2+} transients in HF, although such negative findings are less likely to be reported by investigators and published by journals due to negative publication bias (Dirnagl, 2006). Alternative explanations include differences in the degree of cellular heart failure in the current model which may be less marked in the isolated cell despite the findings of heart failure at the organ level (see chapter 4). In addition there are many determinants of Ca^{2+} transient dyssynchrony at the ultrastructural and molecular level such as reduced t-tubule density, orphaning of RyRs, open probability of dihydropyridine receptors (DHPRs) and RyRs and dyadic space remodelling (Heinzel *et al.*, 2011). Although we have evidence of a reduction in t-tubule density using the cells isolated in this study (J Gorelik, unpublished communication), it is not clear whether compensatory mechanisms in the other elements mentioned above may mitigate effects on Ca^{2+} transient synchronicity.

5.5.3 Ca^{2+} Spark Frequency and Morphology

Ca^{2+} sparks have been introduced in chapter 1, both as building blocks of the Ca^{2+} transient, and also as potential triggers for arrhythmia. Consistent with the lack of difference in Ca^{2+} transient amplitude and SR Ca^{2+} content found, we also found no difference in Ca^{2+} spark frequency and morphology in this study under basal conditions. As detailed in Table 3-2, most previous studies in this model have shown an increased Ca^{2+} spark frequency and more variable effects on Ca^{2+} spark morphology. Discrepancies may be for similar reasons as outlined above. The method of analysis of data is particularly important with respect to spark morphological data since the use of a 3-level hierarchical model alters p-values substantially for these parameters (see Table 3-4).

5.5.4 Effects of β -adrenergic stimulation on transients and sparks

β -adrenergic agonism using isoprenaline has been shown to induce PKA-mediated phosphorylation of various proteins involved in excitation-contraction coupling such as DHPRs, RYRs and phospholamban. These modifications are expected to enhance the amplitude of Ca^{2+} transients and increase their decay rate. SR load is also increased which would be expected to enhance Ca^{2+} spark amplitude and frequency. It has previously been observed that the β -1 adrenoceptor is selectively down-regulated in heart failure (Bristow *et al.*, 1986). This down-regulation is consistent with a reduced ability of isoprenaline to restore impairment of CICR (in terms of CICR-gain) in failing cells of an SHR model of heart failure compared to an earlier compensated hypertrophic phase (Gomez *et al.*, 1997). This is corroborated by other studies in the post-MI rat model which also show reduced responsiveness to β -adrenoceptor stimulation in terms of a blunted increase in Ca^{2+} transient amplitude in HF (Litwin & Morgan, 1992). The chronic hyperadrenergic state *in vivo* in HF has been proposed to induce RyR2 hyperphosphorylation which, by causing detachment of the RyR2-stabilizing protein FKBP12.6 from the RyR complex and also uncoupling adjacent RyR2 complexes, can lead to instability of RyR2 gating and increase Ca^{2+} spark frequency in HF. Both β 1- and β 2-adrenoceptor stimulation have been shown to enhance Ca^{2+} spark frequency and increase their amplitude and size (Cheng & Lederer, 1996; Zhou *et al.*, 1999).

In this study we used a 30nM concentration of isoprenaline which is a concentration of a similar order of magnitude as endogenous circulating catecholamines in human heart failure (Cohn *et al.*, 1984). We showed, as expected, enhanced Ca²⁺ transient amplitude in the presence of isoprenaline with a more rapid decay of the Ca²⁺ transient. However there was no blunting of the response to isoprenaline in HF. This may be related to a lack of alteration in β -adrenergic receptors in the current model. However it could also be a result of enhanced β 2-adrenergic responsiveness as observed in a dog HF model (Altschuld *et al.*, 1995). This, in combination with the expected reduction in β 1-adrenergic responsiveness, may result in a similar effect of non-selective β -agonism in HF and control cells. In terms of dyssynchrony of Ca²⁺ transients, it has previously been shown that isoprenaline improves the synchronicity of the rise-phase of the Ca²⁺ transient. We found this to be the case in AMC cells, with reduced DysTt50P and DysTtP in the presence of isoprenaline (Figure 5-5), although there was no significant reduction in dyssynchrony for HF cells. The differences in the relationships did not reach statistical significance however so further experiments would be required to ensure there is a genuine difference in response. We also found a reduction of the dyssynchrony of transient decay across the cell in the presence of isoprenaline. However isoprenaline is not beneficial in all forms of transient heterogeneity since DysAmp (a measure of variability of amplitude across the cell), was significantly increased in both HF and AMC cells (Figure 5-5C). This is likely to provide a less efficient positive inotropic effect than a uniform increase of Ca²⁺ transient amplitude across the cell and may be a result of heterogeneous RyR2 clustering in the SR membrane. This would also be expected to cause variability of spontaneous SR Ca²⁺ release across the cell resulting in possible arrhythmogenesis. Such intracellular heterogeneity may also set up alternans of Ca²⁺ release which can lead to arrhythmia (Weiss *et al.*, 2011).

The most marked difference in response to isoprenaline in HF was seen in Ca²⁺ spark parameters. Spark amplitude was enhanced to a similar extent in both HF and AMC although only reached significance in HF. There was particular divergence of the response to isoprenaline in the effect on FWHM of sparks. In HF there was a significant increase in FWHM from 2.86 \pm 0.06 to 3.22 \pm 0.12 μ m whereas there was no significant change in FWHM of AMC cells. This produced a similar pattern in spark mass with an approximate doubling of spark mass (13.33 \pm 1.48 to 28.03 \pm 5.96 μ m³) in HF in the presence of isoprenaline, but no significant change in AMC (15.12 \pm 2.56 to 15.33 \pm 1.82 μ m³), see Figure 5-9E. Why there is an enhanced response in HF, where there is typically β 1-adrenoceptor downregulation, is unclear. However, it may relate to a differential effect of β 2 compared with β 1-adrenoceptor agonism. Although this has not been observed specifically for sparks, it has previously been shown in other elements of the CICR apparatus such as DHPR activity (Xiao & Lakatta, 1993; Skeberdis *et al.*, 1997). Since β 2-adrenoceptor activity is proportionally greater in HF (Bristow *et al.*, 1986), one could envisage an increased response within some spark morphological parameters if these are more sensitive to β 2 than β 1-adrenoceptor agonism. The enhanced Ca²⁺ spark mass in HF in response to isoprenaline corresponds with the increase in isoprenaline-mediated arrhythmia we have previously observed *in vivo* in this model (Lyon *et al.*, 2011).

5.5.5 Spontaneous SR Ca²⁺ release is reduced at the borderzone

We hypothesized that the borderzone may exhibit different properties in terms of CICR and spontaneous SR Ca²⁺ release compared with the remote myocardium. Regional differences in myocyte contractility have previously been noted in the rat MI model at 1 week post MI (Lefroy *et al.*, 1996). In our cells we found no difference in Ca²⁺ transient amplitude, morphology or

dyssynchrony in the BZ. This may be related to a gradual normalization of the contractile function in this region which has previously been observed. For example, at an early stage following experimentally-induced MI in sheep there was a marked decline in muscle function assessed by MRI in regions adjacent to the infarct which had mostly resolved by 6 months (Kramer *et al.*, 1998). At the cellular level, increased Ca^{2+} transient amplitude in the borderzone was observed at 1 week post MI in the rat HF model which had normalized to the same level as remote myocardium by 16 weeks (Loennechen *et al.*, 2002).

We also assessed the potential pro-arrhythmic tendencies of BZ myocytes in terms of spontaneous Ca^{2+} spark and wave generation in these cells. Although we found no significant difference in spark frequency and morphology, we did find that Ca^{2+} waves were more likely to occur earlier in remote cells than borderzone cells. At first this seems counterintuitive since, certainly in man, the borderzone appears to be a site that is particularly prone to initiate arrhythmia (Ursell *et al.*, 1985; Yan *et al.*, 2006; Schmidt *et al.*, 2007). The finding of increased wave-free survival of cells from this region may therefore be an epiphenomenon with other aspects of the substrate having the overriding effect on arrhythmogenesis, for example conduction slowing due to connective tissue infiltration (Ursell *et al.*, 1985) and gap junction relocation (Peters *et al.*, 1997). On the other hand the reduction in waves may be detrimental in the borderzone. For example some authorities feel that Ca^{2+} waves may actually be a useful protective mechanism against states of Ca^{2+} overload during positive inotropy (George, 2008). Furthermore local differences in Ca^{2+} waves can promote spatial discordance of elements of CICR which can promote arrhythmia (Weiss *et al.*, 2011), such that the heterogeneity between the BZ and adjacent regions may promote arrhythmia even if SR Ca^{2+} leak is reduced in those regions. The difference in dimensions of BZ cells (shorter than remote cells, Figure 5-1D), points to further heterogeneity between BZ cells and remote cells, all of which may contribute to particular arrhythmogenicity in BZ regions, or more specifically at sites where these regions interact with normal myocardium.

5.6 Conclusions and Implications

Overall we have not been able to show changes in the properties of the cardiomyocytes at the level of the Ca^{2+} transient that explain the declining organ function over time following MI which we observed in chapter 4. The current study is not the first to comment on disparity between cellular function and function at the level of the organ. Anand *et al* found, in the same model, that LVEDP was closely correlated with the length of myocytes from an individual heart but there was no correlation between LVEDP and cellular contractile function (Anand *et al.*, 1997). Although it is clear that something is changing at the level of the cells and tissues to produce the gradual decompensation in cardiac function over time, it is unlikely to be pure derangement of Ca^{2+} handling. Other aspects such as alteration of LV geometry (Mitchell *et al.*, 1992), loss of cardiomyocyte numbers through apoptosis (Narula & Haider, 1996), infiltration of collagen (Caorsi *et al.*, 2013) and changes in proteins of the contractile apparatus which occur during disease (Miyata *et al.*, 2000) may be more important. Toepfer *et al* have recently shown that under conditions of saturating Ca^{2+} , permeabilized trabecular contractile function is better than control at the 4WMI stage but significantly impaired at the 20W stage (Toepfer *et al*, unpublished communication). Of note, the studies of Caorsi *et al* and Toepfer *et al* were performed with tissue derived from the current model and these collaborations help to conclude that the abnormalities seen at the level of the intact LV are likely to be related more to these factors than alterations in Ca^{2+} -cycling.

The findings of similar Ca²⁺ handling under basal conditions in HF vs control cells would have a large impact on the field if generalized and currently there is insufficient evidence to draw this conclusion. Alternative explanations relate to limitations of this particular study. One alternative argument is that in the current model the cells are somehow protected against some of the features of cardiac failure which are commonly seen in HF cardiomyocytes. One such protective factor may be obesity and of note the mean body mass of the HF rats in this study was 629g compared with approximately 550g in previous work by our group. In cross-sectional studies of humans with heart failure an “obesity paradox” has been observed whereby overweight and obese humans are generally protected from adverse events (Oreopoulos *et al.*, 2008). Alternatively the study may have been underpowered to detect differences in Ca²⁺ handling in this particular model, although against this is that the number of cells and animals used exceeds that of the majority of studies referenced in Table 3-1 and Table 3-2.

On the other hand we have observed alterations in Ca²⁺ cycling which could be responsible for the increased propensity to arrhythmia in this model. In particular the enhanced increase in spark mass in the presence of isoprenaline mirrors the increase in isoprenaline induced arrhythmia seen *in vivo* in the model (Lyon *et al.*, 2011). Such arrhythmias might be a result of triggered activity due to spontaneous SR Ca²⁺ release and subsequent activation of NCX producing spontaneous depolarization. We have also shown a potential basis for the enhancement of re-entrant arrhythmias due to heterogeneity of spontaneous SR Ca²⁺ release between the borderzone region and other regions. Such heterogeneity is expected to increase the risk of spatially discordant Ca²⁺ and action-potential alternans and increase the probability of re-entry and subsequent VT and VF.

6 OBLIQUE PLANE MICROSCOPY REVEALS THAT ARRHYTHMOGENIC CALCIUM WAVES ORIGINATE IN REGIONS OF WELL ORGANIZED T-TUBULES IN HEART FAILURE

6.1 Aims

- To assess the feasibility of using a novel form of optically sectioning microscopy – oblique plane microscopy (OPM) - with respect to its ability to image spontaneous Ca^{2+} release events in isolated cardiomyocytes in 2 and 3 Dimensions.
- To address whether Ca^{2+} sparks vary in frequency or morphology depending on local t-tubule structure via hierarchical statistical modelling.
- To assess whether Ca^{2+} waves are more likely to originate in areas of prominent tubules or in detubulated regions in a stage of post-MI HF that exhibits an increase in Ca^{2+} wave frequency (8 weeks post MI)

6.2 Introduction

In order to assess frequency and morphology of spontaneous sparks and waves, optically sectioned imaging at high temporal and spatial resolution is required. Confocal microscopy exhibits many of these properties and is usually required in order to reliably detect Ca^{2+} sparks (Cheng *et al.*, 1993). However, the compromise used to obtain high temporal resolution is that imaging is usually performed in line-scanning mode whereby a single line of the cell is raster scanned to build up a 1-dimensional (1-D) image over time ($x-t$). This typically allows the line to be scanned every 1-2 ms. Although this technique is useful, the limited spatial information results in skewed measurements of spark morphology which would be improved by 2-D imaging (Bray *et al.*, 2007). In terms of imaging Ca^{2+} waves, these are relatively rare events, and therefore in order to ascertain their origin, high speed 3-D fluorescence microscopy is required.

Currently, the fastest optically sectioning 2-D microscopy techniques include multi-beam confocal microscopes (Takahashi *et al.*, 2010) and slit-scanning confocal microscopes (Iribe *et al.*, 2009; Wolleschensky *et al.*, 2013). Slit-scanning confocal microscopy has been used to investigate spark properties in time-lapse 2-D imaging ($x-y-t$) at up to 670 fps with 512×30 pixels (Iribe *et al.*, 2009). Recently, this approach has been combined with rapid axial scanning to achieve time-lapse imaging of trios of image planes, where three 512×31 pixel images separated by 1 micron in the vertical direction were acquired within 5.6 ms (Shkryl *et al.*, 2012).

Another approach to high speed 2-D and 3-D imaging is oblique plane microscopy (OPM). OPM is a light sheet microscopy technique that uses the same high NA microscope objective to provide both the fluorescence illumination and detection (Dunsby, 2008; Kumar *et al.*, 2011). OPM can therefore be implemented on a standard inverted fluorescence microscope and is compatible with a range of conventional sample mounting techniques including coverslip and microscope slide, multi-well plates or superfusion system. The advantages of light sheet microscopy techniques are that only the focal plane being imaged is illuminated, i.e. there is no out-of-plane photobleaching or phototoxicity, and that no image processing or moving parts are required to obtain an optically sectioned image.

In order to usefully apply OPM to the study of Ca^{2+} dynamics in live cells, we developed an OPM system employing multiple excitation laser lines and two high-speed scientific complementary

metal–oxide–semiconductor (sCMOS) cameras to image cardiomyocytes in two spectral channels simultaneously with a pixel/voxel rate of $\sim 10^8 \text{ s}^{-1}$. We then applied video-rate time-lapse 3-D OPM to determine the location of spontaneous Ca^{2+} wave origins in 3-D and to correlate this with local t-tubule structure. Our results show that the majority of spontaneous Ca^{2+} waves originate from regions of the cell with a high degree of t-tubule modulation (visibility). We then used high-speed 2-D OPM to study regional differences in spark characteristics within cells and the results were analysed using hierarchical statistics. This study therefore exemplifies the utility of high-speed 2-D and 3-D OPM to acquire structural and functional information from single cardiac myocytes.

6.3 Methods

6.3.1 The OPM experimental setup

OPM uses a single high numerical aperture microscope objective (O1 in Figure 6-1) to both deliver a tilted sheet of excitation light to the sample and collect the resulting fluorescence emission. It consists of three separate microscopes placed in series. The first microscope (O1 and TL[tube lens]1 in Figure 6-1) is a conventional inverted microscope frame and the second (O2 and TL2) is used to produce an intermediate image of the specimen (FP₂ in Figure 6-1) where the lateral and axial magnifications are equal. A third microscope (O3 and TL3) images a tilted plane within the intermediate image onto sCMOS cameras. The plane of observation of the third microscope is aligned to overlap the excitation sheet within the sample.

The system used in the current study includes continuous wave laser sources operating at 457 nm (Twist-25, Cobolt AB), 488 nm (Sapphire 488 LP, Coherent), 514 nm (Fandango-25, Cobolt AB) and 561 nm (Jive-25, Cobolt AB). These sources were combined using dichroic beamsplitters, and their amplitude was controlled using an acousto-optic tunable filter (AOTFnc-400.650, AA Optoelectronics). The light was then coupled into a single mode optical fibre. The light emitted from the fibre was collimated by lens L1 in Figure 6-1 (10× microscope objective, Olympus), focused in the vertical direction by cylindrical lens C1 ($f = 50 \text{ mm}$) onto the back focal plane of lens L2 (achromatic doublet, $f = 25 \text{ mm}$), which produced a light sheet at O2 that was tilted at an angle of 35° with respect to the front focal plane of O2 (FP2). An image relay consisting of two microscopes placed back to back formed by microscope objective O2 (50×/0.95 NA, Olympus), tube lenses TL2 ($f = 162 \text{ mm}$) and TL1 ($f = 180 \text{ mm}$, Olympus) and microscope objective O1 (60×/1.2 NA water immersion, Olympus) was used to image the light sheet into the sample. The resulting fluorescence from the sample was then relayed back to FP2 by the same optics. Finally, a plane (coplanar with the illumination light sheet) was imaged by the microscope formed by O3 (40×/0.6 NA, Nikon) and tube lenses TL3a & TL3b (achromatic doublets, $f = 100 \text{ mm}$) onto two scientific CMOS cameras (sCMOS, PCO.edge, PCO GmbH). A dichroic beamsplitter DC4 (T585LP, Chroma) was used to split the fluorescence into two separate spectral detection channels that were further defined by emission filters EMa & EMb (ET630/75M & ET525/50 respectively). The effective axial position of the light sheet and tilted observation plane in the sample was determined by the axial position of O2, which was controlled using a piezo-electric objective actuator (Physik Instrumente, Germany). Custom-written software running in LabVIEW was used to provide synchronized control of the AOTF, piezo-electric objective actuator and camera acquisition.

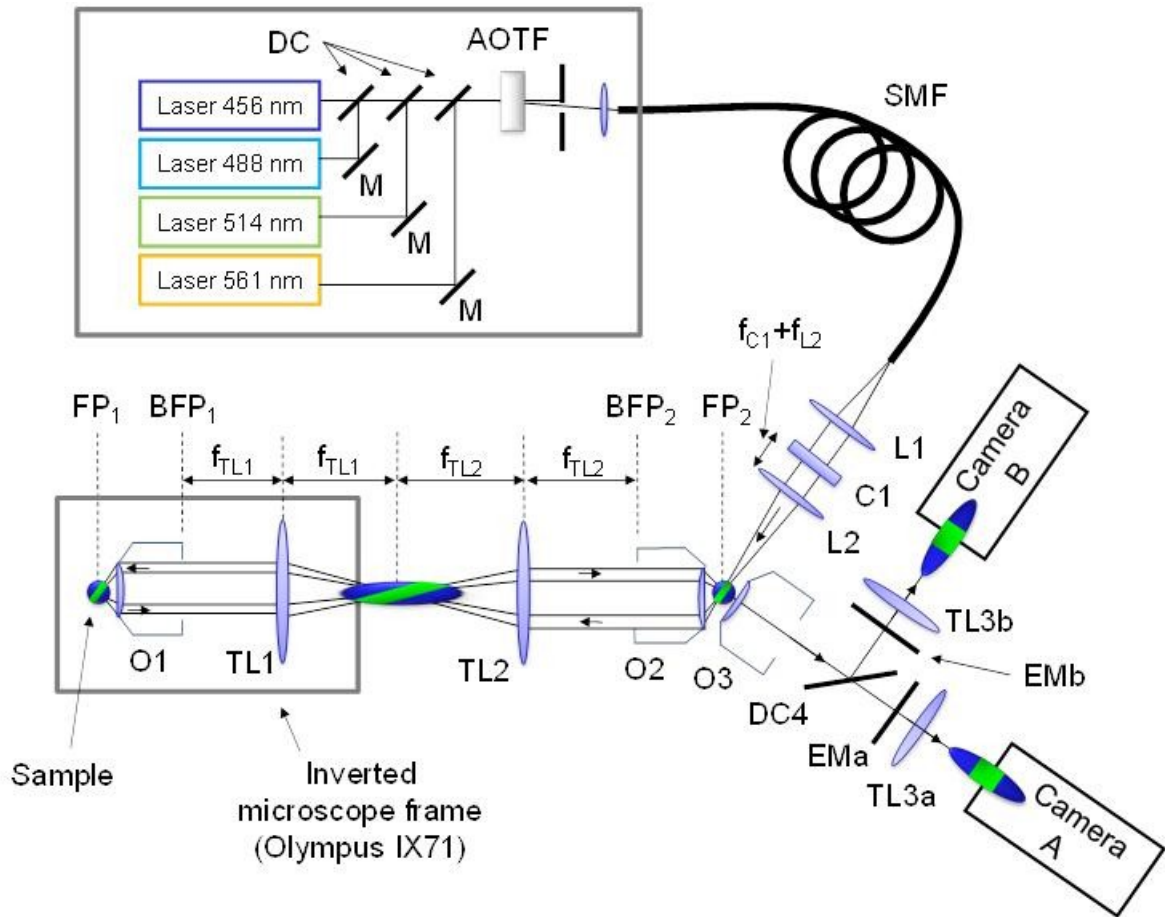


Figure 6-1. The OPM experimental setup.

Experimental configuration for the OPM system illustrated with a fluorescent sphere (blue) placed in the sample plane. The region in the sphere where fluorescence is excited is shown in green. The image of the sphere is illustrated at the image planes in the optical system. See text for further detail. M – mirror; DC – dichroic beamsplitter; AOTF – acousto-optic tunable filter; SMF – single mode optical fibre; L – spherical lens; C – cylindrical lens; FP – front focal plane; BFP – back focal plane; O – microscope objective; TL – microscope tube lens; EM – emission filter.

Fluo-4 and CMO were excited using wavelengths of 488 nm and 561 nm respectively. The corresponding excitation powers at the back aperture of O1 were $\sim 280 \mu\text{W}$ for each wavelength. This power was distributed over an illumination sheet covering the full width of the field of view of the system (limited to $400 \mu\text{m}$ by O2), which is larger than the field imaged by the sCMOS camera of $234 \times 49 \mu\text{m}$. The illumination sheet thickness full width at half maximum was measured to be $3.7 \mu\text{m}$ for both the 488 nm and 561 nm excitation. The lateral spatial resolution of the optical system has already been measured to be $0.41 \pm 0.05 \mu\text{m}$ (Kumar *et al.*, 2011) and the effective pixel size at the sample was $0.24 \mu\text{m}$.

Each 2-D acquisition consisted of 15,000 frames of 960×200 pixels on each sCMOS camera. The camera integration time was set at 1.46 ms and the time between frames was 1.5 ms, resulting in an image acquisition rate of 667 frames per second for a total duration of 22.5 s. The two image stacks representing the different channels were acquired simultaneously and then co-registered using

correction parameters determined from an image of a USAF 1951 test chart (Edmund Optics, Barrington, USA).

3-D data acquisition consisted of 750 volumes of $960 \times 200 \times 20$ voxels on each sCMOS camera. The camera integration and time between frames was the same as for 2-D imaging. During this acquisition, the position of the piezo-electric actuator was used to axially translate O2. The actual position of O2 was recorded by a capacitive position sensor and this information was used for volume transformation during image processing. A delay of 10 ms was then used to allow fly-back of the piezo-electric actuator to its initial position ready for the next volume. Overall, this resulted in an acquisition rate of 25 volumes per second. Co-registration of the image data from the two detection channels was performed in the same way as for 2-D data.

6.3.2 Sample Preparation and Imaging Protocols

Cardiomyocytes were isolated using standard enzymatic techniques (section 2.4). Cells were isolated from rats 8 weeks following MI (section 2.2) with HF as assessed by echocardiography (section 2.3.2), and also from unoperated age matched controls (AMCs). In addition to OPM imaging, some cells were loaded with fura2-AM (2.5.1) and imaged by ratiometric techniques to assess diastolic Ca^{2+} and wave frequency (2.5.5.2) in a diastolic period of 30s following a 2min period of external field stimulation at a frequency of 1Hz. In preparation for OPM imaging, cells were dual labeled with the Ca^{2+} sensitive fluorophore fluo-4 AM and the membrane dye cell mask orange (CMO). Cells were first incubated with $15\mu\text{M}$ fluo-4 AM and 0.16% pluronic acid for 25 mins at room temperature. Cell mask orange at a concentration of $5\mu\text{g/ml}$ was then added to this solution for 5 mins with the temperature increased to 37°C . The suspension of myocytes was mixed using a rotary mixer and protected from light during the incubation period. Cells were then washed twice and resuspended in a low Ca^{2+} ($150\mu\text{M}$) form of normal Tyrode (NT) and kept at room temperature until imaging.

The OPM system was coupled to an inverted microscope (Olympus IX71) which allowed imaging of isolated cardiomyocytes in a similar manner to that previously described using conventional confocal microscopy (Sikkel *et al.*, 2013a). Briefly a low volume chamber (Warner RC-24N) was attached to the microscope stage and myocytes were attached to the coverslip using mouse laminin (Sigma Aldrich). NT containing 2mM Ca^{2+} (section 2.5.3) was superfused over the myocytes at 37°C via a gravity driven superfusion system. Cells were field stimulated for at least 2 mins at 1 Hz. The last 5 transients and a subsequent 15s quiescent period (for Ca^{2+} spark detection) were imaged via 2 channels. 2D imaging, with a single plane selected through the cell repeatedly imaged at 666 frames per second (fps) was performed.

6.3.3 Time-lapse 3-D data analysis

Co-registered 3D datasets were transformed using custom written software in MATLAB utilizing the *tformarray* function to resample the data using linear interpolation from a stack of points lying on oblique planes to a conventional Cartesian x-y-z coordinate set where z is along the optical axis. Calls to this function were implemented in parallel to reduce the time required for data processing.

The time-lapse volumetric Fluo-4 data was then viewed manually and the coordinates of the origin of each spontaneous Ca^{2+} wave recorded. For each wave, the sarcolemma visualised in the CMO channel was manually selected for each z-plane of the volume, thus producing a region of interest defining the extent of the interior of the cell in 3-D. The modulation (visibility) of the t-tubules was

calculated for each plane in the image stack (see section 6.3.5 for details), resulting in a 3-D map of (unnormalised) t-tubule modulation M for the interior of the cell. This data was then used to produce a histogram of t-tubule modulation values for the interior of each cell. The value of t-tubule modulation at each spontaneous Ca^{2+} wave origin was also determined from the 3-D map of t-tubule modulation.

6.3.4 Time-lapse 2-D data analysis

Sparks were assessed using custom written software in MATLAB to assess spark morphology in 2D (Appendix 9.4). Our spark detection algorithm uses the threshold based algorithm of Cheng et al. (Cheng *et al.*, 1999) and Song et al (Song *et al.*, 1997) but is extended to the analysis of 2-D time-lapse (x - y - t) datasets as demonstrated previously (Brum *et al.*, 2000). Figure 6-2A shows how this process can be used to identify sparks in 2-D. Figure 6-2B-C show the extent of information available from this form of imaging compared to standard linescan data – an x - t linescan dataset is available at each y co-ordinate of the cell.

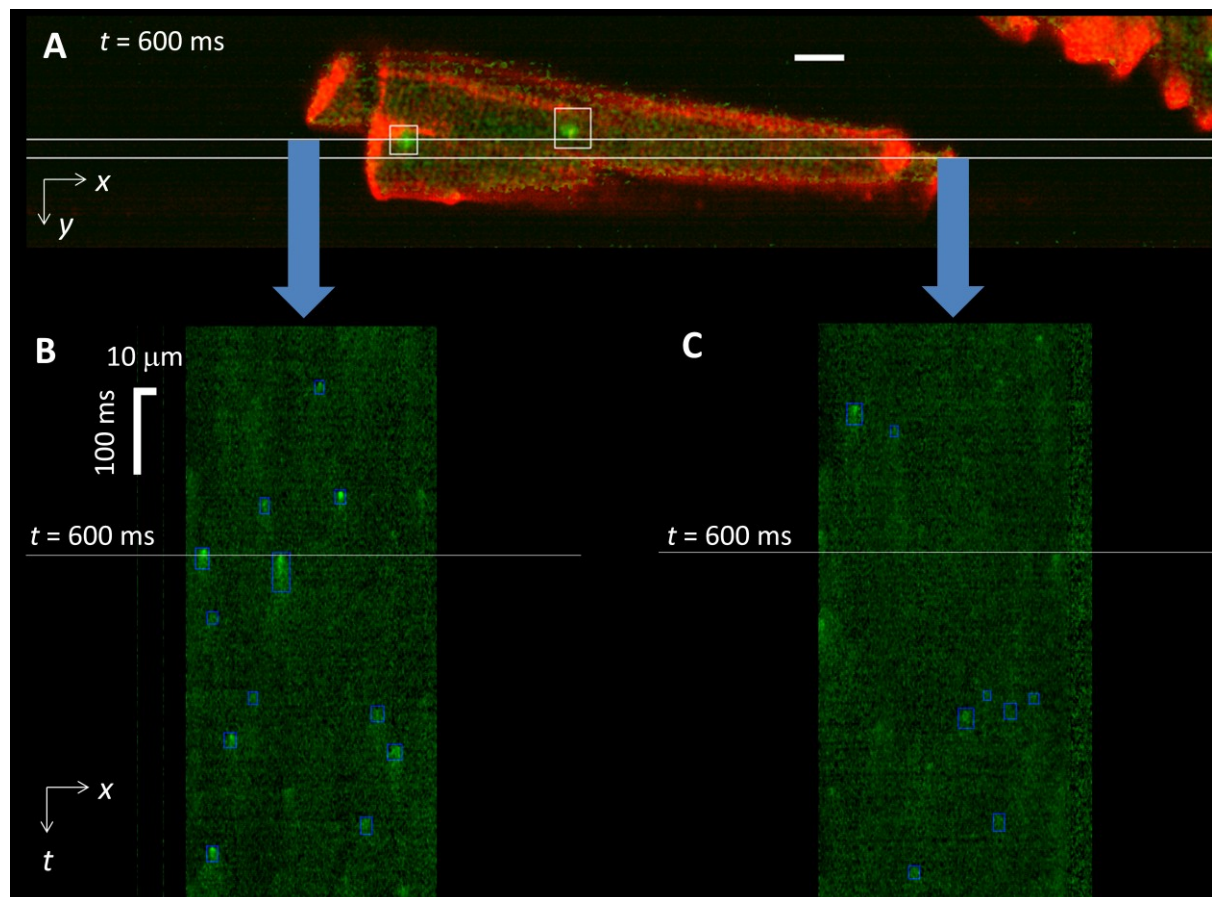


Figure 6-2. Time-lapse 2-D spark imaging with OPM

(A) OPM image of a single isolated MI cardiac myocyte acquired at time $t = 600$ ms from the start of image acquisition. Green and red show the fluorescence intensity of Fluo4 and CMO respectively. Scale bar $10 \mu\text{m}$. x - t slices acquired simultaneously through the Fluo4 dataset are shown along the lines at (B) $y = 26 \mu\text{m}$ and (C) $y = 30 \mu\text{m}$. White horizontal lines on line-scan show 600 ms timepoint corresponding to 2D image. Automatically detected sparks are shown bounded in blue.

6.3.5 Identification of T-tubules

The CMO channel was used to define the ultrastructural properties of the cell in order to relate this to spark properties at particular locations. The raw CMO image was enhanced by taking blocks of 1000 images (1.5s) during quiescence and averaging the fluorescence intensity over that time.

The following algorithm (coded by Vincent Maioli using Matlab, see Acknowledgements) was used to subsequently identify parts of the cell containing t-tubules (Figure 6-3). First, the t-tubule modulation map M was calculated. To do this, the centre line of the sarcolemma of the cell was selected from the CMO fluorescence intensity image using a manually defined region interest (ROI) (Figure 6-3A). The resulting masked image was Fourier transformed (Figure 6-3B) and the centre of the high spatial frequency peak arising from the periodic t-tubule structure was selected manually (u_t, v_t). One-sided (Figure 6-3C) and two-sided (Figure 6-3D) Gaussian Fourier masks of the high spatial frequency peak arising from the periodic t-tubule structure were then produced. The one-sided filtered data was then inverse Fourier transformed and the absolute value taken yielding M . The normalised t-tubule modulation M_N (Figure 6-3E) was then calculated by dividing M by the average fluorescence intensity of the sarcolemma F_{membrane} . F_{membrane} was found by growing the centre line of the sarcolemma by 3 pixels in both directions (resulting in a sarcolemma mask that is 6 pixels/ 1.44 μm wide) and the mean fluorescence intensity from the resulting ROI is calculated.

In order to generate a binary mask of t-tubule locations (Figure 6-3F), the normalised t-tubule modulation image M_N was then thresholded. Regions with $M_N > 0.015$ were defined to be tubulated and the same threshold was applied to all cells imaged. The t-tubule map was generated using the two-sided high-pass spatial frequency filter. This filtered image was masked by the t-tubule locations and binarised using a threshold of zero. The resulting mask has a mark-space ratio of 1:1 and the t-tubule regions were eroded using MATLAB's `imerode` function by 0.49 μm (2 pixels). This process results in an image where a binary t-tubule mask is produced for regions where the peak-to-trough value of the t-tubules is more than 6% of the mean value of the membrane intensity

So that nuclei were not incorrectly defined as a detubulated cytosolic region, each cell was manually assessed for the presence of a nucleus within the section imaged. The nucleus was identified by its characteristic ellipsoid shape and the presence of a prolonged Ca^{2+} transient during evoked contractions as well as their location corresponding spatially to the nucleus identified on the transmission image of each cell. These regions were excluded from further analysis.

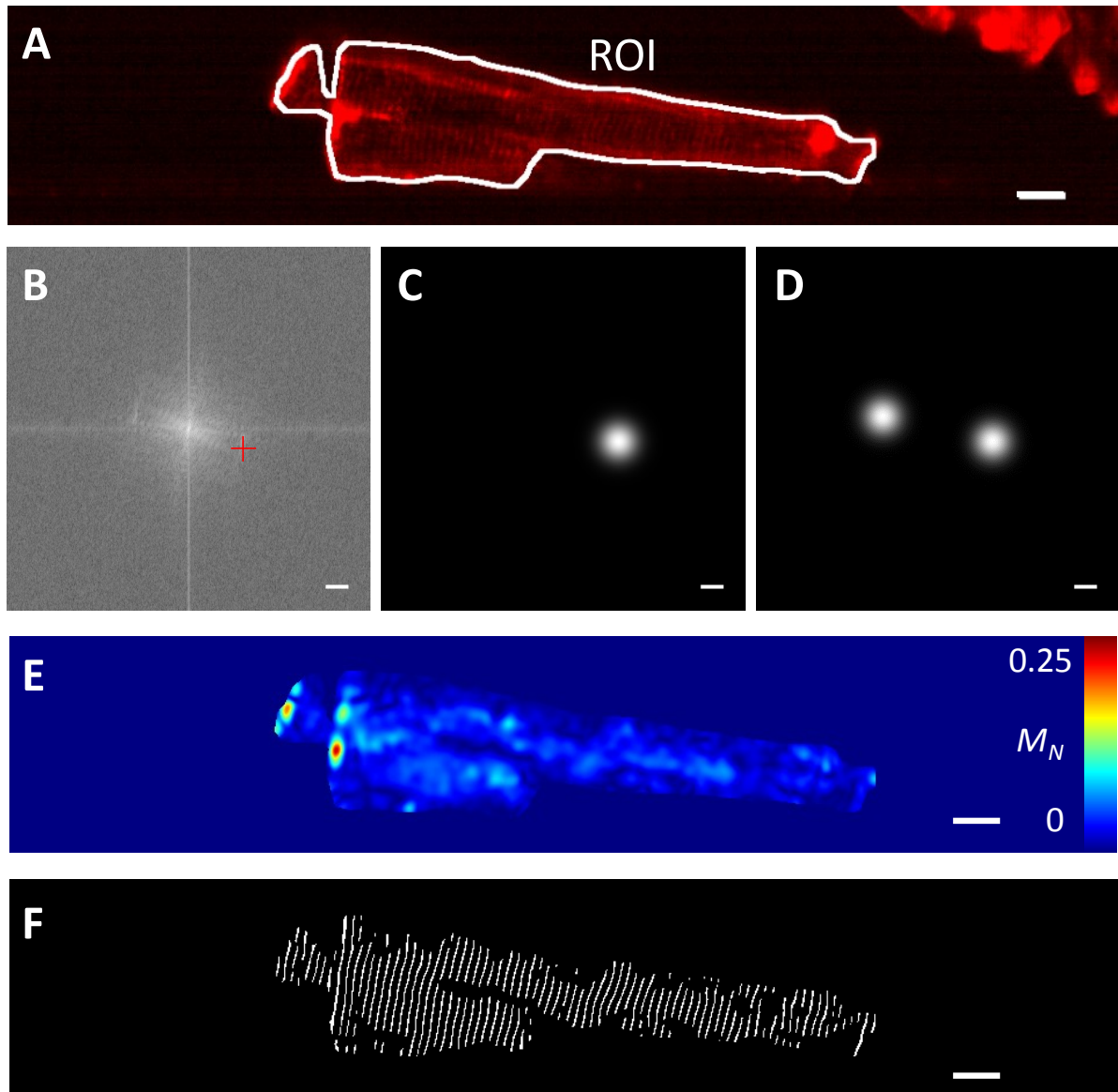


Figure 6-3 Identification of T-Tubule locations within cardiomyocytes.

(A) CMO image of a single isolated MI cardiac myocytes. Red shows the fluorescence intensity of CMO and white shows the sarcolemmal region of interest (ROI). (B) Fourier transform of image shown in A. Red cross indicates position of manually located high spatial frequency corresponding to t-tubule structure. (C) and (D) one- and two-sided Gaussian spatial-frequency filters respectively. (E) calculated map of normalised t-tubule modulation M_N . (F) Binary map of calculated t-tubule locations. Scale bars in A, E & F represent $10\ \mu\text{m}$. Scale bars in B, C & D represent a spatial frequency of $0.25\ \mu\text{m}^{-1}$.

6.3.6 Definitions of Subcellular Locations Used for Analysis

The calculated centre of mass for each identified spark allowed both the organization of t-tubules in its vicinity (normalized modulation) and its distance to the nearest t-tubule to be determined. A first distinction, which is self-explanatory, was between sparks from tubulated regions and detubulated regions as defined in section 6.3.5. A further subclassification was applied for sparks within tubulated regions. The centre of mass of each spark was compared to the location of the nearest t-

tubule. Epitubular sparks were defined as on the t-tubule (within a margin of error of 1 pixel or approx 0.25 μm either side), paratubular sparks were those from a region populated with t-tubules but more than 0.25 μm from the nearest t-tubule.

6.3.7 Linescan Data

The spark dataset was a good opportunity to assess the accuracy of 1-D line-scanning in comparison to the 2-D dataset obtained via OPM. Equivalent data to a linescan (x-t scan) was extracted from the 2-D dataset from each cell in order to compare data obtained via data analysis in 1-D versus 2-D methods. A line was taken along the widest point of the cell (whilst avoiding the nucleus) in the data stack and the “Orthogonal Views” command in ImageJ used to attain the linescan equivalent. Background subtraction was performed in the same way as for the 2-D dataset via subtraction of the extracellular fluorescence level from every pixel prior to analysis. The resulting image was processed using Sparkmaster with detection criteria being set at the same level as used in the 2-D detection algorithm (6 standard deviations). The detection of sparks was confirmed by eye. The same time intervals were analysed using 2-D and 1-D techniques in all cells and data were compared. The results are outlined in Appendix 9.4.4 and shows good correlation between the frequency calculated in 1-D vs 2-D but less accurate assessment of morphology in 1-D.

6.3.8 Statistical Modelling and Significance Testing

Statistical analysis was performed using IBM SPSS statistics. Simple parametric statistics (Student’s t-tests) were carried out for biometric and echocardiographic data. The other data was hierarchical in nature (e.g. multiple cells from a single isolation, multiple sparks from within a single cell), thus linear mixed models are the most appropriate means of analysis (see chapter 3). Such models take into account the relationships between events which occur within a subject. One part of the assessment of hierarchical models includes estimates of covariance parameters which give an assessment of whether this intra-subject clustering is significant. For data that were not significantly clustered within subjects in the hierarchy and where the distribution was not Gaussian (i.e. wave frequency), standard tests such as a Mann-Whitney U test was used for comparison. An example of this is in wave frequency data where there was no intra-rat hierarchical association in terms of wave frequency (estimate of covariance parameter $p=0.16$).

Subcellular frequency was normalised to area and time, giving final units of sparks/100 $\mu\text{m}^2/\text{s}$. The logarithmic transformations of morphological characteristics were used to produce more normally distributed data. These are referred to as LogAmp, LogArea and LogFDHM for the logarithm of spark amplitude, area and full duration at half maximum (FDHM) respectively. Spark frequency and morphological characteristics were the dependent variables in the statistical models. Initial independent variables in each model included regional t-tubule morphology, the presence or absence of HF and the interaction between the two coded as fixed effects. Each model used was assessed for validity by ensuring predicted values closely corresponded to those observed. Residuals were assessed for normality and symmetry. A random intercept was included. Type III tests of fixed effects were used to decide whether variables were significant (p values pertaining to significance of a parameter refer to this) and non-significant independent variables were removed from the model stepwise. P-values quoted for significant effects are from the simplified model following removal of non-significant terms.

6.4 Results

6.4.1 *In Vivo* Cardiac Function and Cellular Phenotype in HF Model Animals Used for OPM Studies

In vivo cardiac function was assessed in 6 AMC and 8 HF animals of the 10 animals total in each group used for this study using echocardiography. Left ventricular hypertrophy and reduced ejection fraction were present in HF animals (Figure 6-4 A-B). Echocardiography also showed significant LV dilatation and reduced maximal blood velocity in the pulmonary artery (PA V_{\max}) (Figure 6-4 C-D). Cells stained with Fura-2AM were used to assess propensity of HF cells for waves in a 30s interval following steady state contraction at 1Hz in 76 AMC cells from 10 isolations and 79 HF cells from 10 isolations. There was a significant increase in wave frequency in cells from HF rats compared with AMC (0.029 ± 0.003 vs 0.016 ± 0.003 waves/s) as seen in Figure 6-4E. This was not due to an increase in diastolic Ca^{2+} as shown in Figure 6-4F.

6.4.2 Study of spontaneous Ca^{2+} wave origins from time-lapse 3-D OPM imaging

16 cells from 4 AMC animals and 18 cells from 5 HF animals were studied in 3-D to assess sites of spontaneous Ca^{2+} wave origin. Table 6-1 shows the number of spontaneous Ca^{2+} waves recorded. For cells in which at least one wave occurred, the median number of waves per cell was 3.5.

	No. of animals	No. of cells	No. of cells with waves	Total no. of waves	No. of waves with origin not overlapping sarcolemma
AMC	4	16	1	1	1
HF	5	18	5	19	14
Total	9	34	6	20	15

Table 6-1. Summary of the number of cells and waves assessed during time-lapse 3-D imaging of spontaneous calcium waves.

Figure 6-5 shows an exemplar montage of a Ca^{2+} wave recorded by time-lapse 3-D OPM imaging. The origin of the wave can be clearly identified and therefore related to the calculated t-tubule modulation at the point of origin of the wave. Figure 6-6A shows an example histogram of the t-tubule modulation values for all voxels within one cell (same cell as shown in Figure 6-5), together with the t-tubule modulation values obtained at each of three spontaneous Ca^{2+} wave origins observed within the interior of that cell. For comparison, a histogram of the modulation values detected for regions outside the cell, i.e. those modulation values generated by noise alone, is also shown (black curve). The black curve provides a lower limit for the ability of the system to detect low t-tubule modulation.

Figure 6-6B shows the t-tubule modulation values measured at the origin of each wave for each cell and provides the median t-tubule modulation and the 95th percentile of the modulation due to noise alone for each cell as comparison. In HF 12 out of 14 wave origins occur at locations with t-tubule modulations greater than the median t-tubule modulation for that cell.

If a voxel within a cell is chosen at random, there is a 50% probability of it having a higher t-tubule modulation than the median t-tubule modulation for that cell. Therefore, using the binomial distribution, the probability of observing by chance 12 or more wave origins with t-tubule modulations greater than the median t-tubule modulation for that cell is $p = 0.0065$, indicating that our observation is statistically significant.

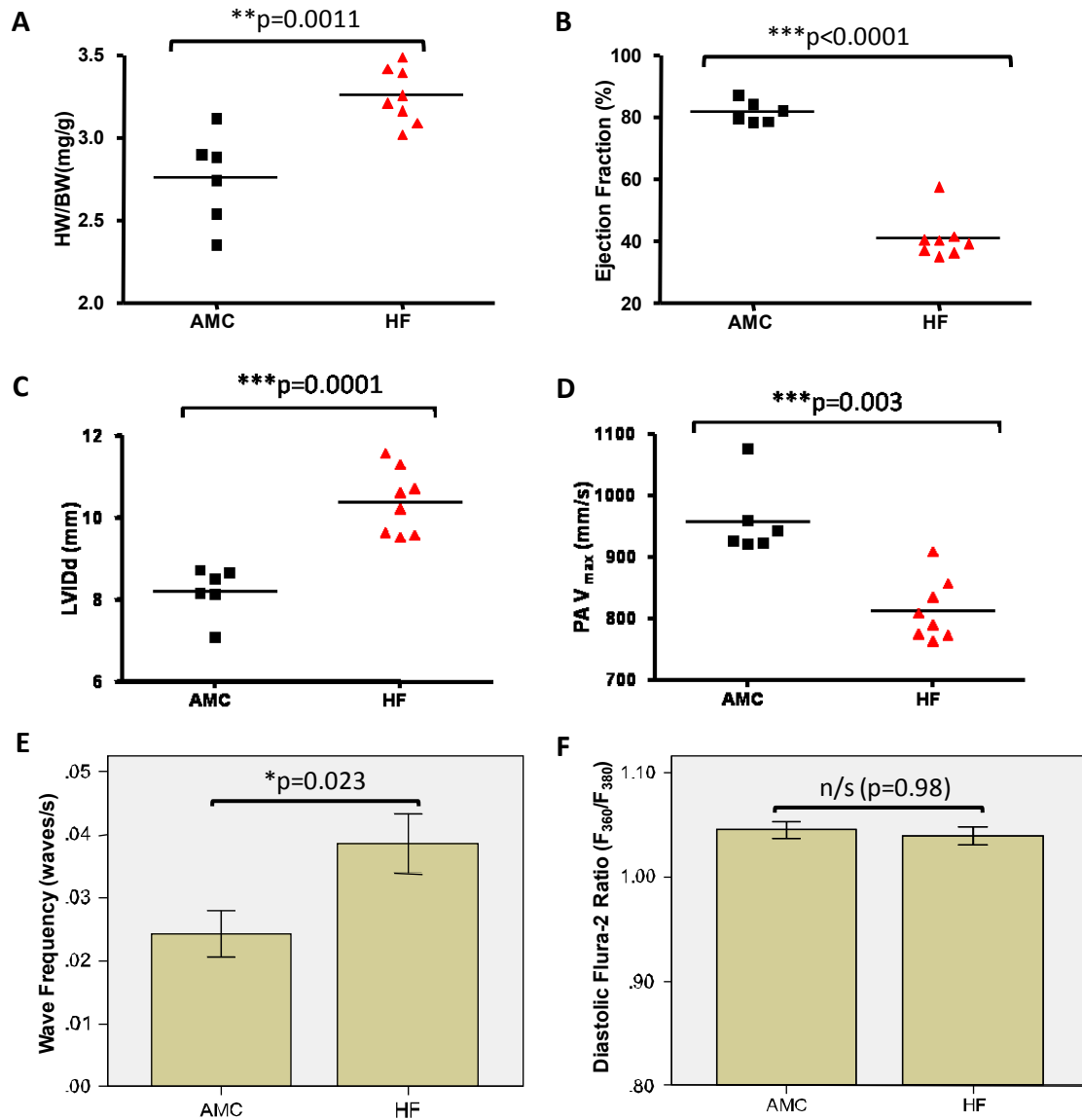


Figure 6-4. *In vivo* cardiac function and cellular phenotype of HF rats.

(A) Biometric measurements showed substantial increase in cardiac mass relative to body mass in HF model. (B) Cardiac contractile function as measured by ejection fraction is significantly reduced. (C) Left ventricular internal diameter in diastole (LVIDd) is significantly increased in HF. (D) Maximal velocity of blood in the pulmonary artery (PA V_{max}) is significantly reduced. Together these results reveal the presence of cardiac dilatation and global contractile dysfunction which are expected in HF. (E) Increased spontaneous Ca²⁺ wave frequency in cells from HF rats compared with cells from AMC. (F) This difference in wave frequency is not due to prevailing diastolic [Ca²⁺]_i as measured by Fura-2

ratio, which is similar in AMC and HF. $n=6$ animals AMC and 8 HF for A-D. $n=76$ AMC cells from 10 isolations and 79 HF cells from 10 isolations for E-F.

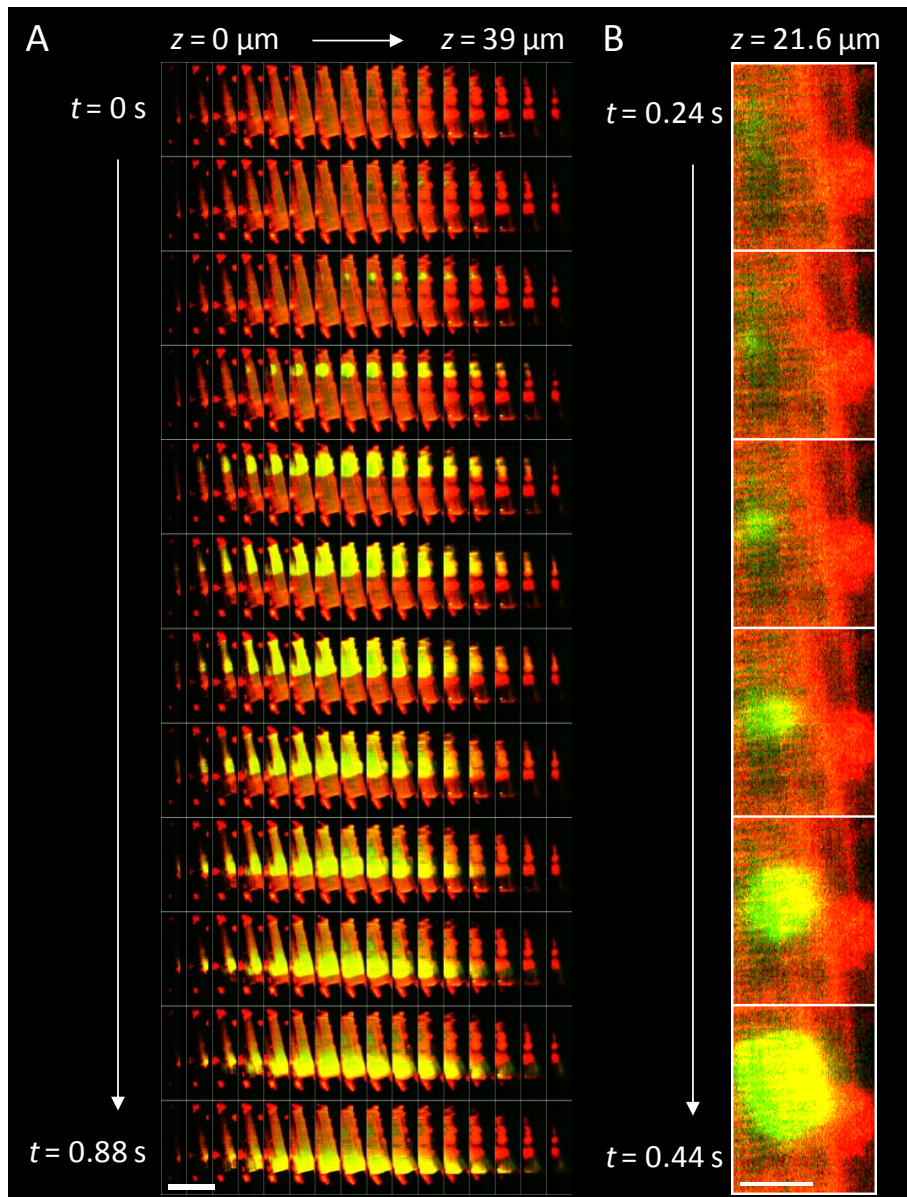


Figure 6-5. Montages showing time-lapse 3-D OPM of spontaneous calcium wave origin.

Fluo-4 is shown in green, *CMO* is shown in red with their overlap shown in yellow. (A) Montage shows images spaced $2.6\ \mu\text{m}$ apart axially (left to right across montage) and every other acquired volume in time (top to bottom), i.e. rows are 80 ms apart. Scale bar $180\ \mu\text{m}$. (B) Close-up of the plane containing the spontaneous wave origin. Here, every acquired time-point is shown, i.e. images are 40 ms apart. Scale bar $15\ \mu\text{m}$.

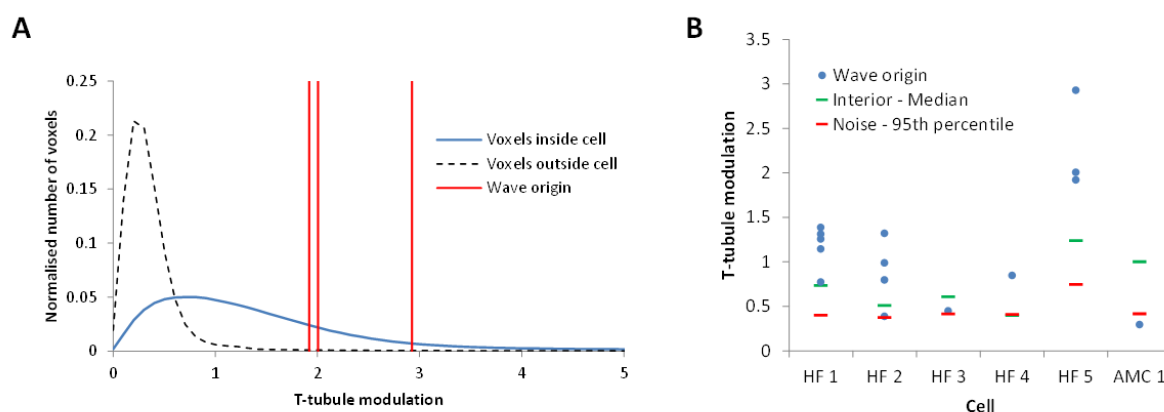


Figure 6-6. T-tubule modulation in relation to wave origin.

(A) Blue curve shows a histogram of calculated t-tubule modulation for all voxels in the interior of cell (same as shown in Figure 6-5). Black dashed curve shows a histogram of calculated modulation for all voxels outside the cell. Red lines indicate the t-tubule modulation values obtained at the origin of each spontaneous Ca^{2+} wave observed for this cell. (B) T-tubule modulation values for each spontaneous Ca^{2+} wave origin for each cell (blue dots). For comparison, the median t-tubule modulation from all voxels are also shown for that cell (green bar) and the 95th percentile of the noise for that cell (red bar).

6.4.3 Spark data from time-lapse 2-D OPM imaging

Results presented are from time-lapse 2-dimensional imaging that resulted in a total of 4510 sparks. 1271 sparks were assessed from 5 myocytes from 3 AMC rats and 3239 from 7 myocytes from 3 HF rats. Spark frequency and morphology was assessed within the different regions of each cell.

6.4.3.1 Spark Frequency

There were 2 analyses: first, spark frequency was compared between detubulated and tubulated regions; and second, frequency was compared between epitubular and paratubular sub-regions lying within the tubulated region. Frequency was significantly greater in tubulated compared with detubulated regions ($p=0.01$, Figure 6-7A and Table 9-17 in Appendix 9.4.6). Within the hierarchical model we assessed whether there might be a difference in the effect of region depending on whether the cell is from an AMC or HF rat. This was performed by testing the significance of the “interaction” between region and HF. There was no statistically significant interaction between region and HF ($p=0.172$) suggesting a similar relationship in AMC and HF cells in this dataset. Within the tubulated region there was a significantly higher spark frequency in epitubular regions compared with paratubular ($p<0.0001$, Figure 6-7B and Table 9-18 in Appendix 9.4.6). Again there was no significant interaction between HF and region ($p=0.126$). Overall these results suggest that in both AMC and HF cells, sparks are more frequent within tubulated regions and in particular in epitubular regions (i.e. at the tubules) rather than paratubular (i.e. between the tubules). This preferential occurrence of sparks at t-tubules within tubulated regions is illustrated by a map of spark occurrence within a single myocyte in Figure 6-7C.

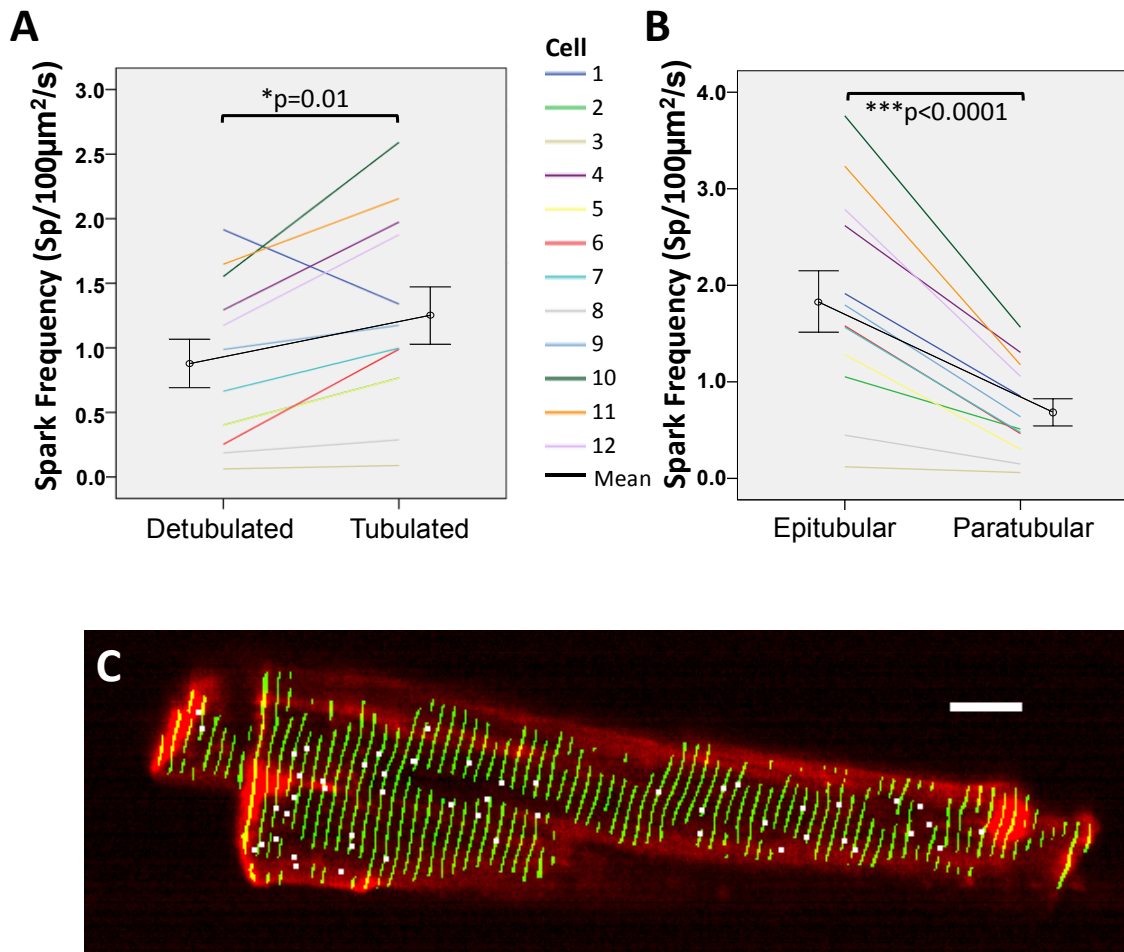


Figure 6-7. Spark frequency varies according to cell region.

(A) There is a significant increase in spark frequency in tubulated regions compared to detubulated regions. (B) Epitubular regions have significantly higher spark frequency than paratubular regions. (C) Map of t-tubule locations (green) and their correspondence to spark location (white dots) during a 1.5 s period in a single HF cell. Sparks are localized on top of, or very close to t-tubules with few sparks in paratubular or detubulated regions. $n=1271$ sparks from 5 myocytes from 3 isolations (AMC) and 3239 sparks from 7 myocytes from 3 isolations (HF).

6.4.3.2 Spark Morphology is Dependent on Subcellular Spark Region

LogAmp did not change significantly between detubulated and tubulated regions ($p=0.334$) or between epitubular and paratubular regions ($p=0.090$), see Figure 6-8A-B and Table 9-19/Table 9-20 in Appendix 9.4.6.

LogArea was significantly greater in sparks in tubulated regions than detubulated regions ($p=0.007$) (Figure 6-8C and Table 9-21 in Appendix 9.4.6). There was no interaction between tubulation and HF ($p=0.687$) suggesting a consistent effect whether or not HF is present. Within tubulated regions, paratubular sparks had significantly greater area than epitubular sparks ($p<0.001$) (Figure 6-8D and Table 9-22 in Appendix 9.4.6), but the interaction between the classification of epitubular vs paratubular and HF was not significant ($p=0.710$).

LogFDHM was no different in tubulated regions compared to detubulated regions ($p=0.926$) (Figure 6-8E and Table 9-23 in Appendix 9.4.6). However, within tubulated regions, paratubular sparks had

significantly greater duration than epitubular sparks ($p < 0.001$) (Figure 6-8F and Table 9-24 in Appendix 9.4.6). There was no interaction between classification as epitubular or paratubular and HF ($p = 0.091$).

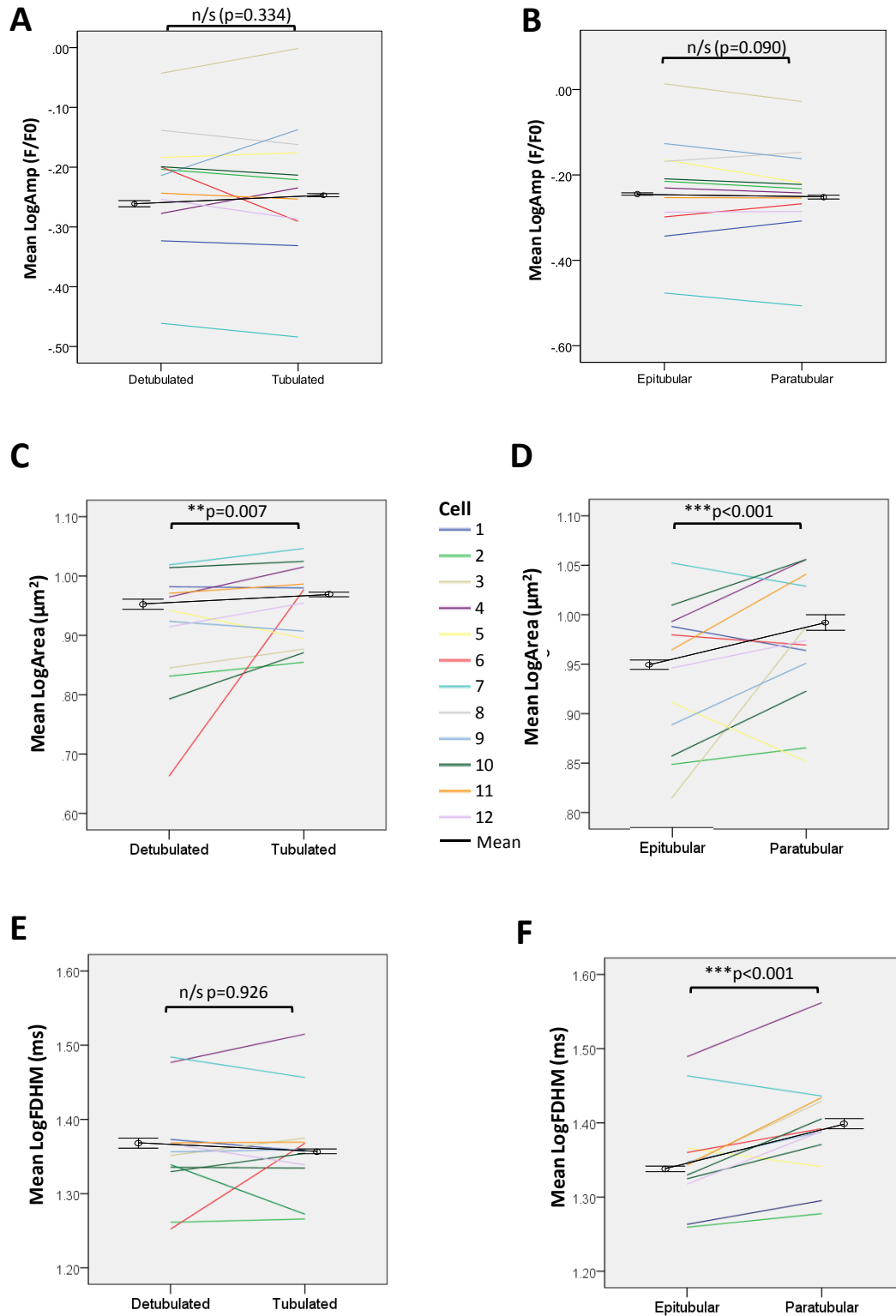


Figure 6-8. Changes in spark morphology by cell region

(A) Comparison of LogAmp between detubulated and tubulated regions and (B) comparison of LogAmp between epitubular and paratubular regions. There is no significant difference in LogAmp with respect to either parameter. (C) However spark area is significantly greater in tubulated regions and (D) within these regions is greatest in paratubular regions. (E) Spark duration is unchanged in tubulated compared to detubulated regions. (F) However sparks are more prolonged in paratubular versus epitubular regions. $n=1271$ sparks from 5 myocytes from 3 isolations (AMC) and 3239 sparks from 7 myocytes from 3 isolations (HF).

6.5 Discussion

6.5.1 Novel methodologies used in this study

The methodological advances detailed in this work have allowed us to advance the understanding of the interplay between cell ultrastructure, Ca^{2+} sparks and Ca^{2+} waves. Most importantly, the use of OPM allows imaging with high temporal resolution in 2-D and 3-D. We have previously demonstrated the potential of OPM to image sparks in isolated cardiomyocytes (Kumar *et al.*, 2011), but significant advances to the system including multiple excitation wavelengths, high resolution and high speed sCMOS cameras and addition of a superfusion system have enabled us to use the system to address pertinent biological questions for the first time. A further advance is the use of CMO as a t-tubule stain. Although CMO has a track record of t-tubule staining comparable to that of DI-8-ANEPPS (Ibarra *et al.*, 2013), we found that its combination with Fluo-4 Ca^{2+} imaging is particularly useful since the overlap of the excitation spectrum of CMO with Fluo-4 is less than that of DI-8-ANEPPS with Fluo-4. This allows the relative signal levels in the Fluo-4 and CMO channels to be controlled independently of staining level by varying the relative powers of the excitation beams for the two probes. In addition to the combination of dyes, we have also used a method based on 2-D Fourier-domain filtering for assessment of t-tubule organization.

6.5.2 Novel biological insights into the origins of Ca^{2+} waves in HF

At this 8W post-MI stage our HF model exhibits an increase in spontaneous Ca^{2+} wave frequency over AMC by 81% (Figure 6-4E). We wished to explore if the altered t-tubule organization of these cardiomyocytes influenced where waves originate by locating their origin in 3-D in the presence of a t-tubule stain. To our knowledge this is the first example of 3-D localization of wave origin within a cardiomyocyte. The combination of imaging t-tubules and Ca^{2+} allowed us to show that waves occur more frequently in regions of organized t-tubule structure than detubulated regions.

Using the same microscope in 2-D mode allows greater temporal resolution and allows us to accurately characterise faster, smaller Ca^{2+} release events (sparks), whilst still considering their position relative to t-tubules. Our data show a significant increase in spark frequency (by 40%) in tubulated regions compared with detubulated regions (Figure 6-7). Within regions classified as tubulated, sparks were more frequent in epitubular regions compared with paratubular regions. There were also significant differences in spark morphology for different regions. Spark area was greater in tubulated compared with detubulated regions. Within regions classified as tubulated, paratubular sparks had a greater area and duration compared with the epitubular sparks. These results may explain why, within an individual cardiomyocyte, Ca^{2+} waves originate from regions in which t-tubules are most prominent since such regions produce the most frequent, largest and longest Ca^{2+} sparks.

6.5.3 Comparisons with previous data

Although the visualization of the origin of Ca^{2+} waves in tubulated regions in HF is unprecedented, previous studies have assessed spontaneous Ca^{2+} spark characteristics in relation to t-tubule structure. Song et al. provided the first exploration of the possibility that subcellular heterogeneity of t-tubules might result in differences in spontaneous SR Ca^{2+} release in their publications identifying “orphaned RyRs” which were not in the vicinity of t-tubules and therefore local dihydropyridine receptors (DHPRs) in HF models (Song *et al.*, 2005, 2006). They hypothesized that regions of SR containing orphaned RyRs would become Ca^{2+} overloaded and more prone to spontaneous Ca^{2+} sparks.

Louch et al. provided experimental data by simultaneously imaging t-tubules and spontaneous Ca^{2+} sparks in control and post-MI mice using confocal line-scanning (Louch *et al.*, 2013). They found that the vast majority (>90%) of sparks, occurred at sites of t-tubules (i.e. equivalent to our epitubular region). They also found that repeating sparks (i.e. those occurring at the same location as an earlier spark) had similar morphologies as the earlier spark, compared with pairs of sparks from different randomly selected locations, suggesting a structural basis for differences in spark morphology. Furthermore in the post-MI mice there was a population of sparks with increased FDHM (slow sparks). Biesmans et al. also assessed how detubulation might affect spontaneous sparks, using a pig model of ischaemic cardiomyopathy (Biesmans *et al.*, 2011). Uncoupled regions (remote from t-tubules) exhibited reduced spark frequency but prolonged spark duration.

Similar to the above studies, we also find the highest frequency of sparks (1.84 ± 0.3 sp/100 $\mu\text{m}^2/\text{s}$) occurring at t-tubules (epitubular), with a lower rate present at either paratubular (0.71 ± 0.1 sp/100 $\mu\text{m}^2/\text{s}$) or detubulated (0.88 ± 0.2 sp/100 $\mu\text{m}^2/\text{s}$) regions. With respect to spark morphology data our findings cannot be compared directly with previous work since sparks were assessed in 2-D versus 1-D in previous work. In addition our classification of spark location was more detailed than in previous work including a paratubular category as well as epitubular and detubulated regions. We found a statistically significant increase in spark area for tubulated regions compared to detubulated regions (Figure 6-8C) and that paratubular sparks have a larger area and are significantly longer compared to epitubular sparks (Figure 6-8D&F).

6.5.4 Explaining the propensity for tubulated regions to initiate waves

It is not possible to explain the regional differences we have found in wave initiation based on the current study alone although our findings are a good starting point for hypothesis generation. It is conceivable that frequent sparks in the epitubular zones might lead to a particularly high Ca^{2+} in the dyadic space that could result in Ca^{2+} induced Ca^{2+} release (CICR) in adjacent RyR2 clusters and thus initiate the fire-diffuse-fire process thought to be responsible for wave propagation (Lemon, 2004). The longer, larger sparks in the paratubular zones of well-organized regions of t-tubules might also produce large rises in dyadic Ca^{2+} and could influence a larger number of surrounding RyR2 clusters to cause internal CICR.

The reasons for differences in spark frequency and morphology depending on local t-tubule structure should be the subject of further work. Epitubular sparks exhibit greater frequency, perhaps because they are local to DHPRs and thus local $[\text{Ca}^{2+}]$ is probably higher in these regions. Dries et al. have recently characterized further the difference in the regulation of spontaneous Ca^{2+} spark activity between coupled and un-coupled RyR clusters (Dries *et al.*, 2013). They have shown that

coupled clusters are influenced more strongly by local Ca^{2+} /calmodulin dependent kinase II activity. CaMKII-dependent RyR2 phosphorylation has previously been shown to occur in this model (Lyon *et al.*, 2011) and in separate studies this has been shown to be responsible for increasing arrhythmogenic SR Ca^{2+} release in HF (Ai *et al.*, 2005; Curran *et al.*, 2010; Van Oort *et al.*, 2010). This suggests that enhanced CaMKII activity within the regions of well organized t-tubules in our study may be responsible for the enhanced SR Ca^{2+} release in terms of sparks and waves within these regions. It is possible that our paratubular sparks represent activity from RyR clusters that are separated from t-tubules by larger gaps. Their reduced frequency is predictable due to both increased distance from DHPRs and reduced Ca^{2+} capacity of the smaller dyads. Additionally this would also be expected to reduce the area and duration whereas we found the opposite. This may be due to (1) an enhanced ability for the network SR to refill the smaller junctional SR volume during the spark (Song *et al.*, 2006; Poláková & Sobie, 2013) and (2) a decrease in activity of local Ca clearance systems (Gomez *et al.*, 1996; Smith *et al.*, 1998).

Can our findings explain the increased Ca^{2+} wave frequency found in HF cells in our study? One possibility is suggested by increased spatial heterogeneity of HF myocytes which leads to loss of co-localization of DHPRs and RyRs, particularly in regions in which t-tubules are lost entirely (Song *et al.*, 2005, 2006; Lyon *et al.*, 2009). We have shown that the regions of t-tubule loss exhibit reduced Ca^{2+} spark release. If SR Ca^{2+} uptake is preserved in these regions and intra-SR diffusion of Ca^{2+} is possible between detubulated and tubulated regions then increased spontaneous Ca^{2+} release would occur in the tubulated region to compensate for the continued uptake and reduced release in the detubulated region. A greater ratio of detubulated regions to tubulated regions would be expected to further enhance spontaneous Ca^{2+} release in tubulated regions which might increase the likelihood of initiating a wave in HF. On a more speculative level, the detubulation of cardiomyocytes and thus reduction of SR Ca^{2+} leak may be a compensatory mechanism for the myocyte to limit the increase in waves seen in HF. It is also likely that additional differences in HF cells also play an important role in the increased wave frequency observed. These may include changes in SERCA activity (Sikkel *et al.*, 2014), CaMKII activity (Curran *et al.*, 2010) and post-translational modification of RyR (Zima & Blatter, 2006; Bovo *et al.*, 2012).

6.5.5 Limitations

A limitation of this study is the relatively small numbers of cells (12 in the 2D section, 34 in the 3D section) studied in the experiments to assess the relationship between t-tubules and Ca^{2+} leak. This was due to a combination of factors, including the experimental nature of the microscope setup meaning that acquisition of data was time-consuming, and the fact that there is a difficult balance to be struck between sufficient laser power to provide adequate imaging and too much power causing phototoxicity. With increasing experience of this new form of microscopy we expect these factors to be less of a problem, particularly with 3D imaging in which the illumination plane is constantly shifting such that phototoxicity is less marked. Notwithstanding the low cell numbers, the high number (>4000) of sparks, analysed within the appropriate framework of hierarchical statistical modeling to assess how they change depending on structure, provides sufficient statistical power to draw conclusions regarding the relationship between sparks and t-tubules. Another limitation is that the resolution of the OPM image, while comparable to confocal microscopy, cannot provide the sort of detail required to define proliferative remodeling of t-tubules such as that recently defined by Wagner *et al.* using stimulated emission depletion microscopy (Wagner *et al.*, 2012). In fact our

measures of t-tubule organization were entirely focused on transverse elements and not longitudinal elements which have recently been characterized (Ferrantini *et al.*, 2013). Given that loss of t-tubules post MI involves a loss of transverse elements and increase in longitudinal elements (Wagner *et al.*, 2012), however, it is appropriate that regions with a lack of regular transverse elements were studied.

6.6 Conclusion

Through the novel use of OPM we have been able, for the first time, to localize the origin of Ca^{2+} waves in 3-D. We have dual-stained the cells so that the origin is contextualized within the t-tubule structure of the myocyte. We have found that the greater frequency of waves in 8WMI HF myocytes originates not from the abnormal detubulated regions but from regions of preserved t-tubule morphology. We have analysed spark morphology within these regions and found more frequent sparks in the epitubular zone and larger and more prolonged sparks in paratubular zones. Overall it is clear that inhomogeneity in t-tubule structure alters spontaneous SR Ca^{2+} release in different regions of the cell and that this contributes to the frequent arrhythmogenic Ca^{2+} waves which occur in HF. Further studies are required to investigate why these regions exhibit enhanced spontaneous Ca^{2+} release and whether they can be specifically modulated to reduce the incidence of ventricular arrhythmia in heart failure.

7 FLECAINIDE REDUCES Ca^{2+} SPARK AND WAVE FREQUENCY VIA INHIBITION OF THE SARCOLEMMAL SODIUM CURRENT

7.1 Aims

- To assess whether flecainide reduces spontaneous SR Ca^{2+} release.
- To assess whether the mechanism of reduction relates to inhibition of RyR2 opening or downstream effects of sarcolemmal I_{Na} reduction

7.2 Introduction

There has been recent interest in pharmacological agents which target potentially arrhythmogenic Ca^{2+} waves. Flecainide, a drug that has been used for many years clinically for its sodium current (I_{Na}) reducing properties, has shown efficacy in the treatment of CPVT patients (Watanabe *et al.*, 2009; van der Werf *et al.*, 2012). However, the mechanism of action producing this clinical effect is debated. In a mouse model of CPVT, Knollmann and colleagues have shown that flecainide reduces Ca^{2+} wave frequency in both intact and permeabilized myocytes and have provided evidence that this is related to a direct action on the cardiac ryanodine receptor (RyR2) via an open-state block of the channel (Watanabe *et al.*, 2009; Hilliard *et al.*, 2010; Galimberti & Knollmann, 2011). In contrast, similar experiments in both intact and permeabilized myocytes have been repeated by Liu *et al.* (albeit in a different mouse model of CPVT) and no effect on Ca^{2+} wave frequency was found despite similar experimental conditions (Liu *et al.*, 2011a). The conclusion of Liu *et al.* was that the reduction in I_{Na} caused by flecainide affected the threshold potential which decreased the number of spontaneous action potentials triggered by delayed after-depolarizations (DADs) associated with Ca^{2+} waves.

Our aim in this study was to assess if flecainide had an effect on Ca^{2+} sparks and waves and further investigate the mechanism. We observed SR Ca^{2+} release events in intact rat ventricular cardiomyocytes from healthy rats. We show via a variety of pharmacological and electrophysiological interventions that a reduction in I_{Na} during cellular contraction can reduce the frequency of Ca^{2+} sparks and waves in the diastolic period. We also show that, in the case of flecainide, the I_{Na} blocking effects are more relevant to wave reduction under our experimental conditions than RyR2 stabilization. Finally we explore the mechanism of this wave reduction using voltage-clamp experiments and further work on permeabilized cardiomyocytes. We conclude that the most likely explanation for the reduction in the presence of I_{Na} blockade is that it prevents an increase in $[\text{Na}^+]_i$ resulting in more effective $\text{Na}^+/\text{Ca}^{2+}$ -exchanger (NCX)-mediated efflux of Ca^{2+} .

7.3 Methods

7.3.1 Ventricular myocyte isolation and Ca^{2+} imaging of intact myocytes

Cardiac myocytes were enzymatically isolated from the left ventricle of healthy adult male Sprague Dawley rats by the Langendorff perfusion technique (section 2.4). Intact isolated myocytes were loaded with the Ca^{2+} sensitive fluorescent dyes fluo-4AM or fura-2AM (section 2.5.1). Myocytes were then imaged via either epifluorescence or confocal microscopy (section 2.5.2-2.5.5). The specific techniques used are mentioned in each relevant results section. Analysis was performed as per section 2.5.6.

Ca^{2+} transients were assessed during steady-state external field stimulation at 0.5Hz. Sparks were recorded following cessation of 0.5 Hz contraction during the last 10s of a 25s period of quiescence. Diaz et al have previously shown that $[\text{Na}^+]_i$ rises when quiescent cardiomyocytes are stimulated and that this, together with higher SR Ca^{2+} content, was correlated with increased wave frequency (Díaz *et al.*, 1996). Similarly, in our experiments, a higher stimulation frequency was associated with an increased wave frequency in a subsequent quiescent period, presumably for similar reasons (Figure 9-10A in Appendix 9.5). This preliminary series of experiments established that 30s of 5Hz stimulation (after 2mins of stable contraction at 0.5Hz) would consistently produce Ca^{2+} waves in normal Tyrode (NT) in the quiescent interval.

7.3.2 Voltage-Clamp Technique

Cells were voltage-clamped using an amphotericin perforated patch technique. Low resistance (2 to 4 M Ω) borosilicate glass micropipettes were filled with (in mM): NaCl (10), KCl (20), KCH₃O₃S (125), HEPES (10), MgCl₂ (5) and 240 $\mu\text{g}\cdot\text{ml}^{-1}$ amphotericin-B, adjusted to pH 7.2 with 1M KOH. The switch-clamp technique (with an Axoclamp 2B amplifier [Axon Instruments]) was used to overcome any changes in access resistance that may have occurred over the course of an experiment. Myocytes were clamped at -80mV or -40mV and depolarized to 0mV for 100ms to cause contraction with and without I_{Na} activation respectively. A 5Hz stimulation train was followed by a quiescent period during which the membrane potential was held at -80mV for 30s and wave frequency was assessed as before.

7.3.3 CamKII Inhibition

CamKII inhibition was achieved using the inhibitor KN-93 and comparing results with its inactive analogue KN-92. Concentrations of both were 1 μM (Liu *et al.*, 2011b). Cardiomyocytes were incubated with the agents for at least 30 mins and they were also included in superfusion solutions.

7.3.4 Assessment and Modulation of NCX function

NCX function (in particular in terms of Ca^{2+} efflux) was assessed under the same conditions as waves (i.e. following a 5 Hz stimulation train for 30s in the absence and presence of flecainide). However instead of wave observation, caffeine was applied in NT following the last evoked transient and was continually superfused during a decay which predominantly represents NCX function. The decay was fit with a monoexponential equation (Clampfit 10.2, MDS Analytical Technologies) from the 50% decay point. τ was provided by the software in ms and the decay constant (λ) was subsequently calculated from the reciprocal of $\tau/1000$ to give λ in units s^{-1} .

Variations in $[\text{Na}^+]_o$ were subsequently used to modulate NCX function. A low $[\text{Na}^+]$ sucrose-based Tyrode solution was made containing (in mM): sucrose (280), KCl (6), Glucose (10), HEPES (10), MgCl₂ (1), pH to 7.4 using 6mM NaOH. This was mixed in varying quantities with usual 140mM $[\text{Na}^+]$ NT to make the appropriate $[\text{Na}^+]$ concentration for the desired experiment. Experiments with flecainide were performed with 2mM $[\text{Ca}^{2+}]_o$. Experiments with veratridine were used to increase I_{Na} and hence alter $[\text{Na}^+]_o$: $[\text{Na}^+]_i$ gradient in the opposite direction to flecainide. These experiments were performed at lower $[\text{Ca}^{2+}]_o$ (1mM) but higher $[\text{Mg}^{2+}]$ (2mM). Wave experiments were performed in a similar manner with veratridine as flecainide except that 2Hz rather than 5Hz stimulation was used for 1 minute prior to wave detection since cells were not able to follow stimulation at 5Hz.

7.3.5 Permeabilized Cardiomyocyte Experiments

Experiments with permeabilized cardiomyocytes were performed to ascertain the direct effect of altering electrolyte or drug concentration at the SR. The following basic mock intracellular solution was used containing (in mM): KCl 90, NaCl 10, K₂ATP 5, Creatine phosphate 10, MgCl₂ 5.5, HEPES 25, K₂EGTA 0.05 and pH to 7.00 with KOH. The quantity of Ca²⁺ that was added was carefully calibrated by comparing fluorescence in the presence of 1μM fura-2 free salt with solutions of known [Ca²⁺] (made by dissolving ultrapure CaCO₃ in water with KOH added to produce pH 7.00). The final solution used to assess wave frequency was as above with 198μl of a 0.01M stock of Ca²⁺ added to 100ml of the mock intracellular solution which resulted in a free [Ca²⁺] of 100nM. For experiments in which [Na⁺] was to be varied, a base solution containing 80mM KCl and 0mM NaCl (as well as other constituents above) was made and then ultrapure KCl and NaCl were added in varying proportions to make up a final solution with the same osmolality but different [Na⁺] between 0 and 20mM.

Initially cells were exposed to a “permeabilization solution”, which was constituted as above but with 0.1mg/ml beta escin added. Cells attached to the microscope cover-slip with laminin in the normal manner (section 2.5.3) were exposed to this solution for 2 minutes (permeabilization was detected via an increase frequency of spontaneous contractions of the myocytes). The permeabilization solution was then washed off using at least 5 mls of the final imaging solution which was the same solution but without escin present and containing 5μM fluo5F salt. Imaging was performed via confocal microscopy as described in section 2.5.4. Analysis of confocal microscopy data was via the same methods outlined in sections 2.5.6.3-2.5.6.4.

7.3.6 Data-Pairing and Statistical Analysis

Where possible, data was obtained in a paired fashion and drugs applied or washed off in the form of a cross-over protocol alternating from cell to cell so that cell damage or exposure to laser light throughout the experiment did not influence final results. For example, the first cell had the drug applied following a control period whereas the next cell had drug applied first with subsequent wash-off (Figure 7-1A). Where there were multiple solution concentrations, we used a latin-square format to dictate the order for similar reasons. For example, 4 concentrations of Na⁺ solutions were applied to permeabilized cells. For the 1st cell the order of application was 0mM, 7.5mM, 12.5mM, 20mM. For the 2nd cell the order was 7.5mM, 12.5mM, 20mM, 0mM. For the 3rd cell the order was 12.5mM, 20mM, 0mM, 7.5mM. For the 4th cell the order was 20mM, 0mM, 7.5mM, 12.5mM to complete the cycle which then began again with the 5th cell.

The data from this chapter was analysed prior to my exploration of hierarchical methods in chapter 3. As such paired t-tests were used for most significance testing since tests involved data on each cell with or without a drug added. A paired t-test can be thought of as a very simple hierarchical model with the cell being the top level of the hierarchy and the measures made pre- and post-drug application being the lower level. The only element missing is the inclusion of which isolation cells came from. However, since each cell acts as its internal control, this would only be of relevance if the efficacy of the drug changes greatly depending on which isolation cells are derived from. To assess this we performed a full hierarchical test on an example dataset for wave frequency pre- and post-flecainide. This confirmed that using hierarchical models does not improve on a paired t-test in this case (Figure 9-12 in Appendix 9.5). Therefore the original analysis using paired t-tests and repeated-measures analysis of variance (ANOVA) were included.

7.4 Results

7.4.1 Flecainide has no effect on the Ca²⁺ Transient or SR Ca²⁺ Load

We first assessed the effect of 5 μ M flecainide on the amplitude of Ca²⁺ transients evoked by external field stimulation at 0.5Hz. Stimulation continued at the same rate during the 5 minute wash-on or wash-off periods. Ca²⁺ transient amplitude did not change significantly in the presence of flecainide (Figure 7-1B). Similarly, transient morphology was unchanged (Figure 9-10B-C in Appendix 9.5). SR load was measured using a 20mM caffeine spritz in 0Na⁺/0Ca²⁺ solution following field stimulation at 5Hz to mimic conditions used to assess waves (Figure 7-1C), and was unchanged by flecainide.

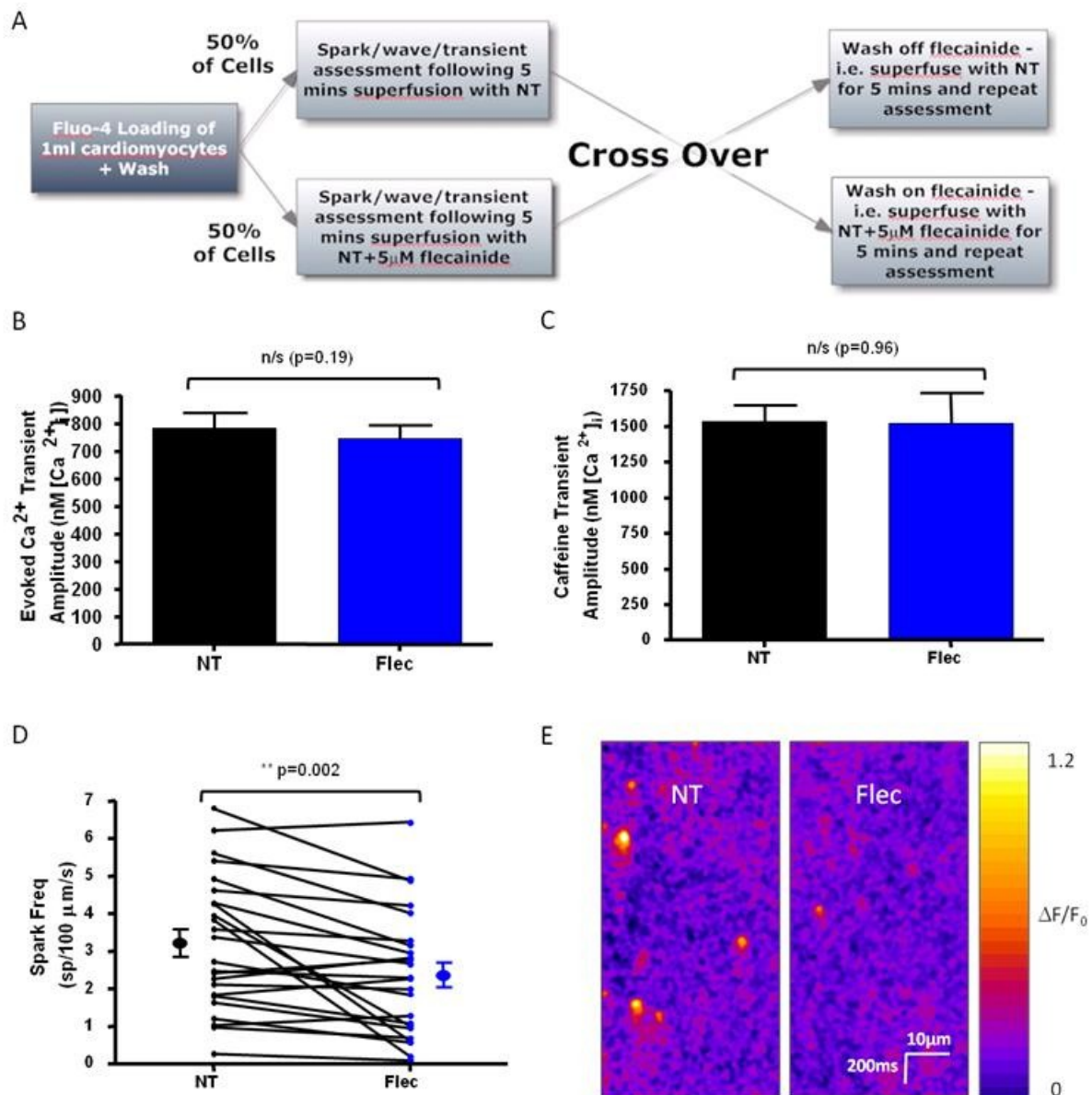


Figure 7-1. Experimental Protocol and Effects of Flecainide on Ca²⁺ transients and Ca²⁺ sparks. (A) Experimental flowchart to explain cross-over protocol used in experiments. 50% of cells had Normal Tyrode (NT) applied first with drug wash-on, whilst 50% had drug applied first and subsequently washed-off. (B) Stimulated Ca²⁺ transients were assessed using the ratiometric dye fura-2 calibrated to give [Ca²⁺]_i. Transient amplitude was not changed in the presence of 5 μ M

flecainide (n=30 cells, p=0.19). (C) 20mM Caffeine in 0Na⁺/0Ca²⁺ solution was used to assess SR Ca²⁺ load following a 5Hz contraction train. The amplitude was unchanged in presence of 5μM flecainide (n=13 cells in each group, p=0.96 by Student's t-test). (D) Spark frequency was reduced following flecainide application (n=24 cells, p=0.002). (E) Representative line-scans showing a reduction in spark frequency with flecainide. The same cell is shown before and after flecainide application.

7.4.2 Flecainide reduces Ca²⁺ Spark and Wave Frequency & Ca²⁺ Wave Velocity

Spark frequency was significantly reduced with exposure to flecainide compared to NT alone from 3.25±0.36 to 2.38 ±0.34 sp/100μm/s (Figure 7-1D-E). Spark morphology was unchanged (Figure 9-13 in Appendix 9.5).

We predicted that the reduction in spontaneous Ca²⁺ sparks from the SR in the presence of flecainide would result in a reduction in wave frequency. In order to test this hypothesis, 5 Hz stimulation was used to produce waves. There was a reduction in Ca²⁺ wave frequency in the presence of flecainide (Figure 7-2A) from 0.23±0.04 to 0.10±0.02 waves/s (p=0.001).

The time from last transient to first wave, defined as the “wave-free survival period” for each cell, and represented in Kaplan-Meier survival curve format in Figure 7-2B, was also significantly increased in the presence of flecainide. In addition, wave velocity was reduced (Figure 7-2C) from 146.4±4.7 to 130±5.8 μm/s (p=0.04 by Student's t-test) suggesting that wave propagation is also altered by flecainide. Confocal line-scanning reveals both the reduction in Ca²⁺ waves and how this is related to a reduction in spark frequency (Figure 7-2D). There was no additional reduction of wave frequency following 30 mins flecainide exposure compared to 5 mins (Figure 9-11A in Appendix 9.5). Wave amplitude did not change significantly in the presence of flecainide (Figure 9-11B in Appendix 9.5).

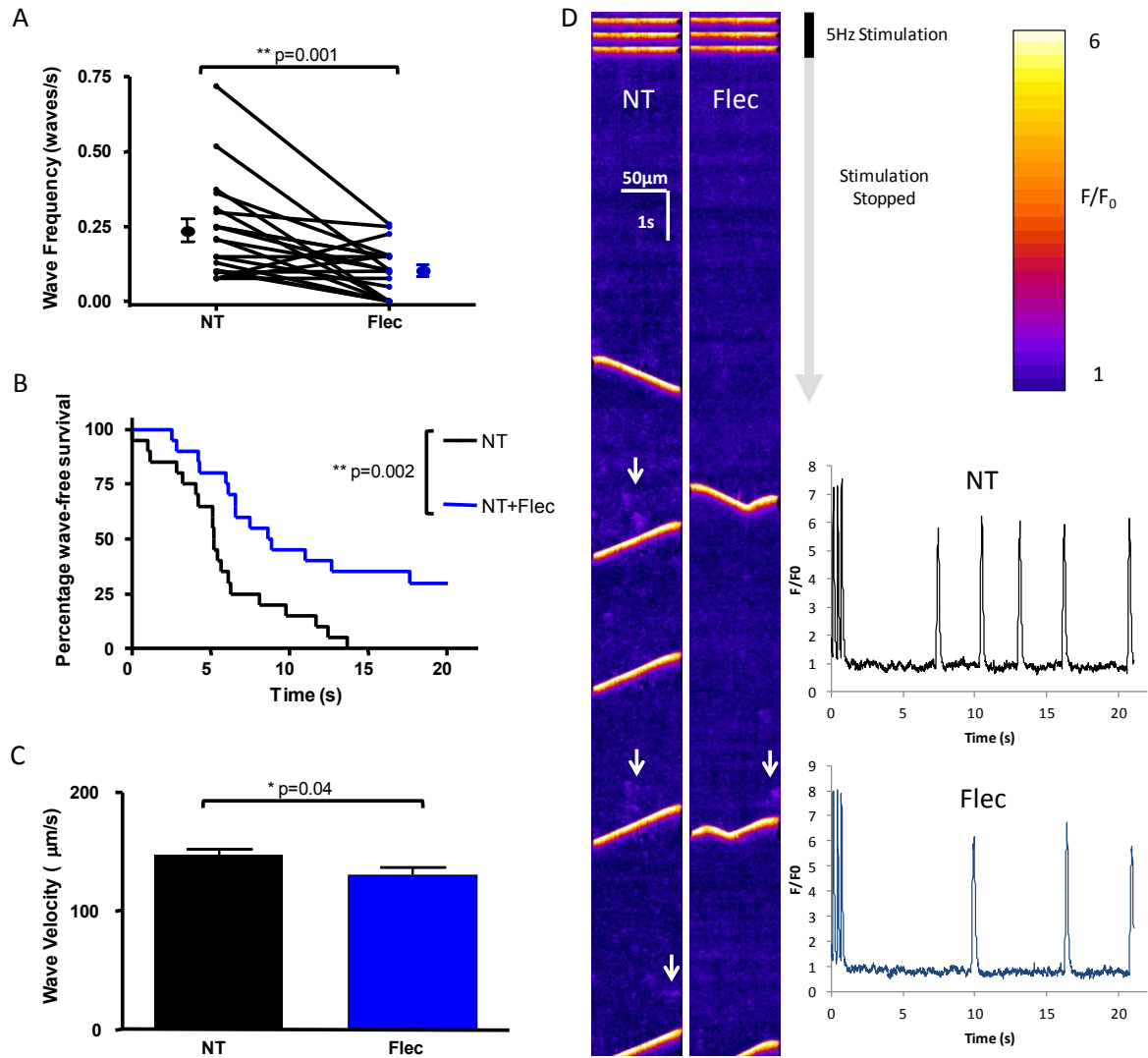


Figure 7-2. Effects of $5\mu\text{M}$ flecainide on Ca^{2+} waves.

(A) Flecainide was washed-on or off via cross-over protocol for 5 minutes. In the presence of flecainide wave frequency was significantly reduced ($p=0.001$, $n=20$ cells). (B) Latency period from last transient to first wave shown in Kaplan-Meier survival format (i.e. wave-free survival). Cells in the presence of flecainide have an increased wave-free survival period ($p=0.002$ by Logrank test, $n=20$ cells). (C) Wave velocity is reduced in the presence of flecainide ($p=0.04$ by Student's t -test, NT: $n=81$ waves; flec: $n=36$ waves from 20 cells). (D) Representative linescans from a cell assessed for waves pre- and post-flecainide application. The end of the 30s period of 5Hz stimulation evoking Ca^{2+} transients can be seen at the top of the scans with subsequent quiescent phase during which waves are observed. Areas of increased spark activity prior to waves are highlighted with white arrows and are more prominent in the absence of flecainide. Inset – linescans converted into F/F_0 plots - reduction of wave frequency and increased latency is apparent.

7.4.3 Specific I_{Na} Blockade Decreases Spark and Wave Frequency

There are two broad mechanisms which may be responsible for the reduction in Ca^{2+} waves in the presence of flecainide. Firstly, by blocking Ca^{2+} release from the RyR2, for which there is conflicting evidence in CPVT myocytes (Hilliard *et al.*, 2010; Liu *et al.*, 2011a), and secondly by inhibiting Na^+

influx with subsequent downstream effects. We aimed to assess the latter possibility – namely whether SR Ca^{2+} release can be altered by reducing Na^+ influx.

We therefore assessed the effect of specific pharmacological inhibition of I_{Na} using 5 μM tetrodotoxin (TTX), a dose which was selected since it provides 25% I_{Na} blockade in cardiomyocytes (Baer *et al.*, 1976), which is similar to that provided by 5 μM flecainide (Nitta *et al.*, 1992), whilst still allowing Ca^{2+} transients to occur with external field stimulation. Spark frequency was reduced (Figure 7-3A) from 3.76 ± 0.48 to 2.24 ± 0.52 sp/ $\mu\text{m/s}$ in the presence of TTX ($p=0.009$). TTX also significantly reduced wave frequency (Figure 7-3B) and caused a reduction in wave velocity (Figure 7-3C) without changing wave amplitude (Figure 9-11B in Appendix 9.5). Similar to results with flecainide, application of TTX at this concentration resulted in no significant alteration of SR load (Figure 7-3D). To assess whether this was a general property of other I_{Na} blockers, further experiments to assess wave frequency under similar degrees of I_{Na} blockade by 5 μM propafenone (Kohlhardt, 1984) and 200 μM lidocaine (Furukawa *et al.*, 1995) were carried out. Both agents reduced waves in a similar manner to flecainide and TTX (Figure 7-3E-F). Together, these results strongly suggest that reducing I_{Na} inhibits Ca^{2+} wave formation.

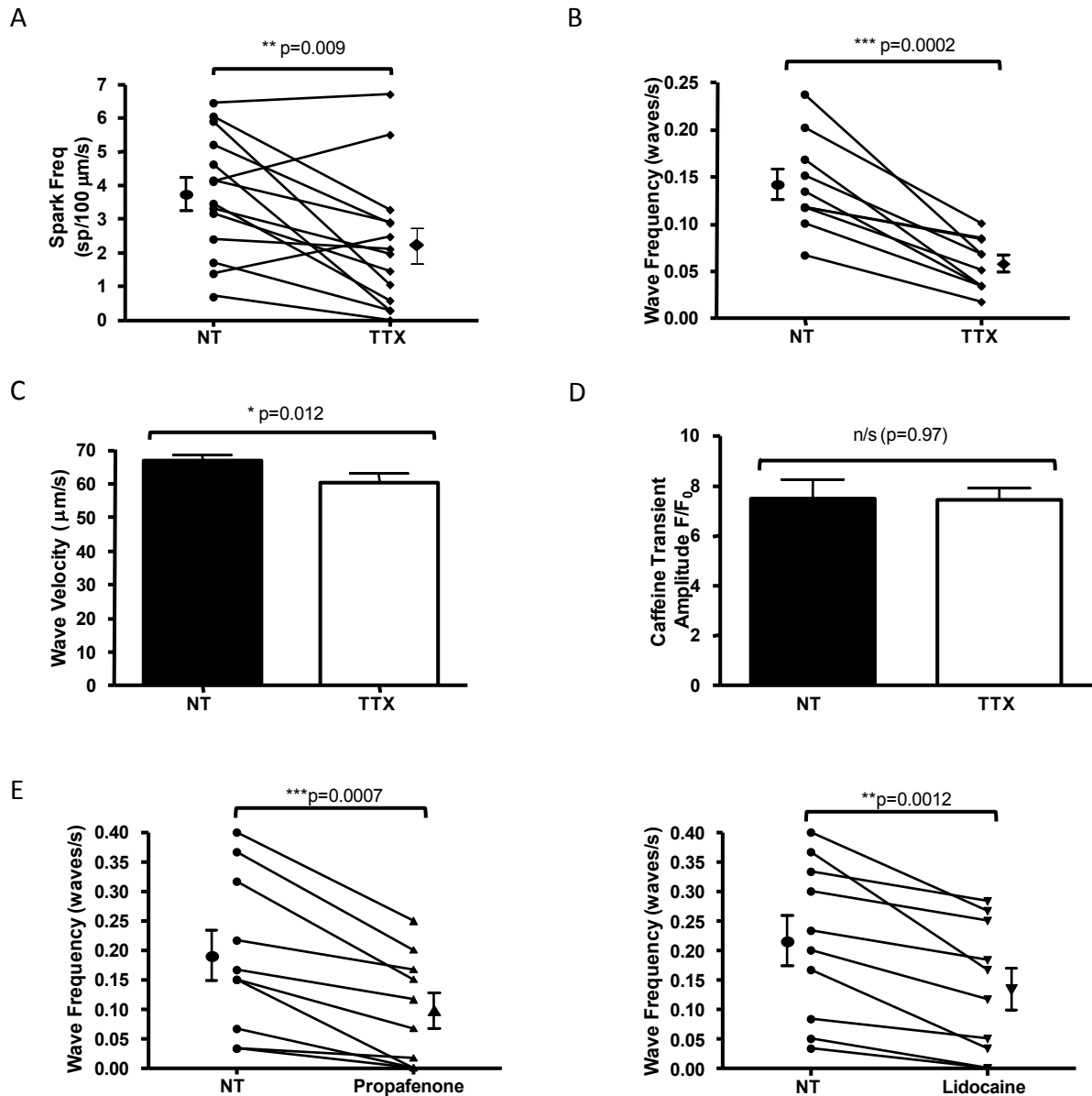


Figure 7-3. Effects of specific I_{Na} inhibition by tetrodotoxin (TTX) on SR Ca^{2+} release events.

(A) 5 μM TTX applied via similar cross-over protocol to flecainide experiments induced a similar reduction in Ca^{2+} spark frequency ($p=0.009$, $n=14$ cells). (B) 5 μM TTX reduced wave frequency ($p=0.0002$, $n=10$ cells) (C) Wave velocity is significantly reduced in the presence of TTX ($p=0.012$), NT $n=84$ waves; TTX $n=34$ waves from 10 cells). (D) Similar to flecainide experiments, no significant change in SR load was seen in the presence of 5 μM TTX ($p=0.97$ by Student's t -test, $n=20$ cells from 3 isolations). (E) 5 μM propafenone reduced Ca^{2+} wave frequency in a similar manner ($p=0.0007$, $n=10$ cells), as did (F) 200 μM lidocaine ($p=0.0012$, $n=10$ cells).

7.4.4 How does I_{Na} reduction decrease Ca^{2+} Waves?

Two main possibilities could explain the involvement of I_{Na} in wave formation. The first is that Na^+ entry via $Na_v1.5$ channels alters the sub-sarcolemmal "fuzzy" space $[Na^+]$ which subsequently modifies wave propagation via a number of possible downstream mechanisms ("Mechanism A" -

Figure 7-4A). The second is that $\text{Na}_v1.5$ channel activation is involved in the process of wave initiation and propagation more directly at the wave-front (“Mechanism B” - Figure 7-4B).

If “Mechanism A” is accurate, then given its dependence on Na^+ influx via $\text{Na}_v1.5$, wave frequency should be reduced by an intervention which reduces Na^+ influx during the contraction train but leaves $\text{Na}_v1.5$ channels available during the quiescent period following the contraction train. Such a scenario was created using a voltage-clamp technique to inactivate I_{Na} during the stimulation train. Cells were stimulated by a 5Hz train of clamp pulses (100 ms in duration) from -80 to 0mV repeatedly for 1min and waves assessed during a subsequent 30s quiescent period when the cells were held at -80mV. The same cell was re-stimulated by another train of pulses from -40 to 0mV, thereby removing Na^+ influx due to I_{Na} inactivation. The final holding potential during the quiescent period was -80mV as before to ensure availability of $\text{Na}_v1.5$ channels (Figure 7-5A). There was a significant reduction in wave frequency from 0.30 ± 0.04 to 0.16 ± 0.03 waves/s following inactivation of I_{Na} by voltage-clamp (Figure 7-5B), suggesting greater importance of “Mechanism A”.

To confirm these finding and assess whether “Mechanism B” might also be playing a role we designed an experiment which would allow normal Na^+ influx during the contraction train but would profoundly reduce availability of $\text{Na}_v1.5$ channels during the quiescent phase. A stimulation train was induced by external field stimulation for 30s at 5Hz and waves were assessed as before in the control condition (NT + vehicle). The same cell was then exposed to the same protocol but high dose TTX ($50\mu\text{M}$ TTX which blocks over 95% of I_{Na} (Baer *et al.*, 1976)) was superfused over cells rapidly after 30s stimulation in NT to stop the contraction train. This caused contractions and stimulated Ca^{2+} transients to cease almost immediately despite continuation of field stimulation at the same voltage (see Figure 9-14 in Appendix 9.5 for further explanation). This provided evidence of $\text{Na}_v1.5$ blockade during the quiescent period whilst ensuring the SR loading protocol was identical. Results of these experiments showed that acute, profound $\text{Na}_v1.5$ blockade in the quiescent phase did not alter Ca^{2+} wave frequency or velocity (Figure 7-5C&D) suggesting that “Mechanism B” either does not occur or is of minor importance compared to “Mechanism A”.

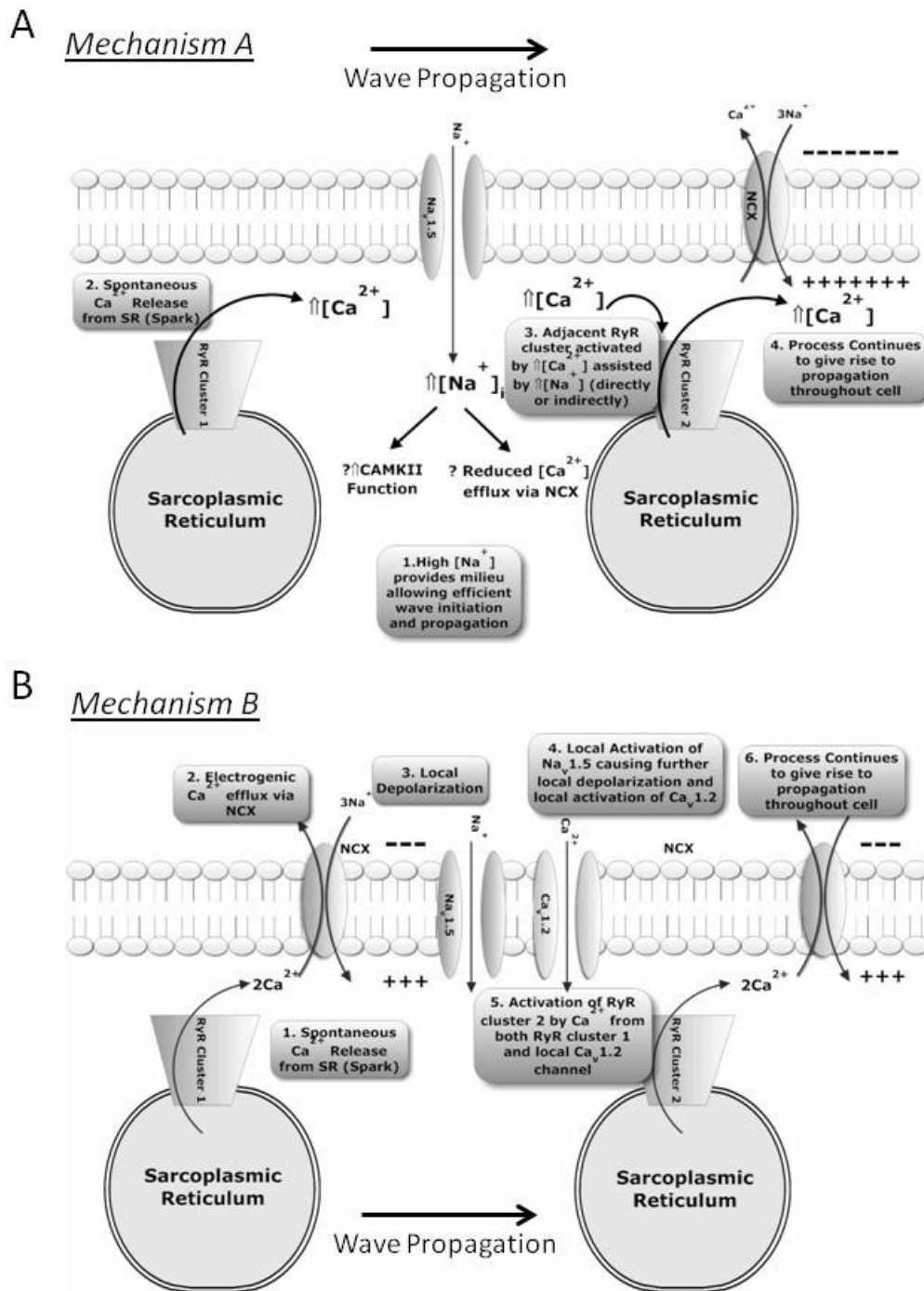


Figure 7-4. Possible hypotheses to explain how I_{Na} can contribute to wave initiation and propagation.

(A) Entry of Na^+ ions occurs via I_{Na} and an alteration of wave properties may result from changes in $[\text{Na}^+]_i$, particularly in the sub-sarcolemmal space. In this proposed mechanism (1) increased fuzzy space $[\text{Na}^+]_i$ provides a milieu that enhances the probability of (2) Ca^{2+} sparks leading to (3) activation and firing of an adjacent RyR cluster to result in (4) wave initiation and propagation throughout the cell. (B) Alternatively $\text{Na}_v1.5$ channels may be involved in wave propagation per-se in the intact cardiomyocyte. Such involvement could comprise (1) Spontaneous SR Ca^{2+} release in the form of a spark resulting in (2) local Ca^{2+} efflux by NCX causing (3) local depolarization of the sarcolemma

which (4) subsequently results in local activation of small populations of I_{Na} and I_{Ca} assisting the rise in local (“fuzzy space”) $[Ca^{2+}]_i$ that can lead to (5) adjacent RyR clusters firing and (6) wave propagation.

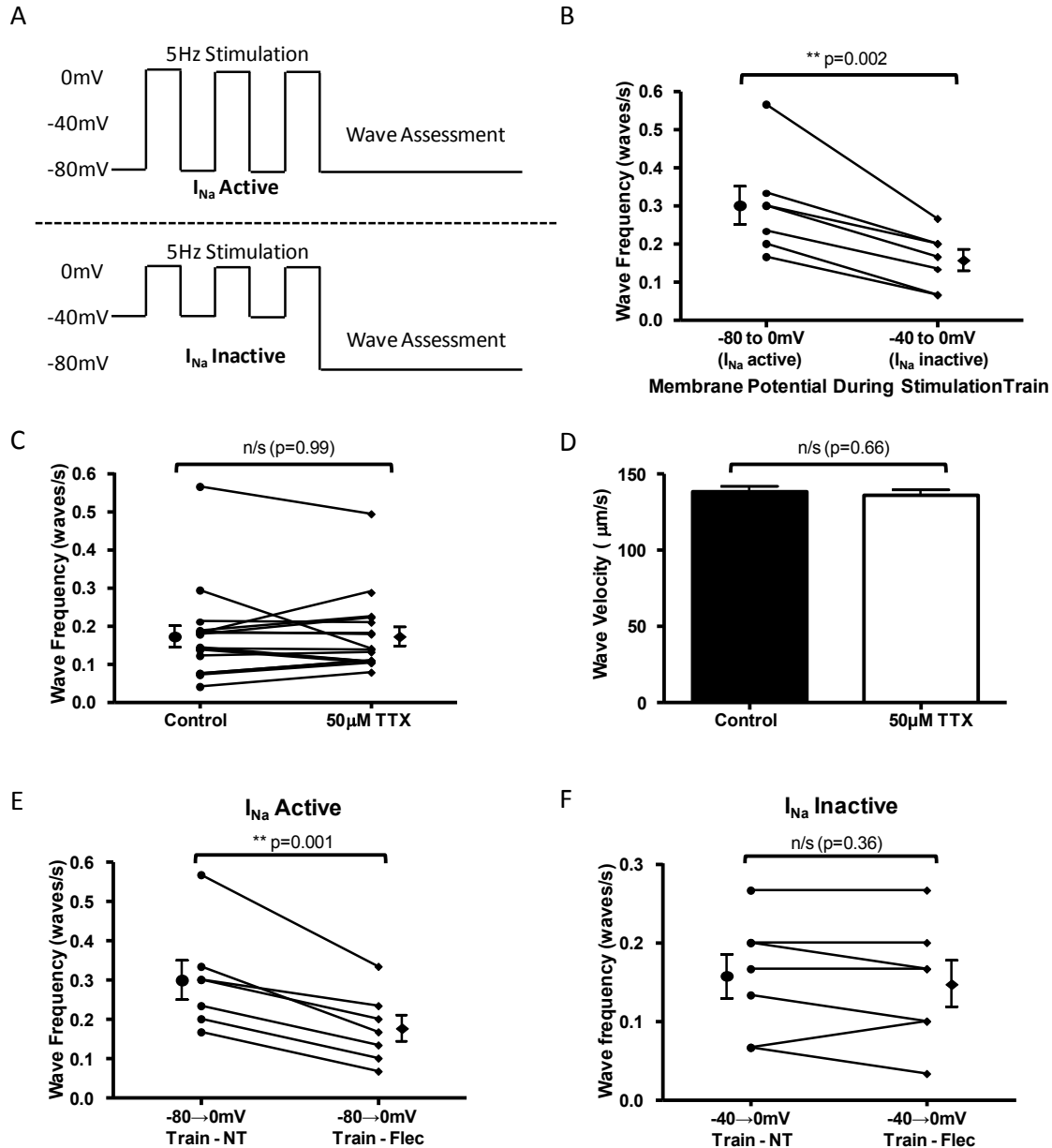


Figure 7-5. Elucidation of “Mechanism A” as most likely cause for reduction in Ca^{2+} waves due to I_{Na} blockade.

(A) Voltage clamp stimulation trains used to assess wave frequency with and without I_{Na} activity. Stimulation was induced by stepping from -80mV to 0mV (I_{Na} active) or -40mV to 0mV (I_{Na} inactive). Pulse duration was 100ms and pulses were applied at 5Hz. Waves were assessed in a subsequent 30s interval during which membrane potential was held at -80mV. (B) With I_{Na} inactive during the stimulation train (but available during the quiescent phase of the experiment), wave frequency was reduced ($p=0.002$, $n=7$ cells). (C) High dose (50μM) TTX was rapidly applied to cells to terminate stimulation following a period of external field stimulation at 5Hz and compared to the control arm in which stimulation was terminated in the usual fashion at 30s (see Figure 9-14 in Appendix 9.5 for

further explanation). This produced the opposite situation to the previous experiment with I_{Na} active during the stimulation train but $Na_v1.5$ channels unavailable for stimulation during the quiescent phase. This produced no change in wave frequency ($p=0.99$, $n=17$ cells). (D) Similarly there was no change in wave velocity ($p=0.66$ by Student's t -test. Control: $n=88$ waves; $50\mu M$ TTX $n=89$ waves from 17 cells). (E) Voltage clamp experiments showing effects of flecainide on wave frequency with I_{Na} active vs inactive. With I_{Na} active flecainide reduces wave frequency ($p=0.001$, $n=7$ cells). (F) However with I_{Na} inactive, no reduction in wave frequency was observed ($p=0.36$, $n=7$ cells).

7.4.5 Mechanism of Wave Reduction with flecainide

Having shown that I_{Na} reduction during the contraction train can reduce the frequency and velocity of Ca²⁺ waves, we wished to assess whether this effect also played a role in the effects we had observed with flecainide. We first assessed whether, in the absence of I_{Na} , flecainide would still reduce wave frequency - potentially through an additional effect on the RyR2. In order to test this possibility, we performed voltage clamp experiments. With a stimulation train of voltage clamp steps from -80 to 0mV, as expected, there was a significant reduction in Ca²⁺ waves (Figure 7-5E) in the presence of flecainide. However, when the stimulation train was induced by voltage steps from -40 to 0mV (and so I_{Na} was inactivated), there was no significant reduction in Ca²⁺ wave frequency (Figure 7-5F) in the presence of flecainide. This provided evidence that reduced Na⁺ influx was crucial in flecainide's mechanism of wave reduction.

To investigate how the changes in Na⁺ influx into the cytosol altered wave frequency we identified two possibilities that we felt were most likely to be the cause of the change. Firstly a reduction in Ca²⁺/calmodulin-dependent protein kinase II (CamKII) activity as a result of reduced $[Na^+]_i$ (Yao *et al.*, 2011) or $[Ca^{2+}]_i$, and secondly as a result of enhanced Ca²⁺ efflux across the sarcolemma via NCX because of an enhanced $[Na^+]_o$: $[Na^+]_i$ gradient.

In order to investigate the former possibility, we used $1\mu M$ KN-93 to inhibit CamKII prior to addition of flecainide. In the presence of either KN-93 (Figure 7-6A) or KN-92 (Figure 9-15A in Appendix 9.5), flecainide remained able to reduce Ca²⁺ wave frequency.

We subsequently assessed NCX function by observing the rate constant of Ca²⁺ efflux following a caffeine transient in NT under the same conditions as waves were assessed. There was a significant increase in Ca²⁺ efflux via NCX following a contraction train in the presence of flecainide (Figure 7-6B). We subsequently assessed how such efflux would affect diastolic $[Ca^{2+}]_i$ in the period following the last field-stimulated contraction and the first Ca²⁺ wave using the ratiometric dye fura-2. We found that there was a significant reduction in diastolic Ca²⁺ by 12% ($p=0.005$, Figure 9-15B in Appendix 9.5).

In order to assess whether the opposite effect would occur with inhibition of Ca²⁺ efflux via NCX we assessed the effects of partial NCX inhibition (Kimura *et al.*, 1987) with $1mM$ NiCl₂ following the contraction train and found an increase in waves (Figure 7-6C). Our working hypothesis at this point was that flecainide enhances Ca²⁺ efflux via a reduction of $[Na]_i$, enhancing the $[Na^+]_o$: $[Na^+]_i$ gradient. However this gradient can also be altered by changing $[Na^+]_o$. We sought to do this in the presence of flecainide to reverse the reduction in wave frequency. We found that a reduction of $[Na^+]_o$ after the contraction train from $140mM$ to $125mM$ was sufficient to reverse the wave reduction seen with

flecainide (Figure 7-6D-E). In order to ascertain whether the opposite effects would occur with I_{Na} enhancement we assessed whether $0.5\mu\text{M}$ veratridine could increase Ca^{2+} wave frequency. There was a significant increase in waves in the presence of veratridine which was reversed by increasing $[\text{Na}]_o$ from 115mM to 140mM (Figure 7-6F).

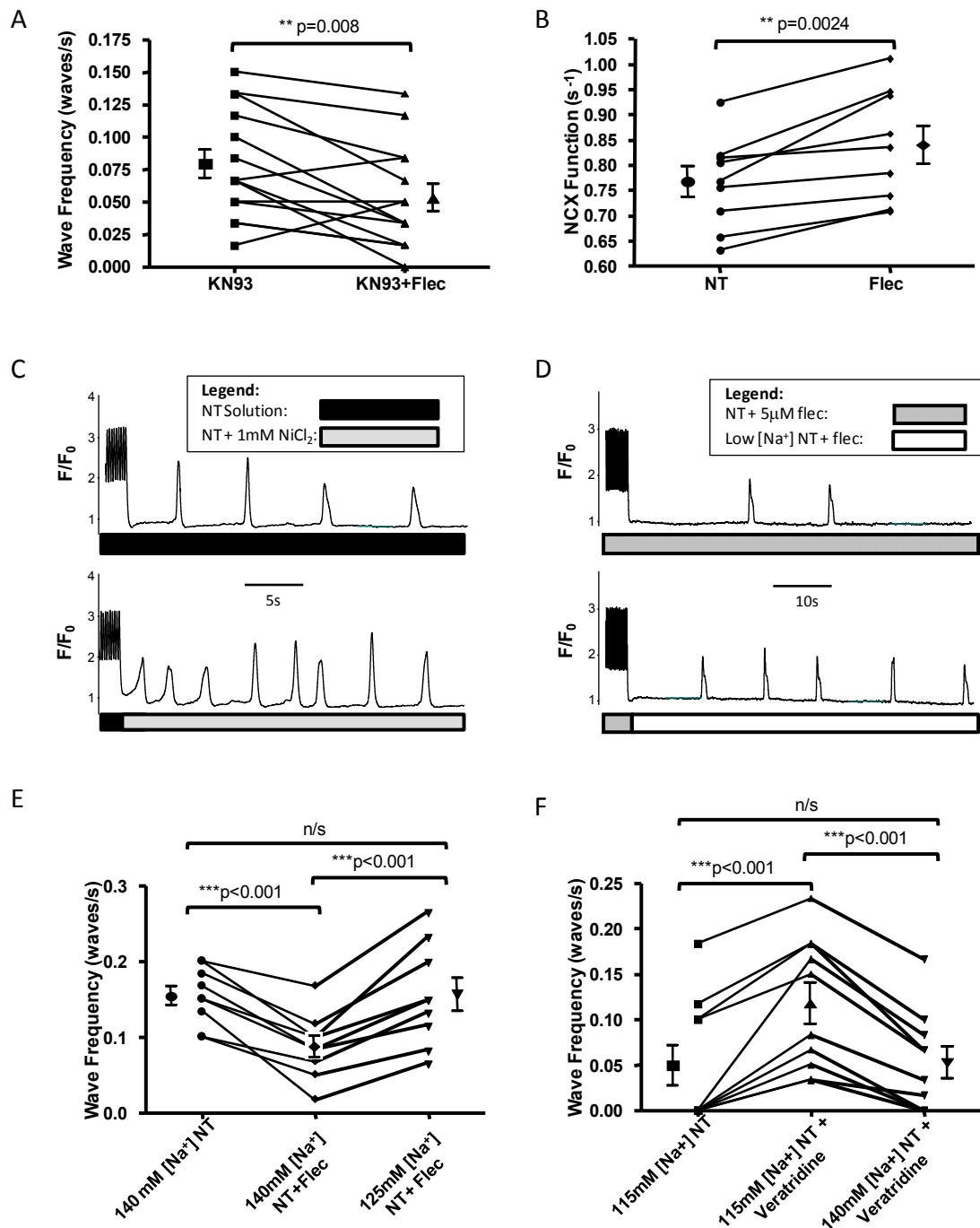


Figure 7-6. Role of CaMKII and NCX in wave reduction by flecainide.

Asa(A) Despite incubation of cells with $1\mu\text{M}$ CaMKII inhibitor KN-93, flecainide was still able to significantly reduce Ca^{2+} wave frequency. Magnitude of reduction was similar in the presence of inactive analogue KN-92 (online Fig VA) suggesting CaMKII inhibition is not the mechanism of wave reduction with flecainide. (B) NCX function in terms of Ca^{2+} efflux efficacy was significantly improved

following a 5Hz contraction train in the presence of flecainide. (C) Direct partial inhibition of NCX by 1mM Ni²⁺ applied after the contraction train increased Ca²⁺ wave frequency. (D) Reduction of [Na⁺]_o after the contraction train can reverse the reduction in wave frequency seen with flecainide. (E) Pooled data from experimental protocol shown in (D) revealing that a reduction in wave frequency induced by flecainide can be reversed by reducing [Na⁺]_o to 125mM. (F) 0.5μM Veratridine can increase Ca²⁺ wave frequency via enhancing I_{Na}. This effect was abolished by increasing [Na⁺]_o from 115 to 140mM.

7.4.6 Experiments on permeabilized myocytes confirm absence of direct effect of Na⁺ and Flecainide on RyR

The experiments thus far appeared to point to a predominant role of changes in rate of Ca²⁺ efflux via NCX in the reduction in Ca²⁺ waves caused by flecainide. However to confirm this we assessed how altering the concentrations of Na⁺ and flecainide within mock intracellular solutions would alter Ca²⁺ wave characteristics in permeabilized cardiomyocytes. To assess the sensitivity of our permeabilised cell preparation we first assessed the response to increasing free [Ca²⁺]. As expected, at 400nM free [Ca²⁺], wave frequency and amplitude was higher than at 100nM (Figure 9-16 in Appendix 9.5). Alteration of [Na⁺] did not change wave frequency or characteristics, and neither did increasing [flecainide] even up to 25μM (a supratherapeutic concentration) (Figure 7-7 & Figure 7-8). One possible reason why an unaltered wave frequency may be seen, even in a substance that is blocking RyR, is autoregulation. This type of effect was seen by Györke et al with application of tetracaine to cardiomyocytes resulting in an initial drop in SR Ca²⁺ release with subsequent normalization as SR Ca²⁺ content increases (Györke *et al.*, 1997), a process termed autoregulation by Eisner and colleagues (Eisner *et al.*, 2000). Since our observations took place at 2 minutes we performed further experiments at an earlier stage following application of flecainide. These showed no change in wave frequency or amplitude even immediately after flecainide application to permeabilised cardiomyocytes (Figure 7-9). Overall these results suggest that neither changing [Na⁺] nor [flecainide] in the vicinity of RyR has any effect on Ca²⁺ wave frequency or propagation.

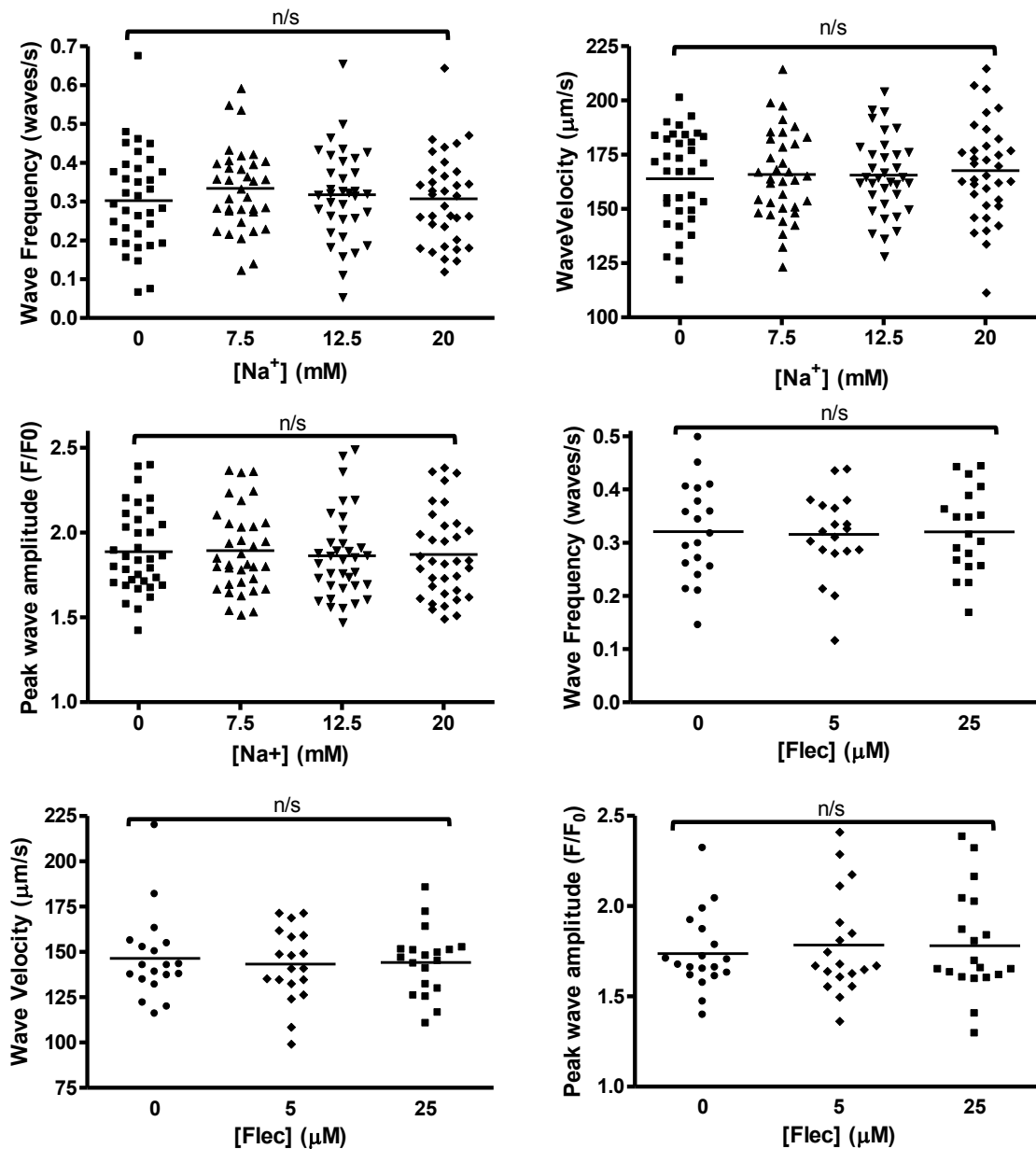


Figure 7-7. Neither changing $[\text{Na}^+]$ nor [flecainide] has any effect on waves in permeabilized cardiomyocytes.

Changing $[\text{Na}^+]$ through a wide range of concentrations has no effect on Ca^{2+} waves in permeabilized cardiomyocytes in terms of (A) frequency, (B) velocity and (C) amplitude. Changing concentration of flecainide from 0 to a therapeutically relevant concentration ($5\mu\text{M}$) and a supratherapeutic concentration ($25\mu\text{M}$) also has no effect on (D) frequency (E) velocity and (F) amplitude. Repeated measures ANOVA was non significant in all cases including pair-wise comparisons. $n=35$ cells for A-C and $n=19$ for D-F.

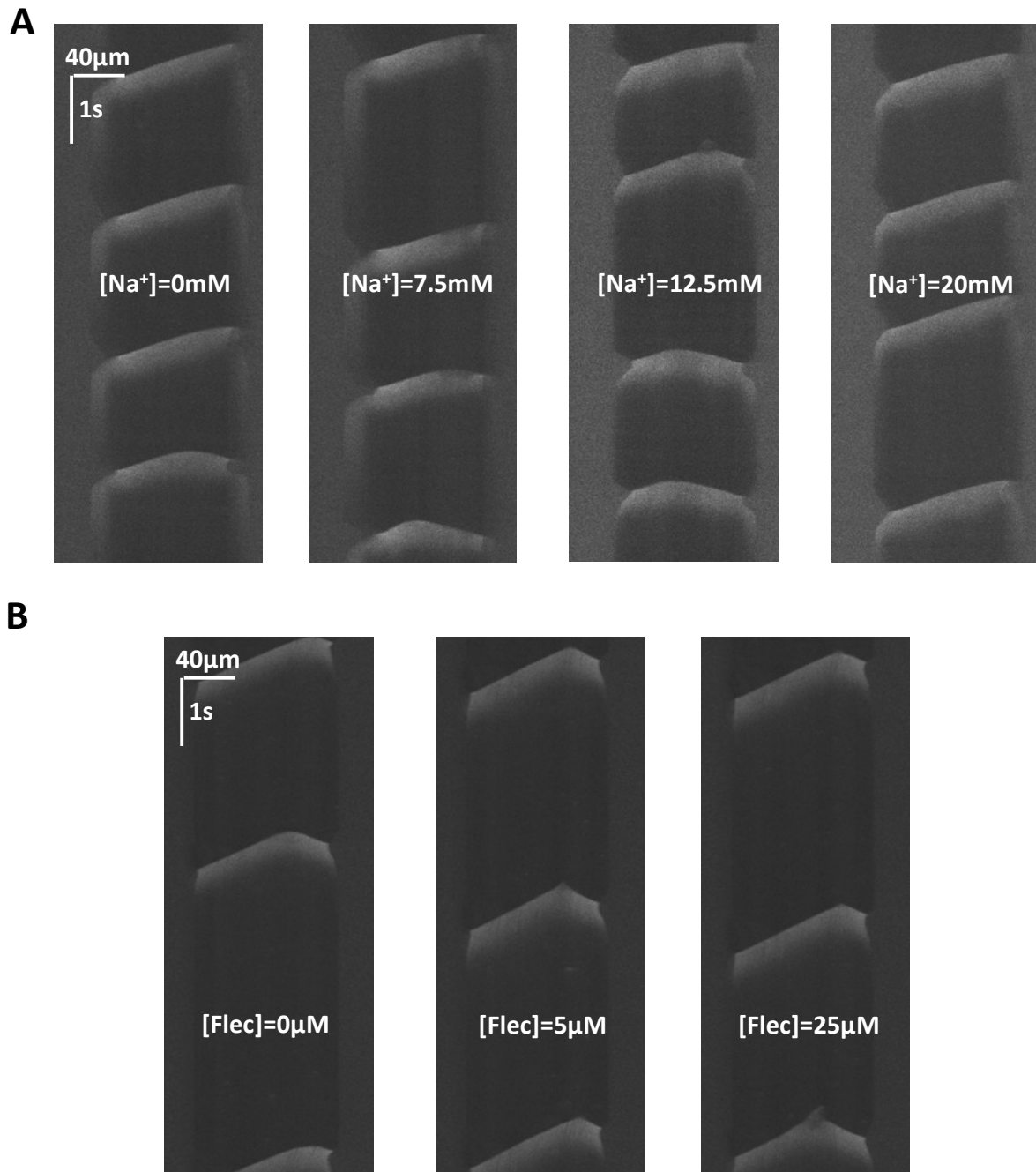


Figure 7-8. Raw data from permeabilized cells.

(A) Line-scans of the same cell with varying [Na⁺] in the mock intracellular solution showing no change in wave frequency or characteristics. (B) Similarly a cell with different concentrations of flecainide with similar wave frequency and characteristics throughout.

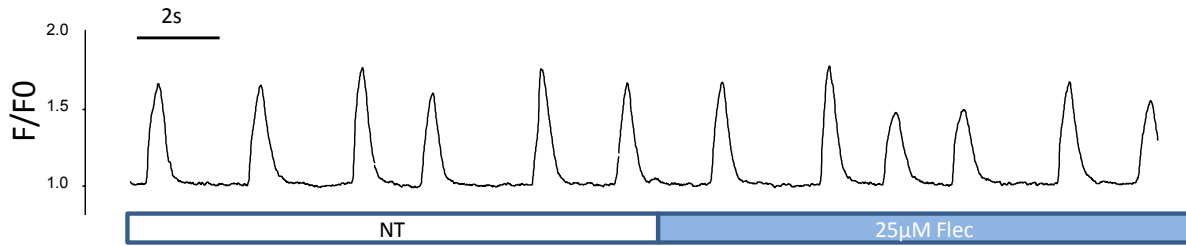


Figure 7-9. Fluorescence trace of permeabilised myocyte immediately after application of flecainide.

There is no drop in Ca^{2+} wave frequency immediately after flecainide is added in contrast with previous data with other RyR blockers such as tetracaine (Györke *et al.*, 1997).

7.5 Discussion

7.5.1 Main Findings

The main finding of this study is that a reduction of I_{Na} can reduce the frequency of Ca^{2+} sparks and waves and the velocity of Ca^{2+} waves. This holds true whether I_{Na} is pharmacologically reduced by a variety of agents or reduced by voltage clamp techniques. Initially we wished to clarify whether this occurred via altering the intracellular ionic milieu (“Mechanism A” – Figure 7-4A) or whether Na^+ influx was involved in the process of wave propagation itself (“Mechanism B” – Figure 7-4B). A series of experiments inactivating I_{Na} either during the stimulation train or the quiescent phase (Figure 7-5) confirmed that a reduction in Na^+ influx is the most important mechanism involved in reducing Ca^{2+} waves rather than implicating a role for $\text{Na}_v1.5$ channels at the Ca^{2+} wave-front. In further support of the importance of changes in cytosolic ionic milieu is the fact that very different I_{Na} blockers including the neurotoxin TTX, class 1c drugs flecainide and propafenone, and the class 1b drug lidocaine produce a similar reduction in Ca^{2+} wave frequency when concentrations producing similar degrees of I_{Na} blockade are used.

We used voltage-clamp to assess whether a reduction in I_{Na} was crucial for this effect. In the absence of I_{Na} , flecainide is not able to reduce Ca^{2+} waves suggesting dominance of this mechanism over RyR2 blockade under our conditions.

The question of how the alteration in cellular ionic milieu reduces Ca^{2+} waves is complex and may be multifactorial. A reduction in $[\text{Na}^+]_i$ is expected to increase $[\text{Ca}^{2+}]$ efflux across the sarcolemma via NCX and so there is additional complexity since both $[\text{Na}^+]_i$ and $[\text{Ca}^{2+}]_i$ may be altered. We went on to investigate how such changes contribute to wave reduction.

7.5.2 Mechanism of Wave Reduction Does Not Depend on CaMKII

Firstly Ca^{2+} /calmodulin complex (CaMKII), a major regulator of SR Ca^{2+} leak (Curran *et al.*, 2010), is effected both by $[\text{Ca}^{2+}]_i$ and also directly by $[\text{Na}^+]_i$ (Yao *et al.*, 2011). We investigated the efficacy of flecainide in Ca^{2+} wave reduction in the presence of KN-93, an inhibitor of CaMKII, and its inactive analog KN-92. Wave reduction still occurred in the presence of either compound. In addition the efficacy of wave reduction was unchanged whether KN-93 or KN-92 was present (35% vs 37% reduction respectively) suggesting that CaMKII inhibition does not have a major role in wave reduction due to I_{Na} inhibition. Another factor against a direct effect of alterations in $[\text{Na}^+]$ altering CaMKII activity is the lack of effect of changing $[\text{Na}^+]$ in permeabilised cells. Guo *et al.* confirmed activity of CaMKII in permeabilised myocytes (Guo *et al.*, 2006), and if changes in $[\text{Na}^+]$ were causing

changes in CaMKII activity directly we would expect a change in Ca²⁺ wave frequency or morphology in permeabilised myocytes exposed to different [Na⁺]_i whereas we observed no changes (Figure 7-7A-C).

7.5.3 Wave Reduction Does Not Result from Reduced SR Ca²⁺ Load

Another major possibility was that reduced [Na⁺]_i was resulting in enhanced Ca²⁺ efflux via NCX. This has the potential to decrease SR luminal [Ca²⁺]_i, however we found that neither 5μM flecainide nor 5μM TTX had significant effects on SR Ca²⁺ content. This is consistent with the work of previous investigators using similar doses of flecainide (Hilliard *et al.*, 2010; Liu *et al.*, 2011a). Altered NCX function could reduce waves by mechanisms unrelated to SR load however. For example, let us assume that almost maximal SR load was produced by our experimental conditions in the rat species, and that a tightly controlled SR luminal Ca²⁺ threshold exists beyond which sparks and waves occur. In this case if I_{Na} blockade enhances Ca²⁺ efflux via NCX, then SR load may reach threshold for spark and wave release less frequently since the SR Ca²⁺-ATPase would have more competition for Ca²⁺ ions in the fuzzy space. Since the threshold per-se would not change in this situation (no RyR2 modification), one may not observe lower SR load but simply less frequent SR Ca²⁺ release.

7.5.4 I_{Na} Reduction Increases Ca²⁺ Efflux via NCX which Reduces Ca²⁺ Waves

We performed experiments to assess the possibility of an NCX-mediated effect on Ca²⁺ waves despite the absence of SR Ca²⁺ load reduction. We assessed NCX function using the decay constant of NCX-mediated [Ca²⁺]_i decline in the presence of caffeine and confirmed that Ca²⁺ efflux via NCX was increased after a contraction train in the presence of flecainide (Figure 7-6B). This resulted in a slight reduction in diastolic [Ca²⁺]_i in the quiescent period following our contraction train as assessed by fura-2 fluorescence (Figure 9-15B in Appendix 9.5). In order to confirm the relevance of this mechanism we modulated NCX function in other ways. Direct partial inhibition of NCX (Kimura *et al.*, 1987) with 1mM Ni²⁺ applied after the contraction train increased Ca²⁺ waves (Figure 7-6C), suggesting that NCX is functioning predominantly in inward mode under our experimental conditions. Impairing NCX increases waves by reducing Ca²⁺ efflux. This helps to clarify how I_{Na} blockade might reduce Ca²⁺ waves. In the presence of lower [Na⁺]_i, NCX would provide more effective Ca²⁺ efflux at resting membrane potentials (Matsuoka & Hilgemann, 1992). On the other hand, a lower [Na⁺]_o would shift the reversal potential of NCX in the negative direction. As such, if altered NCX function resulting from reduced [Na⁺]_i was the cause of wave reduction in the presence of flecainide we expected that such an effect could be abrogated by a reduction in [Na⁺]_o. Indeed we found that reducing [Na⁺]_o from 140 to 125mM in the period following the contraction train completely reversed the reduction in Ca²⁺ waves seen with flecainide Figure 7-6E. These experiments also allow us to predict what reduction in [Na⁺]_i is caused by 5μM flecainide under our experimental conditions. The reversal potential of NCX is -65.9mV with [Na⁺]_o=140mM, [Na⁺]_i=14mM, [Ca²⁺]_o=2mM and [Ca²⁺]_i=150nM. To cause an identical reversal potential when [Na⁺]_o=125mM, [Na⁺]_i must also be reduced proportionally to 12.5mM. This suggests that the reduction in waves can be caused by a reduction in [Na⁺]_i of 1.5mM which seems a plausible effect.

We also provide evidence that an increase in I_{Na} can increase Ca²⁺ wave frequency using the Na_v1.5 channel activator veratridine (Figure 7-6F). The subsequent reduction in wave frequency by increasing [Na]_o shows that increasing Ca²⁺ efflux via NCX can reverse this effect.

Direct blockade of NCX function using a selective NCX blocker may have been a useful approach to highlight the importance of $[\text{Na}^+]_i$ on waves. However, most NCX blockers have off-target effects (Terracciano & Hancox, 2013). Even when these are limited, such as in the case of SEA-0400, they still produce a reduction of I_{Ca} via intracellular accumulation of Ca^{2+} which causes inhibition of the L-type Ca^{2+} current via Ca^{2+} -dependent inactivation (Antoons *et al.*, 2012). Hence it was felt that direct NCX blockade with small molecule inhibitors may yield results that could be more difficult to interpret than modulating NCX function via alterations in $[\text{Na}^+]_o$ to counteract the changes in $[\text{Na}^+]_o:[\text{Na}^+]_i$ gradient caused by I_{Na} blockade.

7.5.5 I_{Na} Blockers and SR Ca^{2+} Release

Although it is accepted that Na^+ influx can, via subsequent efflux by NCX, cause Ca^{2+} entry and generation of contractile force (Larbig *et al.*, 2010), and even that Ca^{2+} entry via the exchanger can induce Ca^{2+} sparks (Ritter *et al.*, 2003), NCX has been largely neglected in the investigation of how I_{Na} inhibitors can reduce SR Ca^{2+} release. This is largely because, at high concentrations (e.g. 20 μM flecainide) some I_{Na} inhibitors appear to have direct effects on RyR2 in permeabilized cells and lipid bilayer experiments (Watanabe *et al.*, 2009; Hilliard *et al.*, 2010; Galimberti & Knollmann, 2011). It is not possible to compare our experiments directly to such previous work since ventricular myocytes from mouse models of CPVT were used. In these studies contrasting results were presented with Knollman and co-workers reporting a reduction in wave frequency but increased spark frequency in both intact *Casq*^{-/-} and permeabilized normal rat ventricular myocytes (Watanabe *et al.*, 2009; Hilliard *et al.*, 2010) and Liu *et al.* finding no changes in sparks or waves with flecainide in either intact or permeabilized ventricular cardiomyocytes from RyR2^{R4496C/+} mice (Liu *et al.*, 2011a).

This inconsistency led us to investigate further despite the provision by Knollman's group of evidence that RyR2 inhibition rather than altered Na^+ flux is the predominant mechanism of action in their experiments. In contrast we find that without an active Na^+ current no reduction in waves can be observed with flecainide. In addition reduction in I_{Na} alone, via various pharmacological agents and voltage clamp techniques, is sufficient to cause a reduction in wave frequency via a reduction in the ability of NCX to efflux Ca^{2+} . Furthermore in permeabilised cardiomyocytes, where there is no active sarcolemmal I_{Na} or NCX activity there is no change in Ca^{2+} waves following flecainide application (Figure 7-7D-F). This lack of difference is not related to normalization of wave frequency over time due to autoregulation since we see no effect even in the early stages following flecainide application (Figure 7-9). Contributory to the differences between our work and other studies may be: (1) Species difference and lack of CPVT model in our experiments, and (2) lack of paired data in other studies which may reduce the power to detect differences in wave frequency, perhaps explaining the lack of efficacy seen with alternative I_{Na} blockers such as TTX and lidocaine by Hwang *et al.* (Hwang *et al.*, 2011).

7.6 Conclusions and Implications

Reducing Na^+ influx during contraction in the intact cardiomyocyte reduces spontaneous diastolic SR Ca^{2+} release both in the form of Ca^{2+} sparks and waves. Given that SR load is unchanged, this is the result of reduced $[\text{Ca}^{2+}]_i$ in the vicinity of the RyR2 (due to enhanced efflux via NCX) which reduces the open probability of the channel. In the intact rat cardiomyocyte this is the predominant mechanism of action for the reduction in Ca^{2+} waves seen with flecainide at therapeutic concentrations. Other means of reducing Na^+ influx, such as $I_{\text{Na,L}}$ reduction would be expected to reduce SR Ca^{2+} leak via similar mechanisms.

8 SUMMARY AND FINAL CONCLUSIONS

This thesis has aimed to investigate potentially arrhythmogenic SR Ca^{2+} leak, particularly with respect to our rat model of ischaemic HF, and to assess a novel mechanism by which this leak could be reduced. The different lines of investigation were quite varied so instead of a single discussion chapter, a relevant discussion section is present at the end of each chapter. As such what follows is a brief summary attempting to highlight the key findings and unify some common threads observed within the course of this work.

8.1 Key methodological techniques

Within this work, the first and most vital step was to ensure sound methodologies which reduce the chances of spurious conclusions being made. There were several important elements of this. Many have been published before, for example the use of planimetry and biometric/echocardiographic/PV data to ensure adequate myocardial infarctions and resultant heart failure (sections 2.2.2 & 2.3). In cellular experiments there are potentially thousands of different cells to choose from as a product of each isolation, of which a maximum of a dozen-or-so can be studied in the type of experiments outlined in this study. Therefore an un-biased method of cell selection is also vital (section 2.5.2). Without this, pre-formed judgements about how HF cells are likely to appear or behave might affect cell selection and therefore results of any study. Simple cross-over or latin-square experimental designs also helped to reduce the risk of bias that might be induced by always applying a pharmacological agent after the control experiment (section 7.3.6).

This thesis also includes some novel ways of analysing data which should also assist with accuracy of results and conclusions drawn. In terms of image processing we found an excellent way to do this was by creating computer based algorithms to analyse the data. We created bespoke macros to analyse Ca^{2+} transient morphology and dyssynchrony as well as Ca^{2+} wave data in ImageJ (Appendices 9.1.2-9.1.6) and used an algorithm that was already in widespread use for spark analysis (Picht *et al.*, 2007). The use of these algorithms ensured that images could be assessed efficiently, in full and in an unbiased manner.

A further methodological step was to ensure that the statistical techniques used were the most appropriate for the data collected (chapter 3). We found that one of the preconditions for using standard statistical methodologies – that of independence of data points – was breached by the data in this study. We found that the structure of the cellular data collected in this work was hierarchical. Hence cell data such as Ca^{2+} transient amplitude was clustered by which isolation the cell had come from (a 2-level hierarchy) and sub-cellular data such as Ca^{2+} spark amplitude was clustered according to which cell the spark was observed in and which isolation that cell had come from (a 3-level hierarchy). Data was significantly clustered within these hierarchical levels with high intra-class correlations in a number of data fields (e.g. 58% for spark amplitude). We applied hierarchical models to the analysis of Ca^{2+} transients and sparks from an the 8W post MI rat HF compared with appropriate AMCs and found that the hierarchical models had a significantly better “fit” to the data than standard techniques suggesting that it is appropriate to use such models with this data. In addition there were major differences in p-values assessed for several parameters when comparing the hierarchical tests with standard tests. We found that using standard methodologies led to a

number of type I errors with this sample dataset. Using hierarchical models we found that at 8W post MI there were no differences in spark parameters, transient rise time or transient decay but there was significant enhancement of Ca^{2+} transient amplitude. This conclusion is not mechanistically appealing but is more accurate than the alternative conclusions that would have been drawn in the absence of hierarchical methodologies (section 3.6). Overall we concluded that analysis of this type of data using standard techniques resulted in an increase in risk of type I error in a similar manner to the pseudoreplication that has previously been well documented in the neuroscience literature (Lazic, 2010).

8.2 *In Vivo* data confirms progression of HF

An important aspect of any animal model is to ensure that features of the human disease for which the model is a surrogate are recapitulated. In the case of HF, the early stages of disease frequently exhibit a compensatory phase where pump function is relatively well preserved (Brutsaert & De Keulenaer, 2006) with a subsequent decline which accelerates towards the end of the disease course.

We found that rats exhibit a gradual accumulation of fluid with significant increases in pulmonary weight and body weight compared with TL^3 by 16W post MI. Surprisingly cardiac hypertrophy was most marked at 4W post MI than 16W, perhaps related to inability to maintain hypertrophy in older animals (Isoyama *et al.*, 1987). LV dilatation assessed both in terms of diastolic dimension (echocardiographic data) and diastolic volume (PV loop data) was assessed at 4 and 16W timepoints post MI corrected to their respective AMCs. We found significant dilatation only at later timepoints. Posterior wall thickness (remote from the infarct) was unchanged compared with AMCs at either timepoint. Hence this conforms with the idea of eccentric hypertrophy over time – similar adverse remodelling is observed in humans post MI (Grossman *et al.*, 1975). Although ejection fraction was unchanged at 16WMI timepoint versus 4WMI, some aspects of cardiac function showed deterioration over time. Particularly marked was the change in ESPVR, a preload independent measure of LV systolic function, between 4 and 16W post MI. Overall, in general agreement with the paradigm of Mann (Mann, 1999), we found that our HF model exhibits an immediate decline following the insult that begins the process of HF (in this case MI), followed by a gradual deterioration which sometimes resulted in premature death (section 2.2.1).

8.3 Cardiomyocyte structure and function in HF

8.3.1 Cell morphology and Ca^{2+} transients

Consistent with the cardiac hypertrophy and adverse LV remodelling observed *in vivo* at later stages post MI we observed significant increases in cell size, both in terms of length and width, at the 16W post MI (established HF) stage. Borderzone cells remodelled slightly differently to cells from remote regions and were significantly shorter. There were no differences in Ca^{2+} transient amplitude or rise/decay kinetics in HF cells compared with AMC. In addition, contrary to much of the published literature (Heinzel *et al.*, 2011), we found no change in transient dyssynchrony post MI. There were some interesting observations in terms of the effect of isoprenaline on the heterogeneity of the Ca^{2+} transient. In agreement with previous published data isoprenaline reduced dyssynchrony of the rise phase of the transient (Litwin *et al.*, 2000), and we also found it reduces dyssynchrony of decay. Isoprenaline also has some adverse effects on cellular heterogeneity since it accentuates regional

differences in transient amplitude. However its effects on transient dyssynchrony were not significantly different between AMC cells and HF cells.

8.3.2 SCR in HF

In terms of spontaneous SR Ca^{2+} release we found some differences in HF compared with AMC. Although at baseline spark frequency and morphological parameters were no different there was a more marked response to isoprenaline in HF. In particular there was a significant rise in spark FWHM and mass in the presence of 30nM isoprenaline which did not occur in AMC. There was also some heterogeneity in SCR events with a more prolonged wave-free survival in borderzone cells compared with remote regions. Overall we concluded that whilst we had found no evidence of change in Ca^{2+} transients which could explain the contractile dysfunction post MI, there were some changes in spontaneous Ca^{2+} leak that might help explain the propensity to ventricular arrhythmia our group has seen in this model previously (Lyon *et al.*, 2011). Notably, at the earlier 8WMI timepoint, albeit under slightly different experimental conditions using Fura-2 instead of Fluo-4 as the Ca^{2+} -sensitive fluorophore our findings were slightly different (presented in chapters 3 and 6). We showed that Ca^{2+} transient amplitude was greater than control at this earlier timepoint and in addition Ca^{2+} waves were more frequent even under basal conditions. The enhanced Ca^{2+} transient amplitude may be part of the mechanism of compensation seen at earlier timepoints post MI. The increased Ca^{2+} wave frequency only at the 8WMI timepoint is surprising since one would expect arrhythmogenic events to increase in later stages of disease. However these finding parallel those in relation to I_{Ca} in various HF models which is often enhanced early in the course of disease (during the compensatory phase) and only normalizes or becomes reduced later on (Tomaselli *et al.*, 1999; Perrier *et al.*, 2004).

8.3.3 Correlation of cell ultrastructure and SCR

We took advantage of the enhanced wave frequency in the 8W post MI model to probe the relationship between cell ultrastructure and SCR in HF. This would not have been possible without the use of a novel form of optically sectioning microscopy – the OPM. This allowed imaging with high temporal and spatial resolution in 2-D and 3-D. We used hierarchical statistics to assess the relationship between visibility of t-tubules (assessed using CMO staining) and SCR events. Using 3-D imaging we found that the point of origin of a Ca^{2+} wave was most likely to be in an area of high t-tubule visibility. We assessed Ca^{2+} spark frequency and morphology using 2-D imaging and again found some significant relationships between where sparks originate and their characteristics. Sparks were most likely to occur in areas in which t-tubules were visible and within these regions at epitubular rather than paratubular sites. On the other hand sparks were both larger (in terms of area) and longer (in duration) at paratubular rather than epitubular sites. The reasons for these subcellular differences in SCR are not clear but suggest that a full understanding of the changes in SCR that occur in HF must take into account how cell ultrastructure changes in the condition.

8.4 Modulating SCR by reducing I_{Na}

We were interested in assessing further the use of flecainide in reducing arrhythmogenic SCR which had recently been proposed to be related to RyR2 blockade (Watanabe *et al.*, 2009; Hilliard *et al.*, 2010; Galimberti & Knollmann, 2011). We found that flecainide reduced both the frequency and velocity of Ca^{2+} waves and the frequency of Ca^{2+} sparks. Surprisingly, given previously published data (Hwang *et al.*, 2011), we found that other I_{Na} blockers had similar effects. In addition reducing I_{Na} by voltage clamp techniques had similar effects suggesting that pharmacological activity on RyR2 was not required to reduce SCR. Furthermore we found that flecainide could not reduce Ca^{2+} waves

when I_{Na} was inactive during voltage clamp experiments. Our suspicion that flecainide was reducing $[Na]_i$ to enhance efflux of Ca^{2+} via NCX was confirmed in further experiments. Finally we confirmed that neither the presence of flecainide nor changes in $[Na^+]_i$ in mock intracellular solutions changed Ca^{2+} wave frequency in permeabilized cells. As such we concluded that the predominant mode of action of flecainide in our experiments was a reduction in I_{Na} . Although flecainide cannot be used in HF (CAST Investigators, 1992), alternative methods of $[Na^+]_i$ reduction such as specific $I_{Na, Late}$ inhibition might be useful in the treatment of excess SCR in HF.

8.5 Final Conclusions

During the course of this thesis we have explored the fascinating contribution that SCR may make to arrhythmogenesis in HF. Furthermore we have made contributions to more robust methodologies which could be much more widely applied in the fields of myocyte biology – of which hierarchical statistics and the OPM probably have the broadest potential. Finally we have explored a novel mechanism for the reduction in SCR which could have application in the reduction of arrhythmogenesis in conditions such as CPVT and HF where such events cause sudden death.

9 APPENDICES

9.1 Appendix for Methods Chapter (2)

9.1.1 Biometric Correction to the Cube of Tibia Length is more appropriate than raw Tibia Length

A simple model was formulated where a heart was modeled as a small cube inside a body (larger cube). As the body weight increases, the heart weight increases in proportion with this. A linear measure was chosen to be the equivalent of tibia length (i.e. body length [BL]). Specific gravity of both the heart and body were assumed to be 1 and heart size in terms of mass increased proportionally to body mass. Figure 9-1A shows the simplified model. HL is heart length and BL is body length. Figure 9-1B shows what happens to the ratio of heart weight (HW) to BL as the animal grows (blue points). This measure is inherently unstable as size increases since a volume scaled measure (i.e. mass) is divided by a linear scaled measure (i.e. length). To correct for this instability BL must be cubed (red points). Data from control animals used in this study (Figure 9-1C-D) mirrors the findings of the simple model.

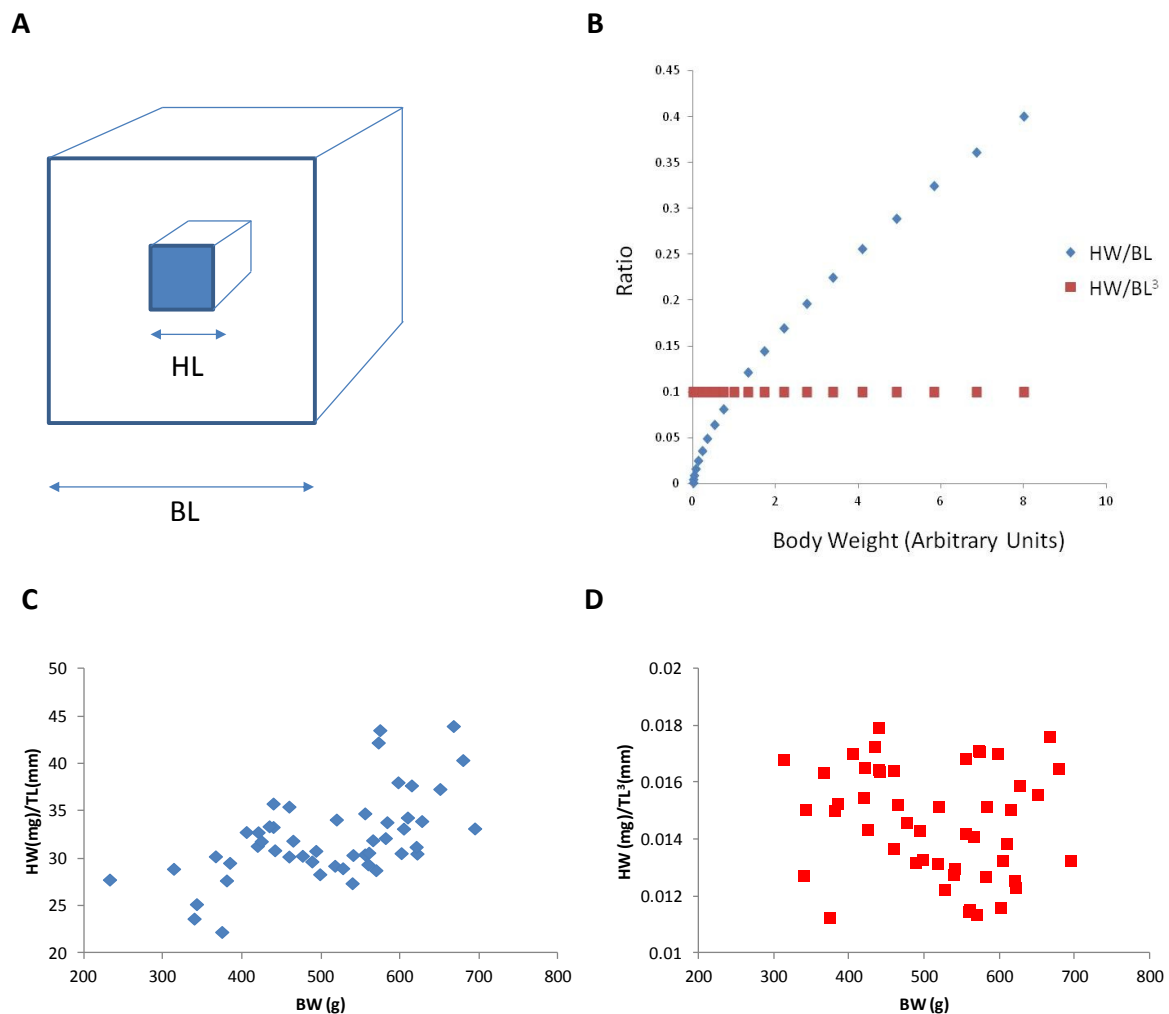


Figure 9-1. Simple model and real data from control rats showing HW/TL^3 is constant with changes of overall body size whilst HW/TL is unstable.

(A) Model system is a simple cube inside a larger cube where the volumes of both increase in proportion with each other. (B) The ratio of HW to BL^3 (blue points) is more stable over different body weights than the ratio of HW to BL (red points). This is mirrored by real data from control animals in which there is a positive correlation between BW and BW/TL but no obvious correlation between BW and BW/TL^3 .

9.1.2 Transient Analysis Macro (ImageJ)

showMessage("Gaussian Filtration and Transient Analysis", "Written By Markus Sikkel - m.sikkel@imperial.ac.uk");

```

title=getTitle();
titlelen=lengthOf(title);
title=substring(title,0,titlelen-4);

width=getWidth();
height=getHeight();

getPixelSize(unit, pw, ph, pd);
mspl=ph*1000;
fs=1/ph;

ms1000=floor(1000/mspl);
ms300=floor(300/mspl);
ms200=floor(200/mspl);
ms100=floor(100/mspl);
ms50=floor(50/mspl);
ms30=floor(30/mspl);
ms10=floor(10/mspl);

backfinal=10000;
for(i=0;i<width-11;i++) {
    makeRectangle(i, 1, 10, 200);
    getStatistics(area, mean);
    if(mean<backfinal) {
        backfinal=mean;
        xback=i;
    }
}

for(i=0;i<height-200;i++) {
    makeRectangle(xback, i, 10, 200);
    getStatistics(area, mean);
    if(mean<backfinal) {
        backfinal=mean;
        yback=i;
    }
}

makeRectangle(xback, yback, 10, 200);

waitForUser("Please adjust selection for background subtraction if required");
getStatistics(area, backfinal);
background=getNumber("Adjust background fluorescence if required", backfinal);

makeRectangle(2*floor(width/5), 1, floor(width/5), height-2);
// Close open windows
if (isOpen("Log")) {
    selectWindow("Log");
    run("Close");
}

if (isOpen("Results")) {
    selectWindow("Results");
    run("Close");
}

if (isOpen("Profile")) {

```

```

        selectWindow("Profile");
        run("Close");
    }

//Batch mode makes
//setBatchMode(true);

// Set alt key down for vertical profiles
setKeyDown("alt");

//Identify a transient

updateDisplay();

p = getProfile();

Array.getStatistics(p, min, max, mean, stdDev);

threshold=(mean+max)/2;

for(i=1;i<height-2;i++)    {
    sum=0;
    for (j=0;j<19;j++)
        sum=sum+p[i+j];

    sum=sum/19;

    sum2=0;
    for (j=10;j<29; j++)
        sum2=sum2+p[i+j];

    sum2=sum2/19;

//makeRectangle(2*floor(width/5), i-floor(height/300), floor(width/5), floor(height/300));
//getStatistics(area,meanrec2);

    if(sum2>threshold && sum<threshold && i>floor(height/150) && p[i+10]>threshold)    {
        a=i+10;
        i=height+5;
        //ie exit loop
    }

}

xmin=0;
xmax=width;

for(i=0;i<floor(400/mspl);i++)    {

    e=0;
    for (x=0;e<1;x++)    {
        value=getPixel(x,a+i);
        if (p[a+i]<mean)
            e=1;
    }
    if (value>=mean)    {
        e=1;

        if (x>xmin)
            xmin = x;
    }
}
}

```

```

e=0;
for (x=width; e<1; x--) {
    value=getPixel(x,a+i);
    if (p[a+i]<mean)
        e=1;
    if (value>=mean) {
        e=1;
        if (x<xmax)
            xmax=x;
    }
}

}

}

xmax=xmax-floor(width/20);
xmin=xmin+floor(width/20);

makeRectangle(xmin, 1, xmax-xmin, height-2);

setTool("rectangle");
waitForUser("Please adjust selection if necessary");
setKeyDown("alt");
// Get profile and display values in "Log" window

profile = getProfile();
profilefilter=newArray(profile.length);

setTool("rectangle");

//print(profile.length);
t=0;

for(filterappropriate=0; filterappropriate<1;t=t+1)
{

fc=getNumber("What is your cutoff frequency as a proportion of the sampling frequency (must be <0.5)", 0.1);
if (fc>0.5)
    exit("fc cannot exceed fs/2");

sigma=0.132505/fc;

if (sigma>=0.62)
    nc=floor(4*sigma);
else
    nc=2;

gausscoeff=newArray(nc+1);

if (sigma>=0.62) {
//nc is # coefficients not counting central

    b=-0.5/(sigma*sigma);
    gausscoeff[0]=1;
    sum=0.5;

    for (i=1; i<nc; i++) {
        temp=exp((i*i)*b);
        gausscoeff[i]=temp;
        sum=sum+temp;
    }
}

```

```

// normalize coefficients such that total =1

sum=sum*2;

for (i=0; i<nc;i++)
    gausscoeff[i]=gausscoeff[i]/sum;

        } else    {
                //Alternate routine if narrow impulse response - only 3 terms used
                gausscoeff[1]=(sigma*sigma)/2;
                gausscoeff[0]=1-(2*gausscoeff[1]);
                }

//print ("nc="+nc);
//
//for (i=-nc; i<=nc; i++)    {
//    j=i;
//    if (j<0)
//        j=-j;
//    print (gausscoeff[j]);
//    }
//
// waitforUser("a");
//Actual filtering steps

for (pointloc=0; pointloc<profile.length; pointloc++)    {
    sum=0;

    for (i=-nc; i<=nc; i++)    {
        j=i;
        if (j<0)
            j=-j;

        pointmask=pointloc+i;
        if (pointmask<0)
            pointmask=0;
        if (pointmask>=profile.length-1)
            pointmask=profile.length-1;

        sum=sum+(gausscoeff[j]*profile[pointmask]);
    }

    profilefilter[pointloc]=sum;

}

Plot.create("Profile", "X", "Value", profilefilter);

run("Clear Results");

sum=0;
for (pointloc=0; pointloc<profile.length;pointloc++)    {
    if(profilefilter[pointloc]>sum)    {
        sum=profilefilter[pointloc];
        maxpointloc=pointloc;
    }

    setResult("original", pointloc, profile[pointloc]);
    setResult("filtered", pointloc, profilefilter[pointloc]);

}

updateResults;
Array.getStatistics(profile,min,max);

```



```

Plot.create("Profile", "X", "Value", profilefilter);
Plot.setLimits(maxpointloc-ms100, maxpointloc+ms30,min,max);
Plot.add("Profile", profile);
Plot.show();

filterappropriate=getBoolean("Filter appropriate?");

if (isOpen("Profile")) {
    selectWindow("Profile");
    run("Close");
}

}

stpt=a-120;

nt=0;
np=0;

transstart=newArray(100);
transend=newArray(100);
baseline=newArray(100);
basepost=newArray(100);

Array.getStatistics(profilefilter,minfilt, maxfilt, meanfilt);
threshfilt=((maxfilt-minfilt)*0.75)+minfilt;

h=ms30;
g=ms50;
    for(i=ms100+h; i<profilefilter.length-ms300;i+=ms10) {
        if(profilefilter[i]<threshfilt && profilefilter[i+ms10]>threshfilt) {
            init=i-ms100;
            np=np+1;

            addn=newArray(h);
            for (k=0;k<h;k++)
                addn[k]=profilefilter[init-k];

            Array.getStatistics(addn,mina,maxa,meana,stdDev);

//print(stdDev);

            baseline[nt]=meana;
            if(maxa>(meana+10*stdDev))
                top=maxa+2;
            else
                top=meana+10*stdDev;

            e=0;
            for(k=0;k<profile.length-init && e<1;k++) {
                if(profilefilter[init+k]>top) {
                    sum=256;
                    for(t=0;sum>meana+10*stdDev;t++)
                        sum=profilefilter[init+k-(t+1)];
                    transstart[nt]=init+k-t;
                    f=0;
                    endfile=profile.length-transstart[nt]-ms200;
                    for(l=ms200;l<endfile && f<1;l+=ms100)
                        {
                            ranger=newArray(g);
                            ranger2=newArray(g);

```

```

        {
            for(j=0;j<g;j++)
            {
                ranger[j]=profilefilter[transstart[nt]+l+j];
                ranger2[j]=profilefilter[transstart[nt]+l+j+ms100];
            }
            Array.getStatistics(ranger,min,max,mean);
            Array.getStatistics(ranger2,min2,max2,mean2);
            if(mean2>mean || pow((mean2-mean),2)<pow(0.5*stdDev,2))
            {
                transend[nt]=transstart[nt]+l;
                basepost[nt]=mean;
                nt=nt+1;
                f=1;
                e=1;
            }
        }
    }

    i=i+ms200;
}

Plot.create("Profile", "X", "Value", profilefilter);
Plot.show();

waitForUser("Macro has identified "+np+" transients "+nt+" of which decay to a stable baseline. "+nt+" will be analysed.");
if (isOpen("Profile")) {
    selectWindow("Profile");
    run("Close");
}

if(baseline[nt-1]>1.2*baseline[0] || baseline[nt-1]<0.8*baseline[0])
    showMessageWithCancel("Warning", "There is greater than 20% drift of baseline. Are you sure we should continue?");

Array.trim(transstart, nt);
Array.trim(transend, nt);
Array.trim(baseline, nt);
Array.trim(basepost, nt);

peakfluo=newArray(nt);
FF0=newArray(nt);

F10=newArray(nt);
F50=newArray(nt);
F90=newArray(nt);

FD70=newArray(nt);

FD10=newArray(nt);
FD50=newArray(nt);

T10to90=newArray(nt);

T80to40=newArray(nt);
T60to30=newArray(nt);
T40to20=newArray(nt);

```

```

tau=newArray(nt);
lamda=newArray(nt);

F90line=newArray(nt);
peakline=newArray(nt);
TtoPeak=newArray(nt);
R50=newArray(nt);
R90=newArray(nt);

for(i=0; i<nt; i++) {

    for(j=transstart[i];j<transend[i];j++) {
        if(profilefilter[j]>peakfluo[i]) {
            peakfluo[i]=profilefilter[j];
            peakline[i]=j;
        }
    }

    TtoPeak[i]=(peakline[i]-transstart[i])*mspl;

    F10[i]=((peakfluo[i]-baseline[i])*0.1)+baseline[i];
    F90[i]=((peakfluo[i]-baseline[i])*0.9)+baseline[i];
    FD10[i]=((peakfluo[i]-basepost[i])*0.1)+basepost[i];
    FD50[i]=((peakfluo[i]-basepost[i])*0.5)+basepost[i];
    FD70[i]=((peakfluo[i]-basepost[i])*0.7)+basepost[i];

    e=0;
    for(j=transstart[i];j<transend[i] && e<1;j++) {
        if(profilefilter[j]>=F10[i] && profilefilter[j]<=F90[i])
            T10to90[i]=T10to90[i]+1;
        if(profilefilter[j]>=F90[i]) {
            e=1;
            F90line[i]=j;
        }
    }

    T10to90[i]=T10to90[i]*mspl;

    e=0;
    sum=0;
    for(j=peakline[i];j<transend[i] && e<1;j++) {
        if(profilefilter[j]<FD50[i]) {
            sum=j;
            e=e+1;
        }
    }

    sum=j-peakline[i];
    R50[i]=sum*mspl;

    e=0;
    sum=0;
    for(j=peakline[i];j<transend[i] && e<1;j++) {
        if(profilefilter[j]<FD10[i]) {
            sum=j;
            e=e+1;
        }
    }
}

```

```

sum=j-peakline[i];
R90[i]=sum*mspl;

e=0;
sum=0;
for(j=peakline[i];j<transend[i] && e<1;j++) {
    if(profilefilter[j]<=FD70[i]) {
        decaystart=j;
        e=1;
    }
}

y=newArray(transend[i]-decaystart);
x=newArray(transend[i]-decaystart);

for(k=0; k<(transend[i]-decaystart); k++) {
    x[k]=k*mspl;
    y[k]=profilefilter[decaystart+k];
}

Fit.doFit("y=a*exp(-x/b)+c", x, y);
Fit.plot;
tau[i]=Fit.p(1);
lamda[i]=1/(tau[i]/1000);

waitForUser("curve fitting for decay of transient "+(i+1));

selectWindow("y=a*exp(-x/b)+c");
run("Close");
}

run("Clear Results");

for (i=0; i<nt; i++) {
    FF0[i]=(peakfluo[i]-background)/(baseline[i]-background);
    setResult("Label", i, i+1);
    // setResult("Transstart",i,transstart[i]);
    // setResult("Transend",i,transend[i]);
    // setResult("Peakline",i,peakline[i]);
    // setResult("Baseline", i, baseline[i]);
    // setResult("Basepost",i,basepost[i]);
    setResult("Peak Fluorescence-BG(u)", i, peakfluo[i]-background);
    // setResult("F10", i, F10[i]);
    // setResult("F90",i,F90[i]);
    // setResult("FD50",i,FD50[i]);
    // setResult("FD10",i,FD10[i]);
    setResult("Baseline-BG(u)", i, baseline[i]-background);
    setResult("Peak Fluorescence (F/F0)", i, FF0[i]);
    setResult("10%-90% Rise Time (ms)", i, T10to90[i]);
    setResult("Time to Peak (ms)", i, TtoPeak[i]);
    setResult("R50 (ms)", i, R50[i]);
    setResult("R90 (ms)", i, R90[i]);
    setResult("Tau (ms)", i, tau[i]);
    setResult("Lamda (s-1)", i, lamda[i]);
}

truebase=newArray(nt);

for(i=0;i<nt;i++)
    truebase[i]=baseline[i];

```

```

Array.getStatistics(peakfluo, min,max, meanpeak);
Array.getStatistics(truebase, min, max, mbase);
Array.getStatistics(FF0, min, max, meanFF0);
Array.getStatistics(T10to90, min, max, T10to90mean);
Array.getStatistics(TtoPeak, min, max, TtoPeakmean);
Array.getStatistics(R50, min, max, R50mean);
Array.getStatistics(R90, min, max, R90mean);
Array.getStatistics(tau, min, max, taumean);
Array.getStatistics(lamda, min, max, lamdamean);

//a="a";
//      setResult("Label", nt, " ");
//      setResult("Peak Fluorescence(u)", nt, a);
//      setResult("Baseline(u)", nt, a);
//      setResult("Peak Fluorescence (F/F0)", nt, a);
//      setResult("10%-90% Rise Time (ms)", nt, a);
//      setResult("Time to Peak (ms)", nt, a);
//      setResult("R50 (ms)", nt, a);
//      setResult("R90 (ms)", nt, a);

      setResult("Label", nt, "Average");
      setResult("Peak Fluorescence-BG(u)", nt, meanpeak-background);
      setResult("Baseline-BG(u)", nt, mbase-background);
      setResult("Peak Fluorescence (F/F0)", nt, meanFF0);
      setResult("10%-90% Rise Time (ms)", nt, T10to90mean);
      setResult("Time to Peak (ms)", nt, TtoPeakmean);
      setResult("R50 (ms)", nt, R50mean);
      setResult("R90 (ms)", nt, R90mean);
      setResult("Tau (ms)", nt, taumean);
      setResult("Lamda (s-1)", nt, lamdamean);

updateResults;

//for(i=0;i<i++ ) {
//      if(profilefilter[i]>mean)
//          a=a+1;
//      }
//

//for(i=0;i<a;i++) {
//      if(profilefilter[i]<mean)
//          proa=a+1;
//      }
//
//Analyse results

//filterstep=19;
//for (i=0; i<profile.length; i++) {
//filterpoint=0;
//      for (filterloop=0; filterloop<filterstep; filterloop++) {
//          pointloc=i+filterloop-((filterstep-1)/2);
//          if (pointloc<0) {
//              pointloc=0;
//          }
//          if (pointloc>511) {
//              pointloc=511;
//          }
//          filterpoint=filterpoint+profile[pointloc];
//      }
//

```

```
//
//filterpoint=filterpoint/filterstep;
//profilefilter[i]=filterpoint;
//print(profile[i]+","+filterpoint);
//
}
```

selectWindow("Results");

9.1.3 Macro for Transient Dyssynchrony Analysis (ImageI)

showMessage("Synchronicity Transient Analysis", "Written By Markus Sikkell - m.sikkell@imperial.ac.uk")

```
width=getWidth();
height=getHeight();

getPixelSize(unit, pw, ph, pd);
mspl=ph*1000;
segwidth=round(1.8/pw);
fs=1/ph;

ms1000=floor(1000/mspl);
ms750=floor(750/mspl);
ms300=floor(300/mspl);
ms200=floor(200/mspl);
ms150=floor(150/mspl);
ms100=floor(100/mspl);
ms75=floor(75/mspl);
ms50=floor(50/mspl);
ms40=floor(40/mspl);
ms30=floor(30/mspl);
ms10=floor(10/mspl);

t=getNumber("How many transients would you like to analyse in this linescan (you should be able to see the whole transient and its
decay)?", 3);

ampmax=newArray(t);
timepeak=newArray(t);
time90=newArray(t);
time50=newArray(t);
timetau=newArray(t);

y=ms50;
makeRectangle(2*floor(width/5), 1, floor(width/5), height-2);
// Close open windows
if (isOpen("Log")) {
    selectWindow("Log");
    run("Close");
}

if (isOpen("Results")) {
    selectWindow("Results");
    run("Close");
}

if (isOpen("Profile")) {
    selectWindow("Profile");
    run("Close");
}

//Batch mode makes
//setBatchMode(true);
// Set alt key down for vertical profiles
setKeyDown("alt");
//Identify a transient

updateDisplay();

p = getProfile();

Array.getStatistics(p, min, max, mean, stdDev);
```

```

threshold=(mean+max)/2;

//transient current=tc

for(tc=1;tc<=t;tc++) {

a=0;

for (x=floor(width/2);a<1;y++) {
//Previous

    makeRectangle((x-50), (y-ms50), 100, 30);
    getStatistics(area, mean);
    valuec=mean;

    makeRectangle((x-50), (y-ms10), 100, 30);
    getStatistics(area, mean);
    valued=mean;

//Current
    makeRectangle((x-50), (y-ms40), 100, 30);
    getStatistics(area, mean);
    valuea=mean;

    makeRectangle((x-50), y, 100, 30);
    getStatistics(area, mean);
    valueb=mean;

    comparisonc=valueb/valuea;
    comparisonp=valued/valuec;

    if ((comparisonc>2.0) && (comparisonc<comparisonp))
        a=a+1;

if (y>height)
    exit("end of file reached");

}

// working out where selection box is located
// yc is the y value at max contraction

if(tc==1) {

yc=y+ms150;

a=0;
for (x=0; a<2; x++) {
    value = getPixel(x,yc);
    if (value>=threshold) {
        a=a+1;
        xmin = x;
    }
}

a=0;
for (x=width; a<2; x--) {
    value = getPixel(x,yc);
    if (value>=threshold) {
        a=a+1;

```


Appendices

```
xmax = x;
    }
}

makeRectangle(floor(width/3), y-ms200, floor(width/3), ms100);

getStatistics(area, mean);
waitForUser("F0 will be recorded here. Adjust if necessary");
getStatistics(area, mean);
background=mean;
    }

w=xmax-xmin;
makeRectangle(xmin, y, w, ms100);

updateDisplay();

//Selecting next transient

setTool("zoom");
waitForUser("Please adjust selection if necessary");
getSelectionBounds(xmin, y, w, selectheight);

td=getBoolean("Would you like to analyse this transient?");

segnum=floor(w/segwidth);

//Analyse the transient
if (td==1) {
    ya=y-ms100;
    run("Clear Results");

    for(i=0;i<segnum;i++) {
        for(j=0;j<=ms750;j++) {
            makeRectangle(xmin+(i*segwidth), ya+j, segwidth,ms75);
            getStatistics(area, mean);
            setResult("segment"+i, j, mean);
        }
    }
    updateResults;

//reset arrays

    amax=newArray(segnum);
    ymax=newArray(segnum);
    a90max=newArray(segnum);
    y90max=newArray(segnum);
    amid=newArray(segnum);
    ymid=newArray(segnum);
    atau=newArray(segnum);
    ytau=newArray(segnum);

// Array.getStatistics(amax, min, max, mean, stdDev);
// print("MaxAmp" + "\t" + mean + "\t" + stdDev + "\t" + (max-min) + "\t" + lengthOf(amax));
// waitForUser("x");

    for(i=0;i<segnum;i++) {
        for(j=0;j<ms750;j++) {
            a=getResult("segment"+i, j);
            if (a>amax[i]) {
                amax[i]=a;
```

```

        ymax[i]=j;
    }
}

for(i=0; i<segnum; i++)
{
    b=getResult("segment"+i, 0);
    for(j=0; a90max[i]<(((amax[i]-b)*0.9)+b);j++) {
        a=getResult("segment"+i, j);
        if (a>a90max[i])
        {
            a90max[i]=a;
            y90max[i]=j;
        }
    }
}

for(i=0; i<segnum; i++)
{
    b=getResult("segment"+i, 0);
    for(j=0; amid[i]<(((amax[i]-b)*0.5)+b);j++) {
        a=getResult("segment"+i, j);
        if (a>amid[i])
        {
            amid[i]=a;
            ymid[i]=j;
        }
    }
}

for(i=0; i<segnum; i++)
{
    b=getResult("segment"+i, 0);
    for(j=ms750; atau[i]<(((amax[i]-b)*0.368)+b);j--) {
        a=getResult("segment"+i, j);
        if (a>atau[i])
        {
            atau[i]=a;
            ytau[i]=j-ymax[i];
        }
    }
}

}

// assign values to that transient

Array.getStatistics(amax, min, max, mean, stdDev);
ampmax[(tc-1)]=stdDev/background;

Array.getStatistics(ymax, min, max, mean, stdDev);
timepeak[(tc-1)]=stdDev*mspl;

Array.getStatistics(y90max, min, max, mean, stdDev);
time90[(tc-1)]=stdDev*mspl;

Array.getStatistics(ymid, min, max, mean, stdDev);
time50[(tc-1)]=stdDev*mspl;

Array.getStatistics(ytau, min, max, mean, stdDev);
timetau[(tc-1)]=stdDev*mspl;

//Move on to starting point for searching for next transient
if (td!=1)

```

Appendices

```
tc=tc-1;

y=y+100;

updateResults;

run("Clear Results");

for (i=0; i<t; i++) {
    setResult("Label", i, i+1);
    setResult("SD PeakAmp (F/F0)", i, ampmax[i]);
    setResult("SD Time to Peak (ms)", i, timepeak[i]);
    setResult("SD Time to 90% (ms)", i, time90[i]);
    setResult("SD Time to 50% (ms)", i, time50[i]);
    setResult("SD Tau (ms)", i, timetau[i]);
}

Array.getStatistics(ampmax, min,max, meanampmax);
Array.getStatistics(timepeak, min, max, meantimepeak);
Array.getStatistics(time90, min, max, meantime90);
Array.getStatistics(time50, min, max, meantime50);
Array.getStatistics(timetau, min, max, meantimetau);

setResult("Label", t, "Average");
setResult("SD PeakAmp (F/F0)", t, meanampmax);
setResult("SD Time to Peak (ms)", t, meantimepeak);
setResult("SD Time to 90% (ms)", t, meantime90);
setResult("SD Time to 50% (ms)", t, meantime50);
setResult("SD Tau (ms)", t, meantimetau);

updateResults;

selectWindow("Results");
```

9.1.4 Macro for Wave Detection and Characterization (ImageJ)

```

showMessage("Wave Assessment", "Written By Markus Sikkel - m.sikkel@imperial.ac.uk");
// number of waves

if (isOpen("Log")) {
    selectWindow("Log");
    run("Close");
}

if (isOpen("Results")) {
    selectWindow("Results");
    run("Close");
}

if (isOpen("Profile")) {
    selectWindow("Profile");
    run("Close");
}

w=getWidth();
h=getHeight();
getPixelSize(unit, pw, ph, pd);
mspl=ph*1000;

backfinal=10000;
for(i=0;i<w-11;i++) {
    makeRectangle(i, 1, 10, 200);
    getStatistics(area, mean);
    if(mean<backfinal) {
        backfinal=mean;
        xback=i;
    }
}

for(i=0;i<h-200;i++) {
    makeRectangle(xback, i, 10, 200);
    getStatistics(area, mean);
    if(mean<backfinal) {
        backfinal=mean;
        yback=i;
    }
}

makeRectangle(xback, yback, 10, 200);

waitForUser("Please adjust selection for background subtraction if required");
getStatistics(area, backfinal);
background=getNumber("Adjust background fluorescence if required", backfinal);

//work out where end of last trans is
makeRectangle(floor(w/3), 1, floor(w/3), h-2);
p = getProfile();
Array.getStatistics(p, minthresh, max, mean, stdDev);
threshold=(mean+max)/2;

e=0;
for(i=0;e<1;i++) {

    makeRectangle(floor(w/3), i+(50/mspl), floor(w/3), 50/mspl);
    getStatistics(area, mean2);
}

```

Appendices

```
makeRectangle(floor(w/3), i, floor(w/3), 50/mspl);
getStatistics(area, mean);

if(mean<threshold)
{
    waitForUser("Upper aspect of rectangle should be after last transient/start of scan");
    getSelectionCoordinates(x, y);
    startscan=y[0];
    e=1;
}

}

if (isOpen("Clipboard"))
{
    selectWindow("Clipboard");
    run("Close");
}

run("Copy to System");
run("System Clipboard");
run("8-bit");
run("Smooth", "stack");
run("Select All");
getStatistics(area, startbase);

if (isOpen("Clipboard"))
{
    selectWindow("Clipboard");
    run("Close");
}

scantime=ph*(h-startscan);

t=getNumber("How many waves?", 3);
wfreq=t/scantime;

velocity=newArray(t);
wavetime=newArray(t);
peak=newArray(t);
base=newArray(t);
interval=newArray(t-1);
abort=newArray(t);
interrupt=newArray(t);
simult=newArray(t);
basepost=newArray(t);

for(tc=0;tc<t;tc++)
{

if (isOpen("Clipboard"))
{
    selectWindow("Clipboard");
    run("Close");
}

setTool("line");
waitForUser("Draw a line along longest stable velocity section of wave number "+(tc+1));

//velocity
getLine(x1, y1, x2, y2, lineWidth);

xdiff=x2-x1;
ydiff=y2-y1;
```

```

xdist=xdiff*pw;
ytime=ydiff*ph;

velocity[tc]=sqrt(pow((xdist/ytime),2));

//time

if(y2<y1) {
    wavestart=y2;
    waveend=y1;
}
else {
    wavestart=y1;
    waveend=y2;
}

wavetime[tc]=ph*(wavestart-startscan);

//interval
if(tc>0)
    interval[tc-1]=wavetime[tc]-wavetime[tc-1];

//Other wave Info
abort[tc]=getBoolean("Is wave aborted (ie stops before going across cell)?");
interrupt[tc]=getBoolean("Is wave interrupted (but still goes across cell)?");
simult[tc]=getBoolean("Does wave have multiple start points (which extinguish)?");

//amplitude

if(waveend+1000/mspl<h)
    addit=2000/mspl;
else
    addit=h-waveend+1000/mspl;

makeRectangle(0, wavestart-1000/mspl,w,waveend-wavestart+addit);
run("Copy to System");
run("System Clipboard");
run("8-bit");

run("Smooth", "stack");
wclip=getWidth();
hclip=getHeight();
xmin=0;
xmax=wclip;

y=floor(hclip/2);

    e=0;
    for (x=0;e<10 && x<wclip;x++) {
        value=getPixel(x,y);
        if (value>=minthresh) {
            e=e+1;
            if (x>xmin)
                xmin = x;
        }
    }

    e=0;

```

Appendices

```

        for (x=wclip; e<10 && x>0; x--) {
            value=getPixel(x,y);
            if (value>=minthresh) {
                e=e+1;
                if (x<xmax)
                    xmax=x;
            }
        }

makeRectangle(xmin, 0, xmax-xmin, hclip);

setTool("rectangle");
waitForUser("Please adjust selection if necessary");
getSelectionBounds(xrec, yrec, wrec, hrec);

maxfluo=newArray(wrec);
linelength=floor(30/mspl);

for(xi=0; xi<wrec; xi++) {
    sum=0;
    for(yi=yrec;yi<yrec+hrec-linelength;yi++) {
        makeLine (xrec+xi,yi,xrec+xi,yi+linelength);
        getStatistics(area, mean);
        if(mean>sum)
            sum=mean;
    }
    maxfluo[xi]=sum;
}

Array.getStatistics(maxfluo, min,max, peak[tc]);

makeRectangle(xrec, yrec, wrec, linelength);
getStatistics(area, base[tc]);

makeRectangle(xrec, yrec+hrec-linelength, wrec, linelength);
getStatistics(area, basepost[tc]);

}
Array.getStatistics(peak, min,max, meanpeak);
Array.getStatistics(base, min,max, meanbase);
Array.getStatistics(basepost, min,max, meanbasepost);
Array.getStatistics(velocity, min,max, meanvelocity);
Array.getStatistics(abort, min,max, meanabort);
Array.getStatistics(interrupt, min,max, meaninterrupt);
Array.getStatistics(simult, min,max, meansimult);
Array.getStatistics(interval, min,max, meaninterval);

sum=startbase;
for(i=0;i<t-1;i++)
    sum=sum+basepost[i];

meanearly=sum/t;

run("Clear Results");

for (i=0; i<t; i++) {
    setResult("Label", i, i+1);
    setResult("Velocity (micrometre/s)", i, velocity[i]);
    setResult("Wave start time (s)",i,wavetime[i]);
}

```

```

    setResult("Peakfluo-BG",i,peak[i]-background);
    }

setResult("EarlyBaseline-BG",0,startbase-background);

for (i=0; i<t; i++)    {
    setResult("PreWBaseline-BG",i,base[i]-background);
    setResult("PostWBaseline-BG",i,basepost[i]-background);
    setResult("FF0",i, (peak[i]-background)/(base[i]-background));
    setResult("Aborted?",i,abort[i]);
    setResult("Interrupted?",i,interrupt[i]);
    setResult("Simultaneous?",i,simult[i]);
    }

for (i=0; i<t-1; i++)
    setResult("EarlyBaseline-BG",i+1,basepost[i]-background);

for(i=0;i<t-1;i++)
    setResult("Inter-Wave Interval (s)",i,interval[i]);


setResult("Label", t, "Average");
setResult("Velocity (micrometre/s)", t, meanvelocity);
setResult("Peakfluo-BG",t,meanpeak-background);
setResult("EarlyBaseline-BG",t,meaneearly-background);
setResult("PreWBaseline-BG",t,meanbase-background);
setResult("PostWBaseline-BG",t,meanbasepost-background);
setResult("FF0",t, (meanpeak-background)/(meanbase-background));
setResult("Aborted?",t,meanabort);
setResult("Interrupted?",t,meaninterrupt);
setResult("Simultaneous?",t,meansimult);
setResult("Inter-Wave Interval (s)",t,meaninterval);
setResult("Overall Frequency",t,wfreq);
setResult("ScanTime",t,scantime);

updateResults;

```


9.1.5 Macro for Spark Image Pre-Processing (Image)

```
showMessage("Spark Pre-Processing", "Written By Markus Sikkel - m.sikkel@imperial.ac.uk");

dir1=File.directory

title=getTitle();
titlelen=lengthOf(title);
title=substring(title,0,titlelen-4);

//Initially remove pixel info
getPixelSize(unit, pw, ph, pd);

showMessageWithCancel("Pixel width is " + pw + " micrometers (copied to clipboard)");
//
y=400;

width=getWidth();
height=getHeight();

ymax=height-1;

makeRectangle (0, 0, width,100);
p = getProfile();
Array.getStatistics(p, min, max, mean, stdDev);
threshold=mean;

a=0;

for (x=0; x<width && a<1; x++) {
    if (p[x]>threshold) {
        a=a+1;
        xmin = x+5;
    }
}

a=0;

for (x=width-1; x>0 && a<1; x--) {
    if (p[x]>threshold) {
        a=a+1;
        xmax= x-5;
    }
}

//define start y value
v=1;
makeRectangle (xmin, v, xmax-xmin, ymax-1);

updateDisplay();

setTool("point");
waitForUser("Please adjust box to exclude unusual features (e.g. waves)");

getStatistics(area, mean);
showMessageWithCancel("Mean Pixel value of selection is " + d2s(mean,2) + " please record");

run("Copy to System");
run("System Clipboard");
run("8-bit");
String.copy(pw);
```

```
run("SparkMaster ");  
  
selectWindow("Clipboard");  
save(dir1+title+"_FF0.tif");
```

9.1.6 Caffeine Transient Macro (ImageJ)

```
showMessage("Caffeine Transient Assessment", "Written By Markus Sikkel - m.sikkel@imperial.ac.uk");
title=getTitle();
titlelen=lengthOf(title);
title=substring(title,0,titlelen-4);

width=getWidth();
height=getHeight();

getPixelSize(unit, pw, ph, pd);
mspl=ph*1000;
fs=1/ph;

ms1000=floor(1000/mspl);
ms300=floor(300/mspl);
ms200=floor(200/mspl);
ms100=floor(100/mspl);
ms50=floor(50/mspl);
ms30=floor(30/mspl);
ms10=floor(10/mspl);

backfinal=10000;
for(i=0;i<width-11;i++) {
    makeRectangle(i, 1, 10, 200);
    getStatistics(area, mean);
    if(mean<backfinal) {
        backfinal=mean;
        xback=i;
    }
}
for(i=0;i<height-200;i++) {
    makeRectangle(xback, i, 10, 200);
    getStatistics(area, mean);
    if(mean<backfinal) {
        backfinal=mean;
        yback=i;
    }
}
makeRectangle(xback, yback, 10, 200);

waitForUser("Please adjust selection for background subtraction if required");
getStatistics(area, backfinal);
background=getNumber("Adjust background fluorescence if required", backfinal);

makeRectangle(2*floor(width/5), 1, floor(width/5), height);
// Close open windows
if (isOpen("Log")) {
    selectWindow("Log");
    run("Close");
}
if (isOpen("Results")) {
    selectWindow("Results");
    run("Close");
}
if (isOpen("Profile")) {
    selectWindow("Profile");
    run("Close");
}

//Batch mode makes
```

```

//setBatchMode(true);

// Set alt key down for vertical profiles
setKeyDown("alt");

//Identify a transient

updateDisplay();

p = getProfile();

Array.getStatistics(p, min, max, mean, stdDev);

runmean=newArray(floor(height/19));

for(i=0; i<height-40; i=i+19)    {
    sum=0;
    for (j=0;j<19;j++)
        sum=sum+p[i+j];
    sum=sum/19;
    runmean[i/19]=sum;
}

Array.getStatistics(runmean, min, max);
threshold=(3*max)/4;
threshlow=max/4;

for(i=runmean.length-1; i>=0; i--){
    if (runmean[i]<threshold && runmean[i-1]>threshold) {
        a=i*19;
        i=-5;
    }
}

xmin=0;
xmax=width;

for(i=0;i<floor(400/mspl);i++)    {

    e=0;
    for (x=0;e<1;x++)    {
        value=getPixel(x,a+i);
        if (value>=threshlow) {
            e=1;
            if (x>xmin)
                xmin = x;
        }
    }

    e=0;
    for (x=width; e<1; x--)    {
        value=getPixel(x,a+i);
        if (value>=threshlow) {
            e=1;
            if (x<xmax)
                xmax=x;
        }
    }
}
}

```

```

xmax=xmax-floor(width/50);
xmin=xmin+floor(width/50);

makeRectangle(xmin, a-ms1000, xmax-xmin, height-a-ms1000-2);
updateDisplay();

makeRectangle(xmin, a-ms1000, xmax-xmin, height-a-ms1000-2);
updateDisplay();

makeRectangle(xmin, a-ms1000, xmax-xmin, height-a+ms1000-2);
updateDisplay();

setTool("rectangle");
waitForUser("Please adjust selection if necessary");
setKeyDown("alt");
// Get profile and display values in "Log" window

profile = getProfile();
profilefilter=newArray(profile.length);

setTool("rectangle");

//print(profile.length);
t=0;

for(filterappropriate=0; filterappropriate<1;t=t+1)
    {

fc=getNumber("What is your cutoff frequency as a proportion of the sampling frequency (must be <0.5)", 0.1);
if (fc>0.5)
    exit("fc cannot exceed fs/2");

sigma=0.132505/fc;

if (sigma>=0.62)
    nc=floor(4*sigma);
else
    nc=2;

gausscoeff=newArray(nc+1);

if (sigma>=0.62)    {
//nc is # coefficients not counting central

    b=-0.5/(sigma*sigma);
    gausscoeff[0]=1;
    sum=0.5;

    for (i=1; i<nc; i++)    {
        temp=exp((i*i)*b);
        gausscoeff[i]=temp;
        sum=sum+temp;
    }

// normalize coefficients such that total =1

    sum=sum*2;

    for (i=0; i<nc;i++)

```

```

    gausscoeff[i]=gausscoeff[i]/sum;

    } else    {
        //Alternate routine if narrow impulse response - only 3 terms used
        gausscoeff[1]=(sigma*sigma)/2;
        gausscoeff[0]=1-(2*gausscoeff[1]);
    }

//print ("nc="+nc);
//
//for (i=-nc; i<=nc; i++)    {
//    j=i;
//    if (j<0)
//        j=-j;
//    print (gausscoeff[j]);
//    }
//
// waitforUser("a");
//Actual filtering steps

for (pointloc=0; pointloc<profile.length; pointloc++)    {
    sum=0;

    for (i=-nc; i<=nc; i++)    {
        j=i;
        if (j<0)
            j=-j;

        pointmask=pointloc+i;
        if (pointmask<0)
            pointmask=0;
        if (pointmask>=profile.length-1)
            pointmask=profile.length-1;

        sum=sum+(gausscoeff[j])*profile[pointmask]);
    }

    profilefilter[pointloc]=sum;
}

Plot.create("Profile", "X", "Value", profilefilter);

run("Clear Results");

sum=0;
for (pointloc=0; pointloc<profile.length;pointloc++)    {
    if(profilefilter[pointloc]>sum)    {
        sum=profilefilter[pointloc];
        maxpointloc=pointloc;
    }

    setResult("original", pointloc, profile[pointloc]);
    setResult("filtered", pointloc, profilefilter[pointloc]);
}

updateResults;
Array.getStatistics(profile,min,max);

Plot.create("Profile", "X", "Value", profilefilter);
Plot.setLimits(maxpointloc-ms200, maxpointloc+(ms1000*2),min,max);
Plot.add("Profile", profile);
Plot.show();

filterappropriate=getBoolean("Filter appropriate?");

```

```

if (isOpen("Profile")) {
    selectWindow("Profile");
    run("Close");
}

}

Array.getStatistics(profilefilter,minfilt, maxfilt, meanfilt);
threshfilt=((maxfilt-minfilt)*0.75)+minfilt;

addn=newArray(ms50);
for (k=0;k<ms50;k++)
    addn[k]=profilefilter[k];
Array.getStatistics(addn,mina,maxa,meana,stdDev);

baseline=meana;

transend=profilefilter.length-ms300;

peakfluo=0;
stop=0;

for(j=0;j<transend && stop<1;j++) {
    if(profilefilter[j]>maxa+2) {
        transstart=j;
        stop=1;
    }
}

for(j=0;j<(profilefilter.length-ms300);j++) {
    if(profilefilter[j]>peakfluo) {
        peakfluo=profilefilter[j];
        peakline=j;
    }
}

TtoPeak=(peakline-transstart)*mspl;

FD70=baseline+((peakfluo-baseline)*0.7);

e=0;
sum=0;
for(j=peakline;j<transend && e<1;j++) {
    if(profilefilter[j]<=FD70) {
        decaystart=j;
        e=1;
    }
}

y=newArray(transend-decaystart);
x=newArray(transend-decaystart);

for(k=0; k<(transend-decaystart); k++) {
    x[k]=k*mspl;
    y[k]=profilefilter[decaystart+k];
}

Fit.doFit("y=a*exp(-x/b)+c", x, y);

```

```
Fit.plot;
tau=Fit.p(1);
lamda=1/(tau/1000);

waitForUser("curve fitting for decay of transient ");

selectWindow("y=a*exp(-x/b)+c");
run("Close");

run("Clear Results");

FF0=(peakfluo-background)/(baseline-background);

//      setResult("Transstart",0,transstart);
//      setResult("Transend",0,transend);
//      setResult("Peakline",0,peakline);
//      setResult("Baseline (u)-BG", 0, baseline-background);
//      setResult("Peak Fluorescence(u)-BG",0, peakfluo-background);
//      setResult("FD70",0,FD70);
//      setResult("Peak Fluorescence (F/F0)", 0, FF0);
//      setResult("Time to Peak (ms)", 0, TtoPeak);
//      setResult("Tau (ms)", 0, tau);
//      setResult("Lamda (s-1)", 0, lamda);

updateResults;

if (isOpen("Results"))
    selectWindow("Results");
```


9.1.7 Assessing Most Appropriate Criterion Value Using the F-Score

9.1.7.1 Selection of Criterion Value for Spark Detection

Sparkmaster's accuracy was first compared to an experienced observer's assessment of sparks. Initially a confidence value out of 10 was assigned to each image. However it was soon decided that a more mathematical test of accuracy was required. Accuracy per se could be used and is defined as follows:

$$\text{accuracy} = \frac{\text{number of true positives} + \text{number of true negatives}}{\text{numbers of true positives} + \text{false positives} + \text{false negatives} + \text{true negatives}}$$

Equation 9-1. Accuracy

However an assessment of accuracy requires an assessment of the number of true negative sparks in an image. i.e. when a spark is not detected and the observer does not think there is a spark present either. This could be said to occur many thousands of times in an an image since there are 10,000 lines per image with a cell width of approximately 250-500 pixels. Hence this would skew results such that the accuracy would tend towards 1 in all cases.

A better measure is the F-score as a measure of sparkmaster's "accuracy". This is a harmonic mean of recall (or sensitivity) and precision (or positive predictive value). These are defined as follows and have the advantage of not including a measure of true negatives:

$$\text{Recall} = \frac{tp}{tp + fn}$$

Equation 9-2. Recall (or sensitivity)

$$\text{Precision} = \frac{tp}{tp + fp}$$

Equation 9-3. Precision (or positive predictive value)

$$F = 2 \cdot \frac{\text{precision} \cdot \text{recall}}{\text{precision} + \text{recall}}$$

Equation 9-4. F-Score

Hence recall is a measure of true sparks picked up by sparkmaster as a proportion of total number of true sparks deemed to be present by the observer (i.e. inclusive of those that sparkmaster has missed). Precision is a measure of the proportion of the total number of objects assessed as being sparks by sparkmaster that the observer deems to be true sparks (i.e. excluding other objects such as pseudosparks). The F-score then allows a combination of these 2 measures and the use of harmonic mean rather than arithmetic mean is a good way of assessing performance of an algorithm

such as sparkmaster. This is because such an algorithm could achieve a score of 0.5 in an arithmetic mean of precision and recall by merely returning all pixels as sparks and thus achieving a recall of 1 whereas a harmonic mean by containing a multiplication factor biases against unbalanced increases in recall at the expense of precision and vice-versa. One potential disadvantage of the F-test is that where there are few sparks to search for it can give an inaccurately low score. For example if there are no sparks in the image an F-score cannot be computed since there are no true positives. In such a case a more subjective measure of image quality must be used, with the F-score being reserved for line scans in which there are 3 or more true sparks to be found.

The criterion value input into sparkmaster (section 2.5.6.4) appeared to be a factor that altered the visually assessed accuracy of sparkmaster. For a randomly selected sample of 19 linescans, sparkmaster was run at both criteria of 4.2 and 3.8. The criterion in use most frequently in published data is 3.8, however under our experimental conditions this was giving high rates of false positive sparks. A criterion of 4.2 gives fewer false positives but the trade-off is missing genuine sparks: an appreciable false negative rate. Such effects were assessed using the F-Score to take into account issues with both criteria used. For 19 matched cells the mean and standard error of F-Scores are shown.

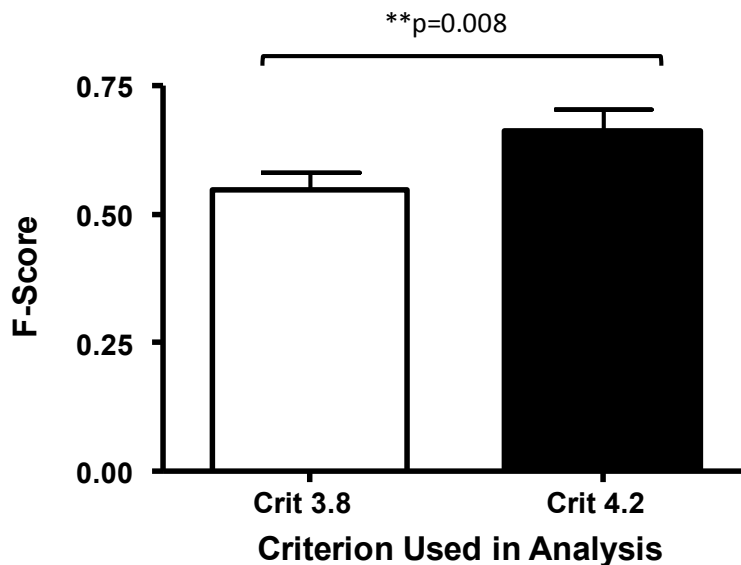


Figure 9-2. F-Score and Criterion.

A random selection of 19 cells were assessed for sparks using different criteria. A criterion of 4.2 is significantly better than one of 3.8 as assessed by F-Score under our experimental conditions.

A paired t-test showed this difference to be statistically significant ($p=0.0197$). Hence a decision was taken to use criterion 4.2 for further analysis. At a later date once image quality had improved and there was no appreciable increase in false negative spark detection at a criterion of 3.8, this value was used instead since it is most often quoted in the literature.(Picht *et al.*, 2007)

9.2 Appendix for Hierarchical Statistics Chapter (3)

9.2.1 Search Strategy For Murine Post-MI Studies of Ca²⁺ Handling

PubMed, Google Scholar and Web of Science were searched using the following search term:

("Calcium transient" OR "Ca²⁺ transient" OR "Ca transient") AND (isolated OR isolation) AND (ventricular) AND (cardiomyocyte OR "cardiac myocyte") AND ("myocardial infarction" OR MI) AND (mouse OR mice OR rat) AND (amplitude OR decay OR tau)

A total of 1097 search results were obtained. The titles of all papers were assessed and the full articles were assessed if titles appeared pertinent. References were also assessed if the text referred to pertinent results from other studies. For spark searches the word transient in the search above was replaced with spark.

9.2.2 Table of Ca²⁺ Handling Changes in Post MI mouse HF models

Publication	Rat/ Mouse	Wks Post MI	Ca ²⁺ Transient Amplitude			Transient Decay Time			SR Ca ²⁺ content			Diastolic [Ca ²⁺] _i		
			↓	↔	↑	↓	↔	↑	↓	↔	↑	↓	↔	↑
Mørk <i>et al.</i> , 2007	Mouse	1			✓	✓					✓			
Louch <i>et al.</i> , 2006	Mouse	3			✓									
Zalvidea <i>et al.</i> , 2012	Mouse	6	✓					✓	✓					✓
Bito <i>et al.</i> , 2013	Mouse	7		✓									✓	
Bito <i>et al.</i> , 2010	Mouse	8		✓				✓		✓			✓	
Louch <i>et al.</i> , 2010	Mouse	10			✓									
Mørk <i>et al.</i> , 2009	Mouse	10			✓		✓				✓			
TOTAL			1	2	4	1	1	2	1	1	2	0	2	1
TOTAL (%)			14	29	57	25	25	50	25	25	50	0	67	33

9.2.3 Table of Spark Parameters in Post MI mouse HF models

Publication	Rat/ Mouse	Wks Post MI	Spontaneous Ca ²⁺ Spark Frequency			Ca ²⁺ Spark Amplitude			Ca ²⁺ Spark Width			Ca ²⁺ Spark Duration		
			↓	↔	↑	↓	↔	↑	↓	↔	↑	↓	↔	↑
Thireau <i>et al.</i> , 2012	Mouse	4			✓		✓							
Bito <i>et al.</i> , 2010	Mouse	8		✓										
Louch <i>et al.</i> , 2013	Mouse	10			✓			✓		✓				✓

9.2.4 Table of Spark Parameters in Pressure Overload Models

Publication	Rat/ Mouse	SHR/ TAC	Cardiac Contract ility	Spontaneous Ca ²⁺ Spark Frequency			Ca ²⁺ Spark Amplitude			Ca ²⁺ Spark Width			Ca ²⁺ Spark Duration		
				↑	↓	↔	↑	↓	↔	↑	↓	↔	↑	↓	↔
Toischer 2010(Toischer <i>et al.</i> , 2010)	Mouse	TAC	↓	✓											
Ling 2009(Ling <i>et al.</i> , 2009)	Mouse	TAC	↓	✓											
Shorofsky 1999(Shorofsky <i>et al.</i> , 1999)	Rat	SHR	↑				✓								
Gomez 1997(Gomez <i>et al.</i> , 1997)	Rat	SHR							✓			✓			✓

9.2.5 Syntax for 3-Level Random Intercept Hierarchical Model in SPSS

Using the example of analysis of LogAmp nested in cells, nested in isolations the following syntax was used:

MIXED LogAmp BY HF

/CRITERIA=CIN(95) MXITER(100) MXSTEP(10) SCORING(1) SINGULAR(0.000000000001)
HCONVERGE(0, ABSOLUTE) LCONVERGE(0, ABSOLUTE) PCONVERGE(0.000001, ABSOLUTE)

/FIXED=HF | SSTYPE(3)

/METHOD=ML

/PRINT=R SOLUTION TESTCOV

/RANDOM=INTERCEPT | SUBJECT(Isolation) COVTYPE(ID)

/RANDOM=INTERCEPT | SUBJECT(Cell*Isolation) COVTYPE(ID)

/SAVE=PRED RESID

/EMMEANS=TABLES(HF) COMPARE ADJ(LSD).

9.3 Appendix for Ca²⁺ Transient and Spark Data in Established HF Chapter (5)

9.3.1 Statistics in multi-level models for Ca²⁺ transient and spark data in 16WMI model

```
MIXED FF0 BY HF Iso
  /CRITERIA=CIN(95) MXITER(100) MXSTEP(10) SCORING(1)
SINGULAR(0.000000000001) HCONVERGE(0, ABSOLUTE) LCONVERGE(0, ABSOLUTE)
PCONVERGE(0.000001, ABSOLUTE)
  /FIXED=HF Iso HF*Iso | SSTYPE(3)
  /METHOD=REML
  /PRINT=G R SOLUTION TESTCOV
  /RANDOM=INTERCEPT | SUBJECT(Isolation) COVTYPE(UN)
  /REPEATED=Iso | SUBJECT(Isolation*CellID) COVTYPE(UN)
  /SAVE=PRED RESID.
```

Table 9-1. Example syntax for assessment of the effects of isoprenaline on transient amplitude in HF and control cells.

*This mixed statistical model syntax from an example SPSS model assess the fixed effects of HF, isoprenaline (Iso) and whether there is any interaction between the two (HF*Iso). This is done within the hierarchical structure by allowing the intercept for each isolation to vary by way of a random effect. The repeated measures occur within each cell (with and without iso in each case).*

Estimates of Fixed Effects ^a							
Parameter	Estimate	Std. Error	df	t	Sig.	95% Confidence Interval	
						Lower Bound	Upper Bound
[HF=0]	-1.626771	1.140250	5.513	-1.427	.208	-4.477656	1.224113
[HF=1]
[Iso=0]	-3.516033	.382750	44.000	-9.186	.000	-4.287415	-2.744652
[Iso=1]
[Iso=0] * [HF=0]	-.242185	.789454	43.000	-.307	.760	-1.834271	1.349901
[Iso=1] * [HF=0]
[Iso=0] * [HF=1]
[Iso=1] * [HF=1]

a. Dependent Variable: Transient amplitude.

Items in italics are reference categories and thus have no p-values associated.

Table 9-2. Estimates of fixed effects for Ca²⁺ transient amplitude +/- isoprenaline in HF vs control cells.

*Table shows that while 30nM isoprenaline significantly enhances transient amplitude (by on average 3.4 F/F₀ units, HF itself does not change Ca²⁺ transient amplitude and there is no significant interaction between Iso and HF (Iso*HF) suggesting that there is no difference between the effects of iso in the presence or absence of HF. Note that data in the table represents the final iteration of the model containing each parameter.*

Estimates of Fixed Effects^a

Parameter	Estimate	Std. Error	df	t	Sig.	95% Confidence Interval	
						Lower Bound	Upper Bound
[HF=0]	4.466628	2.530978	43.000	1.765	.085	-.637576	9.570832
<i>[HF=1]</i>
[Iso=0]	-.553122	1.399614	44	-.395	.695	-3.373858	2.267613
<i>[Iso=1]</i>
[Iso=0] * [HF=0]	2.720074	2.860054	43	.951	.347	-3.047775	8.487923
<i>[Iso=1] * [HF=0]</i>
<i>[Iso=0] * [HF=1]</i>
<i>[Iso=1] * [HF=1]</i>

a. Dependent Variable: Time to peak.

Items in italics are reference categories and thus have no p-values associated.

Table 9-3. Estimates of fixed effects for Ca²⁺ transient time to peak +/- isoprenaline in HF vs control cells.

There are no significant differences based on these parameters.

Estimates of Fixed Effects^a

Parameter	Estimate	Std. Error	df	t	Sig.	95% Confidence Interval	
						Lower Bound	Upper Bound
[HF=0]	-44.255	51.570428	7.146	-.858	.419	-165.695	77.184
<i>[HF=1]</i>
[Iso=0]	43.607	11.993320	43.000	3.636	.001	19.420943	67.794
<i>[Iso=1]</i>
[Iso=0] * [HF=0]	17.1098	15.483310	43.000	1.105	.275	-14.115	48.334
<i>[Iso=1] * [HF=0]</i>
<i>[Iso=0] * [HF=1]</i>
<i>[Iso=1] * [HF=1]</i>

a. Dependent Variable: Tau.

Items in italics are reference categories and thus have no p-values associated.

Table 9-4. Estimates of fixed effects for Ca²⁺ transient time to peak +/- isoprenaline in HF vs control cells.

Isoprenaline significantly reduces tau within a particular cell. However there is no effect of HF nor is there any significant interaction between the presence of HF and the effect of isoprenaline.

Estimates of Fixed Effects^a

Parameter	Estimate	Std. Error	df	t	Sig.	95% Confidence Interval	
						Lower Bound	Upper Bound
[HF=0]	-38.5996	43.002455	6.020	-.898	.404	-143.736	66.536
[HF=1]
[Iso=0]	91.1397	16.893236	43	5.395	.000	57.0712	125.2081
[Iso=1]
[Iso=0] * [HF=0]	22.1251	21.809074	43	1.014	.316	-21.8570	66.1073
[Iso=1] * [HF=0]
[Iso=0] * [HF=1]
[Iso=1] * [HF=1]

a. Dependent Variable: TD90.

Items in italics are reference categories and thus have no p-values associated.

Table 9-5. Estimates of fixed effects for Ca²⁺ transient time to 90% decay (TD90) +/- isoprenaline in HF vs control cells.

Isoprenaline significantly reduces R90 within a particular cell. However there is no effect of HF nor is there any significant interaction between the presence of HF and the effect of isoprenaline.

Estimates of Fixed Effects^a

Parameter	Estimate	Std. Error	df	t	Sig.	95% Confidence Interval	
						Lower Bound	Upper Bound
[HF=0]	.173708	.600872	16.524	.289	.776	-1.096807	1.444223
[HF=1]
[Iso=0]	-.117917	.379389	43.000	-.311	.757	-.883027	.647194
[Iso=1]
[Iso=0] * [HF=0]	.845657	.489789	43.000	1.727	.091	-.142096	1.833410
[Iso=1] * [HF=0]
[Iso=0] * [HF=1]
[Iso=1] * [HF=1]

a. Dependent Variable: DysTt50P.

Items in italics are reference categories and thus have no p-values associated.

Table 9-6. Estimates of fixed effects for Ca²⁺ transient dyssynchrony of time to 50% peak (dysTt50P) +/- isoprenaline in HF vs control cells.

Although estimated marginal means analysis suggests that isoprenaline causes a significant reduction in dysTt50P in AMC cells (p=0.023) but not in HF cells (p=0.757), the interaction term

reaches only borderline statistical significance ($p=0.091$). Neither HF nor isoprenaline alter dysTt50P on their own.

Estimates of Fixed Effects^a

Parameter	Estimate	Std. Error	df	t	Sig.	95% Confidence Interval	
						Lower Bound	Upper Bound
[HF=0]	.782296	1.249037	9.573	.626	.546	-2.017648	3.582240
[HF=1]
[Iso=0]	1.628917	1.067062	43.000	1.527	.134	-.523018	3.780852
[Iso=1]
[Iso=0] * [HF=0]	2.653972	1.377571	43.000	1.927	.061	-.124164	5.432108
[Iso=1] * [HF=0]
[Iso=0] * [HF=1]
[Iso=1] * [HF=1]

a. Dependent Variable: DysTtP.

Items in italics are reference categories and thus have no p-values associated.

Table 9-7. Estimates of fixed effects for Ca^{2+} transient dyssynchrony of time to peak (dysTtP) +/- isoprenaline in HF vs control cells.

Estimated marginal means analysis suggests that isoprenaline causes a significant reduction in dysTtP in AMC cells ($p<0.001$) but not in HF cells ($p=0.134$), the interaction term also approaches statistical significance ($p=0.061$).

Estimates of Fixed Effects^a

Parameter	Estimate	Std. Error	df	t	Sig.	95% Confidence Interval	
						Lower Bound	Upper Bound
[HF=0]	.020583	.068352	43.000	.301	.765	-.117261	.158427
[HF=1]
[Iso=0]	-.145878	.034611	44.000	-4.215	.000	-.215633	-.076123
[Iso=1]
[Iso=0] * [HF=0]	.017287	.071419	43	.242	.810	-.126742	.161316
[Iso=1] * [HF=0]
[Iso=0] * [HF=1]
[Iso=1] * [HF=1]

a. Dependent Variable: DysAmp.

Items in italics are reference categories and thus have no p-values associated.

Table 9-8. Estimates of fixed effects for Ca^{2+} transient dyssynchrony of amplitude (dysAmp) +/- isoprenaline in HF vs control cells.

Isoprenaline significantly increases the dyssynchrony of transient amplitude. The absence of significance of the interaction term suggests that this occurs regardless of whether the cell is from an HF or AMC rat.

Estimates of Fixed Effects ^a							
Parameter	Estimate	Std. Error	df	t	Sig.	95% Confidence Interval	
						Lower Bound	Upper Bound
[HF=0]	.400931	2.969765	6.577	.135	.897	-6.714069	7.515931
[HF=1]
[Iso=0]	7.265361	3.006387	43.000	2.417	.020	1.202403	13.3283
[Iso=1]
[Iso=0] * [HF=0]	6.120120	3.881229	43.000	1.577	.122	-1.707124	13.947
[Iso=1] * [HF=0]
[Iso=0] * [HF=1]
[Iso=1] * [HF=1]

a. Dependent Variable: DysTau.

Items in italics are reference categories and thus have no p-values associated.

Table 9-9. Estimates of fixed effects for Ca^{2+} transient dyssynchrony of Tau (dysTau) +/- isoprenaline in HF vs control cells.

Isoprenaline significantly decreases the dyssynchrony of transient decay. The absence of significance of the interaction term suggests that this occurs regardless of whether the cell is from an HF or AMC rat.

Estimates of Fixed Effects ^a							
Parameter	Estimate	Std. Error	df	t	Sig.	95% Confidence Interval	
						Lower Bound	Upper Bound
[HF=0]	-.804583	.883913	9.166	-.910	.386	-2.798616	1.189450
[HF=1]
[Iso=0]	-.397768	.230844	39.806	-1.723	.093	-.864391	.068855
[Iso=1]
[Iso=0] * [HF=0]	.205458	.341694	38.753	.601	.551	-.485825	.896741
[Iso=1] * [HF=0]
[Iso=0] * [HF=1]
[Iso=1] * [HF=1]

a. Dependent Variable: SparkFreq.

Items in italics are reference categories and thus have no p-values associated.

Table 9-10. Estimates of fixed effects for Spark Frequency +/- isoprenaline in HF vs control cells.

30nM isoprenaline does not significantly change spark frequency ($p=0.093$). The absence of significance of the interaction term suggests that this is similar in both HF and AMC cells.

Estimates of Fixed Effects^a

Parameter	Estimate	Std. Error	df	t	Sig.	95% Confidence Interval	
						Lower Bound	Upper Bound
[HF=0]	-.038052	.052026	14.416	-.731	.476	-.149335	.073231
[HF=1]
[Iso=0]	-.063487	.026207	44.675	-2.423	.020	-.116280	-.010693
[Iso=1]
[Iso=0] * [HF=0]	.008466	.039370	42.717	.215	.831	-.070947	.087878
[Iso=1] * [HF=0]
[Iso=0] * [HF=1]
[Iso=1] * [HF=1]

a. Dependent Variable: SparkAmp.

Items in italics are reference categories and thus have no p-values associated.

Table 9-11. Estimates of fixed effects for Spark Amplitude +/- isoprenaline in HF vs control cells.

30nM isoprenaline significantly increases spark amplitude ($p=0.020$). The absence of significance of the interaction term suggests that this relationship is similar in both HF and AMC cells.

Estimates of Fixed Effects^a

Parameter	Estimate	Std. Error	df	t	Sig.	95% Confidence Interval	
						Lower Bound	Upper Bound
[HF=0]	-.393621	.154804	41	-2.543	.015	-.706254	-.080987
[HF=1]
[Iso=0]	-.371155	.128930	41	-2.879	.006	-.631534	-.110777
[Iso=1]
[Iso=0] * [HF=0]	.483087	.193959	41	2.491	.017	.091378	.874795
[Iso=1] * [HF=0]
[Iso=0] * [HF=1]
[Iso=1] * [HF=1]

a. Dependent Variable: FWHM.

Items in italics are reference categories and thus have no p-values associated.

Table 9-12. Estimates of fixed effects for Spark FWHM +/- isoprenaline in HF vs control cells.

30nM isoprenaline can significantly increase FWHM ($p=0.006$). The relationship is difference for AMC in comparison with HF cells. In AMC cells there is no significant increase in FWHM in the presence of isoprenaline ($p=0.444$) whereas in HF cells there is a significant increase ($P=0.006$). This increase causes significant divergence of FWHM in the presence of isoprenaline with HF cells having greater FWHM than AMC cells by $0.394 \pm 1.6 \mu\text{m}$ ($p=0.015$ by estimated marginal means).

Estimates of Fixed Effects ^a							
Parameter	Estimate	Std. Error	df	t	Sig.	95% Confidence Interval	
						Lower Bound	Upper Bound
[HF=0]	-2.949984	2.452058	9.376	-1.203	.258	-8.463175	2.563208
[HF=1]
[Iso=0]	-2.826770	1.724147	44.079	-1.640	.108	-6.301384	.647844
[Iso=1]
[Iso=0] * [HF=0]	.532099	2.573028	42.316	.207	.837	-4.659334	5.723532
[Iso=1] * [HF=0]
[Iso=0] * [HF=1]
[Iso=1] * [HF=1]

a. Dependent Variable: FDHM.

Items in italics are reference categories and thus have no p-values associated.

Table 9-13. Estimates of fixed effects for Spark FDHM +/- isoprenaline in HF vs control cells.
 30nM isoprenaline has no significant influence on FDHM ($p=0.108$). The interaction term is non significant suggesting there is no significant difference in this relationship in HF vs control cells.

Estimates of Fixed Effects ^a							
Parameter	Estimate	Std. Error	df	t	Sig.	95% Confidence Interval	
						Lower Bound	Upper Bound
[HF=0]	-12.7012	6.907944	41	-1.839	.073	-26.6521	1.249651
[HF=1]
[Iso=0]	-14.7043	4.792318	41	-3.068	.004	-24.3826	-5.026103
[Iso=1]
[Iso=0] * [HF=0]	14.4955	7.209465	41	2.011	.05	-.064227	29.0553
[Iso=1] * [HF=0]
[Iso=0] * [HF=1]
[Iso=1] * [HF=1]

a. Dependent Variable: SparkMass.

Items in italics are reference categories and thus have no p-values associated.

Table 9-14. Estimates of fixed effects for Spark Mass +/- isoprenaline in HF vs control cells.
 30nM isoprenaline increases spark mass significantly ($p=0.004$). Similar to FWHM there is a much greater effect in HF cells such that the interaction term is significant ($p=0.05$).

Estimates of Fixed Effects^a

Parameter	Estimate	Std. Error	df	t	Sig.	95% Confidence Interval	
						Lower Bound	Upper Bound
[HF=0]	-1.032696	.645654	19.752	-1.599	.126	-2.380592	.315199
<i>[HF=1]</i>
[Iso=0]	-1.029812	.386095	43.472	-2.667	.011	-1.808203	-.251421
<i>[Iso=1]</i>
[Iso=0] * [HF=0]	.775672	.578231	42.117	1.341	.187	-.391149	1.942493
<i>[Iso=1] * [HF=0]</i>
<i>[Iso=0] * [HF=1]</i>
<i>[Iso=1] * [HF=1]</i>

a. Dependent Variable: Spark Mediated SR Leak.

Items in italics are reference categories and thus have no p-values associated.

Table 9-15. Estimates of fixed effects for Spark mediated SRMass +/- isoprenaline in HF vs control cells.

30nM isoprenaline increases spark mediated SR leak significantly ($p=0.011$). Although again this effect predominately occurs in HF cells, the interaction term is not significant in this case ($p=0.187$).

9.4 Appendix for OPM Chapter (6)

9.4.1 Code For Spark Detection in 2D (Matlab)

This code was written by Chris Dunsby with my input regarding procedure and thresholds:

9.4.1.1 Description of algorithm

The 2-D time-lapse OPM data was analysed in sections of 1000 frames that were chosen to exclude the presence of Ca^{2+} transients and waves. The algorithm was as follows:

- 1) Pre-processing. The camera digital offset and background light were measured from a dark corner of the image and subtracted. The x - y - t data was then smoothed spatially and temporally using a $3 \times 3 \times 5$ kernel.
- 2) Identification of preliminary sparks. The initial estimate of the mean, μ_1 , and standard deviation, σ_1 , of each x - y point in the image stack were calculated along the t axis. Preliminary spark x - y - t regions were identified according to two criteria. The first criterion was that all pixels within a region are more than $3.2\sigma_1$ above μ_1 . The second criterion was that the region must contain at least one pixel that is more than $6\sigma_1$ above μ_1 .
- 3) Calculation of the fractional change in fluorescence intensity $\Delta F/F_0$, where $\Delta F = F - F_0$. Preliminary sparks (identified in step 2) were removed from the data. Then the first 30 frames of each 1000 frame section were averaged to find the fluorescence intensity at the start of the section, F_0 . The fractional change in fluorescence intensity $\Delta F/F_0$ was then calculated for each pixel of the x - y - t dataset.
- 4) Identification of potential sparks. The mean, μ_2 , and standard deviation, σ_2 , of the fractional change in fluorescence intensity – excluding preliminary sparks – was calculated along the t axis for each x - y point in the image stack. Potential sparks were defined as x - y - t regions meeting the first and second criteria used in step 2.
- 5) Identification of actual sparks. The area of each potential spark was calculated using the maximum x - y extent of the spark as determined using the first criterion. Similarly, the duration of the spark was calculated as the temporal extent of the spark region as determined using the first criterion. Sparks with an area below $3 \mu\text{m}^2$ and a full duration (at the level defined by the first criterion) below 18 ms were excluded.
- 6) Actual spark parameters. The following parameters were calculated for actual sparks: spark amplitude in terms of maximum fractional change in fluorescence intensity $\Delta F/F_0$; spark area measured at the border defined by the first criterion; spark full duration at half maximum (FDHM); spark centre of mass in x and y ; normalised t -tubule modulation at spark centre of mass; and distance of spark centre of mass to a region defined as a t -tubule.

9.4.1.2 Matlab Code

```
close all
clc
```

```

%%% parameters used in data analysis
intensity_threshold = 2.4;
image_max_val = 1000; %set so that time-stamp not included in mask
thresh1 = 5;
thresh2 = 3.2;
min_spark_area = 20;
min_spark_length = 8;
display_initial_images = false;
display_final_images = true;
s_smooth = 3;
t_smooth = 3;
no_of_f0_images = 30;
output_dir = 'results';
display_min = 90;
display_max = 40;

% calculate background
figure
imagesc(squeeze(data(1, :, :)), [display_min display_max+display_min])
colormap(gray)
axis equal
axis tight

disp('Select desired background region and press any key to continue.')
h = imrect(gca, [10 10 50 50]);
pause
bkgndrect = getPosition(h);

bkgnd_level = mean(mean(data(bkgndrect(1):bkgndrect(1)+bkgndrect(3), bkgndrect(2):bkgndrect(2)+bkgndrect(4))))

% remove background from data
data2 = data - bkgnd_level;
disp('Background subtraction complete.')

% smooth the data
smoothing_kernel = ones(t_smooth, s_smooth, s_smooth)/t_smooth/s_smooth^2;
data2 = convn(data2, smoothing_kernel, 'valid');
disp('Data smoothing complete.')

% calculate the mean image and display it
mean_image = squeeze(mean(data2));
figure
imagesc(mean_image, [0 display_max])
colormap(gray)
title('Mean image')
axis equal
axis tight
imwrite(mean_image/max(max(mean_image)), [output_dir '\mean_image.tif'])
disp('Mean image calculation complete.')

% calculate an image threshold
threshold_image = (mean_image > intensity_threshold) & (mean_image < image_max_val);

% mask out very edges of image
threshold_image(1:10, :) = 0;
threshold_image(:, 1:10) = 0;
threshold_image(188:198, :) = 0;
threshold_image(:, 948:958) = 0;
figure
imagesc(threshold_image, [0 1])
title('Threshold image')

```

```

axis equal
axis tight
imwrite(threshold_image, [output_dir '\threshold_image.tif'])

% calculate the standard deviation image and display it
std_image = squeeze(std(data2));
figure
imagesc(std_image, [0 2])
colormap(gray)
title('Standard deviation image')
axis equal
axis tight
imwrite(std_image/max(max(std_image)), [output_dir '\std_image.tif'])

disp('Finding potential sparks...')
prelim_sparks = locate_sparks(data2, mean_image, std_image, threshold_image, thresh1, thresh2);

% calculate f0
mask = (prelim_sparks == 0);
f0 = masked_mean(data2(1:no_of_f0_images, :, :), mask(1:no_of_f0_images, :, :));

% convert data to f/f0
threshold_data = repmat(reshape(threshold_image, [1 size(data2, 2) size(data2, 3)]), [size(data2, 1) 1 1]);
data2 = data2.*threshold_data./repmat(f0, [size(data2, 1) 1 1]);
clear threshold_data

% now recalculate normalised mean and std with potential sparks masked out
[m_mean_image m_std_image] = masked_mean_and_std(data2, mask);
m_mean_image = squeeze(m_mean_image);
m_std_image = real(m_std_image);
m_std_image = squeeze(m_std_image);
figure
%imagesc(m_mean_image, [0 4])
imagesc(m_mean_image, [0 2])
colormap(gray)
title('Masked mean image')
axis equal
axis tight
drawnow
imwrite(m_mean_image/2, [output_dir '\m_mean_image.tif'])

figure
imagesc(m_std_image, [0 0.5])
colormap(gray)
title('Masked standard deviation image')
axis equal
axis tight
drawnow
imwrite(m_std_image/0.5, [output_dir '\m_std_image.tif'])

% find the actual spark locations
disp('Finding initial sparks...')
initial_sparks = locate_sparks(data2, m_mean_image, m_std_image, threshold_image, thresh1, thresh2);

figure
imagesc(squeeze(sum(initial_sparks)))
colormap(gray)
title('Initial spark map')
axis equal
axis tight
drawnow

```



```

CC = bwconncomp(initial_sparks, 6);
clear initial_sparks
n_initial_sparks = CC.NumObjects
L = uint16(labelmatrix(CC));
%clear CC
Region_Props_Output = regionprops(CC);

disp('Are you happy with the initial detected sparks?')
%pause

% Display images
if display_initial_images
    figure
    % find the brightest pixel, excluding the time-stamp
    peak_pixel = max(max(max(data2(:, 8:end, :))));
    %cmap = colormap(jet(double(n_initial_sparks))*0.5;
    cmap = hsv2rgb([0 0 0; rand(n_initial_sparks, 1) ones(n_initial_sparks, 2)])*0.8;
    cmap(1, :) = [0 0 0];
    mkdir([output_dir '\initial sparks']);
    for j = 1:size(data2, 1)
        j
        L_RGB = ind2rgb(squeeze(L(j, :, :)), cmap);
        intensity_image = squeeze(data2(j, :, :))/peak_pixel;
        % remove pixels with negative values in time-stamp (caused by
        % background subtraction
        intensity_image(find(intensity_image < 0 | intensity_image > 1)) = 0;
        intensity_image_RGB = repmat(reshape(intensity_image, [size(intensity_image, 1) size(intensity_image, 2) 1]), [1 1 3]);
        disp_imag = (1-L_RGB).*intensity_image_RGB;
        image(disp_imag)
        axis equal
        axis tight
        drawnow
        imwrite(disp_imag, [output_dir '\initial sparks' '\xyimage' num2str(j, '%06d') '.tif'])
    end
end

figure
set(gcf, 'position', [50 50 600 1000])
t = 1:size(data2, 1);
current_spark = 0;
x_ramp = 1:size(data2, 3);
y_ramp = 1:size(data2, 2);
mkdir([output_dir '\sparkplot'])
for j = 1:n_initial_sparks
    j
    spark_mask_3D = (L == j);
    masked_spark_3D = data2.*spark_mask_3D;
    spark_area_2D = (squeeze(sum(spark_mask_3D, 1)) >= 1);
    spark_area = sum(sum(spark_area_2D));
    spark_on = (squeeze(sum(sum(spark_mask_3D, 2), 3)) >= 1);
    spark_t_pts = find(spark_on);

    if (spark_area >= min_spark_area) & (numel(spark_t_pts) >= min_spark_length)
        spark_image = squeeze(sum(masked_spark_3D, 1));
        spark_intensity = sum(sum(spark_image));

        spark_tube_3D = repmat(reshape(spark_area_2D, [1 size(data2, 2) size(data2, 3)]), [size(data2, 1) 1 1]);
        spark_trace_3D = data2.*spark_tube_3D;
        time_profile = squeeze(sum(sum(spark_trace_3D, 2), 3))/sum(sum(spark_area_2D));
        [max_val max_element] = max(time_profile(spark_t_pts));
        spark_t_peak = max_element + spark_t_pts(1)-1;
        delta_f_max_over_f0 = max_val - 1;
    end
end

```

```

FDHMpts = (time_profile <= delta_f_max_over_f0/2 + 1);
FDHMend = find(FDHMpts(spark_t_peak:end), 1, 'first')+spark_t_peak;
FDHMstart = find(FDHMpts(1:spark_t_peak), 1, 'last');
spark_FDHM = FDHMend - FDHMstart;

if FDHMend <= numel(time_profile)

    current_spark = current_spark+1;

    subplot(3,2,2,'replace')
    plot(t, time_profile, t(spark_t_pts), time_profile(spark_t_pts))
    hold on
    plot(spark_t_peak, max_val, 'X', 'color', 'red')
    plot(FDHMstart, time_profile(FDHMstart), 'X', 'color', 'red')
    plot(FDHMend, time_profile(FDHMend), 'X', 'color', 'red')
    xlabel('Time (frames)')
    ylabel('Intensity in spark ROI')

    x_profile = squeeze(sum(spark_image, 1));
    y_profile = squeeze(sum(spark_image, 2));
    x_cofm = sum(x_profile.*x_ramp)/spark_intensity;
    y_cofm = sum(y_profile.*y_ramp)/spark_intensity;

    subplot(3,2,1,'replace')
    imagesc(squeeze(data2(spark_t_peak, :, :)))
    colormap(gray)
    axis equal
    axis tight
    xlabel('x (pixels)')
    ylabel('y (pixels)')
    xmin = find(x_profile, 1, 'first');
    xmax = find(x_profile, 1, 'last');
    ymin = find(y_profile, 1, 'first');
    ymax = find(y_profile, 1, 'last');
    rectangle('Position',[xmin,ymin,xmax-xmin,ymax-ymin], 'EdgeColor', 'white')

    subplot(3,2,3,'replace')
    imagesc(spark_image)
    %axis equal
    %axis tight
    xlabel('x (pixels)')
    ylabel('y (pixels)')

    subplot(3,2,5,'replace')
    imagesc(squeeze(sum(spark_trace_3D, 2))./repmat(sum(spark_area_2D, 1), [size(data2, 1) 1]))
    %axis equal
    %axis tight
    xlabel('x (pixels)')
    ylabel('t (frames)')

    subplot(3,2,4,'replace')
    imagesc(squeeze(sum(spark_trace_3D, 3))./repmat(sum(spark_area_2D, 2), [1 size(data2, 1)]))
    %axis equal
    %axis tight
    xlabel('t (frames)')
    ylabel('y (pixels)')
    drawnow

    spark{current_spark}.intensity = spark_intensity;
    spark{current_spark}.area = spark_area;
    spark{current_spark}.start = spark_t_pts(1);
    spark{current_spark}.end = spark_t_pts(end);

```

```

spark{current_spark}.x_cofm = x_cofm;
spark{current_spark}.y_cofm = y_cofm;
spark{current_spark}.delta_f_max_over_f0 = delta_f_max_over_f0;
spark{current_spark}.FDHM = spark_FDHM;
spark{current_spark}.BoundingBox = Region_Props_Output(current_spark).BoundingBox;

spark{current_spark}
%pause
saveas(gcf, [output_dir '\sparkplot' '\spark' num2str(current_spark, '%04u') '.emf'], 'emf')
else
    % in this case, the spark doesn't finishe before end of dataset,
    % so remove it from the spark mask
    L(find(L == j)) = 0;
end
else
    % in this case, the spark doesn't meet the criterea for minimum
    % area or duration, so remove it from the spark mask
    L(find(L == j)) = 0;
end
end

disp(['Number of sparks detected after applying criteria for minimum area and duration = ' num2str(current_spark)])

save('spark', 'spark')

% calculate final spark map image
final_spark_map = squeeze(sum((L > 0)));
% plot final spark map
figure
imagesc(final_spark_map)
colormap(gray)
title('Final spark map')
axis equal
axis tight
drawnow
% save final spark map to disk
imwrite(final_spark_map/current_spark, [output_dir '\final_spark_map.tif'])

if display_final_images
    % draw spark bounding boxes

    spark_bounding_boxes = zeros(size(data2));

    for j = 1:current_spark
        bb = floor(spark{j}.BoundingBox);
        bb(find(bb == 0)) = 1;
        % order of params returned by regionprops [y t x]
        for k = bb(2):bb(2)+bb(5)
            spark_bounding_boxes(k, bb(1):bb(1)+bb(4), bb(3)) = j;
            spark_bounding_boxes(k, bb(1):bb(1)+bb(4), bb(3)+bb(6)) = j;
            spark_bounding_boxes(k, bb(1), bb(3):bb(3)+bb(6)) = j;
            spark_bounding_boxes(k, bb(1)+bb(4), bb(3):bb(3)+bb(6)) = j;
        end
    end

    figure
    peak_pixel_value = 1.5;
    pixel_value_offset = 0.5;
    %cmap = colormap(jet(double(n_initial_sparks)));
    cmap = hsv2rgb([0 0 0; rand(n_initial_sparks, 1) ones(n_initial_sparks, 2)]);
    cmap(1, :) = [0 0 0];
    mkdir([output_dir '\finaldata'])

```

```

for j = 1:size(data2, 1)
    %j
    intensity_image = squeeze(data2(j, :, :))/peak_pixel_value - pixel_value_offset;
    intensity_image(find(intensity_image < 0)) = 0;
    intensity_image(find(intensity_image > 1)) = 1;

    intensity_image_RGB = repmat(reshape(intensity_image, [size(intensity_image, 1) size(intensity_image, 2) 1]), [1 1 3]);
    L_RGB = ind2rgb(squeeze(spark_bounding_boxes(j, :, :)), cmap);
    spark_boundaries_mask = (squeeze(spark_bounding_boxes(j, :, :)) > 0);
    disp_imag = repmat(~spark_boundaries_mask, [1 1 3]).*intensity_image_RGB + L_RGB;
    image(disp_imag)
    axis equal
    axis tight
    drawnow
    %pause
    imwrite(disp_imag, [output_dir '\finaldata' '\finaldata' num2str(j, '%04u'), '.tif'])
end
end

% write the spark information to a spreadsheet
clear spark_output
spark_output(1, :) = fieldnames(spark{1});
for j = 1:numel(spark)
    spark_output(j+1, :) = struct2cell(spark{j});
end

xlswrite([output_dir '\sparkdata.xls'], spark_output)

```

9.4.1.3 LOCATE Sparks SUBPROC

```

function sparks = locate_sparks(data, mean_image, std_image, threshold_image, cri1, cri2)

mean_data = repmat(reshape(mean_image, [1 size(data, 2) size(data, 3)]), [size(data, 1) 1 1]);
threshold_data = repmat(reshape(threshold_image, [1 size(data, 2) size(data, 3)]), [size(data, 1) 1 1]);
std_data = repmat(reshape(std_image, [1 size(data, 2) size(data, 3)]), [size(data, 1) 1 1]);

thresh1_data = (data > mean_data + cri1*std_data & threshold_data);
thresh2_data = (data > mean_data + cri2*std_data & threshold_data);
clear mean_data
clear std_data
clear threshold_data

thresh_sum_data = uint8(thresh1_data + thresh2_data);
clear thresh1_data
clear thresh2_data

% find sparks using simplest possible 3D connectivity
sparks = imhmax(thresh_sum_data, 1, 6);

```

9.4.1.4 Masked Mean Subproc

```

function m_mean = masked_mean(x, mask)
% mask - binary array. zero indicates to exclude value from calculated
% mean and std, one indicates inclusion

m_x = x.*mask;
m_sum = sum(m_x);
n = sum(mask);

```

```
m_mean = m_sum./n;
```

9.4.1.5 Masked_mean_and_std Subproc

```
function m_mean = masked_mean(x, mask)
% mask - binary array. zero indicates to exclude value from calculated
% mean and std, one indicates inclusion

m_x = x.*mask;
m_sum = sum(m_x);
n = sum(mask);
m_mean = m_sum./n;
```

9.4.2 Defining Sparks Versus Noise in 2D OPM Data

The assessment of spark morphological characteristics was a key aim in this study and as such it was important to reduce as far as possible any false positive spark detection. The main morphological measurements output by the detection algorithm were area, FDHM and amplitude. The frequency distribution of these measures had a significant positive skew such that logarithmic transformations were used to create a symmetrical, more Gaussian spread of data in order to facilitate statistical testing and detection of outliers (Figure 9-3).

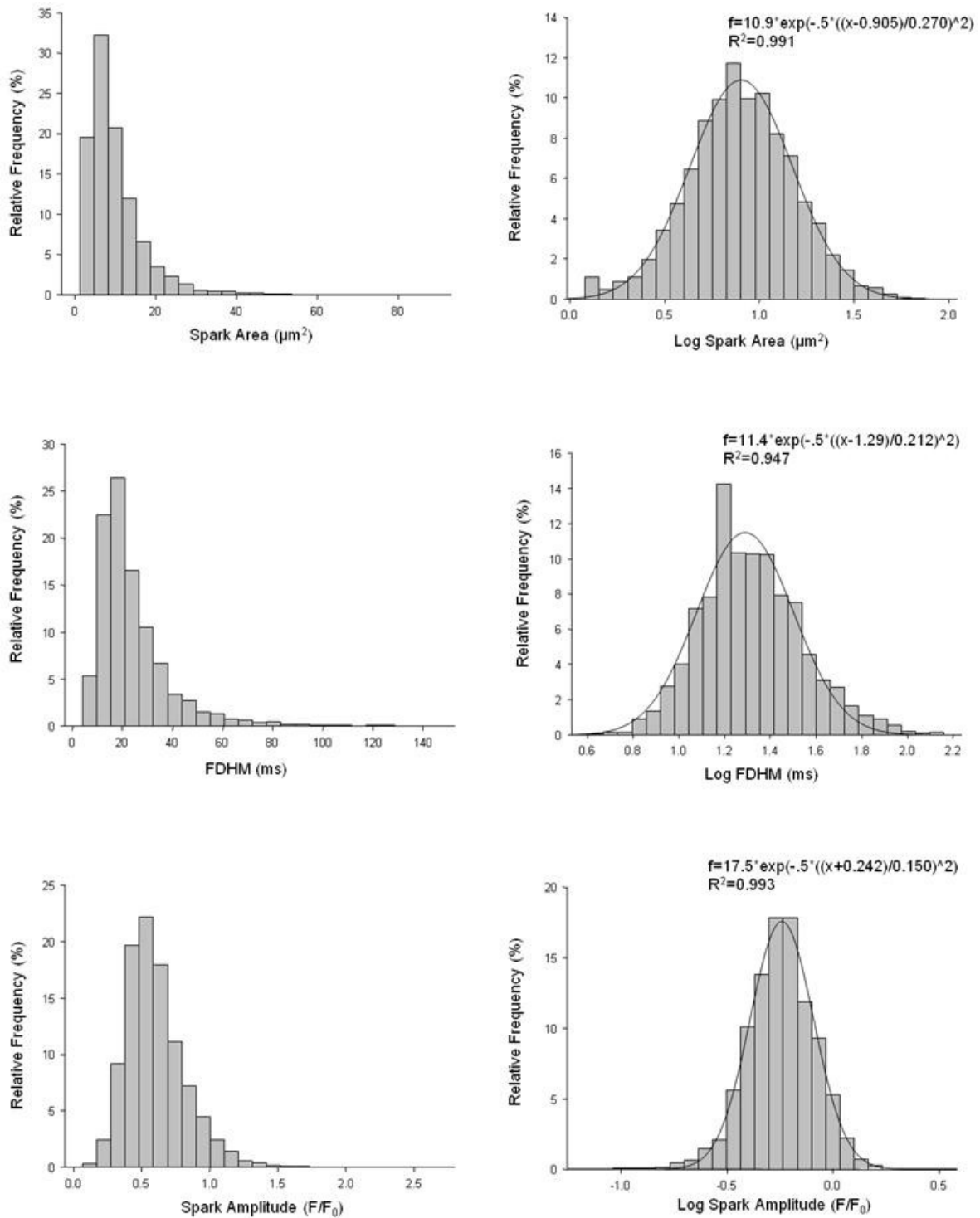


Figure 9-3. Transformations of raw data to give approximately Gaussian distributions.

Approximately Gaussian distributions with good fit to Gaussian functions were produced via logarithmic transformations of spark area, FDHM and amplitude. Although normality tests (e.g. Kolmogorov-Smirnov tests) reject the null hypothesis that these are normally distributed, this

probably relates to the large sample sizes, and the distributions are close enough to normal to perform statistical modelling.

Minimum size limits were defined for spark area and duration to avoid detection of noise. These were initially set as 8 frames (12ms) and 20 pixels². The resulting sparks detected had an area frequency distribution as shown in Figure 9-4.

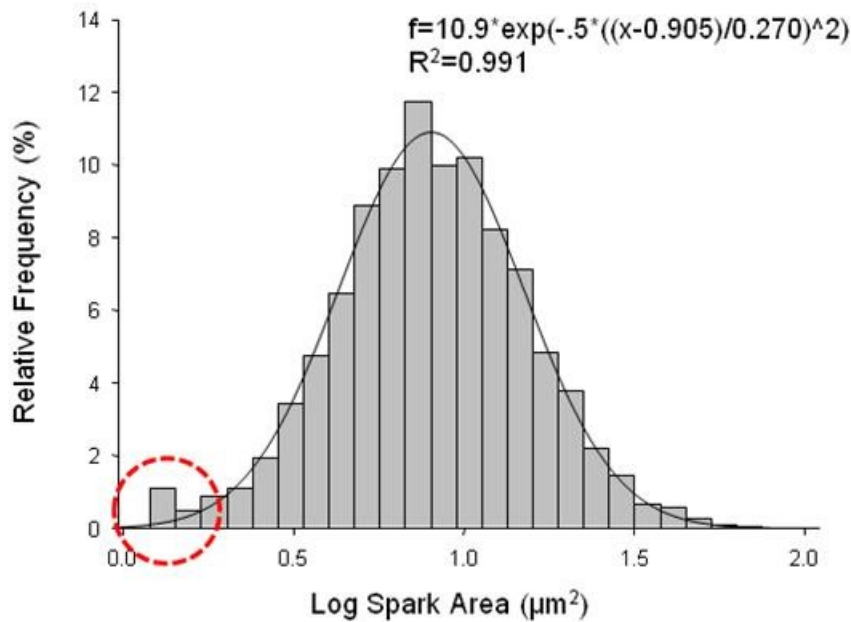


Figure 9-4 Histogram of spark area distribution.

The histogram of the logarithmic transformation of spark area shows a good Gaussian fit with R^2 value of 0.991. There is however an anomalous increase in frequency at low area (circled). These sparks were manually assessed and found to be more likely to represent noise.

This revealed an anomalous group of sparks with small area. Further manual assessment of the small sparks in the images revealed that they appeared more likely to represent noise than a true spark, e.g. a single pixel or two separate pixels becoming brighter for a single frame with spatial and temporal smoothing being responsible for a spark-like appearance being detected by the algorithm. In order to avoid this problem, characteristics within the data were used to assess the probability of sparks being real versus noise. It was hypothesized that sparks produced by noise were likely to have smaller area, duration and amplitude and that these characteristics might be used to exclude such sparks. To start with 126 sparks defined as anomalous via the DETECTANOMALY command in SPSS were assessed manually. To be defined as a real spark >1 contiguous pixel in the raw data had to be consistently brighter over time and versus nearest neighbours for >1 frame. In this way of the 126 sparks assessed, 28 were defined as false positive and 98 were defined as true positive. Receiver operated characteristic (ROC) curves were produced, using area, duration and amplitude, as well as the sum of duration and amplitude as predictors of true positive sparks (Figure 9-5, Figure 9-6.)

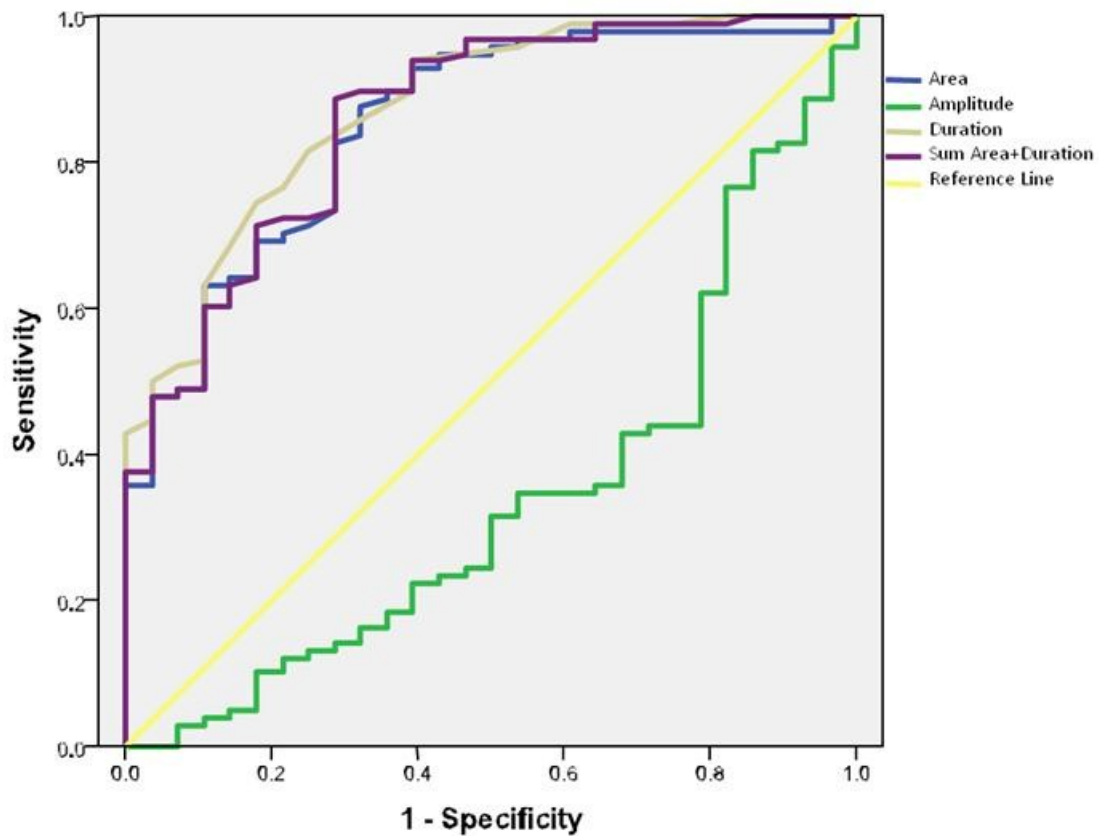


Figure 9-5. ROC curves for automated selection of noise-related sparks.

ROC curves using area, duration and their sum are good predictors of true-positive sparks. Amplitude is a weakly negative predictor.

Test Result Variable(s)	Area	Std. Error ^a	Asymptotic Sig. ^b	Asymptotic 95% Confidence Interval	
				Lower Bound	Upper Bound
Area	.852	.040	.000	.775	.930
Amplitude	.342	.060	.011	.225	.459
Duration	.876	.035	.000	.806	.945
Sum Area+Duration	.862	.039	.000	.785	.938

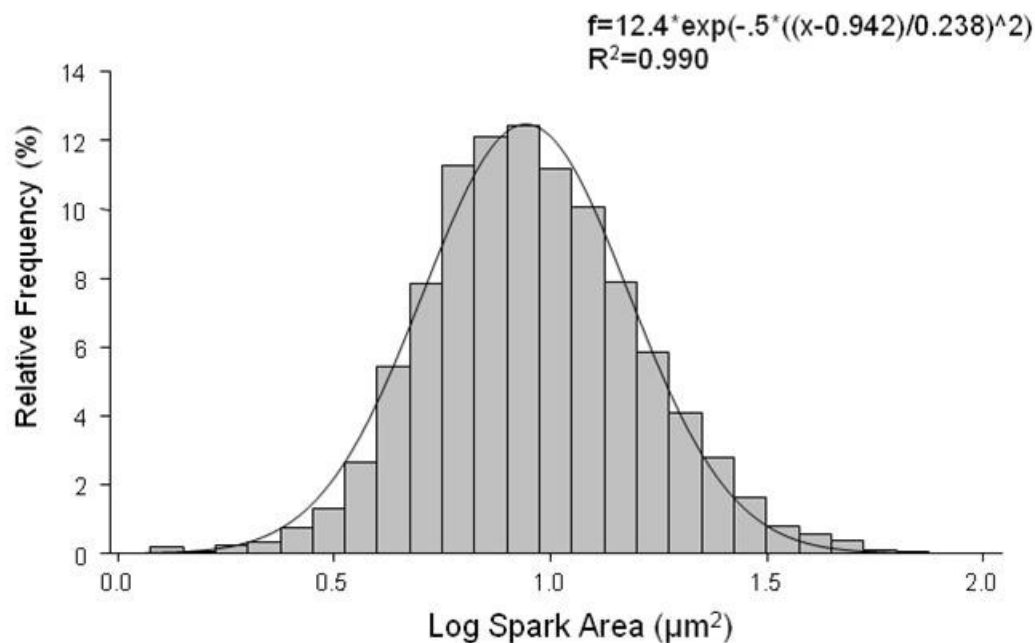
a. Under the nonparametric assumption

b. Null hypothesis: true area = 0.5

Figure 9-6. Table showing area under the curve for each predictor.

All predictors vary significantly from the reference line. Area and duration have similar ROC areas, whilst their sum does not confer any further advantage over the separate parameters.

Small area and short duration were found to identify different individual false-positive sparks. As such, with reference to the ROC co-ordinates table (Appendix 9.4.3), cut-offs were selected to define false positive sparks. Sparks were rejected if full duration was <12 frames (approx 18ms) while the area cut-off remained as before (<20pix² or 3µm²) since the duration criterion gave a good balance between sensitivity and specificity without the requirement for more stringent area criteria. These cut-offs successfully rejected 17/28 (61%) of false positive sparks identified within the anomalous sparks assessed and led to spurious rejection of 6/98 (6%) of true positive sparks. The prominence of the low area peak (which was associated with detection of noise) was also reduced (Figure 9-7).

**Figure 9-7. Noise-exclusion criteria results in a reduction of the prominence of small “noise” sparks.**

Rejection of sparks with full duration <12 frames (<18ms) resulted in reduced prominence of small sparks which had been shown to be largely a result of noise.

9.4.3 Appendix 4 – ROC Co-ordinate Table for Prediction of True Positive Sparks in OPM dataset

Test Result Variable(s)	Positive if Greater Than or Equal To ^a	Sensitivity	1 - Specificity
Area_Pix2	20.0000	1.000	1.000
	21.5000	1.000	.964
	22.5000	.980	.964
	23.5000	.980	.929
	24.5000	.980	.893
	26.0000	.980	.857
	27.5000	.980	.714
	29.5000	.980	.679
	36.0000	.980	.643
	41.5000	.980	.607
	43.0000	.969	.607
	44.5000	.969	.571
	47.0000	.969	.536
	49.5000	.959	.536
	50.5000	.959	.500
	52.0000	.949	.500
	53.5000	.949	.429
	57.5000	.929	.429
	61.5000	.929	.393
	62.5000	.918	.393
	63.5000	.908	.393
	65.0000	.898	.393
	67.5000	.898	.357
	71.5000	.888	.357
	76.5000	.878	.321
	79.5000	.857	.321
	80.5000	.837	.321
	82.0000	.827	.286
	85.0000	.816	.286
	88.5000	.806	.286
	91.0000	.796	.286
	93.0000	.786	.286
	96.0000	.765	.286
	101.5000	.755	.286
	105.5000	.735	.286
	107.0000	.714	.250
	108.5000	.704	.214
	110.5000	.694	.214
	112.5000	.694	.179
	113.5000	.673	.179
	114.5000	.663	.179
	116.0000	.643	.179
	117.5000	.643	.143
	119.0000	.633	.143
	120.5000	.633	.107
	121.5000	.622	.107
	124.0000	.612	.107
	127.5000	.602	.107

	129.5000	.592	.107
	133.5000	.582	.107
	137.5000	.571	.107
	139.0000	.561	.107
	141.0000	.541	.107
	142.5000	.531	.107
	145.0000	.510	.107
	148.5000	.490	.107
	151.5000	.490	.071
	158.0000	.480	.071
	170.0000	.480	.036
	178.0000	.469	.036
	179.5000	.459	.036
	180.5000	.449	.036
	181.5000	.439	.036
	183.0000	.429	.036
	187.0000	.418	.036
	192.0000	.408	.036
	196.5000	.388	.036
	200.0000	.378	.036
	202.0000	.367	.036
	204.5000	.357	.036
	208.0000	.357	.000
	211.5000	.347	.000
	221.5000	.337	.000
	232.0000	.327	.000
	245.0000	.316	.000
	258.5000	.296	.000
	269.0000	.286	.000
	289.5000	.276	.000
	324.5000	.265	.000
	349.0000	.255	.000
	386.0000	.245	.000
	524.0000	.235	.000
	631.5000	.224	.000
	637.0000	.214	.000
	639.0000	.204	.000
	641.5000	.194	.000
	644.5000	.184	.000
	651.0000	.173	.000
	691.0000	.163	.000
	735.0000	.153	.000
	749.0000	.143	.000
	754.5000	.133	.000
	761.5000	.122	.000
	787.0000	.112	.000
	810.5000	.102	.000
	829.5000	.092	.000
	857.0000	.082	.000
	870.5000	.071	.000
	874.5000	.061	.000
	889.5000	.051	.000
	920.5000	.041	.000
	985.0000	.031	.000
	1068.0000	.020	.000
	1299.0000	.010	.000

Appendices

	1493.0000	.000	.000
Amplitude	.9331	1.000	1.000
	.0826	.990	1.000
	.0993	.980	1.000
	.1042	.969	1.000
	.1124	.959	1.000
	.1193	.959	.964
	.1254	.949	.964
	.1326	.939	.964
	.1388	.929	.964
	.1427	.918	.964
	.1462	.908	.964
	.1492	.898	.964
	.1507	.888	.964
	.1518	.888	.929
	.1571	.878	.929
	.1729	.867	.929
	.1990	.857	.929
	.2163	.847	.929
	.2219	.837	.929
	.2272	.827	.929
	.2363	.827	.893
	.2773	.816	.893
	.3133	.816	.857
	.3173	.806	.857
	.3201	.796	.857
	.3313	.786	.857
	.3501	.776	.857
	.3720	.765	.857
	.3965	.765	.821
	.4190	.755	.821
	.4459	.745	.821
	.4642	.735	.821
	.4825	.724	.821
	.5186	.714	.821
	.5466	.704	.821
	.5619	.694	.821
	.5736	.684	.821
	.5901	.673	.821
	.6037	.663	.821
	.6106	.653	.821
	.6213	.643	.821
	.6442	.633	.821
	.6650	.622	.821
	.6676	.622	.786
	.6724	.612	.786
	.6792	.602	.786
	.7247	.592	.786
	.7764	.582	.786
	.7870	.571	.786
	.8194	.561	.786
	.8547	.551	.786
	.8713	.541	.786
	.8854	.531	.786
	.9031	.520	.786
	.9217	.510	.786
	.9267	.500	.786
	.9330	.490	.786
	.9555	.480	.786
	.9834	.469	.786

1.0003	.459	.786
1.0232	.449	.786
1.0492	.439	.786
1.0649	.439	.750
1.0717	.439	.714
1.0742	.429	.714
1.0917	.429	.679
1.1147	.418	.679
1.1244	.408	.679
1.1282	.398	.679
1.1337	.388	.679
1.1397	.378	.679
1.1411	.367	.679
1.1464	.357	.679
1.1537	.357	.643
1.1601	.347	.643
1.1657	.347	.607
1.1731	.347	.571
1.1801	.347	.536
1.1928	.337	.536
1.2116	.327	.536
1.2194	.316	.536
1.2215	.316	.500
1.2240	.306	.500
1.2262	.296	.500
1.2307	.286	.500
1.2354	.276	.500
1.2375	.265	.500
1.2393	.255	.500
1.2419	.245	.500
1.2481	.245	.464
1.2532	.235	.464
1.2550	.235	.429
1.2592	.224	.429
1.2671	.224	.393
1.2772	.214	.393
1.2829	.204	.393
1.2933	.194	.393
1.3097	.184	.393
1.3191	.184	.357
1.3235	.173	.357
1.3261	.163	.357
1.3378	.163	.321
1.3489	.153	.321
1.3663	.143	.321
1.3832	.143	.286
1.3841	.133	.286
1.3891	.133	.250
1.3937	.122	.250
1.4094	.122	.214
1.4262	.112	.214
1.4299	.102	.214
1.4342	.102	.179
1.4526	.092	.179
1.4748	.082	.179
1.4878	.071	.179
1.5131	.061	.179
1.5323	.051	.179
1.5507	.051	.143
1.5751	.041	.143
1.5950	.041	.107
1.6261	.031	.107

Appendices

	1.6487	.031	.071
	1.6528	.020	.071
	1.8048	.010	.071
	2.0932	.000	.071
	2.4498	.000	.036
	3.6692	.000	.000
Duration_Frames	6.0000	1.000	1.000
	7.5000	1.000	.821
	8.5000	.990	.750
	9.5000	.990	.607
	10.5000	.959	.536
	11.5000	.939	.393
	12.5000	.898	.393
	13.5000	.857	.321
	14.5000	.816	.250
	15.5000	.765	.214
	16.5000	.745	.179
	17.5000	.684	.143
	18.5000	.633	.107
	19.5000	.592	.107
	20.5000	.571	.107
	21.5000	.531	.107
	22.5000	.520	.071
	24.0000	.500	.036
	25.5000	.480	.036
	26.5000	.449	.036
	27.5000	.429	.000
	28.5000	.408	.000
	29.5000	.388	.000
	30.5000	.378	.000
	32.0000	.367	.000
	33.5000	.357	.000
	34.5000	.347	.000
	35.5000	.337	.000
	36.5000	.327	.000
	37.5000	.316	.000
	38.5000	.296	.000
	40.5000	.276	.000
	42.5000	.265	.000
	43.5000	.255	.000
	44.5000	.245	.000
	45.5000	.235	.000
	47.5000	.224	.000
	50.0000	.214	.000
	52.0000	.204	.000
	53.5000	.194	.000
	54.5000	.163	.000
	55.5000	.122	.000
	56.5000	.112	.000
	58.0000	.092	.000
	59.5000	.071	.000
	60.5000	.061	.000
	64.0000	.051	.000
	67.5000	.041	.000
	69.5000	.031	.000
	74.0000	.020	.000
	83.5000	.010	.000
	91.0000	.000	.000
Sum_Area_Duration_Raw	27.0000	1.000	1.000
	29.5000	1.000	.964
	32.0000	1.000	.893

33.5000	1.000	.857
35.0000	.990	.821
36.5000	.990	.786
37.5000	.990	.750
40.0000	.990	.679
42.5000	.990	.643
46.5000	.980	.643
51.0000	.969	.643
53.0000	.969	.607
54.5000	.969	.571
57.0000	.969	.536
59.5000	.969	.500
60.5000	.969	.464
62.5000	.959	.464
65.5000	.949	.464
68.5000	.939	.429
71.0000	.939	.393
72.5000	.929	.393
73.5000	.918	.393
75.5000	.908	.393
79.0000	.898	.393
84.5000	.898	.357
89.0000	.898	.321
90.5000	.888	.286
91.5000	.878	.286
93.5000	.867	.286
96.5000	.847	.286
99.5000	.827	.286
101.5000	.816	.286
103.5000	.806	.286
106.5000	.786	.286
111.5000	.776	.286
116.0000	.765	.286
118.0000	.755	.286
119.5000	.745	.286
120.5000	.735	.286
121.5000	.724	.250
122.5000	.724	.214
123.5000	.714	.179
124.5000	.704	.179
125.5000	.694	.179
127.5000	.684	.179
130.0000	.663	.179
131.5000	.653	.179
133.0000	.643	.179
135.0000	.633	.143
137.5000	.622	.143
141.0000	.612	.143
145.0000	.602	.143
151.5000	.602	.107
156.5000	.582	.107
157.5000	.571	.107

159.5000	.561	.107
162.5000	.541	.107
165.0000	.531	.107
168.0000	.520	.107
171.0000	.490	.107
173.5000	.490	.071
178.0000	.480	.071
188.5000	.480	.036
199.5000	.469	.036
205.5000	.459	.036
208.5000	.449	.036
210.5000	.439	.036
215.5000	.418	.036
221.5000	.398	.036
225.0000	.388	.036
227.5000	.378	.036
229.5000	.378	.000
231.5000	.367	.000
235.5000	.357	.000
243.0000	.347	.000
254.5000	.337	.000
266.5000	.327	.000
278.5000	.316	.000
288.0000	.306	.000
295.0000	.296	.000
310.0000	.286	.000
330.0000	.276	.000
362.5000	.265	.000
396.0000	.255	.000
441.0000	.245	.000
579.5000	.235	.000
684.5000	.224	.000
686.5000	.214	.000
689.5000	.204	.000
694.5000	.194	.000
703.5000	.173	.000
744.5000	.163	.000
790.0000	.153	.000
805.0000	.143	.000
809.5000	.133	.000
823.0000	.122	.000
849.5000	.112	.000
869.0000	.102	.000
895.0000	.092	.000
926.0000	.071	.000
937.5000	.061	.000
950.0000	.051	.000
974.0000	.041	.000
1046.5000	.031	.000
1151.5000	.020	.000
1371.0000	.010	.000
1547.0000	.000	.000

The test result variable(s): Area_Pix2, Duration_Frames,

a. The smallest cutoff value is the minimum observed test value minus 1, and the largest cutoff value is the maximum observed test value plus 1. All the other cutoff values are the averages of two consecutive ordered observed test values.

9.4.4 Correlation of linescan data versus 2D data

It has been shown that the positive skew in the distribution of spark amplitude seen using confocal line scan detection of spark events is related to detection of out of focus events which have a far higher frequency than in focus events.(Cheng *et al.*, 1999) We assessed whether this problem would be reduced through the use of the OPM to scan in 2Dimensions. We compared histograms of spark amplitude distribution acquired under similar conditions using the two techniques and also compared their skewness (Figure 9-8)

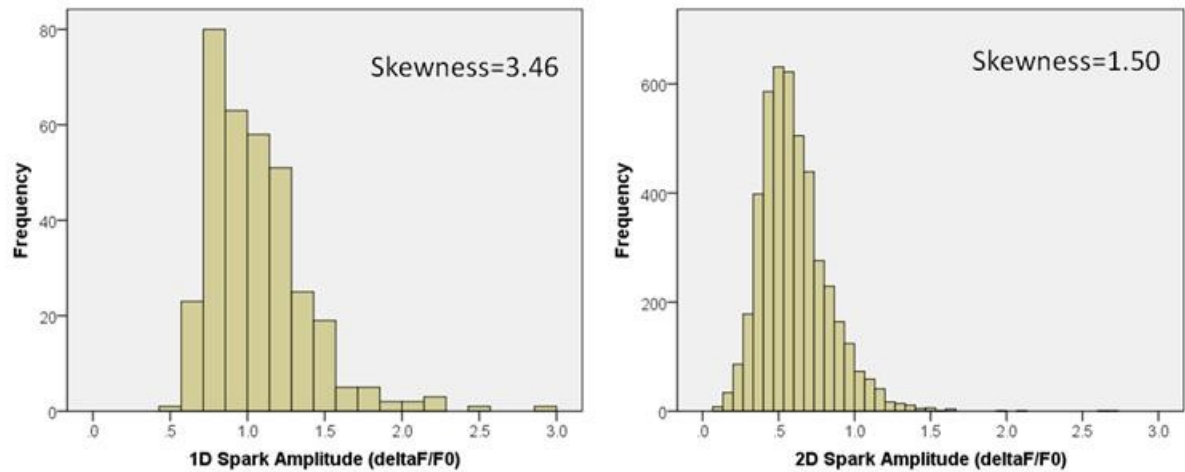


Figure 9-8. Positive skew in 1D spark amplitude data reduced by 2D analysis of same data. Linescan data extracted from 2D dataset shows a greater positive skew (left panel, skewness 3.46) as compared to amplitude data taken from 2D data analysis (right panel, skewness 1.50).

In order to assess whether data analysed from linescans predicts spark characteristics obtained from 2D datasets, the results obtained via the 2 techniques were correlated on a cell by cell basis in our dataset. Only data that was attainable via both techniques (frequency, amplitude, FWHM [in x dimension] and FDHM) were correlated. In the 2D dataset the frequency was corrected to give frequency/100 μm^2 /s whereas in the 1D dataset the measure was frequency/100 μm /s. The results are shown in Figure 9-9 and Table 9-16.

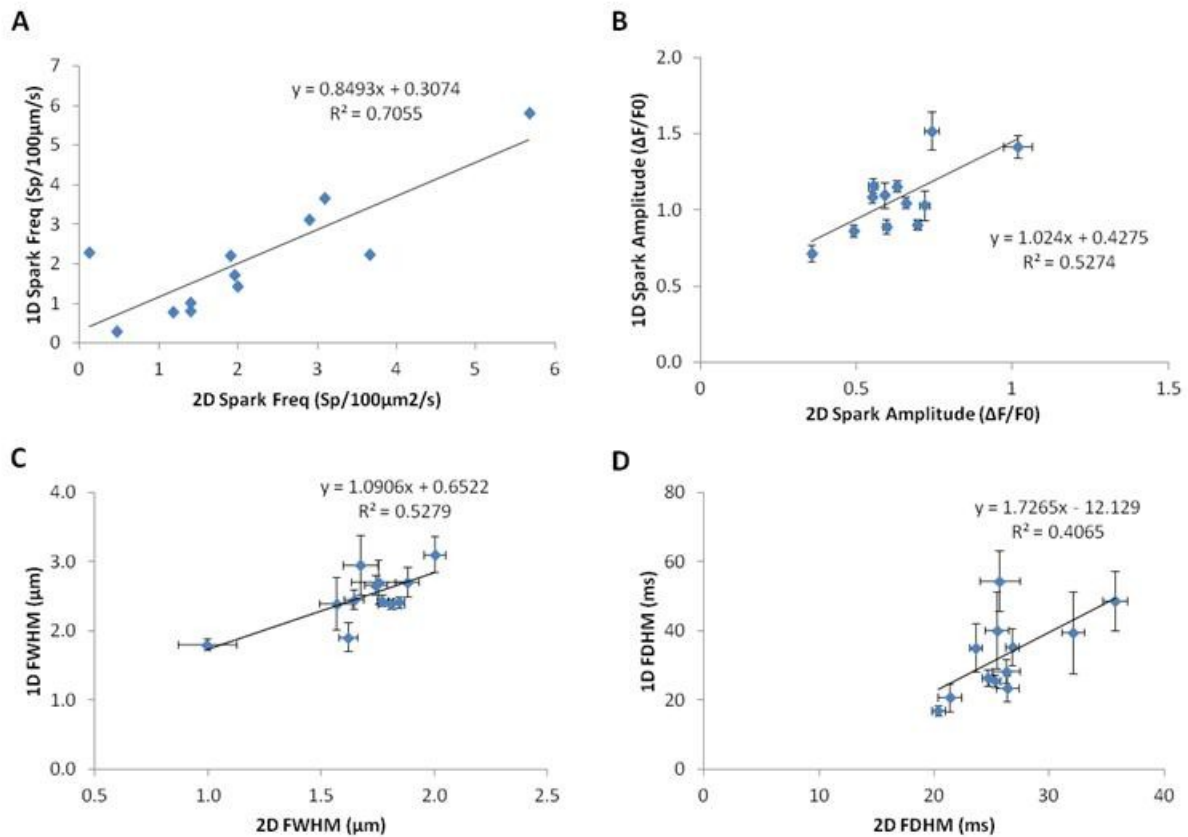


Figure 9-9. Correlation of 2D data with 1D data extracted from the same dataset analysed with criterion 6.

(A) Spark frequency is the best correlated of the four parameters assessed with a clear correlation between frequency assessed in 1D with frequency assessed in 2D (linear regression $R^2=0.706$). Spark amplitude, FWHM and FDHM (B-D) are also correlated but less strongly. Horizontal bars show SEM for 2D data and vertical bars show SEM of 1D data.

Parameter	R^2	Statistical significance of correlation (p value)
Frequency	0.706	*** <0.001
Amplitude	0.527	** 0.007
FWHM	0.528	** 0.007
FDHM	0.407	* 0.026

Table 9-16. R^2 values and p values of correlations between 1D and 2D data.

Although R^2 values are only moderate, all parameters show a significant correlation between the 2D and 1D data. The best correlation is between 2D and 1D frequency with measures of morphology less well correlated.

9.4.5 Example Syntax in SPSS to Give Significance Tests of Pairwise Comparisons of Interaction between HF and Spark_Location

```
MIXED LogAmp BY HF Spark_Zone
  /CRITERIA=CIN(95) MXITER(100) MXSTEP(10) SCORING(1) SINGULAR(0.000000000001)
HCONVERGE(0, ABSOLUTE) LCONVERGE(0, ABSOLUTE) PCONVERGE(0.000001, ABSOLUTE)
  /FIXED=HF Spark_Zone HF*Spark_Zone | SSTYPE(3)
  /METHOD=REML
  /PRINT=G R SOLUTION TESTCOV
  /RANDOM=INTERCEPT | SUBJECT(Cellnumber) COVTYPE(UN)
  /SAVE=PRED RESID
  /EMMEANS=TABLES(HF) COMPARE ADJ(BONFERRONI)
  /EMMEANS=TABLES(OVERALL)
  /EMMEANS=TABLES(Spark_Zone) COMPARE ADJ(BONFERRONI)
  /EMMEANS=TABLES(HF*Spark_Zone) compare (HF) adj (BONFERRONI)
  /EMMEANS=TABLES(HF*Spark_Zone) compare (Spark_Zone) adj (BONFERRONI).
```

9.4.6 Tables of hierarchical statistics for assessment of spark parameters vs location

Estimates of Fixed Effects ^a							
Parameter	Estimate	Std. Error	df	t	Sig.	95% Confidence Interval	
						Lower Bound	Upper Bound
[Tubulated=0]	-.372794	.120923	11	-3.083	.010	-.638943	-.106646
<i>[Tubulated=1]</i>
[HF=0]	-.125933	.388069	10	-.325	.752	-.990604	.738738
<i>[HF=1]</i>
[Tubulated=0] * [HF=0]	.343148	.233241	10	1.471	.172	-.176545	.862840
<i>[Tubulated=1] * [HF=0]</i>
<i>[Tubulated=0] * [HF=1]</i>
<i>[Tubulated=1] * [HF=1]</i>

a. Dependent Variable: Spark Frequency.

Items in italics are reference categories and thus have no p-values associated.

Table 9-17. Estimates of fixed effects for analysis of spark frequency in detubulated vs tubulated regions.

A profile analysis model is used and shows that neither HF or the interaction between HF and whether a region is tubulated have any significant effect on spark frequency. On the other hand whether a region is tubulated or not has a highly significant effect on frequency ($p=0.01$). Note,

values in this table and subsequent tables represent the final iteration of the model involving each parameter.

Estimates of Fixed Effects^a

Parameter	Estimate	Std. Error	df	t	Sig.	95% Confidence Interval	
						Lower Bound	Upper Bound
[Epi_Para=0]	1.133074	.186509	11.000	6.075	.000	.722570	1.543577
<i>[Epi_Para=1]</i>
[HF=0]	-.476290	.453176	10	-1.051	.318	-1.486028	.533449
<i>[HF=1]</i>
[Epi_Para=0] * [HF=0]	-.585079	.350996	10	-1.667	.126	-1.367147	.196988
<i>[Epi_Para=0] * [HF=1]</i>
<i>[Epi_Para=1] * [HF=0]</i>
<i>[Epi_Para=1] * [HF=1]</i>

a. Dependent Variable: Spark Frequency.

Items in italics are reference categories and thus have no p-values associated.

Table 9-18. Estimates of fixed effects for analysis of spark frequency in epitubular vs paratubular regions.

A profile analysis model is used and shows the interaction between HF and whether a region is epitubular or paratubular (within a tubulated region) has no significant effect on spark frequency. On the other hand whether a region is epitubular or paratubular has a highly significant effect on frequency ($p < 0.0001$).

Estimates of Fixed Effects^a

Parameter	Estimate	Std. Error	df	t	Sig.	95% Confidence Interval	
						Lower Bound	Upper Bound
[Tubulated=0]	.005668	.005863	4503.97	.967	.334	-.005827	.017163
<i>[Tubulated=1]</i>
[HF=0]	.063907	.065485	9.888	.976	.352	-.082228	.210041
<i>[HF=1]</i>
[HF=0] * [Tubulated=0]	-.022385	.012470	4504.9	-1.795	.073	-.046831	.002062
<i>[HF=0] * [Tubulated=1]</i>
<i>[HF=1] * [Tubulated=0]</i>
<i>[HF=1] * [Tubulated=1]</i>

a. Dependent Variable: LogAmp.

Items in italics are reference categories and thus have no p-values associated.

Table 9-19 Estimates of fixed effects for analysis of spark amplitude in detubulated vs tubulated regions.

A linear mixed model with random intercept is used and shows no significant effect of whether a region is detubulated or tubulated on LogAmp. Furthermore neither HF itself or the interaction between HF and zone have any significant effect on LogAmp.

Estimates of Fixed Effects ^a							
Parameter	Estimate	Std. Error	df	t	Sig.	95% Confidence Interval	
						Lower Bound	Upper Bound
[HF=0]	.067997	.068127	9.855	.998	.342	-.084104	.220097
[HF=1]
[Epi_Para=0]	.008745	.005149	3642.1	1.698	.090	-.001350	.018840
<i>[Epi_Para=1]</i>
[Epi_Para=0] * [HF=0]	.019651	.011923	3641.5	1.648	.099	-.003725	.043028
<i>[Epi_Para=0] * [HF=1]</i>
<i>[Epi_Para=1] * [HF=0]</i>
<i>[Epi_Para=1] * [HF=1]</i>

a. Dependent Variable: LogAmp.

Items in italics are reference categories and thus have no p-values associated.

Table 9-20. Estimates of fixed effects for analysis of spark amplitude in epitubular vs paratubular regions.

A linear mixed model with random intercept is used and shows no significant effect of whether a region is epitubular or paratubular on LogAmp. Furthermore neither HF itself or the interaction between HF and zone have any significant effect on LogAmp.

Estimates of Fixed Effects^a

Parameter	Estimate	Std. Error	df	t	Sig.	95% Confidence Interval	
						Lower Bound	Upper Bound
[Tubulated=0]	-.025976	.009635	4454.8	-2.696	.007	-.044865	-.007087
<i>[Tubulated=1]</i>
[HF=0]	-.050418	.036846	10.068	-1.368	.201	-.132441	.031605
<i>[HF=1]</i>
[HF=0] * [Tubulated=0]	-.008256	.020454	4301.4	-.404	.687	-.048357	.031846
<i>[HF=0] * [Tubulated=1]</i>
<i>[HF=1] * [Tubulated=0]</i>
<i>[HF=1] * [Tubulated=1]</i>

a. Dependent Variable: LogArea.

Items in italics are reference categories and thus have no p-values associated.

Table 9-21. Estimates of fixed effects for analysis of spark area in detubulated vs tubulated regions.

A linear mixed model with random intercept is used and shows no significant effect of HF or the interaction between HF and tubulation status. However tubulated regions exhibit sparks with significantly greater LogArea than detubulated regions.

Estimates of Fixed Effects^a

Parameter	Estimate	Std. Error	df	t	Sig.	95% Confidence Interval	
						Lower Bound	Upper Bound
[HF=0]	-.053707	.037018	10.046	-1.451	.177	-.136137	.028724
[HF=1]
[Epi_Para=0]	-.041142	.008525	3644.9	-4.826	.000	-.057856	-.024427
<i>[Epi_Para=1]</i>
[Epi_Para=0] * [HF=0]	-.007345	.019744	3646.8	-.372	.710	-.046055	.031366
<i>[Epi_Para=0] * [HF=1]</i>
<i>[Epi_Para=1] * [HF=0]</i>
<i>[Epi_Para=1] * [HF=1]</i>

a. Dependent Variable: LogArea.

Items in italics are reference categories and thus have no p-values associated.

Table 9-22. Estimates of fixed effects for analysis of LogArea in epitubular vs paratubular regions.

A linear mixed model with random intercept is used and shows no significant effect of HF or the interaction between HF and whether a region is epi- or paratubular on LogAmp. However paratubular regions exhibit sparks with significantly greater LogArea than epitubular regions.

Estimates of Fixed Effects^a

Parameter	Estimate	Std. Error	df	t	Sig.	95% Confidence Interval	
						Lower Bound	Upper Bound
[Tubulated=0]	-.000754	.008145	4491.9	-.093	.926	-.016721	.015214
<i>[Tubulated=1]</i>
[HF=0]	.006383	.040636	10.182	.157	.878	-.083942	.096708
<i>[HF=1]</i>
[HF=0] * [Tubulated=0]	-.012339	.017313	4452.5	-.713	.476	-.046282	.021604
<i>[HF=0] * [Tubulated=1]</i>
<i>[HF=1] * [Tubulated=0]</i>
<i>[HF=1] * [Tubulated=1]</i>

a. Dependent Variable: LogFDHM.

Items in italics are reference categories and thus have no p-values associated.

Table 9-23. Estimates of fixed effects for analysis of LogFDHM in detubulated vs tubulated regions.

A linear mixed model with random intercept is used and shows no significant effect of tubulation status, HF, or the interaction between HF and tubulation status on LogArea.

Estimates of Fixed Effects^a

Parameter	Estimate	Std. Error	df	t	Sig.	95% Confidence Interval	
						Lower Bound	Upper Bound
[HF=0]	.006956	.042398	10.308	.164	.873	-.087132	.101045
[HF=1]
[Epi_Para=0]	-.061059	.007166	3644.0	-8.521	.000	-.075109	-.047010
<i>[Epi_Para=1]</i>
[Epi_Para=0] * [HF=0]	.028081	.016592	3644.4	1.692	.091	-.004449	.060611
<i>[Epi_Para=0] * [HF=1]</i>
<i>[Epi_Para=1] * [HF=0]</i>
<i>[Epi_Para=1] * [HF=1]</i>

a. Dependent Variable: LogFDHM.

Items in italics are reference categories and thus have no p-values associated.

Table 9-24 Estimates of fixed effects for analysis of LogFDHM in epitubular vs paratubular regions.

A linear mixed model with random intercept is used and shows no significant effect of HF or the interaction between HF and whether a region is epi- or paratubular on LogFDHM. However paratubular regions exhibit sparks with significantly greater LogFDHM (i.e. spark duration) than epitubular regions.

9.5 Appendix for I_{Na} and waves chapter (7)

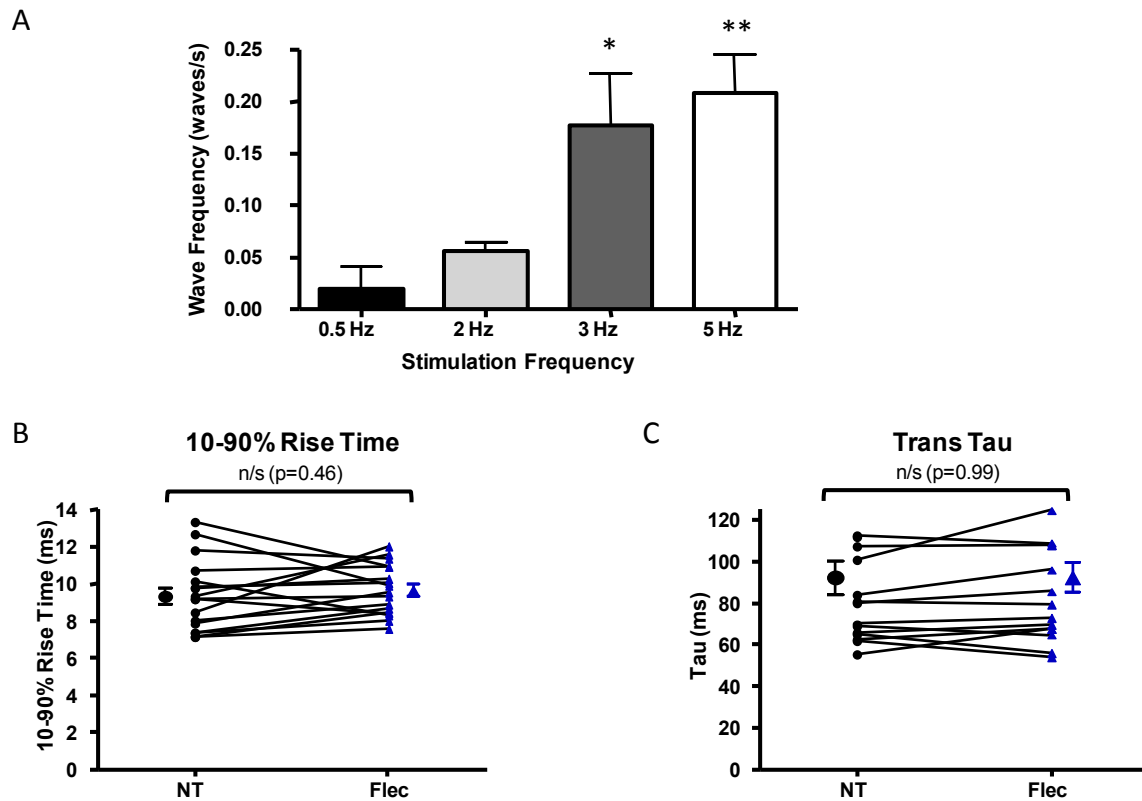


Figure 9-10. Effect of stimulation frequency on Ca^{2+} waves and effect of flecainide on Ca^{2+} transient morphology.

(A) Increasing stimulation frequency during 30s field stimulation increased wave frequency in a subsequent 20s quiescent period. $n=5$ cells at each frequency, * $p<0.05$ ** $p<0.01$ compared to 0.5Hz stimulation frequency by one-way ANOVA with Tukey's post-test. (B-C) Ca^{2+} transient morphology was not significantly altered by flecainide. Transients evoked by external field stimulation at 0.5 Hz exhibited no significant difference in rise or decay as exemplified by (B) 10%-90% rise time and (C) tau. ($n=17$ cells)

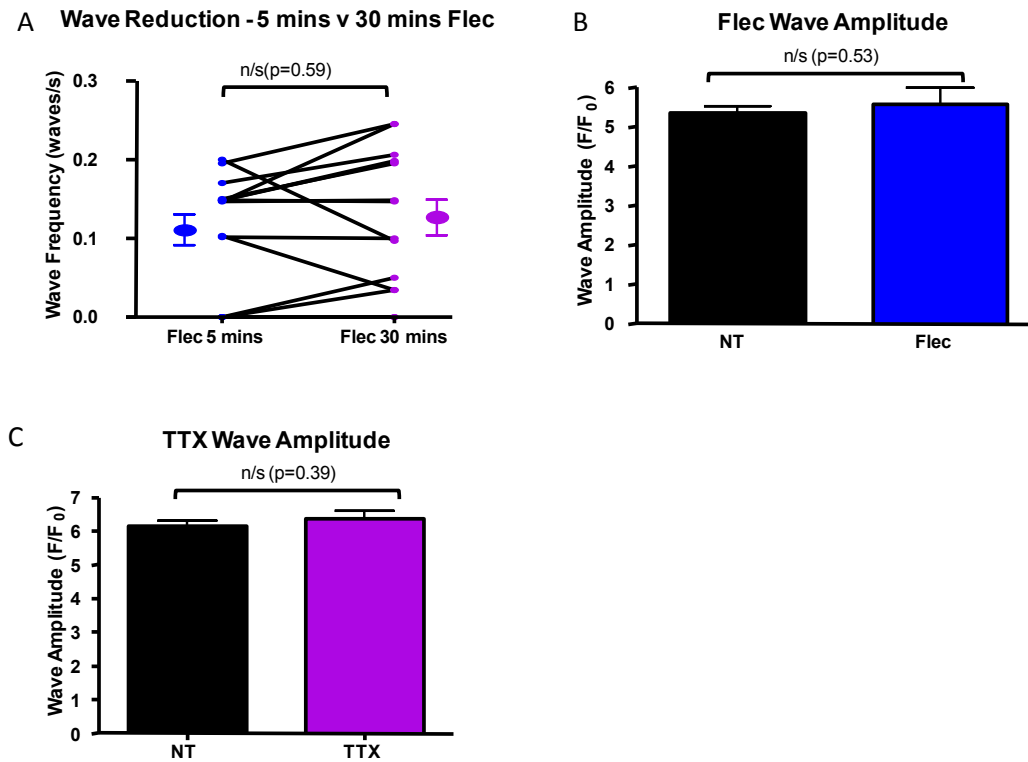


Figure 9-11. Supplementary effects of I_{Na} blockers on Ca^{2+} waves

(A) Wave frequency was not reduced further with 30mins exposure to flecainide vs 5 mins exposure. ($p=0.59$ by paired t -test, $n=15$ cells). (B) Wave amplitude was not significantly altered by $5\mu M$ flecainide ($p=0.53$ by Student's t -test, NT: $n=81$ waves; flec $n=36$ waves from 20 cells). (C) Wave amplitude was also unchanged by $5\mu M$ TTX (NT: $n=84$ waves; TTX $n=34$ waves from 10 cells).

A

MIXED Wave_Freq BY Flec

/CRITERIA=CIN(95) MXITER(100) MXSTEP(10) SCORING(1)

SINGULAR(0.000000000001) HCONVERGE(0, ABSOLUTE) LCONVERGE(0,

ABSOLUTE) PCONVERGE(0.000001, ABSOLUTE)

/FIXED=Flec | SSTYPE(3)

/METHOD=REML

/PRINT=R SOLUTION TESTCOV

/RANDOM=INTERCEPT | SUBJECT(Isolation) COVTYPE(UN)

/REPEATED=Flec | SUBJECT(Isolation*Cell) COVTYPE(UN)

/SAVE=PRED RESID

/EMMEANS=TABLES(Flec) COMPARE ADJ(LSD).

BEstimates of Covariance Parameters^a

Parameter		Estimate	Std. Error	Wald Z	Sig.	95% Confidence Interval	
						Lower Bound	Upper Bound
Repeated Measures	UN (1,1)	.027199	.008824	3.082	.002	.014401	.051370
	UN (2,1)	.004735	.003414	1.387	.166	-.001957	.011427
	UN (2,2)	.007320	.002375	3.082	.002	.003875	.013825
Intercept [subject = Isolation]	Variance	.000000 ^b	.000000

a. Dependent Variable: Wave_Freq.

b. This covariance parameter is redundant. The test statistic and confidence interval cannot be computed.

CEstimates of Fixed Effects^a

Parameter	Estimate	Std. Error	df	t	Sig.	95% Confidence Interval	
						Lower Bound	Upper Bound
Intercept	.100700	.019131	19	5.264	.000	.060659	.140741
[Flec=0]	.134050	.035390	19	3.788	.001	.059978	.208122
[Flec=1]	0 ^b	0

a. Dependent Variable: Wave_Freq.

b. This parameter is set to zero because it is redundant.

Figure 9-12. Hierarchical model analyzing wave frequency with flecainide

A hierarchical model was used to assess whether results would differ between this and a standard paired t-test. (A) SPSS syntax used to apply a random intercept at the level of the isolation and then a repeated measure at the level of the cell pre- and post-flecainide. (B) Output table of covariance parameters. The relevant section is that the intercept is redundant (see note b). This shows that the inclusion of isolation number in the model is not useful, i.e. does not improve the model. (C) The p-value of the hierarchical model pertaining to the effect of flecainide of wave frequency ($p=0.001$), is identical to that of the paired t-test in section 7.4.2.

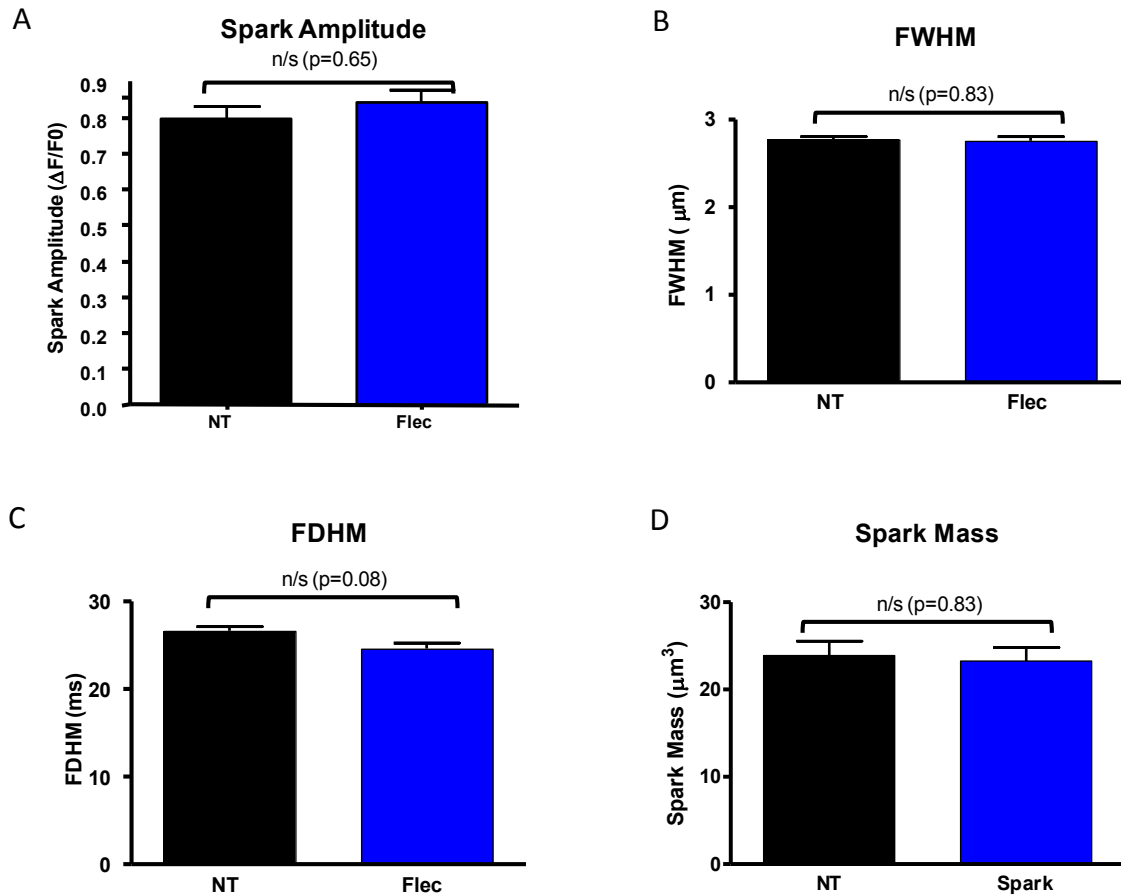


Figure 9-13. Ca^{2+} spark morphology is not significantly altered by flecainide.

Despite a reduction in spark frequency by flecainide, the morphological characteristics of individual sparks including (A) spark amplitude, (B) full-width at half maximum (FWHM), (C) full-duration at half maximum (FDHM) and (D) spark mass were not altered significantly in comparison to the control condition. (NT: n=661 sparks; flec: n=431 sparks from 24 cells)

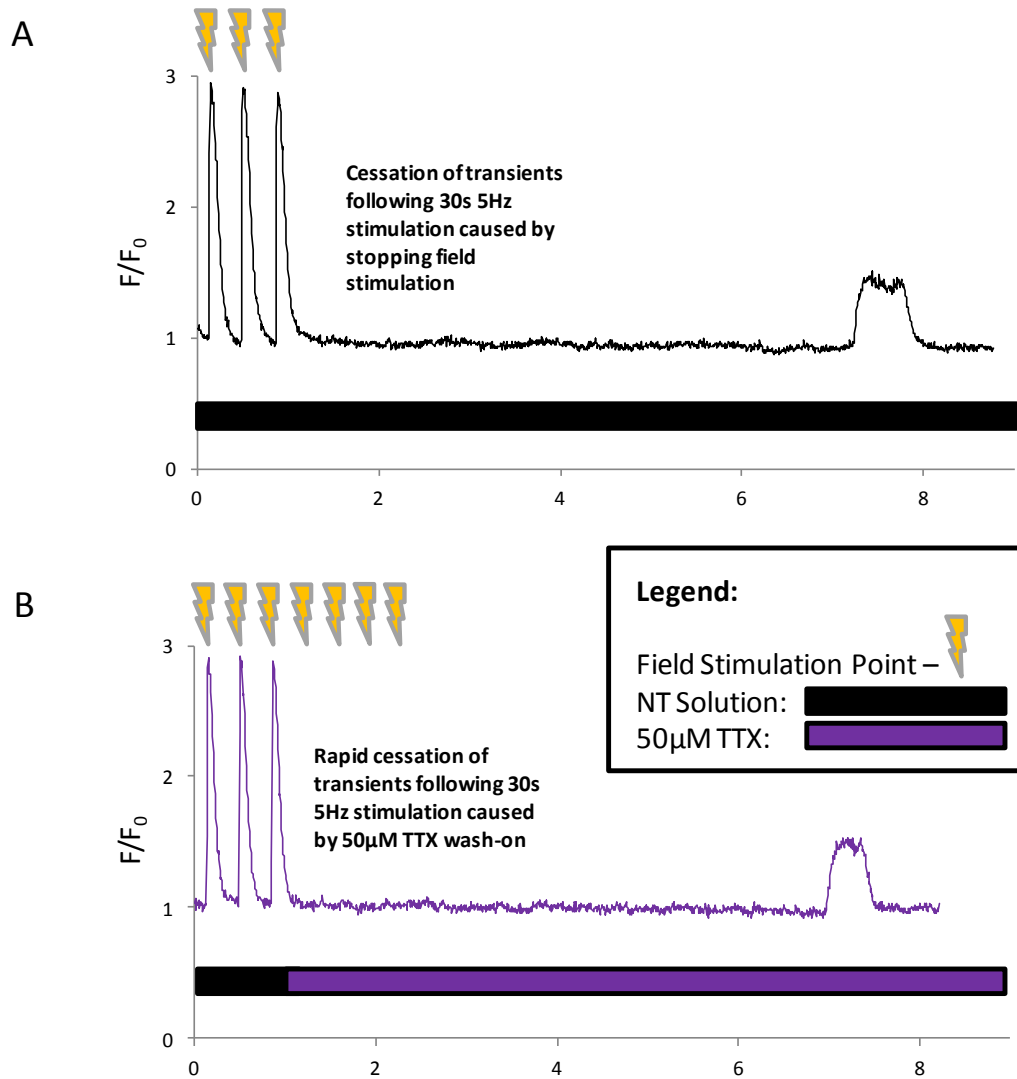


Figure 9-14. F/F_0 traces of a single cell in a control experiment and with rapid wash on of 50μM TTX.

(A) In the control condition external field stimulation at 5Hz for 30s is used to load the SR. Waves are then assessed during a subsequent 30s quiescent period following cessation of external field stimulation in normal Tyrode (NT). (B) The same cell is then exposed to a different protocol (50μM TTX wash-on). Following 30s external field stimulation at 5Hz in NT evoked transients are stopped by rapid wash-on of TTX while stimulation continues. This causes rapid cessation of evoked Ca^{2+} transients. Once it is clear that no further Ca^{2+} transients are occurring, external field stimulation is stopped. This provides evidence that I_{Na} is blocked whilst keeping the SR loading protocol identical to that of the control condition. Waves are then assessed in a subsequent 30s quiescent period as before.

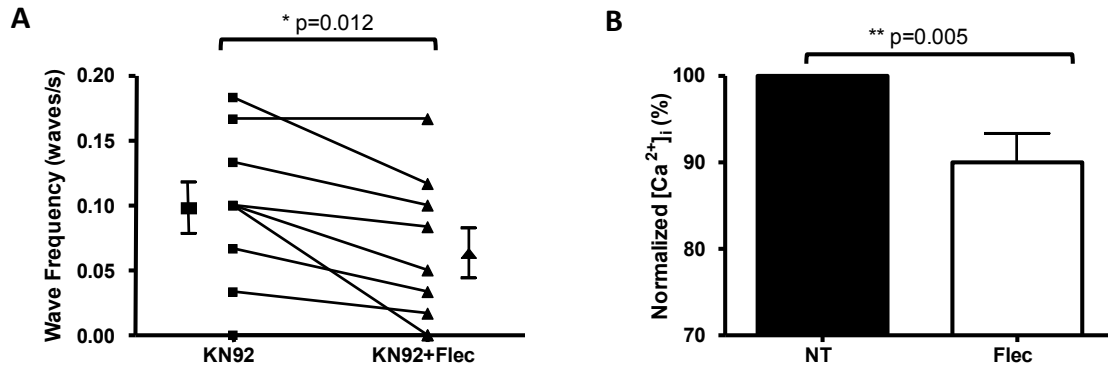


Figure 9-15. Mechanism of wave reduction with flecainide supplementary data

(A) Experiments in the presence of KN-92 revealed waves were reduced to a similar degree by flecainide as with KN-93 present (37% vs 35% reduction respectively). This provides evidence against an important role for CaMKII inhibition in the mechanism of action of flecainide's wave-reducing effects. (B) Whether enhanced Ca^{2+} efflux via NCX resulted in decreased diastolic $[Ca^{2+}]_i$ was assessed using fura-2 in the first 5s following cessation of 5Hz stimulation in field-stimulated cardiomyocytes. $[Ca^{2+}]_i$ was reduced in the presence of flecainide suggesting that reduction of $[Ca^{2+}]_i$ downstream of changes in I_{Na} and reduced $[Na^+]_i$ is part of the mechanism of wave reduction in rat cardiomyocytes (data expressed as % normalized diastolic $[Ca^{2+}]_i$ in NT group, $p=0.005$ by paired t-test on raw data, $n=20$ cells).

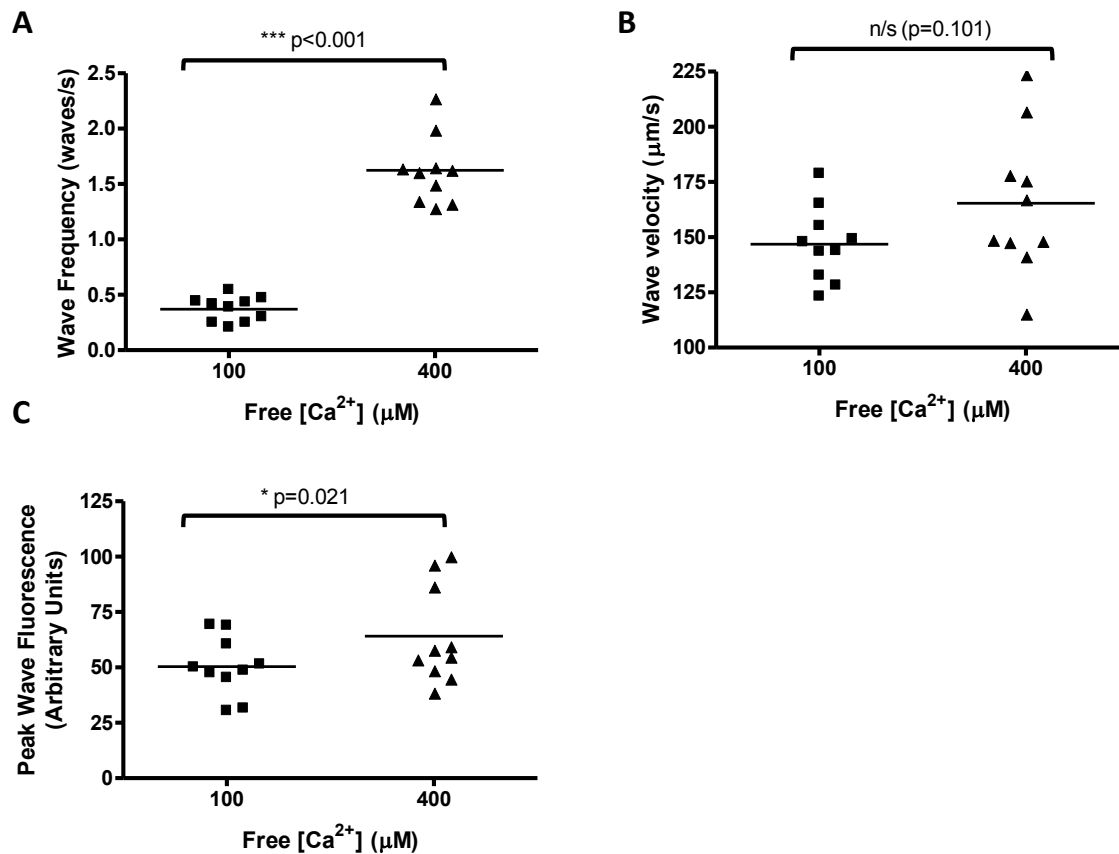


Figure 9-16. Effect of altering concentration of free Ca^{2+} on waves

(A) Wave frequency is substantially increased (over 4-fold) by increasing free $[\text{Ca}^{2+}]$ from 100nM to 400nM. (B) Wave velocity is not significantly increased. (C) Peak wave amplitude in terms of fluorescence units was also significantly increased (F/F_0 not used in this case since waves were so frequent that fluorescence could not fall to baseline levels between waves).

9.6 Appendix of Prizes, Publications and Abstracts Related to this Thesis

9.6.1 Prizes

- *Best Poster Prize*, Basic Science Category (European Working Group on Cardiac Cellular Electrophysiology) at EHRA/Europace Annual Meeting, Athens, 24/6/2013
- *Highly Commended Oral Presentation*, National Heart and Lung Institute Postgraduate Research Day, London, 21/6/2013
- *Best Poster Prize*, Basic Science Category (BAS/BSCR), British Cardiovascular Society Annual Meeting, London, 4/6/13
- *Best Poster Prize*, Imperial College Academic Trainees Annual Event 9/5/2013
- *Travel awards to attend:*
 - o European Working Group on Cardiac Cellular Electrophysiology Meeting, Athens, 06/2013
 - o Gordon Research Conference on Cardiac Arrhythmia Mechanisms, Ventura, California, 02/2013

9.6.2 Publications

- Land S, Niederer SA, Louch WE, Roe AT, Aronsen JM, Stuckey DJ, **Sikkel MB**, Tranter MH, Lyon AR, Harding SE, Smith NP. Computational modelling of Takotsubo cardiomyopathy: Effect of spatially varying beta-adrenergic stimulation in the rat left ventricle. *Am J Physiol Heart Circ Physiol*. 2014 Sep 19. [Epub ahead of print].
- **Sikkel MB**, Hayward C, Macleod KT, Harding SE, Lyon AR. SERCA2a gene therapy in heart failure: an anti-arrhythmic positive inotrope. *Br J Pharmacol*. 2014 Jan;171(1):38-54.
- Wright PT, Nikolaev VO, O'Hara T, Diakonov I, Bhargava A, Tokar S, Schobesberger S, Shevchuk AI, **Sikkel MB**, Wilkinson R, Trayanova NA, Lyon AR, Harding SE, Gorelik J. Caveolin-3 regulates compartmentation of cardiomyocyte beta2-adrenergic receptor-mediated cAMP signaling. *J Mol Cell Cardiol*. 2014 Feb;67:38-48.
- Shah M, **Sikkel MB**. Coronary artery disease and age: beyond atherosclerosis. *J Physiol*. 2013 Dec 1;591(Pt 23):5807-8.
- **Sikkel MB**, MacLeod KT, Gordon F. Letter by Sikkel et al regarding article, "Late sodium current inhibition reverses electromechanical dysfunction in human hypertrophic cardiomyopathy". *Circulation*. 2013 Sep 3;128(10):e156.
- Tranter MH, Wright PT, **Sikkel MB**, Lyon AR. Takotsubo cardiomyopathy: the pathophysiology. *Heart Fail Clin*. 2013 Apr;9(2):187-96.
- **Sikkel MB**, Collins TP, Rowlands C, Shah M, O'Gara P, Williams AJ, Harding SE, Lyon AR, Macleod KT. Triple mode of action of flecainide in Catecholaminergic Polymorphic Ventricular Tachycardia: Reply. *Cardiovasc Res*. 2013 May 1;98(2):327-8.
- Toepfer C, Caorsi V, Kampourakis T, **Sikkel MB**, West TG, Leung MC, Al-Saud SA, Macleod KT, Lyon AR, Marston SB, Sellers JR, Ferenczi MA. Myosin regulatory light chain (RLC) phosphorylation change as a modulator of cardiac muscle contraction in disease. *J Biol Chem*. 2013 May 10;288(19):13446-54.
- Caorsi V, Toepfer C, **Sikkel MB**, Lyon AR, MacLeod KT, Ferenczi MA. Non-Linear Optical Microscopy Sheds Light on Cardiovascular Disease. *PLOS One*. 2013 Feb 7.
- **Sikkel MB**, Collins TP, Rowlands C, Shah M, O'Gara P, Williams AJ, Harding SE, Lyon AR, Macleod KT. Flecainide Reduces Ca^{2+} Spark and Wave Frequency Via Inhibition of The Sarcolemmal Sodium Current. *Cardiovasc Res*. 2013 May 1;98(2):286-96.

- Paur H, Wright PT, **Sikkel MB**, Tranter MH, Mansfield C, O'Gara P, Stuckey DJ, Nikolaev VO, Diakonov I, Pannell L, Gong H, Sun H, Peters NS, Petrou M, Zheng Z, Gorelik J, Lyon AR, Harding SE. High levels of circulating epinephrine trigger apical cardiodepression in a $\beta(2)$ -adrenergic receptor/G(i)-dependent manner: a new model of Takotsubo cardiomyopathy. *Circulation*. 2012 Aug 7;126(6):697-706.
- Lyon AR, Nikolaev VO, Miragoli M, **Sikkel MB**, Paur H, Benard L, Hulot JS, Kohlbrenner E, Hajjar RJ, Peters NS, Korchev YE, Macleod KT, Harding SE, Gorelik J. Plasticity of surface structures and $\beta(2)$ -adrenergic receptor localization in failing ventricular cardiomyocytes during recovery from heart failure. *Circ Heart Fail*. 2012 May 1;5(3):357-65.
- Kumar S, Wilding D, **Sikkel MB**, Lyon AR, MacLeod KT, Dunsby C, High-speed 2D and 3D fluorescence microscopy of cardiac myocytes, *Opt. Express* 2011 19, 13839-13847

9.6.3 Abstracts

- Christopher Toepfer, Valentina Caorsi, Thomas Kampourakis, **Markus B. Sikkel**, Timothy West, Judy C. Leung, Sara A. Al-Saud, Ken Macleod, and others. Myosin Regulatory Light Chain (RLC) Phosphorylation Change as a Modulator of Cardiac Muscle Contraction in Disease. *Biophysical Journal* 2014, Vol. 104, Issue 2, p309a–310a
- Becker M. Al-khayatt, **Markus B. Sikkel**, Anita A. Laviada, Hung-Yen Ke, Christina Rowlands, Kenneth T. Macleod. Ranolazine Reduces Arrhythmogenic Calcium Waves in Ventricular Cardiomyocytes. *Biophysical Journal* 2014, Vol. 106, Issue 2, p721a
- Anita Alvarez-Laviada, **Markus Sikkel**, Becker Al-khayatt, Ken T. MacLeod. Effects of Flecainide and Ranolazine on Intracellular Calcium Handling and Sarcolemmal Sodium Current. *Biophysical Journal* 2014, Vol. 106, Issue 2, p324a.
- Christopher Toepfer, **Markus Sikkel**, Valentina Caorsi, O'Neal Copeland, Iratxe Torre Martinez, Timothy West, Steve Marston, Pradeep Luther, and others. Effects of Chronic Myocardial Infarction on Cardiac Muscle Performance and Structure In-Vivo and In-Vitro. *Biophysical Journal* 2014, Vol. 106, Issue 2, p343a–344a
- **M B Sikkel**, C Rowlands, S Harding, A Lyon, K MacLeod. Reducing Sarcolemmal Sodium Current Decreases Spontaneous SR Ca^{2+} Release. *Heart* 2013;99:suppl 2 A120
- Sophie Schobesberger, Sergiy Tokar, Anamika Bhargava, Peter Wright, **Markus Sikkel**, Niloy Mitra, Aron Monszpart, Alexander Lyon, Sian E. Harding, and Julia Gorelik. Alteration in β_2 -ARs Dependent cAMP Signalling Linked to Post Infarction Remodelling of T-tubules in Rat Cardiomyocytes. *Circulation*. 2013;128:A14993
- Peter T Wright, Viacheslav O Nikolaev, Sergiy Tokar, Anamika Bhargava, Ivan Diakonov, **Markus B Sikkel**, Alexander R Lyon, Sian E Harding, and Julia Gorelik. Caveolin3 Depletion Modifies β_2 -AR-cAMP Responses at Both Cellular and Sub-Cellular Levels in Cardiomyocytes. *Circulation*. 2012;126:A15670
- Anamika Bhargava, Tom O'Hara, **Markus B Sikkel**, Alexander R Lyon, Natalia A Trayanova, and Julia Gorelik. Nanoscale Movement of L-Type Calcium Channels in the Cardiomyocyte Membrane Can Contribute to Arrhythmia During Heart Failure. *Circulation*. 2012;126:A11953
- **M.B. Sikkel**, T.P. Collins, P. O'Gara, S.E. Harding, A.R. Lyon, K.T. Macleod. Elemental SR Ca^{2+} release in failing human cardiomyocytes - a comparison with failing rat cardiomyocytes and inhibition by flecainide. *Eur Heart J* (2012) 33 (suppl 1): 941-1105

- P.T. Wright, I. Diakonov, S. Tokar, A.R. Lyon, **M B. Sikkell**, S.E. Harding and J. Gorelik. Beta-2 adrenergic receptor signaling in adult rat ventricular myocytes at 4, 8 and 16 weeks after myocardial infarction. *Cardiovasc Res* (2012) 93 (suppl 1): S9-S45.
- T.P. Collins, **M.B. Sikkell**, P. O' Gara, A.R. Lyon, S.E. Harding and K.T. Macleod. Is SERCA overexpression anti- or pro-arrhythmic? *Cardiovasc Res* (2012) 93 (suppl 1): S5-S8.
- M. Shah, **M.B. Sikkell**, T. Desplantez, T.P. Collins, P. O'Gara, S.E. Harding, A.R. Lyon and K.T. Macleod. Flecaïnide reduces wave frequency and mean spark amplitude in isolated rat ventricular cardiomyocytes. *Cardiovasc Res* (2012) 93 (suppl 1): S88-S91.
- Miragoli M, Lab MJ, Singh A, **Sikkell MB**, Lyon AR, Gorelik J. The progression towards heart failure exposes the heart to a mechano-arrhythmic response related to the cellular membrane compliance. *Cardiovasc Res* 2012 93 (suppl 1): S46-S51
- Miragoli M, Lab MJ, **Sikkell M**, Lyon AR, Gorelik J. Structural Remodelling in Cardiomyocytes from Infarcted Hearts Potentiates Cellular Mechano-Aarrhythmic Response to Nanoscale Sarcolemmal Perturbation. *Circulation* 2011 124:A11795
- **Sikkell MB**, Shah M, Desplantez T, Collins TP, O'Gara P, Harding SE, Lyon AR, MacLeod KT. Flecaïnide Induces a New Population of Calcium Sparks in Rat Cardiomyocytes. *Circulation* 2011 124:A11948

10 REFERENCE LIST

- Ahmet I, Krawczyk M, Heller P, Moon C, Lakatta EG & Talan MI (2004). Beneficial effects of chronic pharmacological manipulation of beta-adrenoreceptor subtype signaling in rodent dilated ischemic cardiomyopathy. *Circulation* **110**, 1083–1090.
- Ai X, Curran JW, Shannon TR, Bers DM & Pogwizd SM (2005). Ca²⁺/calmodulin-dependent protein kinase modulates cardiac ryanodine receptor phosphorylation and sarcoplasmic reticulum Ca²⁺ leak in heart failure. *Circ Res* **97**, 1314–1322.
- Ait Mou Y, Toth A, Cassan C, Czuriga D, de Tombe PP, Papp Z, Lacampagne A & Cazorla O (2011). Beneficial effects of SR33805 in failing myocardium. *Cardiovasc Res* **91**, 412–419.
- Akiyama T (1981). Intracellular recording of in situ ventricular cells during ventricular fibrillation. *Am J Physiol* **240**, H465–H471.
- Alexander R, Jayes A, Maloiy G & Wathuta E (1979). Allometry of the limb bones of mammals from shrews (Sorex) to elephant (Loxodonta). *J*
- Altschuld RA, Starling RC, Hamlin RL, Billman GE, Hensley J, Castillo L, Fertel RH, Hohl CM, Robitaille P-ML, Jones LR, Xiao R-P & Lakatta EG (1995). Response of Failing Canine and Human Heart Cells to 2-Adrenergic Stimulation. *Circulation* **92**, 1612–1618.
- Anand IS (2002). Ventricular remodeling without cellular contractile dysfunction. *J Card Fail* **8**, S401–S408.
- Anand IS, Liu D, Chugh SSS, Prahash AJC, Gupta S, John R, Popescu F & Chandrashekhar Y (1997). Isolated myocyte contractile function is normal in postinfarct remodeled rat heart with systolic dysfunction. *Circulation* **96**, 3974–3984.
- Andersson DC & Marks AR (2010). Fixing ryanodine receptor Ca leak - a novel therapeutic strategy for contractile failure in heart and skeletal muscle. *Drug Discov Today Dis Mech* **7**, e151–e157.
- Antoons G, Willems R & Sipido KR (2012). Alternative strategies in arrhythmia therapy: evaluation of Na/Ca exchange as an anti-arrhythmic target. *Pharmacol Ther* **134**, 26–42.
- Aracena P, Tang W, Hamilton SL & Hidalgo C (2005). Effects of S-glutathionylation and S-nitrosylation on calmodulin binding to triads and FKBP12 binding to type 1 calcium release channels. *AntioxidRedoxSignal* **7**, 870–881.
- Babu GJ, Bhupathy P, Timofeyev V, Petrashevskaya NN, Reiser PJ, Chiamvimonvat N & Periasamy M (2007). Ablation of sarcolipin enhances sarcoplasmic reticulum calcium transport and atrial contractility. *Proc Natl Acad Sci U S A* **104**, 17867–17872.
- Baer M, Best PM & Reuter H (1976). Voltage-dependent action of tetrodotoxin in mammalian cardiac muscle. *Group* **260**, 619–621.
- Bers DM (2001). *Excitation-Contraction Coupling and Cardiac Contractile Force*, 2nd edn. Springer, Dordrecht.

- Bers DM (2002). Cardiac Excitation-Contraction Coupling. *Nature* **415**, 198–205.
- Bers DM, Bridge JH & MacLeod KT (1987). The mechanism of ryanodine action in rabbit ventricular muscle evaluated with Ca-selective microelectrodes and rapid cooling contractures. *Can J Physiol Pharmacol* **65**, 610–618.
- Beuckelmann DJ, Nabauer M & Erdmann E (1992). Intracellular calcium handling in isolated ventricular myocytes from patients with terminal heart failure. *Circulation* **85**, 1046–1055.
- Beuckelmann DJ, Nabauer M & Erdmann E (1993). Alterations of K⁺ currents in isolated human ventricular myocytes from patients with terminal heart failure. *Circ Res* **73**, 379–385.
- Biesmans L, Macquaide N, Heinzel FR, Bito V, Smith GL & Sipido KR (2011). Subcellular heterogeneity of ryanodine receptor properties in ventricular myocytes with low T-tubule density. *PLoS One* **6**, e25100.
- Bing OH, Brooks WW, Conrad CH, Sen S, Perreault CL & Morgan JP (1991). Intracellular calcium transients in myocardium from spontaneously hypertensive rats during the transition to heart failure. *Circ Res* **68**, 1390–1400.
- Bito V, Biesmans L, Gellen B, Antoons G, Macquaide N, Rouet-Benzineb P, Pezet M, Mercadier J-J & Sipido KR (2013). FKBP12.6 overexpression does not protect against remodelling after myocardial infarction. *Exp Physiol* **98**, 134–148.
- Bito V, de Waard MC, Biesmans L, Lenaerts I, Ozdemir S, van Deel E, Abdel-Mottaleb Y, Driesen R, Holemans P, Duncker DJ & Sipido KR (2010). Early exercise training after myocardial infarction prevents contractile but not electrical remodelling or hypertrophy. *Cardiovasc Res* **86**, 72–81.
- Bode EF, Briston SJ, Overend CL, O'Neill SC, Trafford a W & Eisner DA (2011). Changes of SERCA activity have only modest effects on sarcoplasmic reticulum Ca²⁺ content in rat ventricular myocytes. *J Physiol* **589**, 4723–4729.
- Bovo E, Lipsius SL & Zima A V (2012). Reactive oxygen species contribute to the development of arrhythmogenic Ca²⁺ waves during β -adrenergic receptor stimulation in rabbit cardiomyocytes. *J Physiol* **590**, 3291–3304.
- Braunwald E (2008). *Braunwald's Heart Disease*, 8th edn.ed. Mann DL, Libby P, Bonow R & Zipes D. Elsevier, Philadelphia.
- Bray M-A, Geisse N a & Parker KK (2007). Multidimensional detection and analysis of Ca²⁺ sparks in cardiac myocytes. *Biophys J* **92**, 4433–4443.
- Brillantes AB, Ondrias K, Scott A, Kobrinsky E, Ondriasová E, Moschella MC, Jayaraman T, Landers M, Ehrlich BE & Marks a R (1994). Stabilization of calcium release channel (ryanodine receptor) function by FK506-binding protein. *Cell* **77**, 513–523.
- Bristow MR, Ginsburg R, Umans V, Fowler M, Minobe W, Rasmussen R, Zera P, Menlove R, Shah P & Jamieson S (1986). Beta 1- and beta 2-adrenergic-receptor subpopulations in nonfailing and failing human ventricular myocardium: coupling of both receptor subtypes to muscle contraction and selective beta 1-receptor down- regulation in heart failure. *Circ Res* **59**, 297–309.

- Brochet DX, Xie W, Yang D, Cheng H & Lederer WJ (2011). Quarky calcium release in the heart. *Circ Res* **108**, 210–218.
- Brochet DXP, Yang D, Di Maio A, Lederer WJ, Franzini-Armstrong C & Cheng H (2005). Ca²⁺ blinks: rapid nanoscopic store calcium signaling. *Proc Natl Acad Sci U S A* **102**, 3099–3104.
- Brooksby P, Levi AJ & Jones J V (1993). Investigation of the mechanisms underlying the increased contraction of hypertrophied ventricular myocytes isolated from the spontaneously hypertensive rat. *Cardiovasc ...* **27**, 1268–1277.
- Brum G, González a, Rengifo J, Shirokova N & Ríos E (2000). Fast imaging in two dimensions resolves extensive sources of Ca²⁺ sparks in frog skeletal muscle. *J Physiol* **528**, 419–433.
- Brutsaert DL & De Keulenaer GW (2006). Diastolic heart failure: a myth. *Curr Opin Cardiol* **21**, 240–248.
- Cannell MB, Cheng H & Lederer WJ (1995). The control of calcium release in heart muscle. *Science (80-)* **268**, 1045–1049.
- Caorsi V, Toepfer C, Sikkell MB, Lyon AR, MacLeod K & Ferenczi M a (2013). Non-linear optical microscopy sheds light on cardiovascular disease. *PLoS One* **8**, e56136.
- Capasso JM & Anversa P (1992). Mechanical performance of spared myocytes after myocardial infarction in rats: effects of captopril treatment. *Am J Physiol* **263**, H841–H849.
- CAST Investigators (1992). Effect of the Antiarrhythmic Agent Moricizine on Survival after Myocardial Infarction. *N Engl J Med* **327**, 227–233.
- Catterall WA (2000). Structure and regulation of voltage-gated Ca²⁺ channels. *Annu DevBiol* **16**, 521–555.
- Cerrone M, Noujaim SF, Tolkacheva EG, Talkachou A, O’Connell R, Berenfeld O, Anumonwo J, Pandit S V, Vikstrom K, Napolitano C, Priori SG & Jalife J (2007). Arrhythmogenic mechanisms in a mouse model of catecholaminergic polymorphic ventricular tachycardia. *CircRes* **101**, 1039–1048.
- Cheng H & Lederer M (1996). Calcium sparks and i waves in cardiac myocytes. *Am J*
- Cheng H, Lederer MR, Lederer WJ & Cannell MB (1996). Calcium sparks and [Ca²⁺]i waves in cardiac myocytes. *AmJ Physiol* **270**, C148–C159.
- Cheng H, Lederer WJ & Cannell MB (1993). Calcium sparks: elementary events underlying excitation-contraction coupling in heart muscle. *Science (80-)* **262**, 740–744.
- Cheng H, Song LS, Shirokova N, González a, Lakatta EG, Ríos E & Stern MD (1999). Amplitude distribution of calcium sparks in confocal images: theory and studies with an automatic detection method. *Biophys J* **76**, 606–617.
- Cheng Y, Li W, Mcelfresh TA, Chen X, Berthiaume JM, Castel L, Yu X, Wagoner DR Van, Chandler MP, Ta M, Jm B, Wagoner V & Mp C (2011). Changes in myofilament proteins, but not Ca²⁺

- regulation, are associated with a high-fat diet-induced improvement in contractile function in heart failure. *Am J Physiol - Hear Circ Physiol* **301**, 1438–1446.
- Cheung JY, Musch TI, Misawa H, Semanchick a, Elensky M, Yelamarty R V & Moore RL (1994). Impaired cardiac function in rats with healed myocardial infarction: cellular vs. myocardial mechanisms. *Am J Physiol* **266**, C29–C36.
- Chudin E, Goldhaber J, Garfinkel A, Weiss J & Kogan B (1999). Intracellular Ca(2+) dynamics and the stability of ventricular tachycardia. *BiophysJ* **77**, 2930–2941.
- Cleland JG, Khand A & Clark A (2001). The heart failure epidemic: exactly how big is it? *EurHeart J* **22**, 623–626.
- Clusin WT, Bristow MR, Karagueuzian HS, Katzung BG & Schroeder JS (1982). Do calcium-dependent ionic currents mediate ischemic ventricular fibrillation? *Am J Cardiol* **49**, 606–612.
- Cohn JN, Levine TB, Olivari MT, Garberg V, Lura D, Francis GS, Simon AB & Rector T (1984). Plasma norepinephrine as a guide to prognosis in patients with chronic congestive heart failure. *N Engl J Med* **311**, 819–823.
- Coppini R, Ferrantini C, Yao L, Fan P, Del Lungo M, Stillitano F, Sartiani L, Tosi B, Suffredini S, Tesi C, Yacoub M, Olivotto I, Belardinelli L, Poggesi C, Cerbai E & Mugelli A (2013). Late sodium current inhibition reverses electromechanical dysfunction in human hypertrophic cardiomyopathy. *Circulation* **127**, 575–584.
- Cornea RL, Jones LR, Autry JM & Thomas DD (1997). Mutation and phosphorylation change the oligomeric structure of phospholamban in lipid bilayers. *Biochemistry* **36**, 2960–2967.
- Creemers EEJM, Davis JN, Parkhurst AM, Leenders P, Dowdy KB, Hapke E, Hauet AM, Escobar PG, Cleutjens JPM, Smits JFM, Daemen MJ a P, Zile MR & Spinale FG (2003). Deficiency of TIMP-1 exacerbates LV remodeling after myocardial infarction in mice. *Am J Physiol Heart Circ Physiol* **284**, H364–H371.
- Curran J, Brown KKH, Santiago DJD, Pogwizd S, Bers DM & Shannon TR (2010). Spontaneous Ca waves in ventricular myocytes from failing hearts depend on Ca(2+)-calmodulin-dependent protein kinase II. *J Mol Cell Cardiol* **49**, 25–32.
- Currie S, Elliott EB, Smith GL & Loughrey CM (2011). Two candidates at the heart of dysfunction: The ryanodine receptor and calcium/calmodulin protein kinase II as potential targets for therapeutic intervention - An in vivo perspective. *Pharmacol Ther* **131**, 204–220.
- Díaz ME, Cook SJ, Chamunorwa JP, Trafford AW, Lancaster MK, O'Neill SC, Eisner DA & Diaz ME (1996). Variability of spontaneous Ca²⁺ release between different rat ventricular myocytes is correlated with Na(+)-Ca²⁺ exchange and [Na⁺]_i. *Circ Res* **78**, 857–862.
- Dickstein K et al. (2008). ESC Guidelines for the diagnosis and treatment of acute and chronic heart failure 2008. *Eur Heart J* **29**, 2388–2442.
- Diez-Roux A (1998). Bringing context back into epidemiology: variables and fallacies in multilevel analysis. *Am J Public Health* **88**, 216–222.

- Dirnagl U (2006). Bench to bedside: the quest for quality in experimental stroke research. *J Cereb Blood Flow Metab* **26**, 1465–1478.
- Dixon IM, Lee SL & Dhalla NS (1990). Nitrendipine binding in congestive heart failure due to myocardial infarction. *Circ Res* **66**, 782–788.
- Doi M, Yano M, Kobayashi S, Kohno M, Tokuhisa T, Okuda S, Suetsugu M, Hisamatsu Y, Ohkusa T & Matsuzaki M (2002). Propranolol Prevents the Development of Heart Failure by Restoring FKBP12.6-Mediated Stabilization of Ryanodine Receptor. *Circulation* **105**, 1374–1379.
- Dries E, Bito V, Lenaerts I, Antoons G, Sipido KR & Macquaide N (2013). Selective modulation of coupled ryanodine receptors during microdomain activation of calcium/calmodulin-dependent kinase II in the dyadic cleft. *Circ Res* **113**, 1242–1252.
- Dunsby C (2008). Optically sectioned imaging by oblique plane microscopy. *Opt Express* **16**, 20306–20316.
- Dupont Y (1977). Kinetics and regulation of sarcoplasmic reticulum ATPase. *EurJBiochem* **72**, 185–190.
- Eisner DA, Choi HS, Díaz ME, O'Neill SC, Trafford a W & Diaz ME (2000). Integrative analysis of calcium cycling in cardiac muscle. *CircRes* **87**, 1087–1094.
- Eisner DA, George CH, Smith GL, Trafford AW & Venetucci LA (2010). How does CaMKII phosphorylation of the cardiac ryanodine receptor contribute to inotropy? *Proc Natl Acad Sci* **107**, E123–E123.
- Eisner DA & Trafford AW (2009). What is the purpose of the large sarcolemmal calcium flux on each heartbeat? *Am J Physiol - Hear Circ Physiol* **297**, H493–H494.
- Elliott EB, Hasumi H, Otani N, Matsuda T, Matsuda R, Kaneko N, Smith GL & Loughrey CM (2011). K201 (JTV-519) alters the spatiotemporal properties of diastolic Ca(2+) release and the associated diastolic contraction during β -adrenergic stimulation in rat ventricular cardiomyocytes. *Basic Res Cardiol* **106**, 1009–1022.
- Epstein F & Morgan J (1991). Abnormal intracellular modulation of calcium as a major cause of cardiac contractile dysfunction. *N Engl J Med* **325**, 625–632.
- Fabiato a. & Fabiato F (1972). Excitation-Contraction Coupling of Isolated Cardiac Fibers with Disrupted or Closed Sarcolemmas: CALCIUM-DEPENDENT CYCLIC AND TONIC CONTRACTIONS. *Circ Res* **31**, 293–307.
- Fauconnier J, Thireau J, Reiken S, Cassan C, Richard S, Matecki S, Marks AR & Lacampagne A (2010). Leaky RyR2 trigger ventricular arrhythmias in Duchenne muscular dystrophy. *Proc Natl Acad Sci U S A* **107**, 1559–1564.
- Ferrantini C, Crocini C, Coppini R, Vanzi F, Tesi C, Cerbai E, Poggesi C, Pavone FS & Sacconi L (2013). The transverse-axial tubular system of cardiomyocytes. *Cell Mol Life Sci*; DOI: 10.1007/s00018-013-1410-5.
- Field A (2009). *Discovering Statistics Using IBM SPSS Statistics*, 3rd edn. Sage, London.

- Frank K, Tilgmann C, Shannon TR, Bers DM & Kranias EG (2000). Regulatory role of phospholamban in the efficiency of cardiac sarcoplasmic reticulum Ca^{2+} transport. *Biochemistry* **39**, 14176–14182.
- Franzini-Armstrong C (1975). Membrane particles and transmission at the triad. *FedProc* **34**, 1382–1389.
- Fujiwara K, Tanaka H, Mani H, Nakagami T & Takamatsu T (2008). Burst emergence of intracellular Ca^{2+} waves evokes arrhythmogenic oscillatory depolarization via the Na^{+} - Ca^{2+} exchanger: simultaneous confocal recording of membrane potential and intracellular Ca^{2+} in the heart. *Circ Res* **103**, 509–518.
- Furukawa T, Koumi S, Sakakibara Y, Singer DH, Jia H, Arentzen CE, Backer CL & Wasserstrom JA (1995). An analysis of lidocaine block of sodium current in isolated human atrial and ventricular myocytes. *J Mol Cell Cardiol* **27**, 831–846.
- Fuster V & Kelly BB. eds. (2010). *Promoting Cardiovascular Health in the Developing World: A Critical Challenge to Achieve Global Health*. The National Academies Press, Washington DC.
- Galfré E, Pitt SJ, Venturi E, Sitsapesan M, Zaccai NR, Tsaneva-Atanasova K, O'Neill S & Sitsapesan R (2012). FKBP12 activates the cardiac ryanodine receptor Ca^{2+} -release channel and is antagonised by FKBP12.6. *PLoS One* **7**, e31956.
- Galimberti ES & Knollmann BC (2011). Efficacy and potency of class I antiarrhythmic drugs for suppression of Ca^{2+} waves in permeabilized myocytes lacking calsequestrin. *J Mol Cell Cardiol* **51**, 760–768.
- Gaur N & Rudy Y (2011). Multiscale Modeling of Calcium Cycling in Cardiac Ventricular Myocyte: Macroscopic Consequences of Microscopic Dyadic Function. *Biophys J* **100**, 2904–2912.
- Georgakopoulos D, Mitzner WA, Chen CH, Byrne BJ, Millar HD, Hare JM & Kass DA (1998). In vivo murine left ventricular pressure-volume relations by miniaturized conductance micromanometry. *Am J Physiol Hear Circ Physiol* **274**, H1416–H1422.
- George CH (2008). Sarcoplasmic reticulum Ca^{2+} leak in heart failure: mere observation or functional relevance? *Cardiovasc Res* **77**, 302–314.
- Gerdes a. M, Kellerman SE, Moore J a., Muffly KE, Clark LC, Reaves PY, Malec KB, McKeown PP & Schocken DD (1992). Structural remodeling of cardiac myocytes in patients with ischemic cardiomyopathy. *Circulation* **86**, 426–430.
- Gerdes AM (2002). Cardiac myocyte remodeling in hypertrophy and progression to failure. *J Card Fail* **8**, S264–S268.
- Giannini G, Conti a, Mammarella S, Scrobogna M & Sorrentino V (1995). The ryanodine receptor/calcium channel genes are widely and differentially expressed in murine brain and peripheral tissues. *J Cell Biol* **128**, 893–904.
- Gill C, Mestril R & Samali A (2002). Losing heart: the role of apoptosis in heart disease--a novel therapeutic target? *FASEB J* **16**, 135–146.

- Goldstein H, Browne W & Rasbash J (2002). Multilevel modelling of medical data. *Stat Med* **21**, 3291–3315.
- Gomez a. M, Guatimosim S, Dilly KW, Vassort G & Lederer WJ (2001). Heart Failure After Myocardial Infarction: Altered Excitation-Contraction Coupling. *Circulation* **104**, 688–693.
- Gomez A, Valdivia H & Cheng H (1997). Defective excitation-contraction coupling in experimental cardiac hypertrophy and heart failure. *Science (80-)*; DOI: 10.1126/science.276.5313.800.
- Gomez AM, Cheng H, Lederer WJ, Bers DM & Gómez a M (1996). Ca²⁺ diffusion and sarcoplasmic reticulum transport both contribute to [Ca²⁺]_i decline during Ca²⁺ sparks in rat ventricular myocytes. *J Physiol* **496**, 575–581.
- Grossman W, Jones D & McLaurin LP (1975). Wall stress and patterns of hypertrophy in the human left ventricle. *J Clin Invest* **56**, 56–64.
- Guatimosim S, Dilly K, Ferno Santana L, Saleet Jafri M, Sobie EA & Lederer WJ (2002). Local Ca²⁺ Signaling and EC Coupling in Heart: Ca²⁺ Sparks and the Regulation of the [Ca²⁺]_i Transient. *J Mol Cell Cardiol* **34**, 941–950.
- Guo T, Zhang T, Mestril R & Bers DM (2006). Ca²⁺/Calmodulin-dependent protein kinase II phosphorylation of ryanodine receptor does affect calcium sparks in mouse ventricular myocytes. *Circ Res* **99**, 398–406.
- Gwathmey JK, Copelas L, MacKinnon R, Schoen FJ, Feldman MD, Grossman W & Morgan JP (1987). Abnormal intracellular calcium handling in myocardium from patients with end-stage heart failure. *Circ Res* **61**, 70–76.
- Gwathmey JK & Morgan JP (1985). Altered calcium handling in experimental pressure-overload hypertrophy in the ferret. *Circ Res* **57**, 836–843.
- Gyorke I & Gyorke S (1998). Regulation of the cardiac ryanodine receptor channel by luminal Ca²⁺ involves luminal Ca²⁺ sensing sites. *Biophys J* **75**, 2801–2810.
- Gyorke S & Fill M (1993). Ryanodine Receptor Adaptation: Control Mechanism of Ca-Induced Ca-Release in Heart. *Science (80-)* **260**, 807–809.
- Györke S, Lukyanenko V & Györke I (1997). Dual effects of tetracaine on spontaneous calcium release in rat ventricular myocytes. *J Physiol* **500 (Pt 2)**, 297–309.
- Hagemann D, Kuschel M, Kuramochi T, Zhu W, Cheng H & Xiao RP (2000). Frequency-encoding Thr17 phospholamban phosphorylation is independent of Ser16 phosphorylation in cardiac myocytes. *J Biol Chem* **275**, 22532–22536.
- Hajdu STEP & Leonard EDWA (1961). Action of Ryanodine on Mammalian Cardiac Muscle: Effects on Contractility, and Reversal of Digitalis-induced Ventricular Arrhythmias. *Circ Res* **9**, 1291–1298.
- Hasenfuss G (1998). Alterations of calcium-regulatory proteins in heart failure. *Cardiovasc Res* **37**, 279–289.

- Hasenfuss G, Schillinger W, Lehnart SE, Preuss M, Pieske B, Maier LS, Prestle J, Minami K & Just H (1999). Relationship between Na⁺-Ca²⁺-exchanger protein levels and diastolic function of failing human myocardium. *Circulation* **99**, 641–648.
- Heinzel FR, Bito V, Biesmans L, Wu M, Detre E, von Wegner F, Claus P, Dymarkowski S, Maes F, Bogaert J, Rademakers F, D’hooge J & Sipido K (2008). Remodeling of T-tubules and reduced synchrony of Ca²⁺ release in myocytes from chronically ischemic myocardium. *Circ Res* **102**, 338–346.
- Heinzel FR, MacQuaide N, Biesmans L & Sipido K (2011). Dyssynchrony of Ca²⁺ release from the sarcoplasmic reticulum as subcellular mechanism of cardiac contractile dysfunction. *J Mol Cell Cardiol* **50**, 390–400.
- Hill MF & Singal PK (1996). Antioxidant and oxidative stress changes during heart failure subsequent to myocardial infarction in rats. *Am J Pathol* **148**, 291–300.
- Hilliard FA, Steele DS, Laver D, Yang Z, Le Marchand SJ, Chopra N, Piston DW, Huke S & Knollmann BC (2010). Flecainide inhibits arrhythmogenic Ca²⁺ waves by open state block of ryanodine receptor Ca²⁺ release channels and reduction of Ca²⁺ spark mass. *J Mol Cell Cardiol* **48**, 293–301.
- Hoit BD (2006). Echocardiographic characterization of the cardiovascular phenotype in rodent models. *Toxicol Pathol* **34**, 105–110.
- Hollingworth S, Peet J, Chandler WK & Baylor SM (2001). Calcium sparks in intact skeletal muscle fibers of the frog. *J Gen Physiol* **118**, 653–678.
- Holt E, Tønnessen T, Lunde PK, Semb SO, Wasserstrom J a, Sejersted OM & Christensen G (1998). Mechanisms of cardiomyocyte dysfunction in heart failure following myocardial infarction in rats. *J Mol Cell Cardiol* **30**, 1581–1593.
- Hou Z, Kelly EM & Robia SL (2008). Phosphomimetic mutations increase phospholamban oligomerization and alter the structure of its regulatory complex. *JBiolChem* **283**, 28996–29003.
- Hox JJ (2010). *Multilevel Analysis: Techniques and Applications*, 2nd edn. Routledge Academic, Hove, United Kingdom.
- Hoyt RH, Cohen ML & Saffitz JE (1989). Distribution and three-dimensional structure of intercellular junctions in canine myocardium. *Circ Res* **64**, 563–574.
- Huang B, Wang S, Qin D, Boutjdir M & El-Sherif N (1999). Diminished Basal Phosphorylation Level of Phospholamban in the Postinfarction Remodeled Rat Ventricle : Role of beta-Adrenergic Pathway, Gi Protein, Phosphodiesterase, and Phosphatases. *Circ Res* **85**, 848–855.
- Huang K, Huang D, Shengquan F, Yang C & Liao Y (2008). Abnormal Calcium “Sparks” in Cardiomyocytes of Post-myocardial Infarction Heart. *J Huazhong Univ Sci Technol* **28**, 401–408.
- Hunt DJ, Jones PP, Wang R, Chen W, Bolstad J, Chen K, Shimoni Y & Chen SRW (2007). K201 (JTV519) suppresses spontaneous Ca²⁺ release and [3H]ryanodine binding to RyR2 irrespective of FKBP12.6 association. *Biochem J* **404**, 431–438.

- Hunt SA et al. (2005). ACC/AHA 2005 Guideline Update for the Diagnosis and Management of Chronic Heart Failure in the Adult--Summary Article: A Report of the American College of Cardiology/American Heart Association Task Force on Practice Guidelines (Writing Committee to Update. *Circulation* **112**, 1825–1852.
- Hwang HS, Hasdemir C, Laver D, Mehra D, Turhan K, Faggioni M, Yin H & Knollmann BC (2011). Inhibition of cardiac Ca²⁺ release channels (RyR2) determines efficacy of class I antiarrhythmic drugs in catecholaminergic polymorphic ventricular tachycardia. *Circ Arrhythm Electrophysiol* **4**, 128–135.
- Ibarra C, Vicencio JM, Estrada M, Lin Y, Rocco P, Rebellato P, Munoz JP, Garcia-Prieto J, Quest AFG, Chiong M, Davidson SM, Bulatovic I, Grinnemo K-H, Larsson O, Szabadkai G, Uhlén P, Jaimovich E & Lavandero S (2013). Local control of nuclear calcium signaling in cardiac myocytes by perinuclear microdomains of sarcolemmal insulin-like growth factor 1 receptors. *Circ Res* **112**, 236–245.
- Ibrahim M, Navaratnarajah M, Siedlecka U, Rao C, Dias P, Moshkov A V, Gorelik J, Yacoub MH & Terracciano CM (2012). Mechanical unloading reverses transverse tubule remodelling and normalizes local Ca(2+)-induced Ca(2+)release in a rodent model of heart failure. *Eur J Heart Fail* **14**, 571–580.
- Iribe G, Ward CW, Camelliti P, Bollensdorff C, Mason F, Burton RA, Garny A, Morpew MK, Hoenger A, Lederer WJ & Kohl P (2009). Axial stretch of rat single ventricular cardiomyocytes causes an acute and transient increase in Ca²⁺ spark rate. *CircRes* **104**, 787–795.
- Isoyama S, Wei JY, Izumo S, Fort P, Schoen FJ & Grossman W (1987). Effect of age on the development of cardiac hypertrophy produced by aortic constriction in the rat. *Circ Res* **61**, 337–345.
- Ito H & Takaki M (1996). Left ventricular volumetric conductance catheter for rats. *Am J Physiol* **270**, H1509–H1514.
- Jhund PS, Macintyre K, Simpson CR, Lewsey JD, Stewart S, Redpath A, Chalmers JW, Capewell S & McMurray JJ (2009). Long-term trends in first hospitalization for heart failure and subsequent survival between 1986 and 2003: a population study of 5.1 million people. *Circulation* **119**, 515–523.
- Jiang D, Xiao B, Yang D, Wang R, Choi P, Zhang L, Cheng H & Chen SRW (2004). RyR2 mutations linked to ventricular tachycardia and sudden death reduce the threshold for store-overload-induced Ca²⁺ release (SOICR). *Proc Natl Acad Sci U S A* **101**, 13062–13067.
- Johns TN & Olson BJ (1954). Experimental myocardial infarction. I. A method of coronary occlusion in small animals. *AnnSurg* **140**, 675–682.
- Johnson DM, Heijman J, Bode EF, Greensmith DJ, van der Linde H, Abi-Gerges N, Eisner DA, Trafford AW & Volders PGA (2013). Diastolic Spontaneous Calcium Release From the Sarcoplasmic Reticulum Increases Beat-to-Beat Variability of Repolarization in Canine Ventricular Myocytes After +¹-Adrenergic Stimulation. *Circ Res* **112**, 246–256.
- Jones PP, Jiang D, Bolstad J, Hunt DJ, Zhang L, Demareux N & Chen SRW (2008). Endoplasmic reticulum Ca²⁺ measurements reveal that the cardiac ryanodine receptor mutations linked to

cardiac arrhythmia and sudden death alter the threshold for store-overload-induced Ca²⁺ release. *Biochem J* **412**, 171–178.

Kajita J & Yamaguchi H (1993). Calcium mobilization by muscarinic cholinergic stimulation in bovine single airway smooth muscle. *Am J Physiol ...* **264**, L496–L503.

Kalthof B, Sato N, Iwase M & Shen Y (1995). Effects of ryanodine on cardiac contraction, excitation-contraction coupling and “treppe” in the conscious dog. *J Mol ...* **27**, 2111–2121.

Kaneko N, Matsuda R, Ohtani N, Nakajima T, Arikawa T, Suzuki H, Toyoda S, Kikuchi M, Hata Y, Abe S, Taguchi I & Shimamoto K (2006). K201 Improves norepinephrine-induced diastolic dysfunction with preserved ejection fraction. *Drug Dev ...* **861**, 852–861.

Kapiloff MS, Jackson N & Airhart N (2001). mAKAP and the ryanodine receptor are part of a multi-component signaling complex on the cardiomyocyte nuclear envelope. *J Cell Sci* **114**, 3167–3176.

Kaprielian R, Wickenden a D, Kassiri Z, Parker TG, Liu PP & Backx PH (1999). Relationship between K⁺ channel down-regulation and [Ca²⁺]_i in rat ventricular myocytes following myocardial infarction. *J Physiol* **517** (Pt 1, 229–245.

Kashimura T, Briston SJ, Trafford AW, Napolitano C, Priori SG, Eisner D a & Venetucci L a (2010). In the RyR2(R4496C) mouse model of CPVT, β-adrenergic stimulation induces Ca waves by increasing SR Ca content and not by decreasing the threshold for Ca waves. *Circ Res* **107**, 1483–1489.

Kass RS, Lindegger N, Hagen B & Lederer WJ (2008). Another calcium paradox in heart failure. *J Mol Cell Cardiol* **45**, 28–31.

Keller M, Kao JP, Egger M & Niggli E (2007). Calcium waves driven by “sensitization” wave-fronts. *Cardiovasc Res* **74**, 39–45.

Kho C, Lee A, Jeong D, Oh JG, Chaanine AH, Kizana E, Park WJ & Hajjar RJ (2011). SUMO1-dependent modulation of SERCA2a in heart failure. *Nature* **477**, 601–605.

Kimura J, Miyamae S & Noma A (1987). Identification of sodium-calcium exchange current in single ventricular cells of guinea-pig. *J Physiol* **4**, 199–222.

Kimura Y, Kurzydowski K, Tada M & MacLennan DH (1997). Phospholamban Inhibitory Function Is Activated by Depolymerization. *J Biol Chem* **272**, 15061–15064.

Knollmann B & Chopra N (2006). Casq2 deletion causes sarcoplasmic reticulum volume increase, premature Ca²⁺ release, and catecholaminergic polymorphic ventricular tachycardia. *J ...*; DOI: 10.1172/JCI29128.2510.

Kohlhardt M (1984). Block of sodium currents by antiarrhythmic agents: analysis of the electrophysiologic effects of propafenone in heart muscle. *AmJ Cardiol* **54**, 13D – 19D.

De Koninck P (1998). Sensitivity of CaM Kinase II to the Frequency of Ca²⁺ Oscillations. *Science (80-)* **279**, 227–230.

- Kramer CM, Rogers WJ, Park CS, Seibel PS, Shaffer A, Theobald TM, Reichek N, Onodera T & Gerdes AM (1998). Regional Myocardial Dysfunction During Post-infarct Remodeling. **1778**, 1773–1778.
- Kumar S, Wilding D, Sikkell MB, Lyon AR, MacLeod KT & Dunsby C (2011). High-speed 2D and 3D fluorescence microscopy of cardiac myocytes. *Opt Express* **19**, 13839–13847.
- Kushnir A & Marks AR (2010). The ryanodine receptor in cardiac physiology and disease. *AdvPharmacol* **59**, 1–30.
- Lappe D & Lakatta E (1980). Intensity fluctuation spectroscopy monitors contractile activation in “resting” cardiac muscle. *Science (80-)* **207**, 1369–1371.
- Larbig R, Torres N, Bridge JHB, Goldhaber JJ & Philipson KD (2010). Activation of reverse Na⁺-Ca²⁺ exchange by the Na⁺ current augments the cardiac Ca²⁺ transient: evidence from NCX knockout mice. *J Physiol* **588**, 3267–3276.
- Lazic SE (2010). The problem of pseudoreplication in neuroscientific studies: is it affecting your analysis? *BMC Neurosci* **11**, 5 – .
- Leberer E, Hartner KT, Brandl CJ, Fujii J, Tada M, MacLennan DH & Pette D (1989). Slow/cardiac sarcoplasmic reticulum Ca²⁺-ATPase and phospholamban mRNAs are expressed in chronically stimulated rabbit fast-twitch muscle. *Eur J Biochem* **185**, 51–54.
- Lee J, Stagg M a, Fukushima S, Soppa GKR, Siedlecka U, Youssef SJ, Suzuki K, Yacoub MH & Terracciano CMN (2009). Adult progenitor cell transplantation influences contractile performance and calcium handling of recipient cardiomyocytes. *Am J Physiol Heart Circ Physiol* **296**, H927–H936.
- Lefroy DC, Crake T, Del Monte F, Vescovo G, Dalla Libera L, Harding S & Poole-Wilson P a (1996). Angiotensin II and contraction of isolated myocytes from human, guinea pig, and infarcted rat hearts. *Am J Physiol* **270**, H2060–H2069.
- Lehnart SE, Mongillo M, Bellinger A, Lindegger N, Chen BX, Hsueh W, Reiken S, Wronska A, Drew LJ, Ward CW, Lederer WJ, Kass RS, Morley G & Marks AR (2008). Leaky Ca²⁺ release channel/ryanodine receptor 2 causes seizures and sudden cardiac death in mice. *J Clin Invest* **118**, 2230–2245.
- Lemon G (2004). Fire-diffuse-fire calcium waves in confined intracellular spaces. *Bull Math Biol* **66**, 65–90.
- Li Y, Eisner DA & O’Neill SC (2012). Do calcium waves propagate between cells and synchronize alternating calcium release in rat ventricular myocytes? *J Physiol* **590**, 6353–6361.
- Li Y, Kranias EG, Mignery GA & Bers DM (2002). Protein kinase A phosphorylation of the ryanodine receptor does not affect calcium sparks in mouse ventricular myocytes. *Circ Res* **90**, 309–316.
- Ling H, Zhang T, Pereira L, Means CK, Cheng H, Gu Y, Dalton ND, Peterson KL, Chen J, Bers D & Brown JH (2009). Requirement for Ca²⁺ / calmodulin – dependent kinase II in the transition from pressure overload – induced cardiac hypertrophy to heart failure in mice. ; DOI: 10.1172/JCI38022.1230.

- Lipp P & Niggli E (1996). Submicroscopic calcium signals as fundamental events of excitation--contraction coupling in guinea-pig cardiac myocytes. *J Physiol* **492**, 31–38.
- Lipp P & Niggli E (1998). Fundamental calcium release events revealed by two-photon excitation photolysis of caged calcium in guinea-pig cardiac myocytes. *J Physiol* **508**, 801–809.
- Litwin S, Katz S & Weinberg E (1995). -doppler assessment of left ventricular geometry and function in rats with pressure-overload hypertrophy Chronic angiotensin-converting enzyme inhibition attenuates. *Circulation*.
- Litwin SE, Katz SE, Morgan JP & Douglas PS (1994). Serial echocardiographic assessment of left ventricular geometry and function after large myocardial infarction in the rat. *Circulation* **89**, 345–354.
- Litwin SE & Morgan JP (1992). Captopril enhances intracellular calcium handling and beta-adrenergic responsiveness of myocardium from rats with postinfarction failure. *Circ Res* **71**, 797–807.
- Litwin SE, Zhang D & Bridge JHB (2000). Dyssynchronous Ca²⁺ Sparks in Myocytes From Infarcted Hearts. *Circ Res* **87**, 1040–1047.
- Liu N, Denegri M, Ruan Y, Avelino-Cruz JE, Perissi A, Negri S, Napolitano C, Coetzee W a, Boyden P a & Priori SG (2011a). Short communication: flecainide exerts an antiarrhythmic effect in a mouse model of catecholaminergic polymorphic ventricular tachycardia by increasing the threshold for triggered activity. *Circ Res* **109**, 291–295.
- Liu N, Ruan Y, Denegri M, Bachetti T, Li Y, Colombi B, Napolitano C, Coetzee W a & Priori SG (2011b). Calmodulin kinase II inhibition prevents arrhythmias in RyR2(R4496C+/-) mice with catecholaminergic polymorphic ventricular tachycardia. *J Mol Cell Cardiol* **50**, 214–222.
- Lloyd-Jones DM, Larson MG, Leip EP, Beiser A, D'Agostino RB, Kannel WB, Murabito JM, Vasan RS, Benjamin EJ & Levy D (2002). Lifetime risk for developing congestive heart failure: the Framingham Heart Study. *Circulation* **106**, 3068–3072.
- Loennechen JP (2002). Effects of Cariporide and Losartan on Hypertrophy, Calcium Transients, Contractility, and Gene Expression in Congestive Heart Failure. *Circulation* **105**, 1380–1386.
- Loennechen JP, Wisløff U, Falck G & Ellingsen Ø (2002). Cardiomyocyte contractility and calcium handling partially recover after early deterioration during post-infarction failure in rat. *Acta Physiol Scand* **176**, 17–26.
- Louch WE, Bito V, Heinzel FR, Macianskiene R, Vanhaecke J, Flameng W, Mubagwa K & Sipido KR (2004). Reduced synchrony of Ca²⁺ release with loss of T-tubules-a comparison to Ca²⁺ release in human failing cardiomyocytes. *Cardiovasc Res* **62**, 63–73.
- Louch WE, Hake J, Jølle GF, Mørk HK, Sjaastad I, Lines GT & Sejersted OM (2010). Control of Ca²⁺ release by action potential configuration in normal and failing murine cardiomyocytes. *Biophys J* **99**, 1377–1386.
- Louch WE, Hake J, Mørk HK, Hougen K, Skrbic B, Ursu D, Tønnessen T, Sjaastad I & Sejersted OM (2013). Slow Ca(2+) sparks de-synchronize Ca(2+) release in failing cardiomyocytes: Evidence for altered configuration of Ca(2+) release units? *J Mol Cell Cardiol* **58**, 41–52.

- Louch WE, Mørk HK, Sexton J, Strømme T a, Laake P, Sjaastad I & Sejersted OM (2006). T-tubule disorganization and reduced synchrony of Ca²⁺ release in murine cardiomyocytes following myocardial infarction. *J Physiol* **574**, 519–533.
- Loughrey CM, Otani N, Seidler T, Craig M a, Matsuda R, Kaneko N & Smith GL (2007). K201 modulates excitation-contraction coupling and spontaneous Ca²⁺ release in normal adult rabbit ventricular cardiomyocytes. *Cardiovasc Res* **76**, 236–246.
- Lukyanenko V, Subramanian S, Gyorke I, Wiesner TF & Gyorke S (1999). The role of luminal Ca²⁺ in the generation of Ca²⁺ waves in rat ventricular myocytes. *J Physiol* **518** (Pt 1), 173–186.
- Lutgens E, Daemen MJ, de Muinck ED, Debets J, Leenders P & Smits JF (1999). Chronic myocardial infarction in the mouse: cardiac structural and functional changes. *Cardiovasc Res* **41**, 586–593.
- Lygren B, Carlson CR, Santamaria K, Lissandron V, McSorley T, Litzenberg J, Lorenz D, Wiesner B, Rosenthal W, Zaccolo M, Tasken K & Klussmann E (2007). AKAP complex regulates Ca²⁺ re-uptake into heart sarcoplasmic reticulum. *EMBO Rep* **8**, 1061–1067.
- Lyon AR, Bannister ML, Collins T, Pearce E, Sepehripour AH, Dubb SS, Garcia E, O’Gara P, Liang L, Kohlbrenner E, Hajjar RJ, Peters NS, Poole-Wilson P a, Macleod KT & Harding SE (2011). SERCA2a gene transfer decreases sarcoplasmic reticulum calcium leak and reduces ventricular arrhythmias in a model of chronic heart failure. *Circ Arrhythm Electrophysiol* **4**, 362–372.
- Lyon AR, MacLeod KT, Zhang Y, Garcia E, Kanda GK, Lab MJ, Korchev YE, Harding SE & Gorelik J (2009). Loss of T-tubules and other changes to surface topography in ventricular myocytes from failing human and rat heart. *Proc Natl Acad Sci U S A* **106**, 6854–6859.
- MacDonnell SM, García-Rivas G, Scherman J a, Kubo H, Chen X, Valdivia H & Houser SR (2008). Adrenergic regulation of cardiac contractility does not involve phosphorylation of the cardiac ryanodine receptor at serine 2808. *Circ Res* **102**, e65–e72.
- MacLennan D, Asahi M & Tupling R (2003). The Regulation of SERCA-Type Pumps by Phospholamban and Sarcolipin. *Ann N Y Acad Sci* **986**, 472–480.
- MacLennan DH & Green NM (2000). Structural biology: Pumping ions. *Nature* **405**, 633–634.
- MacQuaide N, Dempster J & Smith GL (2007). Measurement and Modeling of Ca²⁺ Waves in Isolated Rabbit Ventricular Cardiomyocytes. *Biophys J* **93**, 2581–2595.
- Maczewski M & Mackiewicz U (2008). Effect of metoprolol and ivabradine on left ventricular remodelling and Ca²⁺ handling in the post-infarction rat heart. *Cardiovasc Res* **79**, 42–51.
- Maier LS & Bers DM (2007). Role of Ca²⁺/calmodulin-dependent protein kinase (CaMK) in excitation-contraction coupling in the heart. *Cardiovasc Res* **73**, 631–640.
- Mann DL (1999). Mechanisms and Models in Heart Failure : A Combinatorial Approach. *Circulation* **100**, 999–1008.
- Manni S, Mauban JH, Ward CW & Bond M (2008). Phosphorylation of the cAMP-dependent protein kinase (PKA) regulatory subunit modulates PKA-AKAP interaction, substrate phosphorylation, and calcium signaling in cardiac cells. *JBiolChem* **283**, 24145–24154.

- Marban E & Wier WG (1985). Ryanodine as a tool to determine the contributions of calcium entry and calcium release to the calcium transient and contraction of cardiac Purkinje fibers. *Circ Res* **56**, 133–138.
- Marks AR, Marx SO & Reiken S (2002). Regulation of ryanodine receptors via macromolecular complexes: a novel role for leucine/isoleucine zippers. *Trends Cardiovasc Med* **12**, 166–170.
- Marks AR, Reiken S & Marx SO (2014). Progression of Heart Failure: Is Protein Kinase A Hyperphosphorylation of the Ryanodine Receptor a Contributing Factor? Andrew R. Marks, Steven Reiken and Steven O. Marx *Circulation*. 2002;105:272-275. 272–275.
- Marx SO, Ondrias K & Marks A (1998). Coupled Gating Between Individual Skeletal Muscle Ca²⁺ Release Channels (Ryanodine Receptors). *Science (80-)* **281**, 818–821.
- Marx SO, Reiken S, Hisamatsu Y, Jayaraman T, Burkhoff D, Rosemblyt N & Marks AR (2000). PKA phosphorylation dissociates FKBP12.6 from the calcium release channel (ryanodine receptor): defective regulation in failing hearts. *Cell* **101**, 365–376.
- Matsuoka S & Hilgemann DW (1992). Steady-state and dynamic properties of cardiac sodium-calcium exchange. Ion and voltage dependencies of the transport cycle. *J Gen Physiol* **100**, 963–1001.
- McKay RG, Pfeffer M a., Pasternak RC, Markis JE, Come PC, Nakao S, Alderman JD, Ferguson JJ, Safian RD & Grossman W (1986). Left ventricular remodeling after myocardial infarction: a corollary to infarct expansion. *Circulation* **74**, 693–702.
- Meissner G (1986). Ryanodine activation and inhibition of the Ca²⁺ release channel of sarcoplasmic reticulum. *J Biol Chem* **261**, 6300–6306.
- Meissner G (1994). Ryanodine receptor/Ca²⁺ release channels and their regulation by endogenous effectors. *Annu Rev Physiol* **56**, 485–508.
- Mejia-Alvarez R, Kettlun C, Rios E, Stern M & Fill M (1999). Unitary Ca²⁺ current through cardiac ryanodine receptor channels under quasi-physiological ionic conditions. *J GenPhysiol* **113**, 177–186.
- Mercer EN & Dower GE (1966). NORMAL AND ARRHYTHMIC BEATING IN ISOLATED CULTURED HEART CELLS AND THE EFFECTS OF DIGOXIN, QUINIDINE AND PROCAINE AMIDE. *J Pharmacol Exp Ther* **153**, 203–210.
- Merillat JC, Lakatta EG, Hano O & Guarnieri T (1990). Role of calcium and the calcium channel in the initiation and maintenance of ventricular fibrillation. *Circ Res* **67**, 1115–1123.
- Miller SG & Kennedy MB (1986). Regulation of brain type II Ca²⁺/calmodulin-dependent protein kinase by autophosphorylation: a Ca²⁺-triggered molecular switch. *Cell* **44**, 861–870.
- Mitchell GF, Lamas G a, Vaughan DE & Pfeffer M a (1992). Left ventricular remodeling in the year after first anterior myocardial infarction: a quantitative analysis of contractile segment lengths and ventricular shape. *J Am Coll Cardiol* **19**, 1136–1144.

- Miyata S, Minobe W, Bristow MR & Leinwand L a. (2000). Myosin Heavy Chain Isoform Expression in the Failing and Nonfailing Human Heart. *Circ Res* **86**, 386–390.
- Del Monte F, O’Gara P, Poole-Wilson PA, Yacoub M & Harding S (1995). Cell geometry and contractile abnormalities of myocytes from failing human left ventricle. *Cardiovasc ...* **30**, 281–290.
- Mørk H, Sjaastad I, Sejersted OM & Louch WE (2009). Slowing of cardiomyocyte Ca²⁺ release and contraction during heart failure progression in postinfarction mice. *Am J Physiol - Hear Circ Physiol* **296**, H1069–H1079.
- Mørk HK, Sjaastad I, Sande JB, Periasamy M, Sejersted OM & Louch WE (2007). Increased cardiomyocyte function and Ca²⁺ transients in mice during early congestive heart failure. *J Mol Cell Cardiol* **43**, 177–186.
- Mozaffarian D, Anker SD, Anand I, Linker DT, Sullivan MD, Cleland JG, Carson PE, Maggioni AP, Mann DL, Pitt B, Poole-Wilson PA & Levy WC (2007). Prediction of mode of death in heart failure: the Seattle Heart Failure Model. *Circulation* **116**, 392–398.
- Nahrendorf M, Wiesmann F, Hiller KH, Hu K, Waller C, Ruff J, Lanz TE, Neubauer S, Haase a, Ertl G & Bauer WR (2001). Serial cine-magnetic resonance imaging of left ventricular remodeling after myocardial infarction in rats. *J Magn Reson Imaging* **14**, 547–555.
- Narula J & Haider N (1996). Apoptosis in myocytes in end-stage heart failure. ... *Engl J*
- National Clinical Guideline Centre (2010). *National Clinical Guideline Centre. (2010) Chronic heart failure: the management of chronic heart failure in adults in primary and secondary care. London: National Clinical Guideline Centre. Available from: <http://guidance.nice.org.uk/CG108/Guidance/pdf/E>.*
- NHS England (2009). *NHS Information Centre, Lifestyle Statistics. Statistics on Alcohol: England, 2009. UK: Health and Social Care Information Centre.*
- Nitta J, Sunami a, Marumo F & Hiraoka M (1992). States and sites of actions of flecainide on guinea-pig cardiac sodium channels. *Eur J Pharmacol* **214**, 191–197.
- Noma K, Brändle M & Jacob R (1988). Evaluation of left ventricular function in an experimental model of congestive heart failure due to combined pressure and volume overload. *Basic Res Cardiol* **83**, 58–64.
- O’Flaherty M & Bishop J (2009). Coronary heart disease mortality among young adults in Scotland in relation to social inequalities: time trend study. *BMJ Br Med ...* **9**, b2613.
- Oda T, Yano M, Yamamoto T, Tokuhisa T, Okuda S, Doi M, Ohkusa T, Ikeda Y, Kobayashi S, Ikemoto N & Matsuzaki M (2005). Defective regulation of interdomain interactions within the ryanodine receptor plays a key role in the pathogenesis of heart failure. *Circulation* **111**, 3400–3410.
- Okuda S, Yano M, Doi M, Oda T, Tokuhisa T, Kohno M, Kobayashi S, Yamamoto T, Ohkusa T & Matsuzaki M (2004). Valsartan restores sarcoplasmic reticulum function with no appreciable effect on resting cardiac function in pacing-induced heart failure. *Circulation* **109**, 911–919.

- Olivetti G, Capasso JM, Meggs LG, Sonnenblick EH & Anversa P (1991). Cellular basis of chronic ventricular remodeling after myocardial infarction in rats. *Circ Res* **68**, 856–869.
- Omichi C, Lamp ST, Lin SF, Yang J, Baher A, Zhou S, Attin M, Lee MH, Karagueuzian HS, Kogan B, Qu Z, Garfinkel A, Chen PS & Weiss JN (2004). Intracellular Ca dynamics in ventricular fibrillation. *Am J Physiol - Hear Circ Physiol* **286**, H1836–H1844.
- Van Oort RJ, McCauley MD, Dixit SS, Pereira L, Yang Y, Respress JL, Wang Q, De Almeida AC, Skapura DG, Anderson ME, Bers DM & Wehrens XHT (2010). Ryanodine receptor phosphorylation by calcium/calmodulin-dependent protein kinase II promotes life-threatening ventricular arrhythmias in mice with heart failure. *Circulation* **122**, 2669–2679.
- Oreopoulos A, Padwal R, Kalantar-Zadeh K, Fonarow GC, Norris CM & McAlister F a (2008). Body mass index and mortality in heart failure: a meta-analysis. *Am Heart J* **156**, 13–22.
- Osterrieder W, Brum G, Hescheler J, Trautwein W, Flockerzi V & Hofmann F (1982). Injection of subunits of cyclic AMP-dependent protein kinase into cardiac myocytes modulates Ca²⁺ current. *Nature* **298**, 576–578.
- Owan TE, Hodge DO, Herges RM, Jacobsen SJ, Roger VL & Redfield MM (2006). Trends in prevalence and outcome of heart failure with preserved ejection fraction. *NEnglJMed* **355**, 251–259.
- Pacher P, Nagayama T, Mukhopadhyay P, Bátkai S & Kass D a (2008). Measurement of cardiac function using pressure-volume conductance catheter technique in mice and rats. *Nat Protoc* **3**, 1422–1434.
- Park J, Lyon A, Hector L & Griffiths M (2009). MECHANICAL STRAIN AT THE PULMONARY MICROVASCULATURE INDUCES MONOCYTE CHEMOATTRACTANT PROTEIN-1 WHICH CONTRIBUTES TO PULMONARY INFLAMMATION AND REMODELLING IN CHRONIC HEART FAILURE. *Thorax* **64**, A58.
- Park S & Lake ET (2005). Multilevel Modeling of a Clustered Continuous Outcome. *Nurs Res* **54**, 406–413.
- Perrier E, Kerfant B-G, Lalevee N, Bideaux P, Rossier MF, Richard S, Gómez AM & Benitah J-P (2004). Mineralocorticoid receptor antagonism prevents the electrical remodeling that precedes cellular hypertrophy after myocardial infarction. *Circulation* **110**, 776–783.
- Peters NS, Coromilas J, Severs NJ & Wit AL (1997). Disturbed Connexin43 Gap Junction Distribution Correlates With the Location of Reentrant Circuits in the Epicardial Border Zone of Healing Canine Infarcts That Cause Ventricular Tachycardia. *Circulation* **95**, 988–996.
- Peterson JT, Li H, Dillon L & Bryant JW (2000). Evolution of matrix metalloprotease and tissue inhibitor expression during heart failure progression in the infarcted rat. *Cardiovasc Res* **46**, 307–315.
- Pfeffer JM, Pfeffer M a, Fletcher PJ & Braunwald E (1991). Progressive ventricular remodeling in rat with myocardial infarction. *Am J Physiol* **260**, H1406–H1414.
- Pfeffer JM, Pfeffer MA & Braunwald E (1985a). Influence of chronic captopril therapy on the infarcted left ventricle of the rat. *Circ Res* **57**, 84–95.

- Pfeffer M a., Pfeffer JM, Steinberg C, Finn P, Desk R, Williams L & Health K (1985b). Survival after an experimental myocardial infarction: beneficial effects of long-term therapy with captopril. *Circulation* **72**, 406–412.
- Picht E, Zima A V, Blatter LA & Bers DM (2007). SparkMaster: automated calcium spark analysis with ImageJ. *Am J Physiol Cell Physiol* **293**, C1073–C1081.
- Pickering JD, White E, Duke AM & Steele DS (2009). DHPR activation underlies SR Ca²⁺ release induced by osmotic stress in isolated rat skeletal muscle fibers. *J Gen Physiol* **133**, 511–524.
- Pieske B, Hasenfuss G, Holubarsch C, Schwinger R, Böhm M & Just H (1992). Alterations of the force-frequency relationship in the failing human heart depend on the underlying cardiac disease. *Basic Res Cardiol* **87 Suppl 1**, 213–221.
- Pogwizd SM, Schlotthauer K, Li L, Yuan W & Bers DM (2001). Arrhythmogenesis and contractile dysfunction in heart failure: Roles of sodium-calcium exchange, inward rectifier potassium current, and residual beta-adrenergic responsiveness. *Circ Res* **88**, 1159–1167.
- Poláková E & Sobie E a (2013). Alterations in T-tubule and dyad structure in heart disease: challenges and opportunities for computational analyses. *Cardiovasc Res* **98**, 233–239.
- Prabhu S & Rozek M (1997). Ryanodine and left ventricular function in intact dogs: dissociation of force-based and velocity-based indexes. *Am J Physiol* **273**, H1561–H1568.
- Priori SG & Chen SRW (2011). Inherited dysfunction of sarcoplasmic reticulum Ca²⁺ handling and arrhythmogenesis. *Circ Res* **108**, 871–883.
- Putney JW (1998). Calcium Signaling: Up, Down, Up, Down.... What's the Point? *Science (80-)* **279**, 191–192.
- Qu Z, Weiss JN & Garfinkel A (1999). Cardiac electrical restitution properties and stability of reentrant spiral waves: a simulation study. *Am J Physiol - Hear Circ Physiol* **276**, H269–H283.
- Raudenbush SW & Bryk AS (2002). *Hierarchical linear models: Applications and data analysis methods*, 2nd edn. Sage, Thousand Oaks, CA.
- Raya TE, Gay RG, Aguirre M & Goldman S (1989). Importance of venodilatation in prevention of left ventricular dilatation after chronic large myocardial infarction in rats: a comparison of captopril and hydralazine. *Circ Res* **64**, 330–337.
- Reid DS, Tynan M, Braidwood L & Fitzgerald GR (1975). Bidirectional tachycardia in a child. A study using His bundle electrography. *Br Heart J* **37**, 339–344.
- Reiken S, Gaburjakova M, Gaburjakova J, He K -I., Prieto A, Becker E, Yi G -h., Wang J, Burkhoff D & Marks a. R (2001). Beta-Adrenergic Receptor Blockers Restore Cardiac Calcium Release Channel (Ryanodine Receptor) Structure and Function in Heart Failure. *Circulation* **104**, 2843–2848.
- Reiken S, Wehrens XHT, Vest J a, Barbone A, Klotz S, Mancini D, Burkhoff D & Marks AR (2003). Beta-blockers restore calcium release channel function and improve cardiac muscle performance in human heart failure. *Circulation* **107**, 2459–2466.

- Respress JL, van Oort RJ, Li N, Rolim N, Dixit SS, deAlmeida A, Voigt N, Lawrence WS, Skapura DG, Skårðal K, Wisløff U, Wieland T, Ai X, Pogwizd SM, Dobrev D & Wehrens XHT (2012). Role of RyR2 phosphorylation at S2814 during heart failure progression. *Circ Res* **110**, 1474–1483.
- Reuter H (1974). Localization of beta adrenergic receptors, and effects of noradrenaline and cyclic nucleotides on action potentials, ionic currents and tension in mammalian cardiac muscle. *J Physiol* **242**, 429–451.
- Ritter M, Sui Z, Philipson KD, Li F, Spitzer KW, Ishida H & Barry WH (2003). Ca²⁺ sparks induced by Na/Ca exchange. *Cell Calcium* **34**, 11–17.
- Robinson W (1950). Ecological correlations and the behavior of individuals. *Am Sociol Rev* **15**, 351–357.
- Rousseau E, Smith JS & Meissner G (1987). Ryanodine modifies conductance and gating behavior of single Ca²⁺ release channel. *Am J Physiol* **253**, C364–C368.
- Sande JB, Sjaastad I, Hoen IB, Bøkenes J, Tønnessen T, Holt E, Lunde PK & Christensen G (2002). Reduced level of serine(16) phosphorylated phospholamban in the failing rat myocardium: a major contributor to reduced SERCA2 activity. *Cardiovasc Res* **53**, 382–391.
- Saraiva RM, Chedid NGB, Quintero H CC, Díaz G LE & Masuda MO (2003). Impaired beta-adrenergic response and decreased L-type calcium current of hypertrophied left ventricular myocytes in postinfarction heart failure. *Braz J Med Biol Res* **36**, 635–648.
- Sato M, O’Gara P, Harding SE & Fuller SJ (2005). Enhancement of adenoviral gene transfer to adult rat cardiomyocytes in vivo by immobilization and ultrasound treatment of the heart. *Gene Ther* **12**, 936–941.
- Schlotthauer K & Bers DM (2000). Sarcoplasmic Reticulum Ca²⁺ Release Causes Myocyte Depolarization : Underlying Mechanism and Threshold for Triggered Action Potentials. *Circ Res* **87**, 774–780.
- Schmidt A, Azevedo CF, Cheng A, Gupta SN, Bluemke D a, Foo TK, Gerstenblith G, Weiss RG, Marbán E, Tomaselli GF, Lima J a C & Wu KC (2007). Infarct tissue heterogeneity by magnetic resonance imaging identifies enhanced cardiac arrhythmia susceptibility in patients with left ventricular dysfunction. *Circulation* **115**, 2006–2014.
- Schulte LM, Navarro J & Kandarian SC (1993). Regulation of sarcoplasmic reticulum calcium pump gene expression by hindlimb unweighting. *Am J Physiol* **264**, C1308–C1315.
- Selvin H (1958). Durkheim’s Suicide and problems of empirical research. *Am J Sociol* **63**, 607–619.
- Semb SO, Lunde PK, Holt E, Tønnessen T, Christensen G & Sejersted OM (1998). Reduced myocardial Na⁺, K⁽⁺⁾-pump capacity in congestive heart failure following myocardial infarction in rats. *J Mol Cell Cardiol* **30**, 1311–1328.
- Shan J, Betzenhauser MJ, Kushnir A, Reiken S, Meli AC, Wronska A, Dura M, Chen BX & Marks AR (2010a). Role of chronic ryanodine receptor phosphorylation in heart failure and beta-adrenergic receptor blockade in mice. *J Clin Invest* **120**, 4375–4387.

- Shan J, Kushnir A, Betzenhauser MJ, Reiken S, Li J, Lehnart SE, Lindegger N, Mongillo M, Mohler PJ & Marks AR (2010b). Phosphorylation of the ryanodine receptor mediates the cardiac fight or flight response in mice. *J Clin Invest* **120**, 4388–4398.
- Shannon TR, Ginsburg KS & Bers DM (2000). Reverse mode of the sarcoplasmic reticulum calcium pump and load-dependent cytosolic calcium decline in voltage-clamped cardiac ventricular myocytes. *Biophys J* **78**, 322–333.
- Shannon TR, Pogwizd SM & Bers DM (2003). Elevated Sarcoplasmic Reticulum Ca²⁺ Leak in Intact Ventricular Myocytes From Rabbits in Heart Failure. *Circ Res* **93**, 592–594.
- Shkryl VM, Blatter LA & Ríos E (2012). Properties of Ca²⁺ sparks revealed by four-dimensional confocal imaging of cardiac muscle. *J Gen Physiol* **139**, 189–207.
- Shorofsky S, Aggarwal R & Corretti M (1999). Cellular Mechanisms of Altered Contractility in the Hypertrophied Heart Big Hearts, Big Sparks. *Circ ...* **84**, 424–434.
- Sikkel MB, Collins TP, Rowlands C, Shah M, O’Gara P, Williams AJ, Harding SE, Lyon AR & MacLeod KT (2013a). Flecainide reduces Ca²⁺ spark and wave frequency via inhibition of the sarcolemmal sodium current. *Cardiovasc Res* **98**, 286–296.
- Sikkel MB, Hayward C, Macleod KT, Harding SE & Lyon AR (2014). SERCA2a Gene Therapy in Heart Failure - An Anti-arrhythmic Positive Inotrope. *Br J Pharmacol* **171**, 38–54.
- Sikkel MB, Macleod KT & Gordon F (2013b). Letter by Sikkel et Al regarding article, “late sodium current inhibition reverses electromechanical dysfunction in human hypertrophic cardiomyopathy”. *Circulation* **128**, e156.
- De Simone G, Daniels SR, Devereux RB, Meyer R a, Roman MJ, de Divitiis O & Alderman MH (1992). Left ventricular mass and body size in normotensive children and adults: assessment of allometric relations and impact of overweight. *J Am Coll Cardiol* **20**, 1251–1260.
- Siri FM, Krueger J, Nordin C, Ming Z, Aronson RS & Aronson RS (2013). Depressed intracellular calcium transients and contraction in myocytes from hypertrophied and failing guinea pig hearts Depressed intracellular calcium transients and contraction in myocytes from hypertrophied and failing guinea pig hearts. 1522–1539.
- Skeberdis V, Jurevičius J & Fischmeister R (1997). Beta-2 adrenergic activation of L-type Ca⁺⁺ current in cardiac myocytes. *J Pharmacol ...* **283**, 452–461.
- Smith GD, Keizer JE, Stern MD, Lederer WJ & Cheng H (1998). A simple numerical model of calcium spark formation and detection in cardiac myocytes. *Biophys J* **75**, 15–32.
- Song L, Sobie EA, McCulle S, Lederer WJ, Balke CW & Cheng H (2006). Orphaned ryanodine receptors in the failing heart. *Proc Natl Acad Sci USA* **103**, 4305–4310.
- Song L-S, Pi Y, Kim S-J, Yatani A, Guatimosim S, Kudej RK, Zhang Q, Cheng H, Hittinger L, Ghaleh B, Vatner DE, Lederer WJ & Vatner SF (2005). Paradoxical cellular Ca²⁺ signaling in severe but compensated canine left ventricular hypertrophy. *Circ Res* **97**, 457–464.

- Song LS, Stern MD, Lakatta EG & Cheng H (1997). Partial depletion of sarcoplasmic reticulum calcium does not prevent calcium sparks in rat ventricular myocytes. *J Physiol* **505** (Pt 3, 665–675.
- Soppa GKR, Lee J, Stagg M a, Felkin LE, Barton PJR, Siedlecka U, Youssef S, Yacoub MH & Terracciano CMN (2008). Role and possible mechanisms of clenbuterol in enhancing reverse remodelling during mechanical unloading in murine heart failure. *Cardiovasc Res* **77**, 695–706.
- Sossalla S, Fluschnik N, Schotola H, Ort KR, Neef S, Schulte T, Wittkopper K, Renner A, Schmitto JD, Gummert J, El-Armouche A, Hasenfuss G & Maier LS (2010). Inhibition of Elevated Ca²⁺/Calmodulin-Dependent Protein Kinase II Improves Contractility in Human Failing Myocardium. *Circ Res* **107**, 1150–1161.
- Stern M & Lakatta E (1992). Excitation-contraction coupling in the heart: the state of the question. *FASEB J* **6**, 3092–3100.
- Stern MD & Cheng H (2004). Putting out the fire: what terminates calcium-induced calcium release in cardiac muscle? *Cell Calcium* **35**, 591–601.
- Stern MD, Kort AA, Bhatnagar GM & Lakatta EG (1983). Scattered-Light Intensity Fluctuations in Diastolic Rat Cardiac Muscle Cellular Mechanical Oscillations.
- Stewart PS & MacLennan DH (1974). Surface particles of sarcoplasmic reticulum membranes. Structural features of the adenosine triphosphatase. *JBiolChem* **249**, 985–993.
- Subramanian S V, Jones K, Kaddour A & Krieger N (2009). Revisiting Robinson: the perils of individualistic and ecologic fallacy. *Int J Epidemiol* **38**, 342–360; author reply 370–373.
- Suga H (2003). Muscle Mechanics and Energetics : A Comparative View CARDIAC ENERGETICS : FROM E MAX TO PRESSURE – VOLUME AREA. 580–585.
- Suga H, Igarashi Y, Yamada O & Goto Y (1985). Mechanical efficiency of the left ventricle as a function of preload, afterload, and contractility. *Heart Vessels* 3–8.
- Suga H, Sagawa K & Shoukas a. a. (1973). Load Independence of the Instantaneous Pressure-Volume Ratio of the Canine Left Ventricle and Effects of Epinephrine and Heart Rate on the Ratio. *Circ Res* **32**, 314–322.
- Sutko JL, Airey JA, Welch W & Ruest L (1997). The Pharmacology of Ryanodine and Related Compounds. *Pharmacol Rev* **49**, 53–98.
- Tada M, Kirchberger MA & Katz AM (1975). Phosphorylation of a 22,000-dalton component of the cardiac sarcoplasmic reticulum by adenosine 3':5'-monophosphate-dependent protein kinase. *JBiolChem* **250**, 2640–2647.
- Takahashi N, Sasaki T, Matsumoto W, Matsuki N & Ikegaya Y (2010). Circuit topology for synchronizing neurons in spontaneously active networks. *Proc Natl Acad Sci U S A* **107**, 10244–10249.
- Takahashi S, Barry a C & Factor SM (1990). Collagen degradation in ischaemic rat hearts. *Biochem J* **265**, 233–241.

- Takamatsu T & Wier W (1990). Calcium waves in mammalian heart: quantification of origin, magnitude, waveform, and velocity. *FASEB J* **4**, 1519–1525.
- Takasago T, Imagawa T, Furukawa K, Ogurusu T & Shigekawa M (1991). Regulation of the cardiac ryanodine receptor by protein kinase-dependent phosphorylation. *JBiochem* **109**, 163–170.
- Takeshima H, Nishimura S & Matsumoto T (1989). Primary structure and expression from complementary DNA of skeletal muscle ryanodine receptor. *Nature* **339**, 439–445.
- Talosi L, Edes I & Kranias EG (1993). Intracellular mechanisms mediating reversal of beta-adrenergic stimulation in intact beating hearts. *AmJPhysiol* **264**, H791–H797.
- Terracciano CM & Hancox JC (2013). ORM-10103: a significant advance in sodium-calcium exchanger pharmacology? *Br J Pharmacol* **170**, 765–767.
- Terracciano CM & Macleod KT (1996). Reloading of Ca²⁺-depleted sarcoplasmic reticulum during rest in guinea pig ventricular myocytes. *Am J Physiol - Hear Circ Physiol* **40**, H1814–H1822.
- Thandroyen FT, McCarthy J, Burton KP & Opie LH (1988). Ryanodine and caffeine prevent ventricular arrhythmias during acute myocardial ischemia and reperfusion in rat heart. *Circ Res* **62**, 306–314.
- Thireau J, Karam S, Fauconnier J, Roberge S, Cassan C, Cazorla O, Aimond F, Lacampagne A, Babuty D & Richard S (2012). Functional evidence for an active role of B-type natriuretic peptide in cardiac remodelling and pro-arrhythmogenicity. *Cardiovasc Res* **95**, 59–68.
- Thum Y (1997). Hierarchical linear models for multivariate outcomes. *J Educ Behav Stat* **22**, 77–108.
- Timerman a. P, Onoue H, Xin H-B, Barg S, Copello J, Wiederrecht G & Fleischer S (1996). Selective Binding of FKBP12.6 by the Cardiac Ryanodine Receptor. *J Biol Chem* **271**, 20385–20391.
- Toischer K et al. (2010). Differential cardiac remodeling in preload versus afterload. *Circulation* **122**, 993–1003.
- Tomaselli GF, Marbán E & Marban E (1999). Electrophysiological remodeling in hypertrophy and heart failure. *Cardiovasc Res* **42**, 270–283.
- Trafford AW, Diaz ME, Sibbring GC & Eisner DA (2000). Modulation of CICR has no maintained effect on systolic Ca²⁺: simultaneous measurements of sarcoplasmic reticulum and sarcolemmal Ca²⁺ fluxes in rat ventricular myocytes. *JPhysiol* **522 Pt 2**, 259–270.
- Ullah A, Hoang-Trong TM, Williams G, Winslow RL, Lederer JW & Jafri MS (2014). Critical Requirements for the Initiation of a Cardiac Arrhythmia in Heart: Cell Number. *Biophys J* **106**, 431a.
- Ursell PC, Gardner PI, Albala a., Fenoglio JJ & Wit a. L (1985). Structural and electrophysiological changes in the epicardial border zone of canine myocardial infarcts during infarct healing. *Circ Res* **56**, 436–451.
- Valdivia HH, Kaplan JH, Ellis-Davies GC & Lederer WJ (1995). Rapid adaptation of cardiac ryanodine receptors: modulation by Mg²⁺ and phosphorylation. *Science (80-)* **267**, 1997–2000.

- Vassort G & Lacampagne A (2005). The role of ryanodine receptors and consequences of their alterations during cardiac insufficiency. *Exp Clin Cardiol* **10**, 196–199.
- Venetucci L a, Trafford a W, Díaz ME, O'Neill SC & Eisner D a (2006). Reducing ryanodine receptor open probability as a means to abolish spontaneous Ca²⁺ release and increase Ca²⁺ transient amplitude in adult ventricular myocytes. *Circ Res* **98**, 1299–1305.
- Volders PGA, Vos MA, Szabo B, Sipido KR, de Groot SHM, Gorgels APM, Wellens HJJ & Lazzara R (2000). Progress in the understanding of cardiac early afterdepolarizations and torsades de pointes: time to revise current concepts. *Cardiovasc Res* **46**, 376–392.
- Wagner E, Lauterbach M a, Kohl T, Westphal V, Williams GSB, Steinbrecher JH, Streich J-H, Korff B, Tuan H-TM, Hagen B, Luther S, Hasenfuss G, Parlitz U, Jafri MS, Hell SW, Lederer WJ & Lehnart SE (2012). Stimulated emission depletion live-cell super-resolution imaging shows proliferative remodeling of T-tubule membrane structures after myocardial infarction. *Circ Res* **111**, 402–414.
- Watanabe H, Chopra N, Laver D, Hwang HS, Davies SS, Roach DE, Duff HJ, Roden DM, Wilde A a M & Knollmann BC (2009). Flecainide prevents catecholaminergic polymorphic ventricular tachycardia in mice and humans. *Nat Med* **15**, 380–383.
- Wehrens XH, Lehnart SE, Reiken S, van der Nagel R, Morales R, Sun J, Cheng Z, Deng SX, de Windt LJ, Landry DW & Marks AR (2005a). Enhancing calstabin binding to ryanodine receptors improves cardiac and skeletal muscle function in heart failure. *Proc Natl Acad Sci USA* **102**, 9607–9612.
- Wehrens XHT, Lehnart SE & Marks AR (2005b). Intracellular calcium release and cardiac disease. *Annu Rev Physiol* **67**, 69–98.
- Wehrens XHT, Lehnart SE, Reiken SR & Marks AR (2004). Ca²⁺/calmodulin-dependent protein kinase II phosphorylation regulates the cardiac ryanodine receptor. *Circ Res* **94**, e61–e70.
- Weiss JN, Nivala M, Garfinkel A & Qu Z (2011). Alternans and arrhythmias: from cell to heart. *Circ Res* **108**, 98–112.
- Van der Werf C, Kannankeril PJ, Sacher F, Krahn AD, Viskin S, Leenhardt A, Shimizu W, Sumitomo N, Fish FA, Bhuiyan ZA, Willems AR, van der Veen MJ, Watanabe H, Laborderie J, Haissaguerre M, Knollmann BC & Wilde AA (2011). Flecainide therapy reduces exercise-induced ventricular arrhythmias in patients with catecholaminergic polymorphic ventricular tachycardia. *J Am Coll Cardiol* **57**, 2244–2254.
- Van der Werf C, Zwilander AH & Wilde A a M (2012). Therapeutic approach for patients with catecholaminergic polymorphic ventricular tachycardia: state of the art and future developments. *Europace* **14**, -.
- Wolleschensky R, Zimmermann B & Kempe M (2013). High-speed confocal fluorescence imaging with a novel line scanning microscope. *J Biomed Opt* **11**, 064011.
- Wuytack F, Raeymaekers L & Missiaen L (2002). Molecular physiology of the SERCA and SPCA pumps. **32**, 279–305.

- Xiao B, Sutherland C, Walsh MP & Chen SRW (2004). Protein kinase A phosphorylation at serine-2808 of the cardiac Ca²⁺-release channel (ryanodine receptor) does not dissociate 12.6-kDa FK506-binding protein (FKBP12.6). *Circ Res* **94**, 487–495.
- Xiao RP & Lakatta EG (1993). Beta 1-adrenoceptor stimulation and beta 2-adrenoceptor stimulation differ in their effects on contraction, cytosolic Ca²⁺, and Ca²⁺ current in single rat ventricular cells. *Circ Res* **73**, 286–300.
- Yamamoto T, Yano M, Xu X, Uchinoumi H, Tateishi H, Mochizuki M, Oda T, Kobayashi S, Ikemoto N & Matsuzaki M (2008). Identification of Target Domains of the Cardiac Ryanodine Receptor to Correct Channel Disorder in Failing Hearts. *Circulation* **117**, 762–772.
- Yan AT, Shayne AJ, Brown K a, Gupta SN, Chan CW, Luu TM, Di Carli MF, Reynolds HG, Stevenson WG & Kwong RY (2006). Characterization of the peri-infarct zone by contrast-enhanced cardiac magnetic resonance imaging is a powerful predictor of post-myocardial infarction mortality. *Circulation* **114**, 32–39.
- Yano M, Kobayashi S, Kohno M, Doi M, Tokuhisa T, Okuda S, Suetsugu M, Hisaoka T, Obayashi M, Ohkusa T & Matsuzaki M (2003). FKBP12.6-mediated stabilization of calcium-release channel (ryanodine receptor) as a novel therapeutic strategy against heart failure. *Circulation* **107**, 477–484.
- Yano M, Ono K, Ohkusa T, Suetsugu M, Kohno M, Hisaoka T, Kobayashi S, Hisamatsu Y, Yamamoto T, Noguchi N, Takasawa S, Okamoto H & Matsuzaki M (2000). Altered Stoichiometry of FKBP12.6 Versus Ryanodine Receptor as a Cause of Abnormal Ca²⁺ Leak Through Ryanodine Receptor in Heart Failure. *Circulation* **102**, 2131–2136.
- Yano M, Yamamoto T, Ikeda Y & Matsuzaki M (2006). Mechanisms of Disease: ryanodine receptor defects in heart failure and fatal arrhythmia. *Nat Clin Pract Cardiovasc Med* **3**, 43–52.
- Yao L, Fan P, Jiang Z, Viatchenko-Karpinski S, Wu Y, Kornyejev D, Hirakawa R, Budas GR, Rajamani S, Shryock JC & Belardinelli L (2011). Nav1.5-dependent persistent Na⁺ influx activates CaMKII in rat ventricular myocytes and N1325S mice. *AmJPhysiol Cell Physiol* **301**, C577–C586.
- Yoshida H, Tanonaka K, Miyamoto Y, Abe T, Takahashi M, Anand-Srivastava MB & Takeo S (2001). Characterization of cardiac myocyte and tissue beta-adrenergic signal transduction in rats with heart failure. *Cardiovasc Res* **50**, 34–45.
- Zafeiridis a., Jeevanandam V, Houser SR & Margulies KB (1998). Regression of Cellular Hypertrophy After Left Ventricular Assist Device Support. *Circulation* **98**, 656–662.
- Zalvidea S, André L, Loyer X, Cassan C, Sainte-Marie Y, Thireau J, Sjaastad I, Heymes C, Pasquié J-L, Cazorla O, Aimond F & Richard S (2012). ACE inhibition prevents diastolic Ca²⁺ overload and loss of myofilament Ca²⁺ sensitivity after myocardial infarction. *Curr Mol Med* **12**, 206–217.
- Zeng J & Rudy Y (1995). Early afterdepolarizations in cardiac myocytes: mechanism and rate dependence. *BiophysJ* **68**, 949–964.
- Zhang XQ, Moore RL, Tenhave T & Cheung JY (1995). [Ca²⁺]_i transients in hypertensive and postinfarction myocytes. *Am J Physiol* **269**, C632–C640.

- Zhao W, Uehara Y, Chu G, Song Q, Qian J, Young K & Kranias EG (2004). Threonine-17 phosphorylation of phospholamban: a key determinant of frequency-dependent increase of cardiac contractility. *J Mol Cell Cardiol* **37**, 607–612.
- Zhao Z, Wen H, Fefelova N, Allen C, Baba A, Matsuda T & Xie L-H (2012). Revisiting the ionic mechanisms of early afterdepolarizations in cardiomyocytes: predominant by Ca waves or Ca currents? *Am J Physiol Heart Circ Physiol* **302**, H1636–H1644.
- Zhou L, Aon M a, Liu T & O'Rourke B (2011a). Dynamic modulation of Ca²⁺ sparks by mitochondrial oscillations in isolated guinea pig cardiomyocytes under oxidative stress. *J Mol Cell Cardiol* **51**, 632–639.
- Zhou Q et al. (2011b). Carvedilol and its new analogs suppress arrhythmogenic store overload-induced Ca²⁺ release. *Nat Med* **17**, 1003–1009.
- Zhou YY, Song LS, Lakatta EG, Xiao RP & Cheng H (1999). Constitutive beta2-adrenergic signalling enhances sarcoplasmic reticulum Ca²⁺ cycling to augment contraction in mouse heart. *J Physiol* **521 Pt 2**, 351–361.
- Zima A V & Blatter L a (2006). Redox regulation of cardiac calcium channels and transporters. *Cardiovasc Res* **71**, 310–321.
- Zima A V, Bovo E, Bers DM & Blatter L a (2010). Ca²⁺ spark-dependent and -independent sarcoplasmic reticulum Ca²⁺ leak in normal and failing rabbit ventricular myocytes. *J Physiol* **588**, 4743–4757.
- Zima A V, Picht E, Bers DM & Blatter LA (2008). Partial Inhibition of Sarcoplasmic Reticulum Ca Release Evokes Long-Lasting Ca Release Events in Ventricular Myocytes: Role of Luminal Ca in Termination of Ca Release. *Biophys J* **94**, 1867–1879.
- Zissimopoulos S, Docrat N & Lai FA (2007). Redox sensitivity of the ryanodine receptor interaction with FK506-binding protein. *JBiolChem* **282**, 6976–6983.